MECHANISM OF INTERNAL OXIDATION OF ALLOY 617 IN CONTROLLED IMPURITY HELIUM ENVIRONMENTS AT HIGH TEMPERATURES

by

Gokce Gulsoy

A dissertation submitted in partial fulfillment
of the requirements for the degree of
Doctor of Philosophy
(Materials Science and Engineering)
in the University of Michigan
2014

Doctoral Committee:

Professor Gary S. Was, Chairman
Professor Michael Atzmon
Professor J. Wayne Jones
Adjunct Professor Anton Van der Ven

© Gokce Gulsoy
All Rights Reserved 2014

To my parents

ACKNOWLEDGEMENTS

First and foremost, I would like to thank my academic advisor and the chair of my dissertation committee, Dr. Gary S. Was, for his continuous support and invaluable guidance in completing this work. I would also like to offer my sincere thanks to my dissertation committee members Dr. Michael Atzmon, Dr. J. Wayne Jones and Dr. Anton Van der Ven for providing constructive critique to my thesis research and to my dissertation.

I am very thankful to Mr. Harald Eberhart for fabricating all the essential quartz parts in my experimental setup. I would like to specially thank Dr. Ovidiu Toader for his assistance with the preparation of the Rhines pack experiment setup. I am also deeply grateful to Dr. Zhijie Jiao and Dr. Kai Sun for their assistance with my TEM work. Special gratitude is also extended to Mr. Alexander Flick for his assistance and help at HTCL for my experiments.

I would like to thank to my colleagues Dr. Deepak Kumar, Dr. Elaine A. West, Dr. Pantip Ampornrat, Dr. Janelle J. Penisten Wharry, Dr. Anne Campbell, Dr. Yugo Ashida, Dr. Peng Wang, Mike McMurtrey, Cheng Xu, Kale Stephenson, Tyler Moss, Stephen Raiman, Shyam Dwaraknath, Elizabeth Beckett, and Alfred Okello for their encouragement, support and many useful intellectual discussions we have had throughout my time in the graduate school.

I would like to express my deep gratitude to Dr. Christine Feak for her guidance to improve my academic writing style and for the excellent critique she provided to my manuscripts and dissertation.

I owe a great deal to Xiao Guo for her continuous support and patience especially before my thesis defense, and to my dearest friends Irem Daloglu, Eren Cetinkaya, Salih Saran, Elif Saran, Musa Umut Sirma, Cigdem Sirma, Burcu Guldur, Emre Insel, Cihan Yilmaz, Gizem Yilmaz, Cumhur Kutlubay, Ozge Kutlubay, Murat Yazici, Bilgehan Donmez, Emre Tuncel, Oguz Deniz, Hakan Tozkoparan, Aysegul Topcu, Dan Nathan-Roberts and Erkan Aktakka for their continuous support and friendship.

Last but far from least, I would like to express my heartfelt gratitude to my dearest parents Hilmi Turhan Gulsoy and Emel Gulsoy, to whom this dissertation is dedicated, for their continuous support and encouragement in all of my endeavors. The positive energy I received from both of you provided me the motivation to finish my Ph.D. studies. I feel very lucky to have both of you in my life, thank you for always being there for me.

This work was supported by the U.S. Department of Energy under award number 00087993. In addition, I would like to thank the Horace H. Rackham Graduate School of the University of Michigan to provide travel funding for the conferences I attended throughout my Ph.D.

TABLE OF CONTENTS

LIST OF FIGURES

LIST OF TABLES

ABSTRACT

MECHANISM OF INTERNAL OXIDATION OF ALLOY 617 IN CONTROLLED IMPURITY HELIUM ENVIRONMENTS AT HIGH TEMPERATURES

by

Gokce Gulsoy

Chair: Gary S. Was

Alloy 617 has been identified as the primary candidate alloy for the intermediate heat exchangers of the High temperature gas-cooled reactors featuring very high core outlet temperatures in the range of 750 - 850 °C. In this temperature regime, the impurities in the helium coolant result in carburization, surface and internal oxidation of Alloy 617. Among these degradation modes, selective internal aluminum oxidation along the grain boundaries of the alloy is likely to be the life-limiting corrosion process as it can significantly lower the creep ductility and fatigue resistance of the alloy.

Alloy 617 was exposed in a Cr-Cr_2O_3 Rhines pack and He-CO-CO_2 gas with the objective of characterizing the surface and internal oxidation behavior and determining the

governing oxygen transport mechanisms of rapid internal aluminum oxidation of Alloy 617 in the temperature range of 750 - 850 °C.

Surface Cr oxidation is facilitated by grain boundary diffusion of Cr cations, whereas the internal aluminum oxidation kinetics are predominantly governed by the accelerated oxygen transport along the incoherent Al_2O_3 - metal interfaces in the internal oxidation zone of Alloy 617. The oxygen diffusion coefficients along these interfaces are several orders of magnitude greater than those reported in pure nickel and binary nickel based alloys.

Another contribution to the rapid internal oxidation is the gas permeability of Cr_2O_3, which results in enhanced oxygen concentration at the alloy - Cr_2O_3 interfaces. Despite formation of a surface Cr_2O_3 film, the atomic fraction of oxygen established at the alloy - Cr_2O_3 interfaces in He-CO-CO_2 environments is a factor of 4 greater than that did at the alloy surface by the dissociation oxygen partial pressure of Cr_2O_3 in the Rhines pack exposure at 850 °C.

The oxygen solubility and diffusion coefficient values determined in this dissertation are used to determine that internal oxidation of Alloy 617 in He-CO-CO_2 environments can be mitigated by increasing the Al concentration of the alloy at least to 5.0 at.%.

CHAPTER 1

INTRODUCTION

The U.S. Department of Energy (DOE) established the Next Generation Nuclear Plant (NGNP) program to advance current nuclear energy technology by designing, building and commercializing economically more feasible, more sustainable, safer and versatile nuclear reactors, which produce heat and hydrogen for industrial use in addition to electricity. The program also aims to design reactors with service lifetimes of 60 years. These design conditions require the reactor outlet temperatures to be as high as 1000 °C. Achieving such high temperatures further necessitates switching to a new coolant technology such as gas, liquid metal and molten salt. Among these alternatives, DOE has identified the high temperature gas-cooled reactor (HTGR) design as the primary candidate for the NGNP program. HTGRs are mid-sized, graphite moderated, helium cooled, thermal neutron spectrum reactors with a pebble bed or prismatic core using TRISO coated fuel [1,2], as shown in Figure 1.1 [3]. This reactor size and core configuration facilitate an important safety feature namely self-sustaining, passive-decay heat removal designed to avoid fuel damage and radioactive material release during accidents. In addition, very high reactor core outlet temperatures results in high fuel burn-up with minimum waste generation, high electrical generation efficiency (~50%) and high thermal power output

(600 - 800 MWt). Given these features, HTGRs are very suitable for hydrogen and process heat generation for industrial use.

Current HTGR designs connect the hydrogen production plant to the reactor core using an intermediate heat exchanger (IHX) system to transfer heat between the primary and secondary helium coolant systems. Even though there is no prior industrial application of a heat exchanger with the designated IHX operating conditions, the system is expected to operate at temperatures up to 950 °C, under cyclic stresses of 7 - 9 MPa and in purified helium [1,2]. Despite the use of advanced purification systems, helium coolant still contains CO, CO_2, H_2, H_2O and CH_4 in ppm levels (Table 1.1) due to the leaks in the seals and welds, or outgassing of the reactor core internals and thermal insulators [4,5]. These impurities in helium can result in severe oxidation, carburization or decarburization of the IHX materials. When these corrosion modes are coupled with cyclic stresses at high temperatures, material properties are expected to degrade significantly. Given these extreme operating conditions the IHX is the most vulnerable metallic component of the whole HTGR design. Failure of IHX would have major safety and economic ramifications due to the possibility of damage to the coolant system, a power plant shut-down and interruption in process heat and hydrogen production for the industry. For this reason, DOE has funded research and development programs that primarily focus on IHX material selection and evaluate the life-limiting processes that may degrade the candidate IHX materials.

IHX material selection criteria require superior oxidation, carburization/ decarburization resistance accompanied with good creep-rupture properties at a temperature range of 750 - 1000 °C. Desired material characteristics are availability in various product forms, good formability and weldability, high thermal conductivity, low thermal expansion and compliance with the ASME Boiler and Pressure Vessel Code specifications [6]. Based on these material

requirements, three nickel based superalloys, Alloy 617, Alloy X and Alloy 230, and an iron based superalloy, Alloy 800H, have been identified as the candidate IHX materials. Among these alloys, only Alloy 800H has previously been used as the steam generator material in German HTGRs, and has also been qualified for use in the U.S. nuclear systems according to the ASME Boiler and Pressure Vessel Code Section III [1,7–9]. However, its oxidation resistance and creep-rupture properties have been certified for safe operation only up to 760 °C and a maximum service lifetime of 30 years [1,8,9]. Thus, Alloy 800H cannot be used in the desired IHX system and Alloy X, Alloy 230 and Alloy 617, which have superior high temperature deformation and oxidation properties, remain as the candidate IHX materials. Alloy X has superior oxidation properties compared to the other two alloys; however, its susceptibility to form brittle intermetallic phases above 750 °C is extremely detrimental to its high temperature mechanical properties [1,9]. Alloy 617 and Alloy 230 exhibit similar oxidation and carburization resistance, yet Alloy 617 features superior creep properties. Alloy 617 is also characterized by its high thermal conductivity, low thermal expansion, good weldability and formability, which makes it the primary candidate IHX material for the NGNP HTGR design [1,3,7–9].

As the primary IHX material, Alloy 617 has been extensively tested to identify its corrosion, creep-rupture and fatigue properties in HTGR helium at temperatures 850 - 1000 °C [4,10–18]. Research has shown that the life limiting corrosion processes for Alloy 617 are likely to be decarburization, at temperatures between 900 - 950 °C, and selective internal oxidation of aluminum along the grain boundaries. These corrosion modes can significantly impact the mechanical properties of the alloy. Lack of carbide stability in the alloy in decarburizing conditions results in significant reduction in the creep strength [17], and the internal Al_2O_3

precipitates can increase the propensity of surface crack initiation decreasing the creep and fatigue resistance of the alloy [17,18].

Failure of Alloy 617 due to decarburization has been addressed by lowering the reactor core outlet temperatures, which concomitantly decrease the operating temperature range of IHX to 750 - 850 °C. This leaves selective internal aluminum oxidation as the life-limiting process for Alloy 617, posing a major concern especially for the thin sections of the compact IHX designs. However, in this temperature regime scant data on both surface and internal oxidation kinetics of Alloy 617 is available in the literature. To ensure safe operation of the IHX during the desired service lifetime, surface and internal oxidation behavior of Alloy 617 must be characterized and associated oxidation kinetics must be determined.

Furthermore, little attention has been paid to identifying the oxygen transport processes controlling the internal aluminum oxidation kinetics of Alloy 617 in IHX equivalent helium environments. The classical theory of internal oxidation [19–23] assumed ideal conditions, according to which internal aluminum oxidation of Alloy 617 should be governed by the concentration of dissolved oxygen at the alloy - Cr_2O_3 interface, limited by the dissociation oxygen partial pressure of Cr_2O_3, and diffusion of atomic oxygen through the alloy matrix surrounding the internal Al_2O_3 precipitates. However, recent research has shown that Cr_2O_3 is indeed permeable to molecular oxidants [24–28] which can significantly enhance oxygen solubility at the alloy - Cr_2O_3 and that the unique rod - like morphology of the Al_2O_3 precipitates result in formation of incoherent interfaces with the alloy matrix, which act as easy-diffusion paths for oxygen [29–31]. To date, no study has correlated the increase in the oxygen solubility and diffusion coefficient due to these effects with the measured kinetics as a means to identify

the rate-controlling mechanism(s) for the internal aluminum oxidation of Alloy 617 in IHX equivalent helium environments.

Chapter 2 provides relevant background information, states the objective of this dissertation and outlines the experimental approach. Chapter 3 describes the experiment and post-experiment sample characterization procedures. Chapter 4 presents the results of the surface and internal oxidation kinetics of Alloy 617 in two He-CO-CO_2 environments at 750 - 850 °C as well as the internal aluminum oxidation kinetics of Alloy 617 in a Cr-Cr_2O_3 Rhines pack exposure at 850 °C, which is specifically designed to measure the oxygen diffusion coefficient in the subsurface region of Alloy 617 at an ambient oxygen activity equal to the dissociation oxygen partial pressure of Cr_2O_3. Chapter 5 discusses the rate controlling mechanisms of internal Al oxidation and surface Cr oxidation of Alloy 617 at 750 - 850 °C. Chapter 6 summarizes the conclusions of this study and finally Chapter 7 presents a critical assessment of this dissertation work and future suggested work.

Table 1.1. Impurity content in the helium coolants of the previous HTGRs (in molppm) [9].

	H_2O	H_2	CO	CO_2	CH_4	O_2	N_2
Dragon	0.1	0.1	0.05	0.02	0.1	0.1	0.05
Peach bottom	0.5	10.0	0.5	0.05	1.0	-	0.5
Fort St. Vrain	1.0	7.0	3.0	1.0	0.1	-	-
AVR	0.15	9.0	15.0	0.25	1.0	-	22.0
THTR	0.01	0.8	0.4	0.2	0.1	-	0.1

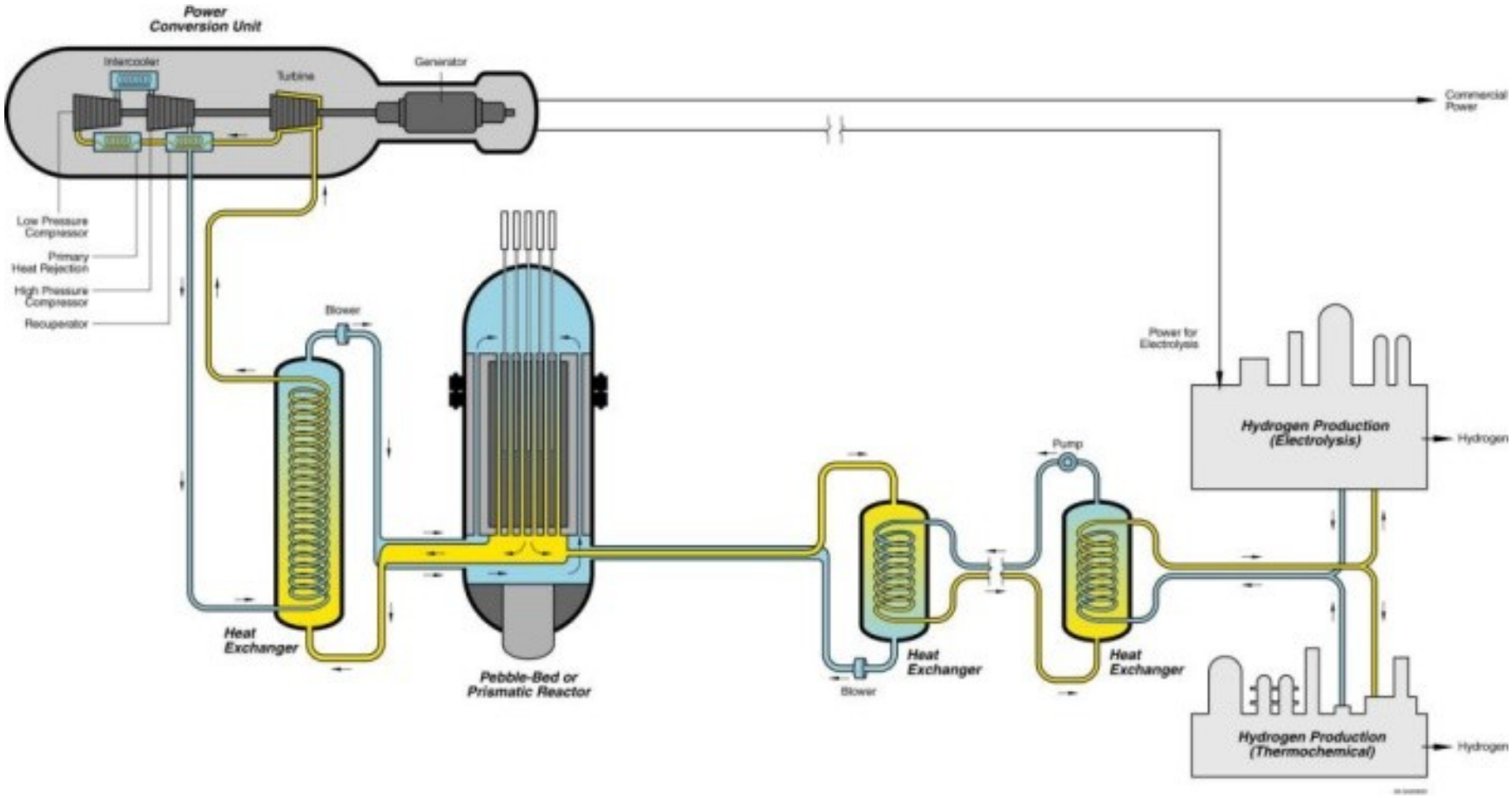

Figure 1.1 The schematics of the HTGR design [3].

CHAPTER 2

BACKGROUND

This chapter reviews the theory and experimental data pertinent to the high temperature surface and internal oxidation of Alloy 617 and similar alloys in IHX helium equivalent environments. The classical theory of oxidation is also reviewed to provide insight into the mechanisms that control the rates of surface Cr and internal Al oxidation in Alloy 617. Section 2.1 describes the metallurgical properties and the thermal stability of Alloy 617 to give a brief overview of microstructure - mechanical property and chemical composition - oxidation resistance relationships. Section 2.2 summarizes the fundamental thermodynamic and kinetic aspects of gas - metal interactions and the published literature on the oxidation kinetics of Ni-Cr based alloys in IHX helium. Section 2.3 reviews Wagner's theory of oxidation with the emphasis on describing the mechanisms of surface and internal oxidation of an alloy. Section 2.4 examines the kinetics and mechanism of Cr_2O_3 growth on pure Cr and chromia forming alloys. Section 2.5 reviews the classical internal oxidation theory. Section 2.6 discusses the oxidation of Al in binary Ni-Al and Ni-Cr-Al systems with the emphasis on understanding the transition from internal to external oxidation of Al. Section 2.7 states the objective of this work and describes the proposed experimental approach to achieve it.

2.1. Metallurgy and thermal stability of Alloy 617

Alloy 617 is a face centered cubic, nickel based, solid-solution strengthened alloy developed for high temperature applications above 800°C. The alloy is characterized by high thermal conductivity, low thermal expansion, good weldability and formability, good oxidation and carburization resistance as well as superior creep properties [1,3,7–9]. Because of these desirable features, Alloy 617 has been considered for use in numerous applications such as gas turbines, chemical and metallurgical plants, and power generation structures. Recently it has also been identified as the primary candidate alloy for IHX use in HTGRs at service temperatures up to 1000°C [9].

Alloy 617 is solid solution alloy with a highly stable austenitic nickel-based matrix [32]. Solid solution strengthening is achieved through additions of Co, Mo and W. Further improvement in the mechanical properties of the alloy is realized due to the precipitation of Al and Ti containing intermetallics, Cr, Mo and W rich carbides, and Ti based carbonitrides. Good corrosion resistance of the alloy is attributable to Cr and Al additions.

The microstructure and phase stability of Alloy 617 has been extensively investigated by thermal aging treatments in the HTGR temperature range of interest for up to 100,000 hours [33–36]. Microstructure characterization has shown that the primary phases observed in the microstructure of Alloy 617 are Cr rich $M_{23}C_6$ (where M = metal atom), Mo rich M_6C, $Ti(C,N)$ and $\gamma'(Ni_3Al)$. In addition, $M_{12}C$ and $Ni_2(Mo,Cr)$ type phases may precipitate yet are not very abundant in a typical microstructure of the alloy.

Figure 2.1 shows a time-temperature-transformation (T-T-T) diagram summarizing the stability of the observed phases in Alloy 617 microstructure during a long-term heat treatment. The diagram indicates that the observed precipitates can be completely dissolved by annealing

the alloy above 1100 °C. However, Ren and Swimdeman [35] showed that *M(C,N)* and M_6C precipitates are thermodynamically stable up to 1400 °C these phases may still be present in exceess of 1 wt% at 1177 °C. At temperatures below 1000 °C, $M_{23}C_6$ becomes stable and may precipitate at the expense of M_6C below 871 °C [36]. Another important phase for precipitation hardening of the alloy is γ', which is stable in the temperature range of 482 - 871°C and can be present as much as 8 wt% in the microstructure of the alloy below 550 °C. Depending on the Al content of the alloy, γ' may be stable up to 1000 °C. γ' precipitation can result in significant hardening in the alloy; however γ' precipitates are likely to dissolve after prolonged aging above 100,000h.

Phase stability is essential for the high temperature deformation properties of Alloy 617. Precipitation hardening is mainly achieved owing to the presence of $M_{23}C_6$ and M_6C type carbides and fine γ' precipitates in the matrix. Fine carbide precipitates decorating the grain boundaries greatly enhance the creep strength of the alloy by pinning the grain boundary migration [37]. These beneficial effects of precipitation hardening can best be utilized in the temperature range of 482 - 704 °C [36]. Exposures above this temperature range will most probably result in agglomeration, coarsening and eventually dissolution of the $M_{23}C_6$, M_6C and γ' phases causing significant losses in the creep strength of Alloy 617.

2.2. Corrosion of Ni-Cr based superalloys in IHX helium

The interplay among the impurities in the helium coolant (CO, CO_2, H_2, H_2O, N_2 and CH_4), temperature and alloy composition results in oxidation, carburization and decarburization of the candidate IHX alloys. Section 2.2.1 presents the thermodynamic and kinetic factors that are considered to determine the oxygen and carbon activities of multicomponent IHX helium. In Section 2.2.2, IHX helium - alloy interactions are discussed on a Cr - C - O stability diagram to

predict the dominant corrosion modes as a function of the environment chemistry, temperature and the chromium activity of a given alloy. Finally, Section 2.2.3 presents the selected experimental results that report the oxidation kinetics of Ni-Cr based alloys in simulated IHX helium environments.

2.2.1. Thermodynamic and kinetic aspects of corrosion in IHX helium

Predicting the mode by which the alloy will degrade is indeed quite complex as multiple corrosive molecules are present in the high pressure helium coolant flowing at very high rates. Due to these very high flow rates the corrosive molecules do not achieve thermodynamic equilibrium on metal surface. Therefore, Quadakkers and coworkers [11–13] comprehensively studied the kinetics of different oxygen and carbon transferring reactions in a simulated IHX helium environment and predicted the corrosion of a Ni-Cr based alloy by determining the steady state oxygen and carbon activities of the environment.

They determined the steady state carbon activity in the alloy by equating the rates of the reactions transferring carbon to the alloy surface and that consuming carbon from the alloy surface. Carbon transfer to the alloy surface can be attributed to the decomposition of methane at the alloy surface according to the following reaction:

$$CH_4 \rightleftarrows \underline{C} + 2H_2, \quad (2.1)$$

where $\underline{C}$ is the carbon in solution at the alloy surface. The rate of carbon transfer to the alloy surface according to the Reaction (2.1) is as follows:

$$(d[C] / dt)^{+} = k_{(2.1)} \times \left(P_{CH_4} - P_{CH_4}^{(s)}\right), \quad (2.2)$$

where $k_{(2.1)}$ is the forward reaction rate constant of Equation (2.1), P_{CH_4} is the partial pressure of methane in helium and $P_{CH_4}^{(s)}$ is the partial pressure of methane at the alloy surface, which has a

carbon chemical potential equal to that of the alloy. At steady-state, $P_{CH_4}^{(s)}$ is much smaller than P_{CH_4}; hence Equation (2.2) reduces to:

$$(d[C] / dt)^{+} = k_{(2.1)} \times \left(P_{CH_4}\right). \quad (2.3)$$

On the other hand, the carbon transferred to the alloy surface by decomposition of methane is simultaneously consumed by another reaction with water at the alloy surface:

$$H_2O + \underline{C} \rightleftarrows CO + H_2, \quad (2.4)$$

To determine the rate of carbon consumption, the two elementary chemical reactions that establish Reaction (2.4) should be considered:

$$H_2O \rightleftarrows H_2 + \underline{O} \quad (2.5)$$

and

$$\underline{C} + \underline{O} \rightleftarrows CO, \quad (2.6)$$

where $\underline{O}$ is the oxygen adsorbed at the alloy surface. The kinetics of Reaction (2.6) are much more rapid than that of Reaction (2.5) [12]. Thus, it is assumed that Reaction (2.6) reaches equilibrium at the alloy surface. This leaves the slower water dissociation reaction to control the rate of Reaction (2.4), which is equal to the rate of carbon consumption from the alloy surface:

$$(d[C]/ dt)^{-} = k_{(2.5)} \times P_{H_2O} - k'_{(2.5)} \times P_{H_2} \times \left(P_{O_2}^{s}\right)^{1/2}, \quad (2.7)$$

where $\left(P_{O_2}^{s}\right)^{1/2}$ is the oxygen partial pressure at the alloy surface, $k_{(2.5)}$ and $k'_{(2.5)}$ are the forward and backward reaction rate constants of Reaction (2.5), respectively. Carbon and oxygen activities at the alloy surface are coupled according to the Reaction (2.6) as it reaches equilibrium at the alloy surface rapidly:

$$a_c^s = P_{CO} / \left(K_{(2.6)} \times \left(P_{O_2}^{s}\right)^{1/2}\right), \quad (2.8)$$

where a_c^s is the carbon activity at the alloy surface and $K_{(2.6)}$ is the equilibrium constant of Reaction (2.6). Substitution of Equation (2.8) into Equation (2.7) gives:

$$(d[C]/dt)^- = k_{(2.5)} \times P_{H_2O} - k'_{(2.5)} \times P_{H_2} \times P_{CO} \times K_{(2.6)} / a_c^s . \quad (2.9)$$

Rearranging the terms in Equation (2.9) gives:

$$(d[C]/dt)^- = k_{(2.5)} \times P_{H_2O} \times \left(1 - \frac{k'_{(2.5)} \times P_{H_2} \times P_{CO} \times K_{(2.6)}}{k_{(2.5)} \times P_{H_2O} \times a_c^s}\right), \quad (2.10)$$

where $\left(k_{(2.5)}/k'_{(2.5)}\right)$ is equal to the equilibrium constant of Reaction (2.5). Therefore, Equation (2.10) becomes:

$$(d[C]/dt)^- = k_{(2.5)} \times P_{H_2O} \times \left(1 - \frac{P_{CO} \times K_{(2.6)}}{P_{O_2}^{1/2} \times a_c^s}\right), \quad (2.11)$$

where

$$\left(P_{CO} \times K_{(2.6)}/P_{O_2}^{1/2}\right) = a_c^{(2.4)}, \quad (2.12)$$

where $a_c^{(2.4)}$ is equal to the equilibrium carbon activity of Reaction (2.4). As such, the rate of carbon consumption due to reaction with water at the alloy surface is equal to:

$$(d[C]/dt)^- = k_{(2.5)} \times P_{H_2O} \times \left(1 - a_c^{(2.4)} / a_c^s\right). \quad (2.13)$$

The steady state carbon activity of the environment, a_c^{ss}, is reached when the rate of carbon transfer to the alloy surface by methane is equal to that of carbon consumption by water:

$$(d[C]/dt)^+ = (d[C]/dt)^- . \quad (2.14)$$

Substituting the Equations (2.3) for carbon transfer and (2.13) for carbon consumption into Equation (2.14) results in:

$$a_c^{ss} = a_c^{(2.4)} \times \left(1 - \frac{k_{(2.1)} \times P_{CH_4}}{k_{(2.5)} \times P_{H_2O}}\right)^{-1} . \quad (2.15)$$

Since reaction given in Equation (2.6) is rapid enough to reach equilibrium, it is reasonable to assume that the carbon and oxygen activities of the environment are coupled by its

equilibrium constant, $K_{(2.6)}$, as given in Equation (2.8). This is also valid for the steady state carbon and oxygen activities of the environment; therefore $P_{O_2}^{ss}$ is related to a_c^{ss} according to Equation (2.8):

$$\left(P_{O_2}^{ss}\right)^{1/2} = K_{(2.6)} \times P_{CO} \,/\, a_c^{ss} \,. \tag{2. 16}$$

Substituting Equation (2.15) into (2.16) gives:

$$\left(P_{O_2}^{ss}\right)^{1/2} = \frac{K_{(2.6)} \times P_{CO}}{a_c^{(2.4)}} \times \left(1 - \frac{k_{(2.1)} \times P_{CH_4}}{k_{(2.5)} \times P_{H_2O}}\right). \tag{2. 17}$$

Finally, substituting Equation (2.12) into (2.17) gives the relationship between the steady-state oxygen activity of the environment with the equilibrium oxygen activity of the elementary reactions of Reaction (2.4), $P_{O_2}^{(2.5),(2.6)}$:

$$\left(P_{O_2}^{ss}\right)^{1/2} = P_{O_2}^{(2.5),(2.6)} \times \left(1 - \frac{k_{(2.1)} \times P_{CH_4}}{k_{(2.5)} \times P_{H_2O}}\right). \tag{2. 18}$$

This analysis concludes that the steady state oxygen and carbon activities of an environment can significantly deviate from the equilibrium values depending on the partial pressures of CH_4 and H_2O molecules in the environment and the rates of Reactions (2.1) and (2.5). Equations (2.15) and (2.18) indicate that increasing the methane concentration in the environment results in an increase in the a_c^{ss}, whereas a decrease in $P_{O_2}^{ss}$. However, in order for the steady state activities to significantly deviate from the equilibrium values, P_{CH_4}/P_{H_2O} ratio in the environment should exceed the ratio of the rates of the methane decomposition reaction to that of the water dissolution reaction ($k_{(2.1)}/k_{(2.5)}$). Short time exposures conducted by Quadakkers [12] revealed that the rate of Reaction (2.5) is approximately 100 times that of Reaction (2.1). Therefore, increasing the P_{CH_4}/P_{H_2O} ratio above 100 can yield a very high value of the steady state carbon activity and a significant reduction in the equilibrium oxygen partial pressure of the environment below the dissociation oxygen partial pressure of the oxide forming

on the alloy surface, resulting in a shift from an oxidation and carburization regime to a rapid carburization regime.

2.2.2. Cr - C - O stability diagram and predicting the corrosion of Cr bearing alloys in IHX helium

The corrosion mode(s) by which an alloy will degrade in a given HTGR helium composition can be determined by comparing the steady-state oxygen and carbon activities of the environment with the equilibrium oxygen and carbon activities of the oxide and carbide phases stable in an alloy. The most stable carbide and oxide phases in the candidate Ni-Cr based IHX alloys are $Cr_{23}C_6$ and Cr_2O_3. Therefore, a Cr-C-O stability diagram can be used to determine corrosion modes of the alloys. Figure 2.2 shows a Cr-C-O stability diagram constructed by assuming a fixed chromium activity in an alloy at a fixed temperature. The diagram describes the stability regions of Cr, its oxide and its carbide with respect to the oxygen and carbon activities.

The horizontal line "*AO*" represents a critical carbon activity, a_C^*, at which the Cr in the alloy and its carbide is in equilibrium according to the following reaction:

$$x\underline{Cr} + y\underline{C} \rightleftarrows Cr_xC_y, \tag{2. 19}$$

where $\underline{Cr}$ is the chromium in solution at the alloy surface and Cr_xC_y can be any of the carbide phases $Cr_{23}C_6$, Cr_7C_3 or Cr_3C_2. Henceforth, $Cr_{23}C_6$ will be considered as the primary carbide phase that is stable in the alloy microstructure. Assuming the activity of $Cr_{23}C_6$ is unity, the critical carbon activity is given as:

$$a_C^* = \left[1/\left(K_{(2.19)} \times a_{Cr}^{23}\right)\right]^{1/6}. \tag{2. 20}$$

The vertical line "*BO*" represents a critical oxygen partial pressure, $P_{O_2}^*$, at which the Cr in the alloy is in equilibrium with its oxide, given by:

$$2\underline{Cr} + 3/2O_2 \rightleftarrows Cr_2O_3. \quad (2.21)$$

Assuming unit activity of Cr_2O_3, the critical oxygen partial pressure is equal to:

$$P^*_{O_2} = \left[1/\left(K_{(2.17)} \times a^2_{Cr}\right)\right]^{2/3}. \quad (2.22)$$

The diagonal line "*CO"* designates the equilibrium between the oxide and carbide of the Cr in the alloy:

$$4Cr_{23}C_6 + 69O_2 \rightleftarrows 46Cr_2O_3 + 24\underline{C}\,. \quad (2.23)$$

The co-existence of the carbide and oxide phases require the equilibrium oxygen and carbon activities of these phases to be bound to each other by the equilibrium constant of the reaction given in Equation (2.23):

$$K_{(2.23)} = (a_C)^{24}/\left(P_{O_2}\right)^{69}. \quad (2.24)$$

The triple point *O* designates the equilibrium between the Cr in the alloy, its oxide and its carbide according to the following reaction:

$$2Cr_2O_3 + Cr_{23}C_6 \rightleftarrows 27\underline{Cr} + 6CO. \quad (2.25)$$

Assuming the activities of Cr_2O_3 and $Cr_{23}C_6$ are unity, the triple point is given by:

$$P^*_{CO} = \left[K_{(2.25)}/(a_{Cr})^{27}\right]^{1/6}, \quad (2.26)$$

where P^*_{CO} is the critical partial pressure of carbon monoxide, which designates the equilibrium between the alloy, oxide, carbide and environment. According to the Equation (2.26), P^*_{CO} is not dependent on the oxygen and carbon activities of the oxide and carbide phases present in the alloy; thus it can be extended along the line "*DOE*". The slope of the line is dictated by the following reaction:

$$2CO \rightleftarrows 2C + O_2\,, \quad (2.27)$$

which further indicates that the oxygen and carbon activities of the environment are bound to each other according to Equation (2.8). If the ambient CO partial pressure is lower than the

critical CO partial pressure ($P_{CO} < P_{CO}^{*}$), the forward reaction given in Equation (2.25) is favored. As such, the surface oxide is reduced by the bulk carbides leading to the formation of metallic chromium and evolution of CO. If $P_{CO} > P_{CO}^{*}$, then the backward reaction dominates resulting in simultaneous oxidation and carburization of the alloy.

Quadakkers and coworkers [11–13] compared the steady-state oxygen partial pressure and carbon activity of a typical HTGR environment with the Cr-C-O stability diagram of an alloy of known Cr activity and summarized five possible degradation modes as shown in Figure 2.2:

- Interval I: Cr stable region, the alloy cannot be oxidized or carburized. Pre-existing oxides and carbides are reduced to metallic chromium according to the reaction given in Equation (2.25).
- Interval II: Alloy is decarburized because the ambient CO partial pressure is lower than P_{CO}^{*}.
- Interval III: Alloy is simultaneously oxidized and carburized because the ambient CO partial pressure is greater than P_{CO}^{*}. Even though the steady-state carbon activity of the environment, a_c^{ss}, is smaller than a_C^{*} carburization is still possible.
- Interval IV: Alloy is simultaneously oxidized and carburized even though the steady-state oxygen activity of the environment, $P_{O_2}^{ss}$, is smaller than $P_{O_2}^{*}$. Very high carbon activity of the environment may result in surface carburization.
- Interval V: Heavy surface and internal carburization of the alloy is expected.

The cross-hatched region in Figure 2.2 qualitatively represents the increase in P_{CO}^{*} with decreasing chromium activity at the metal-oxide interface due to surface oxidation. Quadakkers [11] assumed that oxidation rate increases with increasing oxygen partial pressure and the

decrease in the Cr activity is proportional to the ratio of oxidation rate constant to the diffusion coefficient of Cr in the alloy. If the environments oxygen partial pressure is equal to $P^*_{O_2}$, the surface of the alloy does not oxidize; therefore no shift in P^*_{CO} occurs. As the environment oxygen partial pressure increases above $P^*_{O_2}$, more Cr depletion is expected due to increasing oxidation rate which results in an increase in P^*_{CO}.

P^*_{CO} is also strongly temperature dependent as a_{Cr} and $K_{(2.20)}$ can change significantly with temperature. The temperature at which $P_{CO} = P^*_{CO}$ is defined as the "critical temperature", above which decarburization is accompanied by the reduction of the surface Cr_2O_3 scale and evolution of CO as the forward reaction given in Equation (2.25) is favored [4,10–12,14–16,38]. Consider an environment E with a fixed carbon monoxide partial pressure, P_{CO}, as shown in Figure 2.3. The critical temperature is designated as T_{cr} at which the reaction given in Equation (2.25) is in equilibrium and neither carburization nor decarburization of the alloy is favored. At temperature T1, the condition $P_{CO} > P^*_{CO}$ is satisfied; therefore oxidation and carburization should occur because the reverse reaction given in Equation (2.25) is favored. If the temperature is increased to T2, the value of $K_{(2.25)}$ increases and a_{Cr} decreases with temperature. Therefore, the value of P^*_{CO} increases according to the Equation (2.26). If the increase in P^*_{CO} is significantly high such that $P_{CO} < P^*_{CO}$, forward reaction given in Equation (2.25) is favored and the corrosion behavior of the alloy changes from oxidation + carburization to decarburization accompanied by the reduction of the surface oxide.

Mechanical properties of the alloys severely degrade when exposed to heavily carburizing or decarburizing environments. Corrosion modes designated by intervals IV and V in Figure 2.2 results in formation of surface carbides (M_2C_3 or M_7C_3 type), and extensive precipitation of coarse carbides ($M_{23}C_6$ and M_6C type) at the bulk of the alloy and along the grain

boundaries. Normally, carbide precipitates enhance the creep strength by pinning the grain boundary migration [37]; however in the case of severe carburization, densely populated coarse precipitates may act as preferential sites for the formation and propagation of intergranular cracks. The tensile ductility and creep-rupture strain are expected to reduce due to a possible cleavage fracture [9,37].

Decarburization, on the other hand, results in significant loss of creep strength of an alloy due to the dissolution of the bulk carbides. Alloy 617 is susceptible to decarburization in the temperature range of 900 - 950°C [4,16,38], which sets the alloys maximum service temperature in IHX helium [9]. Therefore the recommended IHX service temperature range for Alloy 617 is 750 - 850°C.

In the temperature range of 750 - 850°C, the oxygen and carbon activities of the IHX helium environment are outside of Interval I, as shown in Figure 2.2. This means that, an oxidizing and slightly carburizing helium composition (Interval III) is the least detrimental environment for Alloy 617. However, selective internal oxidation along the grain boundaries is a growing concern especially for the thin sections of the compact heat exchanger designs [9]. The reason for this is that the intergranular oxides are likely to initiate subsurface cracks which can subsequently merge with the alloy surface, resulting in large open cracks [18]. Intergranular crack nucleation and propagation is also associated with the selective oxidation along the grain boundaries leading to reduced creep-fatigue life of the candidate IHX alloys [39,40].

2.2.3. Oxidation kinetics of Ni based superalloys in IHX helium

The oxidation reactions rates can be determined by measuring the accumulation of the corrosion product as a function of time. The conventional technique used for this purpose is gravimetric measurements with high precision microbalances. These measurements can be

performed in-situ by utilizing thermogravimetric analyzers. Alternatively, weight gain can be measured intermittently by weighing multiple samples exposed to the same environment-temperature conditions at different times. If the corrosion product is solid and stable, the change in the specific weight (weight per surface area) of a sample, $\Delta W/A$, as a function of time will reflect its oxidation rate. If metal volatilization occurs, most commonly due to formation of volatile oxides, then the weight loss of the sample as a function of time will indicate the corrosion rate.

If the corrosion product is a compact scale providing an ultimate diffusion barrier to the corrosive species, the corrosion rate is controlled by parabolic kinetics. The solid state diffusion of the corrosive species through the compact scale is the rate determining step and the corrosion rate is proportional to the square root of the exposure time. The enabling theory for the oxidation of metals was first established by Wagner [41]. Wagner's theory of oxidation will be reviewed more comprehensively in Section 2.3.

The rate constant determined from weight gain analysis is given by:

$$[\Delta W/A]^2 = 2k_W \times t, \tag{2. 28}$$

where k_W is the weight gain rate constant and t is the oxidation time. Assuming formation of a single stoichiometric surface oxide, M_aO_b, the thickness of the oxide, X, can be related to the measured specific weight gain according to the following relation:

$$X = (\Delta W/A) \times V_{M_aO_b}/([A.W.]_O \times b), \tag{2. 29}$$

where $V_{M_aO_b}$ is the molar volume of the oxide and $[A.W.]_O$ is the atomic mass of oxygen which is equal to 16 g-atom. In general, surface oxidation is a diffusion controlled process that leads to the parabolic oxidation kinetics:

$$dX/dt = k_S^{M_aO_b}/X, \tag{2. 30}$$

where $k_S^{M_aO_b}$ is the surface oxidation rate constant and t is the oxidation time. Integrating Equation (2.30) gives:

$$X^2 = 2k_S^{M_aO_b} \times t. \quad (2.31)$$

Inserting the Equations (2.28) and (2.31) into Equation (2.29) yields the relationship between the weight gain rate constant and the surface oxidation rate constant:

$$k_S^{M_aO_b} = \left(V_{M_aO_b}^M/16y\right)^2 \times k_W. \quad (2.32)$$

The oxidation of Ni-Cr based alloys has been extensively studied in simulated IHX helium and equivalent low oxygen partial pressure environments in the temperature range 850-1000°C. Figure 2.4 summarizes the parabolic weight gain rate constants of the most common Ni-Cr based IHX candidate alloys in these environments. The rate constants from each reference are obtained by fitting the reported weight gain data according to the Equation (2.28). The data in Figure 2.4 exclude the rate constants measured in decarburizing environments.

Quadakkers [12] tested samples of IN617 and Hastelloy X in a simulated IHX helium environment consisted of H_2O, CO, CH_4 and H_2 in molppm levels at temperatures 850-950 °C for up to 2000h. In these exposures, gas flow rates were maintained in the range of 1080 - 3300 ml/min. The measured values of k_W for IN617 and Hastelloy X samples were in the range of 1.0×10^{-4} - 4.8×10^{-4} mg^2/cm^4-h and 0.3×10^{-4} - 2.0×10^{-4} mg^2/cm^4-h, respectively. Surface oxidation, carburization and internal oxidation of the alloys contributed to the measured weight gains. Common corrosion products that formed in both alloys were Cr_2O_3, Cr and Ti rich spinels and internal Al_2O_3. In addition to these phases, Hastelloy exhibited formation of Cr and Mn rich spinel and a Ti rich oxide. In general, Hastelloy X exhibited better carburization and oxidation resistance than IN617.

Christ et al. [14,15,42] studied the short-term oxidation kinetics of IN617 and IN713LC in simulated IHX helium, He-CO-CO_2 and Ar - H_2 - H_2O environments in the temperature range of 850 - 950°C. The flow rates sustained during the exposures was 154 ml/min. The weight gain kinetics of IN617 in helium based environments was in the range 1.0×10^{-4} - 3.0×10^{-4} mg^2/cm^4-h. Formation of surface Cr_2O_3 and internal Al_2O_3 mainly contributed to the measured weight gain kinetics. Exposures to Ar - H_2 - H_2O environments resulted in significantly greater weight gains at 850 - 1000 °C. k_W values determined for IN617 and IN713LC were in the range of 4.0×10^{-4} - 8.8×10^{-3} mg^2/cm^4-h and 9.9×10^{-4} - 1.8×10^{-2} mg^2/cm^4-h, respectively. Even though IN713LC is an alumina former in air at high temperatures, it exhibited much worse oxidation resistance than did IN617 in Ar - H_2 - H_2O due to massive internal oxidation of Al.

Kumar et al. [16,38] studied the oxidation of IN617 in He - CO - CO_2 environments with six different CO/CO_2 ratios in the range of 9 - 1320, at 850 - 1000 °C. In this study, gas flow rate was sustained at 85 ml/min during the exposures. The range of k_W values determined upon exposures to the most oxidizing environment (CO/CO_2 = 1320) and the least oxidizing environment (CO/CO_2 = 9) were 1.8×10^{-4} - 1.9×10^{-3} mg^2/cm^4-h and 1.0×10^{-4} - 2.6×10^{-4} mg^2/cm^4-h, respectively.

Guillou et al. [43] oxidized samples of Alloy 230 in eight different He - H_2 - H_2O gas mixtures with H_2 / H_2O ratios in the range of 5 - 4000 at 850 °C. In this study, the gas flow rate was set at a fairly low value of 33 ml/min. Alloy 230 exhibited formation of Cr and Mn rich spinel, surface Cr_2O_3 and internal Al_2O3. k_W values exhibited significant dependence on the H_2/H_2O ratio and varied in the range of 1.3×10^{-4} - 4.9×10^{-3} mg^2/cm^4-h.

Cabet and Duprey [44] studied the oxidation of Alloy 617 and Alloy 230 in a simulated IHX helium environment at 950°C for up to 5000 h. The environment consisted of 160 molppm

H_2, 16 molppm CH_4, 40 molppm CO and 1.6 molppm H_2O in helium and the gas flow rate during exposures was maintained in the range of 833-1667 ml/min. Alloy 617 exhibited greater weight gain rate constants (2.9×10^{-4} - 4.5×10^{-4} mg^2/cm^4-h) than that did Alloy 230 (2.2×10^{-4} mg^2/cm^4-h).

Kim et al. [45] tested the short-term oxidation resistance of Alloy 617 and Alloy 230 in ultra-high purity grade helium gas containing small amounts of moisture, oxygen, nitrogen and hydrocarbons at 900°C. As can be seen from Figure 2.4, k_W values measured in purified helium are greater than those measured for the same alloys in impure helium environments.

The relatively narrow scatter in the weight gain rate constant measurements plotted in Figure 2.4 can be attributed to the differences in the alloy composition and the environment chemistry. It appears that the variation in the gas flow rates used in different exposures does not seem to have a major influence on the measured weigh gains. Main corrosion features observed in most alloys were surface Cr_2O_3 and internal Al_2O_3. In addition to these phases, Cr and Mn rich spinels formed over Cr_2O_3 on the surface of Alloy 230 and Hastelloy X. Only Alloy 713LC exhibited formation of both surface and internal Al_2O_3. Furthermore, simulated IHX helium and He-CO-CO_2 environments resulted in formation of internal and in some cases surface carbide phases. It appears that the environments containing substantial amounts of H_2 and H_2O result in greater weight gains than do the simulated IHX helium environments.

Weight gain rate constants presented in Figure 2.4 shows that, Alloy 230 and Hastelloy X exhibit slightly better oxidation resistance in low oxygen partial pressure environments than does Alloy 617. However, it is not possible to interpret the rate limiting mechanisms of surface or internal oxidation of, for instance, Alloy 617 based on the Arrhenius parameters determined from Figure 2.4, which indeed reflect the combined contributions of mainly surface Cr, internal Al

oxidation and depending on the environment composition, possible carburization of the alloy. To understand the rate-controlling processes for Cr_2O_3 growth on Alloy 617, the growth kinetics and mechanism of Cr_2O_3 on pure Cr and Ni-Cr based alloys are examined in Section 2.4 after outlining the enabling theory for surface oxidation in Section 2.3. Similarly, to understand the rate limiting processes for internal oxidation of Alloy 617, the kinetics and mechanism of internal Al oxidation in model Ni-Al and Ni-Cr-Al alloys are reviewed in Section 2.6 after the enabling theory of internal oxidation is presented in Section 2.5.

2.3. Wagner's theory of surface oxidation

Wagner [41] described the kinetics of surface oxidation in relation to the transport of ions and electrons and the chemical potential gradients of metal and oxygen across the growing oxide scale. Birks et al. [46] provided a comprehensive summary of Wagner's treatment, which will be presented in this section. First, the derivation of oxidation rate constant will be reviewed. Afterwards, the effects of oxygen partial pressure, temperature, and oxide microstructure on the oxidation kinetics will be covered.

Figure 2.5 is the schematic representation of the transport of the mobile species across a growing oxide scale. Wagner [41] made the following assumptions to derive the oxidation rate constant:

1. Lattice diffusion of ions or transport of electrons through the oxide scale is the rate-controlling process,
2. The oxide is thermodynamically ideal and can only slightly deviate from stoichiometry,
3. Thermodynamic equilibrium is established at the metal-oxide and oxide-gas interfaces,
4. Charge separation can be sustained within the oxide,
5. Net electric current across the oxide scale is zero,

6. A continuous, non-porous and perfectly adherent oxide scale is formed,
7. Oxygen solubility in the metal may be neglected.

Assuming that the metal-oxide and oxide-gas interfaces are in equilibrium, metal cations migrate outward whilst oxygen anions migrate inward due to the activity gradients established across the oxide scale. Migration of the ionic species in opposite directions further creates an electric field across the oxide scale. The net driving force for the migration of ions is established both by the chemical potential and electrical potential gradients across the oxide scale. Therefore, the flux of the ionic species can be defined as follows:

$$J_i = -\frac{\kappa_i}{Z_i^2 F^2}\left(\frac{\partial \mu_i}{\partial x} + Z_i F \frac{\partial \phi}{\partial x}\right), \tag{2. 33}$$

where $\partial \mu_i / \partial x$ is the chemical potential gradient of species i with conductivity κ_i and carrying a charge, Z_i. $\partial \phi / \partial x$ is the electrical potential gradient and F is Faraday's constant.

In most oxide structures cations are the predominantly mobile species. The flux of a cation carrying charge Z_c can be written as follows:

$$J_c = -\frac{\kappa_c}{Z_c^2 F^2}\left(\frac{\partial \mu_c}{\partial x} + Z_c F \frac{\partial \phi}{\partial x}\right). \tag{2. 34}$$

The electric field induced across the oxide scale due to migration of the ionic species, drives electrons to migrate outward. The flux of the electrons can be written based on the Equation (2.33):

$$J_e = -\frac{\kappa_e}{Z_e^2 F^2}\left(\frac{\partial \mu_e}{\partial x} + Z_e F \frac{\partial \phi}{\partial x}\right). \tag{2. 35}$$

The relative migration of anions, cations and electrons are balanced and no net charge transfer across the scale occurs. The electrical neutrality across the oxide scale requires:

$$Z_c J_c + Z_e J_e = 0, \tag{2. 36}$$

which enables the electrical potential gradient term to be determined by solving Equations (2.34) - (2.36) together:

$$\frac{\partial \phi}{\partial x} = -\frac{1}{(\kappa_c+\kappa_e)F}\left(\frac{\kappa_c}{Z_c}\frac{\partial \mu_c}{\partial x} + \frac{\kappa_e}{Z_e}\frac{\partial \mu_e}{\partial x}\right). \quad (2.37)$$

The flux of metal cations can be defined by substituting Equation (2.37) into Equation (2.34):

$$J_c = -\frac{\kappa_c\kappa_e}{Z_c^2F^2(\kappa_c+\kappa_e)}\left(\frac{\partial \mu_c}{\partial x} - \frac{Z_c}{Z_e}\frac{\partial \mu_e}{\partial x}\right), \quad (2.38)$$

where $Z_e = -1$. The chemical potential gradients of cations and electrons can be related to each other by considering the ionization reaction of a metal *M*:

$$\mathrm{M} = M^{Z_c+} + Z_c e^-. \quad (2.39)$$

At equilibrium, the chemical potentials of cations and electrons can be written as follows:

$$\mu_M = \mu_c + Z_c\mu_e. \quad (2.40)$$

Therefore, the term in parenthesis on the right-hand side of the Equation (2.38) is equal to the chemical potential gradient of the metal *M* and the flux equation becomes:

$$J_c = -\frac{\kappa_c\kappa_e}{Z_c^2F^2(\kappa_c+\kappa_e)}\frac{\partial \mu_M}{\partial x}. \quad (2.41)$$

Integrating Equation (2.41) over the thickness of the surface oxide layer, gives the flux of the cations in terms of the metal chemical potentials established at the metal-oxide and oxide-environment interfaces:

$$J_c = -\frac{1}{Z_c^2F^2x}\int_{\mu_M^{int}}^{\mu_M^{ext}} \frac{\kappa_c\kappa_e}{\kappa_c+\kappa_e}\partial\mu_M \; [mol/cm^2\text{-}s], \quad (2.42)$$

where μ_M^{int} and μ_M^{ext} are the chemical potentials of *M* at the metal-oxide and oxide-environment interfaces. For oxide structures, where inward diffusing oxygen anions are more mobile than outward diffusing metal cations, the flux equation for oxygen anions can be derived similarly:

$$J_O = \frac{1}{Z_O^2F^2x}\int_{\mu_O^{int}}^{\mu_O^{ext}} \frac{\kappa_O\kappa_e}{\kappa_O+\kappa_e}\partial\mu_O \; [mol/cm^2\text{-}s], \quad (2.43)$$

where μ_O^{int} and μ_O^{ext} are the chemical potentials of O at the metal-oxide and oxide-environment interfaces.

Now that the flux equations for metal cations and oxygen anions are determined, they can be related to their diffusive fluxes across the surface oxide scale:

$$J_c = C_M \, dx/dt \ [mol/cm^2\text{-}s], \tag{2. 44}$$

$$J_O = C_O \, dx/dt \ [mol/cm^2\text{-}s], \tag{2. 45}$$

where dx/dt is related to the oxidation rate constant, $k_S^{M_aO_b}$, according to Equation (2.30). Combining Equations (2.42), (2.44) and (2.30) gives the oxidation rate constant when metal cations are the mobile species in the oxide scale:

$$k_S^{M_aO_b} = \frac{1}{Z_c^2 F^2 C_M} \int_{\mu_M^{ext}}^{\mu_M^{int}} \frac{\kappa_c \kappa_e}{\kappa_c + \kappa_e} \partial \mu_M \ [cm^2/s]^1. \tag{2. 46}$$

Similarly the oxidation rate constant when oxygen anions are the predominant mobile species can be written as follows:

$$k_S^{M_aO_b} = \frac{1}{Z_O^2 F^2 C_O} \int_{\mu_O^{int}}^{\mu_O^{ext}} \frac{\kappa_O \kappa_e}{\kappa_O + \kappa_e} \partial \mu_O \ [cm^2/s]. \tag{2. 47}$$

Recalling the Nerst-Einstein relationship, which relates the diffusion coefficient of the ionic species, $D_i^{M_aO_b}$, to their conductivities:

$$D_i^{M_aO_b} = \frac{\kappa_i RT}{Z_O^2 F^2 C_i}, \tag{2. 48}$$

and assuming that the conductivities of ionic species are much smaller that of electrons, the oxidation rate constants given in Equations (2.46) and (2.47) can be rewritten as:

$$k_S^{M_aO_b} = \frac{1}{RT} \int_{\mu_M^{ext}}^{\mu_M^{int}} D_M^{M_aO_b} \, \partial \mu_M \ [cm^2/s], \tag{2. 49}$$

$$k_S^{M_aO_b} = \frac{1}{RT} \int_{\mu_O^{int}}^{\mu_O^{ext}} D_O^{M_aO_b} \, \partial \mu_O \ [cm^2/s]. \tag{2. 50}$$

[1] Minus sign in front of the Equation (2.42) is omitted by swapping the upper and lower bounds of the integral.

Equations (2.49) and (2.50) predict the oxidation rates of oxides growing via outward cation diffusion and inward anion diffusion, respectively. Most oxide systems grow by way of outward cation diffusion. Depending on the defect structure of the oxides, metal cations can migrate via either interstitial or vacancy diffusion mechanisms. Based on the dominant diffusion mechanism the oxygen partial pressure dependence of the oxidation kinetics can significantly be influenced. Section 2.3.1 will present the oxidation kinetics of two oxide systems growing by way of interstitial and vacancy diffusion mechanisms and examine the oxygen partial pressure dependence of the oxidation rate constants derived for each mechanism.

2.3.1. Oxygen partial pressure dependence of the surface oxidation rate constant

First, the growth of an n-type oxide, M_2O_3, which predominantly grows by the diffusion of triple charged interstitial metal cations, is examined. The point defect equation for M interstitials can be written as follows:

$$3/2O_O^X + M_M^X = M_i''' + 3e' + 3/4O_2(g), \quad (2.51)$$

where O_O^X and M_M^X designate the normal lattice positions of O and M in the M_2O_3 lattice, e' is electrons and M_i''' represents the triple charged M interstitials. The equilibrium rate constant of the reaction given in Equation (2.51) can be written as follows:

$$K_{(2.51)} = C_{M_i'''} \times C_{e'}^3 \times P_{O_2}^{3/4}. \quad (2.52)$$

The charge neutrality in M_2O_3 requires:

$$C_{e'} = 3 \times C_{M_i'''}. \quad (2.53)$$

Substituting Equation (2.53) into Equation (2.52) gives the oxygen partial pressure dependence of the concentration of M_i''':

$$C_{M_i'''} \propto P_{O_2}^{-3/16}. \quad (2.54)$$

Assuming that M_2O_3 shows only small deviations from stoichiometry, the chemical potentials of M and O can be related as follows:

$$2\mu_M + 3\mu_O = \mu_{M_2O_3} \approx constant, \tag{2. 55}$$

where μ_O is equal to:

$$\mu_O = \mu_O^\circ + RTlnP_{O_2}^{1/2}. \tag{2. 56}$$

Taking the derivative of Equation (2.54) gives:

$$2d\mu_M = -3d\mu_O. \tag{2. 57}$$

Taking the derivative of Equation (2.56) and substituting into (2.57) results in:

$$d\mu_M = -3/4RTdlnP_{O_2}. \tag{2. 58}$$

Next, Equation (2.58) is substituted in Equation (2.49) to obtain the oxidation rate constant in terms of the oxygen partial pressure:

$$k_S^{M_2O_3} = -3/4 \int_{P_{O_2}^{ext}}^{P_{O_2}^{int}} D_M^{M_2O_3}\, dlnP_{O_2}\ [cm^2/s], \tag{2. 59}$$

where $P_{O_2}^{int}$ and $P_{O_2}^{ext}$ are the oxygen partial pressures at the metal-oxide and oxide-environment interfaces. The diffusion coefficient of M in M_2O_3, $D_M^{M_2O_3}$ is equal to:

$$D_M^{M_2O_3} = D_{M_i}^{\circ,M_2O_3} C_{M_i'''}, \tag{2. 60}$$

where $D_{M_i}^{\circ,M_2O_3}$ is the diffusion coefficient of M interstitials at P_{O_2}= 1atm. Substituting Equations (2.54) and (2.60) into Equation (2.59) gives:

$$k_S^{M_2O_3} = 3/4 \int_{P_{O_2}^{int}}^{P_{O_2}^{ext}} D_{M_i}^{\circ,M_2O_3} P_{O_2}^{-3/16}\, dlnP_{O_2}\ [cm^2/s], \tag{2. 61}$$

which upon integration yields:

$$k_S^{M_2O_3} = 4 \times D_{M,i}^{o,M_2O_3} \times \left[\left(P_{O_2}^{int}\right)^{-3/16} - \left(P_{O_2}^{ext}\right)^{-3/16}\right]. \tag{2. 62}$$

For the general case of $P_{O_2}^{ext} \gg P_{O_2}^{int}$, Equation (2.62) simplifies to:

$$k_S^{M_2O_3} = 4 \times D_{M,i}^{o,M_2O_3} \times \left(P_{O_2}^{int}\right)^{-3/16}, \quad (2.63)$$

which shows that if the oxide is growing predominantly by interstitial diffusion of metal cations, $k_S^{M_2O_3}$ is independent of the ambient oxygen partial pressure.

Now let's examine the case where M_2O_3 is a p-type oxide which predominantly grows by the diffusion of triple charged metal cation vacancies. The point defect equation for M vacancies can be written as follows:

$$O_2(g) = 4/3V_M''' + 4h^{\cdot} + 2/3O_O^X, \quad (2.64)$$

where $h^{\cdot}$ and V_M''' designate holes and triple charged M vacancies, respectively. The equilibrium rate constant of the Equation (2.64) can be written as follows:

$$K_{(2.64)} = C_{V_M'''}^{4/3} \times C_{h^{\cdot}}^4 / P_{O_2}^{3/4}, \quad (2.65)$$

where the charge neutrality in M_2O_3 requires:

$$C_{h^{\cdot}} = 3 \times C_{V_M'''}. \quad (2.66)$$

Substituting Equation (2.66) into Equation (2.65) gives the oxygen partial pressure dependence of the concentration of the metal vacancies:

$$C_{V_M'''} \propto P_{O_2}^{3/16}. \quad (2.67)$$

In this case, the self-diffusion coefficient of M in M_2O_3, $D_M^{M_2O_3}$ is equal to:

$$D_M^{M_2O_3} = D_{V_M'''}^{\circ,M_2O_3} C_{V_M'''}, \quad (2.68)$$

where $D_{V_M'''}^{\circ,M_2O_3}$ is the diffusion coefficient of metal vacancies in M_2O_3 at P_{O_2}= 1atm. Substituting Equations (2.67) and (2.68) into Equation (2.59) and integrating gives the oxidation rate constant of M_2O_3 as follows:

$$k_S^{M_2O_3} = 4 \times D_{V_M'''}^{\circ,M_2O_3} \times \left[\left(P_{O_2}^{ext}\right)^{3/16} - \left(P_{O_2}^{int}\right)^{3/16}\right], \quad (2.69)$$

which for the general case of $P_{O_2}^{ext} \gg P_{O_2}^{int}$ reduces to:

$$k_S^{M_2O_3} = 4 \times D_{V_M'''}^{\circ,M_2O_3} \times \left(P_{O_2}^{ext}\right)^{3/16}. \quad (2.70)$$

As can be seen from Equation (2.70) the oxidation rate constant of an oxide growing predominantly by cation vacancy diffusion mechanism is highly dependent on the ambient oxygen partial pressure.

The oxygen partial pressure dependence of the surface oxidation rate constant can also be significantly influenced by the ionization state of the predominantly mobile species in the oxide scale. Let's assume that M_2O_3 grows by the diffusion of single charged metal cation vacancies instead of the triple charged vacancies. In this case, the point defect equation given in Equation (2.64) for M cations can be written as:

$$O_2(g) = 4/3V_M' + 4/3h^{\cdot} + 2/3O_O^X, \quad (2.71)$$

and the equilibrium rate constant of Equation (2.71) is equal to:

$$K_{(2.64)} = C_{V_M'}^{4/3} \times C_{h^{\cdot}}^{4/3} / P_{O_2}^{3/4}. \quad (2.72)$$

Here, the charge neutrality in M_2O_3 requires:

$$C_{h^{\cdot}} = C_{V_M'}. \quad (2.73)$$

Substituting Equation (2.73) into Equation (2.72) gives the oxygen partial pressure dependence of the concentration of the single charged metal vacancies as follows:

$$C_{V_M'} \propto P_{O_2}^{9/32}. \quad (2.74)$$

Therefore, the oxidation rate constant given in Equation (2.69) becomes:

$$k_S^{M_2O_3} = 8/3 \times D_{V_M'}^{\circ,M_2O_3} \times \left[\left(P_{O_2}^{ext}\right)^{9/32} - \left(P_{O_2}^{int}\right)^{9/32}\right]. \quad (2.75)$$

Comparison of Equations (2.75) and (2.69) explicitly shows the variation in the oxygen partial pressure dependence of $k_S^{M_2O_3}$ due to the change in the ionization state of the predominantly mobile cation.

Wagner's treatment of the kinetics of an outward growing oxide scale indicates that if the primarily mobile species are cation vacancies, the oxidation rate constant rate constant depends on the ambient oxygen partial pressure, which is a function of the ionization state of the vacancies. On the other hand, if the oxide scale grows predominantly by interstitial diffusion mechanism, the ambient oxygen partial pressure dependence of the oxidation rate constant is negligible.

2.3.2. The effect of temperature on the surface oxidation rate constant

The temperature dependence of the growth of an oxide layer can be attributed to three major factors:

1. The diffusion coefficient, $D_M^{M_aO_b}$, is thermally activated and follows the Arrhenius-type relationship:

$$D_M^{M_aO_b} = \left(D_M^{M_aO_b}\right)_0 \exp(-Q/RT), \tag{2. 76}$$

where $\left(D_M^{M_aO_b}\right)_0$ is the athermal pre-exponential coefficient, Q is the activation energy for diffusion and R is the gas constant.

2. The oxygen activity at the metal/oxide interface, $P_{O_2}^{int}$, is constrained by the temperature dependent equilibrium between the metal and its oxide:

$$\left(P_{O_2}^{int}\right)^{b/2} = \exp(\Delta H^{\circ}(M_aO_b)/RT) \times \exp(-\Delta S^{\circ}(M_aO_b)/R). \tag{2. 77}$$

The temperature dependence of $P_{O_2}^{int}$ is unimportant for the oxidation rate constant of an oxide growing predominantly by cation vacancy diffusion mechanism, according to the Equation

(2.70). However, if a double-layered surface oxide is growing predominantly by the diffusion of cation vacancies, then $P_{O_2}^{ext}$ for the inner layer is fixed at the dissociation oxygen partial pressure of the outer layer, which is significantly lower than the ambient oxygen partial pressure. This may also greatly reduce the oxidation kinetics of the inner layer.

3. The degree of non-stoichiometry of the oxide, δ, which is significant only if the oxide phase has a highly disordered structure.

2.3.3. Effect of the oxide microstructure on the surface oxidation rate constant

Wagner's theory is mostly valid at high-temperatures but experimentally measured $k_S^{M_aO_b}$ values may exhibit significant deviations from the theory at low temperatures and in oxides with less defective lattices. Diffusion through the short-circuit paths become more important at lower temperatures as it is experimentally verified that the activation energy for oxidation has smaller values than that at high temperatures. This is attributed to the presence of the grain boundaries that are highly disordered structures providing easy diffusion paths. In addition, at low temperatures finer grained oxide structures with greater fraction of grain boundaries tend to form. As such, oxidation rates are much higher than that predicted by Wagner's theory, which assumes diffusion is controlled only via lattice sites.

Diffusion in polycrystalline oxides can be described by defining an effective diffusion coefficient term which involves weighted fractions of the lattice and boundary diffusivities:

$$D_M^{M_aO_b}(eff) = D_M^{M_aO_b}(lat) \times (1 - f) + D_M^{M_aO_b}(GB) \times f, \quad (2.78)$$

where f is the fraction of the easy-diffusion paths (predominantly grain boundaries), $D_M^{M_aO_b}(lat)$ and $D_M^{M_aO_b}(GB)$ are the lattice and boundary diffusivities, respectively. f is generally given by:

$$f = 3\delta/\phi, \quad (2.79)$$

where δ is the grain boundary width, assumed to be 1nm and ϕ is the oxide grain size [47].

Comparison of the lattice diffusivities of metal cations in most single crystal oxides with the effective diffusivity values measured in their polycrystalline forms revealed that $D_M^{M_aO_b}(GB) > D_M^{M_aO_b}(lat)$. In almost all cases, in an appropriate temperature regime, the activation energy for boundary diffusion is significantly less than that for lattice diffusion. As such, the boundary diffusion becomes the predominant mechanism for oxidation resulting in increased oxidation rates [21] and $k_S^{M_aO_b}$ can be approximated as:

$$k_S^{M_aO_b} = V_{M_aO_b}\Delta C D_M^{M_aO_b}(GB)\, f, \tag{2. 80}$$

where ΔC is the concentration gradient of the metal cations across an oxide scale having molar volume of $V_{M_aO_b}$.

2.3.4. Deviations from Wagner's theory of surface oxidation

If an interfacial process or gas phase mass transfer is slower than the solid-state diffusion in the oxide scale, parabolic oxidation kinetics is not necessarily observed. In such cases, gas adsorption through the oxide scale or gas phase mass transfer (diffusion of gas molecules through a boundary layer at the metal-gas interface) may govern the oxidation kinetics. Here, the basics of interface controlled oxidation and mass transfer in dilute multicomponent gas mixtures are reviewed.

2.3.4.1. Surface controlled processes and linear oxidation kinetics:

When an interfacial process is the rate controlling rather than diffusion through the surface oxide layer, linear oxidation kinetics can be observed. Linear rate law can be defined as follows:

$$X = k_L^{M_aO_b} \times t, \tag{2. 81}$$

where X is the thickness of oxide M_aO_b and $k_L^{M_aO_b}$ is the linear oxidation rate constant.

Linear oxidation kinetics indicates that thermodynamic equilibrium is not necessarily achieved at the metal-oxide and oxide-gas interfaces and reactions at the metal-oxide interface predominantly govern the oxidation kinetics. These surface reactions may involve adsorption of gas molecules and their dissociation to produce adsorbed oxygen.

One example of such surface controlled oxidation kinetics is the oxidation of iron in CO-CO_2 mixtures resulting in formation of $Fe_{1-\delta}O$ [48]. It is assumed that the rate limiting step for oxidation of Fe in CO-CO_2 mixtures is the following reaction:

$$\mathrm{CO_2(g) \rightleftarrows CO(g) + [O]}, \tag{2. 82}$$

where $[O]$ is the adsorbed oxygen atom. The corresponding reaction with Fe resulting in $Fe_{1-\delta}O$ formation can be written as:

$$\mathrm{Fe + CO_2(g) \rightleftarrows FeO + CO(g)}\ , \tag{2. 83}$$

The rate of the reaction 2.83 is equal to:

$$Rate = k_{(2.83)}P'\left(1 + K_{(2.83)}\right) \times \left(N_{CO_2} - N_{CO_2}^{eq}\right), \tag{2. 84}$$

where P' is the total pressure, $N_{CO_2}^{eq}$ is the mole fraction of CO_2 molecule when Reaction (2.83) is in equilibrium, $k_{(2.83)}$ and $K_{(2.83)}$ are the rate constant of the forward reaction and equilibrium constant of the reaction given in Equation (2.83), respectively. Equation (2.84) indicates that the reaction rate is proportional to both the mol fraction of CO_2 and the total pressure. Data shown in Figure 2.6 indicates that the linear rate constant for $Fe_{1-\delta}O$ growth increases with increasing mol fraction of CO_2 and the total gas pressure, verifying the predictions of Equation (2.84). Furthermore, Figure 2.6 shows that the oxidation rate ceases if the CO-CO_2 gas mixture reaches an equilibrium with iron and $Fe_{1-\delta}O$, which is the underlying assumption for derivation of Equation (2.84). Therefore, it is concluded that the rate limiting step is the dissociation of CO_2 molecules and adsorption of oxygen atom at the iron surface.

2.3.4.2. Mass transfer in dilute multicomponent gas mixtures:

When a metal is reacting with an inert environment containing very small amounts of oxidizing molecules, the oxidizing molecules very near to the sample surface are rapidly depleted. The rate of mass transfer from the environment to the metal is limited by the diffusion of the oxidizing molecules through the depleted zone (gas boundary layer). As such, the gas flow rate, the thickness of the gas boundary layer, the partial pressure of the oxidant molecules and the property of the gas mixture influence the rate of mass transfer [21,46].

The flux of an oxidant molecule from a gas mixture flowing parallel to a flat surface is given by:

$$J_i = k_m\left(P_i^{\circ} - P_i^{(s)}\right)/(RT), \tag{2. 85}$$

where k_m is the mass transfer coefficient, P_i° and $P_i^{(s)}$ are the partial pressures of each oxidant molecule in the bulk gas mixture and at the metal surface, respectively. The mass transfer coefficient is given by:

$$k_m = 0.664(D_{mix}^4/\nu_{mix})^{1/6}(\vartheta/L)^{1/2}, \tag{2. 86}$$

where D_{mix} is the interdiffusion coefficient of a binary gas mixture in units cm^2/s, L is the length of the metal surface, and ν_{mix} and ϑ are the kinematic viscosity and the linear velocity of the binary gas mixture, respectively. The interdiffusion coefficient is given by the Chapman - Enskog formalism [21,49]:

$$D_{mix} = 1.858 \times 10^{-3} \times \sqrt{T^3 \times (1/MW_A + 1/MW_B)}/(P_T\sigma_{AB}^2\Omega_{AB}), \tag{2. 87}$$

where MW_A and MW_B are the molecular weights of the two species forming the binary gas, P_T is the ambient gas pressure, σ_{AB} is their average collision cross-section in units $\AA$ and Ω_{AB} is a dimensionless collision integral term, which is a function of temperature and the interaction potential between the molecules in the gas mixture.

The kinematic viscosity is defined as:

$$\nu_{mix} = \eta_{mix}/\rho_{mix}, \tag{2. 88}$$

where ρ_{mix} is the density and η_{mix} is the viscosity of the binary gas mixture in units *Poise*, which is given by:

$$\eta_{mix} = \sum_{i=1}^{n}\left(P_i^{\circ}\eta_i/\sum_{j=1}^{n}P_j^{\circ}\Phi_{ij}\right), \tag{2. 89}$$

where Φ_{ij} is equal to:

$$\Phi_{ij} = 1/\sqrt{8}\times\left(1+MW_i/MW_j\right)^{-1/2}\times\left[1+\sqrt{\eta_i/\eta_j}\times\left(MW_j/MW_i\right)^{1/4}\right]^2, \tag{2. 90}$$

and η_i is the viscosity of the each constituent of the gas mixture, given as:

$$\eta_i = 2.669\times10^{-5}\times\sqrt{MW_iT}/(\sigma_i^2\Omega_{\mathrm{i}}). \tag{2. 91}$$

σ_i is the collision cross-section and Ω_{i} is the collision integral of pure *i* molecules. Equation (2.91) is valid when the gas flow is laminar, which requires Schmidt number, S_C to be 0.6 - 50. Schmidt number can be calculated as:

$$S_C = \vartheta/D_{mix}. \tag{2. 92}$$

In dilute multi-component gas environments, linear oxidation kinetics may be observed which indicates that the gas phase surface or interfacial processes may be rate controlling. In such cases, less stable phases may grow instead of the most thermodynamically stable oxide phase corresponding to the equilibrium oxygen partial pressure of the gas mixture. The analysis above is useful to determine the flux of the gas molecules that primarily react with the metal at the gas-metal interface. In reality, the gas phase mass transfer may not necessarily be the rate-controlling step and instead impingement of the most abundant molecules and their chemisorption may govern the oxidation kinetics.

2.3.5. Summary

Wagner's oxidation theory assumes that the diffusion of ionic species is controlling the surface oxidation kinetics. His model relates the parabolic surface oxidation rate constant to the defect structure of the oxides, mobility of the lattice species, ambient oxygen partial pressure and temperature. In n-type oxides, primary mobile species are cation interstitials and the ambient oxygen partial pressure dependence of the oxidation rate constant is negligible. In p-type oxides, cation vacancy diffusion dominates the growth kinetics, which is highly dependent on the ambient oxygen partial pressure. The ionization state of the mobile species has a strong influence on the oxygen partial pressure dependence of the oxidation rate constant. In dilute multicomponent environments, the surface reactions may be rate controlling rather than diffusion of ionic species across the oxide scale. This results in linear oxidation kinetics and can explain the deviations observed from parabolic oxidation kinetics during the transient period of oxidation in simulated IHX environments. Next section focuses on the kinetics and growth mechanisms of Cr_2O_3 at high temperatures.

2.4. Kinetics and mechanism of Cr_2O_3 growth at high temperatures

High temperature oxidation resistance of Alloy 617 can mainly be attributable to formation of Cr_2O_3. Therefore, the defect and transport properties that determine the growth rate of Cr_2O_3 in wide range of temperatures and environments with widely varying oxygen partial pressure is of particular interest. This section reviews the kinetics and mechanism of chromia growth kinetics on pure Cr and Ni-Cr based alloys in an effort to examine the factors that control the surface oxidation kinetics of Alloy 617 in IHX helium equivalent environments.

2.4.1. Kinetics of surface Cr_2O_3 growth

Figure 2.7 shows the weight gain rate constants measured for single crystal and polycrystalline Cr_2O_3 growth, k_W, on pure Cr [50] and on chromia forming alloys[2] [5,44,51–53]. Two important observations can be made from Figure 2.7: the growth rate of polycrystalline Cr_2O_3 is at least an order of magnitude faster than that of single crystal Cr_2O_3 and the rate of polycrystalline Cr_2O_3 growth on chromia forming alloys is at least a factor of 10 slower than that on pure Cr. Weight gain rate constants range over 4 orders of magnitude with activation energy values in the range of 157 - 330 kJ/mol [50,54]. Such wide scatter in the data can be attributed to several factors including the microstructure and the transport properties of the Cr_2O_3 films [50], evaporation of Cr_2O_3 especially at high temperatures and oxygen partial pressures [52,55–61], blistering of Cr_2O_3 films due to growth stresses [50–52,58,62,63], segregation of more reactive elements/impurities to the grain boundaries of Cr_2O_3 [53,61,64,65].

2.4.2. Mechanism of surface Cr_2O_3 growth

Caplan and Sproule [50] observed that well-adhered, single crystal Cr_2O_3 films formed on pure Cr specimens etched in HCl at a growth rate 30 - 90 times slower than that of the polycrystalline Cr_2O_3 films developed on the surface of the electropolished pure Cr and Fe-Cr alloy samples in the temperature range of 980 - 1200°C. The authors deduced that stress-free single crystal Cr_2O_3 grows at the oxide-gas interface by outward diffusion of Cr cations with an activation energy of 243 kJ/mol. Kofstad and Lillerud [57,58,63,66,67] assumed that the Cr cations mainly diffuse interstitially in Cr_2O_3 lattice at ambient oxygen partial pressures near the Cr/Cr_2O_3 phase boundary with an activation energy of 230 - 245 kJ/mol. However, the activation energy by itself is not sufficient to be indicative of the interstitial type diffusion mechanism

[2] k_W values are either associated with only Cr_2O_3 formation or determined from the independent measurements of $k_S^{Cr_2O_3}$ using Equation (2.32).

which is characterized by the measured oxidation rate constants to be independent of the ambient oxygen partial pressure according to Equation (2.63). Hindam and Whittle [51,52] showed that the Cr oxidation rate constant is independent of the oxygen partial pressure in the range of 10^{-8} - 10^{-14} atm at 1000°C and that the Cr interstitials are the predominantly mobile species. They also indicated that the lower surface oxidation kinetics measured for chromia forming alloys compared to that measured for pure Cr (as shown in Figure 2.7) is another indication of the interstitial type diffusion mechanism. It is apparent that the chromium activity in the alloys is less than unity, thus the equilibrium oxygen partial pressure at the alloy - oxide interface is greater than that when Cr_2O_3 is in equilibrium with pure Cr. Such increase in the oxygen partial pressure at the metal-oxide interface would make no difference in the oxidation rate constants if vacancy diffusion were to be the dominant mechanism (Section 2.3.1). Even though the chromium interstitials seemed to be the predominantly mobile species in Cr_2O_3, the four-point conductivity measurements conducted by Park and Natesan [59] indicated that Cr_2O_3 exhibited p-type semiconductor behavior, which requires primary charge carriers in Cr_2O_3 to be Cr vacancies, in the temperature range of 577 - 1088°C. On the other hand, Atkinson and Taylor [68] proposed that at low oxygen partial pressures Cr interstitials are the dominant, whereas at low oxygen partial pressures Cr vacancies are the dominant defects. Figure 2.8 shows three regions indicating the oxygen partial pressure dependence of Cr diffusion coefficient. Region I ($P_{O_2}^{ext} < 10^{-15}$ atm) indicates a regime where the Cr diffusion coefficient is inversely proportional with the oxygen partial pressure. In region II (10^{-15} atm $< P_{O_2}^{ext} < 10^{-10}$ atm) the Cr diffusion coefficient is independent of the oxygen partial pressure, which suggests that Frenkel defects may be the dominant defects ($C_{V_M'''}=C_{M_i'''}$) due to formation of a stoichiometric Cr_2O_3 [69]. In

Region III ($P_{O_2}^{ext}$ > 10^{-10} atm) Cr diffusion coefficient exhibits a positive oxygen partial pressure dependence indicating that the vacancies are the predominantly mobile species.

Lattice diffusion in Cr_2O_3 appears to be too slow to sustain the experimentally measured growth kinetics of polycrystalline Cr_2O_3 films which suggests grain boundary diffusion to be the dominant growth mechanism [50,53,61,64,66,67,70–74]. Caplan and Sproule [50] observed that the new oxide particles nucleated within the existing Cr_2O_3 scale, which further induced compressive stresses resulting in wrinkling of the fine grained films. This indicated that Cr_2O_3 growth occurred also by anion diffusion. Since no compressive stress was observed in the monocrystalline part of the oxide, the authors deduced that anion diffusion must be facilitated along the oxide grain boundaries. Thus, the growth of polycrystalline Cr_2O_3 can be attributed to the counter-current diffusion of both chromium cations and oxygen anions along the grain boundaries. However, Giggins and Pettit [75] observed that the position of platinum markers deposited on the pristine surface of Ni-30Cr alloy remained at the metal-oxide interface after an oxidation treatment at 1200°C. They deduced that the Cr_2O_3 film grows outward, predominantly by the diffusion of Cr cations. These competing observations point to another question of how important inward O diffusion is relative to the outward Cr diffusion in Cr_2O_3 growth.

The oxygen and chromium diffusion in Cr_2O_3 was also studied by analyzing the diffusion profiles of ^{18}O and ^{54}Cr radiotracers across the Cr_2O_3 scales using SIMS. Figure 2.8 shows the lattice, grain boundary and effective oxygen and chromium diffusion coefficients in Cr_2O_3 determined from the analysis of the radiotracer diffusion profiles reported in the literature [53,61,72–74]. Sabioni et al. [61,72–74] found that oxygen diffusion is faster than the chromium diffusion in the bulk and along the grain boundaries of Cr_2O_3. However, the diffusion coefficients that they determined are significantly lower than the rest of the values shown in

Figure 2.9 and even too low to account for the oxidation rate constant that they measured in their study. In addition, if the oxygen diffusion were to be dominant, then Cr_2O_3 would grow inwards at the metal - oxide interface, which obviously is not the case.

Tsai et al. [53] determined that lattice and grain boundary diffusion of chromium in Cr_2O_3 was faster but the inward oxygen diffusion could not be neglected. They concluded that the oxide grows both at the oxide-gas interface via outward diffusion of chromium vacancies and at the metal-oxide interface via inward oxygen interstitial diffusion without nucleation of new oxide particles within the existing Cr_2O_3 scale. On the other hand, Cotell et al. [64] observed that inward oxygen diffusion was relatively unimportant and Cr_2O_3 growth is controlled entirely by outward Cr diffusion along the grain boundaries.

2.4.3. Summary

Previous studies have determined that Cr_2O_3 grows mainly outward via Cr cation diffusion. Lattice diffusion is dominated by interstitial mechanism at low ambient oxygen partial pressures, whereas at high oxygen partial pressure chromium vacancies are the primary mobile species. The lattice diffusion coefficients appear to be slower than that can sustain the observed growth kinetics of polycrystalline Cr_2O_3. Thus, it is concluded that Cr_2O_3 growth is driven primarily by grain boundary diffusion.

2.5. Theory of internal oxidation

Internal oxidation occurs when a gas phase oxidant dissolves in an alloy and diffuses inward oxidizing solute elements more reactive than the base metal [36]. When the inward flux of oxygen could not be compensated by the outward flux of the solute element, dispersed internal oxide precipitates form at the sub-surface. The necessary conditions for internal oxidation to occur are listed as follows [46]:

1. The solute metal oxide, BO_ν[3] in an alloy AB must be more stable than the oxide of the base metal, AO_ν,
2. The formation energy of BO_ν must be negative, such that the solubility and diffusivity of oxygen in the base metal is sufficient to establish the required oxygen chemical potential for the formation of BO_ν,
3. The solute concentration of the alloy must be lower than that required for the formation of a surface oxide,
4. The solubility product for local equilibrium between the precipitate and the matrix ($N_O^\nu N_B$) should be very small, such that oxygen diffuses through the alloy matrix without interfering with the internal precipitates.

This section will cover the internal oxidation kinetics both in the absence of surface oxidation and beneath a growing surface oxide, and a criterion for transition from internal oxidation to surface oxidation.

2.5.1. Internal oxidation kinetics in the absence of surface oxidation

Internal oxidation kinetics can be analyzed by solving the coupled diffusion equations for outward diffusing solute element B and inward diffusing oxygen [19,76]:

$$\partial N_i/\partial t = D_i \partial^2 N_i/\partial x^2, \quad (2.93)$$

where N_i and D_i are the atomic fraction and diffusion coefficient of component i, respectively. The schematic description of the diffusion problem is given in Figure 2.10. The figure describes the case of atomic oxygen diffusing into the metal matrix surrounding the previously formed internal oxide precipitates and reacting with the outward diffusing B at the internal oxidation

[3] ν designates the ratio of oxygen atoms to metal atoms in a given stoichiometric internal oxide phase.

reaction front which is at a depth X_i from the surface. X_i can be defined in terms of the oxygen diffusion distance within the internal oxidation zone:

$$X_i = 2\gamma \times \sqrt{D_O t}, \tag{2. 94}$$

where γ is a dimensionless proportionality constant.

The initial and boundary conditions to solve Equation (2.93) for both the diffusion of solute B and oxygen are listed as follows:

i. $N_B = N_B^{(o)}$ for $x = 0, t = 0,$ (2. 95)

ii. $N_B = 0$ for $x \leq X_i, t > 0,$ (2. 96)

iii. $N_O = N_O^{(s)}$ for $x = 0, t > 0,$ (2. 97)

iv. $N_O = 0$ for $x \geq X_i, t > 0,$ (2. 98)

where the superscripts " (s) " and " ° " denote the surface and bulk concentrations of N_i. The solutions to Equation (2.93) are:

$$N_O = N_O^{(s)}\left[1 - erf\left(x/2\sqrt{D_O t}\right)/erf\gamma\right], \tag{2. 99}$$

and

$$N_B = N_B^{(o)}\left[1 - erf\left(x/2\sqrt{D_B t}\right)/erf\left(\gamma\phi^{1/2}\right)\right], \tag{2. 100}$$

where

$$\phi = D_O/D_B. \tag{2. 101}$$

It is important to note that the internal oxide penetration depth X_i given in Equation (2.94) has a parabolic time dependence, which can also be defined in the form of:

$$X_i^{\,2} = 2k_I^{BO_v} \times t, \tag{2. 102}$$

where $k_I^{BO_\nu}$ is the internal oxidation rate constant. Thus, the proportionality constant γ in Equations (2.94), (2.99) and (2.100) can be written in terms of experimentally measurable quantities:

$$\gamma = \sqrt{k_I^{BO_\nu}/2D_O}. \tag{2. 103}$$

Wagner assumed that new oxide precipitates nucleate at the alloy-oxide interface located at a depth X_i from the surface. Therefore, the fluxes of B and O are equal at this location:

$$-D_B(\partial N_B/\partial x)_{x=X_i} = \nu D_O(\partial N_O/\partial x)_{x=X_i}. \tag{2. 104}$$

Substituting the differentials of the Equations (2.99) and (2.100) into Equation (2.104) yields:

$$N_O^{(s)}/N_B^{(o)} = [\nu \times erf\gamma \times exp(\gamma^2)]/\left[\phi^{1/2}exp(\gamma^2\phi)erfc(\gamma\phi^{1/2})\right], \tag{2. 105}$$

where $N_O^{(s)}$ is the atomic fraction of dissolved oxygen often referred as "oxygen solubility" in the literature. For brevity, the atomic fraction of dissolved oxygen in the alloy will be referred as "oxygen solubility" throughout the rest of this dissertation.

If the diffusion of B is very slow relative to oxygen and the oxygen solubility in the alloy is relatively small compared to the content of B in the alloy, the case represented in Figure 2.10a applies:

$$D_B/D_O \ll N_O^{(s)}/N_B^{(o)} \ll 1. \tag{2. 106}$$

As such, $\gamma \ll 1$ and $\gamma\phi^{1/2} \gg 1$ and Equation (2.103) becomes:

$$\gamma \approx \left[N_O^{(s)}/\left(2\nu N_B^{(o)}\right)\right]^{1/2}. \tag{2. 107}$$

Substituting Equation (2.107) into Equation (2.103) gives the parabolic internal oxidation constant when the diffusion of B is insignificant compared to that of O:

$$k_I^{BO_\nu} = D_O N_O^{(s)}/\left(\nu N_B^{(o)}\right). \tag{2. 108}$$

If, on the other hand, the diffusion of B is comparable to that of oxygen, as represented in Figure 2.10b, then:

$$N_O^{(s)}/N_B^{(o)} \ll D_B/D_O \ll 1. \tag{2. 109}$$

As such, $\gamma \ll 1$ and $\gamma\phi^{1/2} \ll 1$ and Equation (2.103) becomes:

$$\gamma \approx \left(\pi^{1/2}\phi^{1/2}N_O^{(s)}\right)/\left(2\nu N_B^{(o)}\right). \tag{2. 110}$$

Substituting Equation (2.110) into Equation (2.103) gives the parabolic internal oxidation constant when the diffusion of B is comparable to that of oxygen:

$$k_I^{BO_\nu} = \pi/D_B\left[D_O N_O^{(s)}/\left(2\nu N_B^{(o)}\right)^2\right]. \tag{2. 111}$$

2.5.2. Internal oxidation kinetics beneath a growing surface oxide

In the case of internal oxide BO_ν growing beneath a surface oxide, M_aO_b, the original alloy surface recedes in association with surface oxidation. The shift in the original alloy surface position is corrected by modifying Equation (2.99) [23,76,77]:

$$N_O = N_O^{(s)}\left\{\left[erf\gamma - erf\left(x/2\sqrt{D_O t}\right)\right]/erf\gamma - erf\left(1/2\sqrt{k_C^{M_aO_b}/D_O}\right)\right\}, \tag{2. 112}$$

where $k_C^{M_aO_b}$ is the rate of M recession at the alloy sub-surface in association with surface M_aO_b formation and can be related to $k_S^{M_aO_b}$ term defined in Equation (2.31) as follows:

$$k_C^{M_aO_b} = \left(2V_M/V_{M_aO_b}\right)^2 \times k_S^{M_aO_b}\ , \tag{2. 113}$$

where V_M and $V_{M_aO_b}$ are the molar volumes of M and M_aO_b. Writing the flux balance given by Equation (2.104) establishes the relationship between the oxygen solubility and the oxygen diffusion coefficient with the rate of internal oxidation measured beneath an oxidizing alloy surface:

$$\frac{N_O^{(s)}}{N_{Al}^{(o)}} = \frac{\nu\left[erf\gamma - erf\left(1/2\sqrt{k_C^{M_aO_b}/D_O}\right)\right]exp(\gamma^2)}{\left[\phi^{1/2}exp(\gamma^2\phi)erfc(\gamma\phi^{1/2})\right]}. \quad (2.\ 114)$$

2.5.3. Transition from internal to external oxidation

Wagner [19] proposed that the transition from internal to external oxidation takes place if the concentration of the more active component *B* in an alloy is sufficiently high for the volume fraction of internal BO_ν precipitates to reach a critical value which is required for the formation of laterally growing sub-surface oxide layer.

The volume fraction of the BO_ν precipitates in the sub-surface of an alloy, g_{BO_ν}, can be defined as follows:

$$g_{BO_\nu} = N_{BO_\nu} V_{BO_\nu}/V_M\ , \quad (2.\ 115)$$

where N_{BO_ν} denotes the mole fraction of the BO_ν precipitates. N_{BO_ν} can be defined in terms of the bulk concentration of solute B in the alloy:

$$N_{BO_\nu} = \propto N_B^\circ, \quad (2.\ 116)$$

where $\propto$ is the degree of the enrichment of the solute *B* atoms at the internal oxidation reaction front. The degree of solute enrichment is given by:

$$\propto = \left[\pi^{1/2}(\gamma\phi^{1/2})exp(\gamma^2\phi)erfc(\gamma\phi^{1/2})\right]^{-1}. \quad (2.\ 117)$$

When the volume fraction of the internal oxide precipitates reaches to a critical value, $g_{BO_\nu}^{crit}$, transition from internal oxidation to external oxidation of *B* can be realized. Rapp [20] determined that Ag - In alloys oxidized in air at 550 °C exhibited transition from internal to external oxidation if N_{In}° was greater than 0.15. For Ag - In alloy system, $\propto$ in Equation (2.116) is 1. Thus, using Equation (2.115) the critical volume fraction of $InO_{1.5}$ precipitates was determined to be 0.30, which is accepted as the characteristic value for $g_{BO_\nu}^{crit}$ in this dissertation

work. The critical concentration of B atoms which can is sufficiently high for BO_v precipitates to reach $g_{BO_v}^{crit}$ is equal to:

$$N_B^{\circ,crit} = \sqrt{\pi}\gamma\sqrt{\phi}exp(\gamma^2\phi)erfc\left(\gamma\sqrt{\phi}\right)g_{BO_v}^{crit}V_M/V_{BO_v}. \quad (2.\ 118)$$

If the diffusion of B is comparable to that of oxygen and the condition presented in Equation (2.99) is valid, $\propto$ given in Equation (2.117) can be simplified to:

$$\propto = 2\nu N_B^{\circ,crit}D_B/\left(\pi N_O^{(s)}D_O\right), \quad (2.\ 119)$$

and Equation (2.118) can be simplified to:

$$N_B^{\circ,crit} = \sqrt{\left(g_{BO_v}^{crit} \times \pi/2\nu\right) \times \left(V_M/V_{BO_v}\right) \times \left(N_O^{(s)}D_O/D_B\right)}. \quad (2.\ 120)$$

It is important to note that Equation (2.120) indicates that the critical concentration of B to prevent the internal oxidation of an alloy increases with $N_O^{(s)}$ and D_O. Any process that enhances either the oxygen solubility at the alloy surface or the oxygen diffusion coefficient within the internal oxidation zone may result in severe internal oxidation of an alloy. Such processes may result in significant deviations from the predictions of the classical surface internal oxidation theories previously presented in this section. The processes that can cause deviations from the ideal assumptions of the classical oxidation theory are briefly presented in the following section.

2.5.4. Deviations from the classical internal oxidation theory

According to the classical theory, internal oxidation in an alloy occurs by dissolution of oxygen at the alloy surface and inward diffusion of atomic oxygen through the alloy matrix surrounding discrete, spherical oxide particles. Based on these assumptions, Equations (2.105) and (2.114) relate the oxygen solubility at the surface of an alloy and oxygen diffusion coefficient in the alloy to the internal oxidation rate constants.

Ni - Al alloy system is of particular interest because experimentally measured internal oxidation rate constants are much greater than those predicted by the classical internal oxidation theory. One of the reasons for this discrepancy could be enhanced oxygen diffusion along the incoherent internal Al_2O_3 - alloy interfaces which act as easy-diffusion paths for oxygen [29–31]. Furthermore, recent research has shown that Cr_2O_3 that forms on pure Cr and chromia forming alloys is gas permeable [24–28], which can significantly enhance oxygen solubility at the alloy-oxide interface.

These findings do not invalidate Equations (2.105) and (2.114); rather they indicate that the internal oxidation kinetics can be accelerated by processes that enhance oxygen solubility and diffusion coefficient. Therefore, the main focus of this section is to provide a review of the internal oxidation in Ni-Al system and gas permeability of surface oxide scales.

2.5.4.1. Internal oxidation of binary Ni - Al alloys

Whittle et al. [29] and Stott et al. [30,31] and observed that the depths of internal oxidation in binary Ni - xAl (x: 1 - 8 at. %) alloys oxidized in Ni/NiO Rhines packs are independent of the alloy composition. This is in contradiction with the prediction of Equation (2.108) under the limiting conditions stated in Equation (2.106). Equation (2.108) states that the internal oxidation rate constant is inversely proportional with the solute concentration in the alloy, $N_B^{(o)}$. Therefore, the depth of internal oxidation varies inversely with the square root of $N_B^{(o)}$ according to Equation (2.102). As can be seen in Figure 2.11, the penetration depth measured in Ni - Cr alloys as a function of $N_{Cr}^{(o)}$ is in agreement with Equation (2.108), whereas in Ni - Al alloys it does not. This was attributed to the formation of rod-like Al_2O_3 precipitates, as shown in Figure 2.12, which forms incoherent boundaries with the alloy matrix facilitating

inward oxygen diffusion. Therefore, internal oxidation of Ni-Al alloys display two notable distinctions from the assumptions of the classical internal oxidation theory:

1. Formation of rod-shaped elongated internal oxide precipitates instead of spherical and discrete particles,
2. Oxygen diffusion is facilitated along the Al_2O_3-alloy interfaces rather than occurring through the alloy matrix.

Whittle et al. [29] and Stott et al. [30,31] assumed that observed internal Al oxidation kinetics is sustained by an effective oxygen flux, $J_O\,(eff)$, which is the sum of flux through the alloy matrix, Al_2O_3-alloy interfaces and Al_2O_3 precipitates. The oxygen flux through the Al_2O_3 precipitates was neglected and thus the effective oxygen diffusion coefficient, $D_O^{Ni-Al}\,(eff)$ was related to those in the lattice, $D_O^{Ni-Al}\,(lat)$, and along the Al_2O_3-alloy interfaces, $D_O^{Ni-Al}\,(int)$, according to the following equation:

$$\frac{D_O^{Ni-Al}\,(eff)}{D_O^{Ni-Al}\,(lat)} = 1 + \left(V_{Al_2O_3} N_{Al_2O_3}^{\mathrm{Ni-Al}} / V_{Ni-Al}\right)\left[2\delta_i D_O^{Ni-Al}\,(int)/\left(r D_O^{Ni-Al}\,(lat)\right) - 1\right], \qquad (2.\ 121)$$

where $D_O^{Ni-Al}\,(lat)$ is assumed to be equal to the lattice oxygen diffusion coefficient in pure Ni, D_O^{Ni}, $V_{Al_2O_3}$ and V_{Ni-Al} are the molar volumes of Al_2O_3 and the alloy, respectively; $N_{Al_2O_3}^{\mathrm{Ni-Al}}$ is the mole fraction of internal Al_2O_3 precipitates; δ_i is the interface width and r is the average radius of the internal Al_2O_3 precipitates.

The above treatment of the internal oxidation behavior of Ni-Al alloys clearly indicates that morphology of the internal oxides can influence the internal oxidation kinetics by facilitating interfacial oxygen diffusion.

2.5.4.2. Permeation of molecular oxidants through the surface oxides:

Isothermal oxidation of pure Cr, Fe-Cr and Ni-Cr alloys in environments containing CO, CO_2, N_2, SO_2 and H_2O revealed that the internal oxidation front keeps advancing at significantly

high rates beneath a sufficiently thick and continuous surface scale [24–27]. More interestingly, internal carbide, nitride and sulfide phases grow beneath surface Cr_2O_3 scale even though the solubility of carbon, nitrogen and sulfur in Cr_2O_3, Al_2O_3, FeO or Fe_3O_4 is negligible. As such, the growth of these phases beneath a continuous oxide scale can be attributed to the transport of molecular oxidants through imperfections that are present in the surface scales. This section summarizes the experimental observations which provide evidence to the permeability of surface oxides to molecular oxidants present in the environment.

Wolf and Grabke [78] equilibrated samples of single crystal and polycrystalline FeO, Fe_3O_4, MnO, MgO, Cr_2O_3 and Al_2O_3 in a CO/CO_2 gas mixture containing radiotracers at 1000°C. Carbon diffusion through the lattices and/or grain boundaries of the specimens was studied with an autoradiography technique with a minimum ^{14}C detection limit of 0.01 weight ppm. The results showed no carbon presence in the lattice or grain boundaries of the samples except in cracks, pores or grain boundaries. It was concluded that there is no measureable solubility of elemental C in the oxides and carbon permeation through such scales can only occur via transport of CO and/or CO_2 through the pores and cracks present in the scales.

Oxidation of pure Cr, Mn and Fe as well as binary Fe-Cr, Co-Cr and Ni-Cr alloys in various gas mixtures containing CO, CO_2, H_2, H_2O, N_2 and SO_2 revealed that the equilibrium activities of elemental oxygen, carbon and sulfur are insufficient to sustain the observed oxidation, sulfidation and carburization rates. The primary reacting species were determined as CO, CO_2 and SO_2 [24–27,79,80]. Figure 2.13 shows that internal carbide and nitride scales continue to grow beneath a surface Cr_2O_3 growing on pure Cr. This was attributed to the permeability of Cr_2O_3 to the molecular oxidants as the solubility and atomic diffusion of elemental C and N are negligible in compact Cr_2O_3 [24–27].

Permeability of Cr_2O_3 to molecular oxidants depends on the environment composition and whether the substrate is pure chromium or a chromium containing alloy. Young and Zheng [24–27] oxidized pure chromium in H_2-H_2O-N_2 environments and observed formation of surface Cr_2O_3 only (Figure 2.14a). Upon subsequent exposure to a CO-CO_2-N_2 environment with identical equilibrium oxygen and nitrogen activities, internal carbide and nitride layers formed beneath the surface Cr_2O_3 (Figures 2.14b and c). It was found that water vapor containing environments result in formation of Cr_2O_3 which is impermeable to nitrogen. On the other hand, oxidation in CO-CO_2-N_2 mixture causes Cr_2O_3 to be permeable to both carbon and nitrogen. Subsequent addition of SO_2 to CO-CO_2-N_2 makes Cr_2O_3 impermeable to nitrogen; but not to sulfur and carbon. These observations were explained by the preferential adsorption of certain molecules by the Cr_2O_3 scale.

Young and Zheng [24,26] stated that oxidation of Fe-Cr, Co-Cr or Ni-Cr binary alloys in similar multicomponent environments results in segregation of Fe and Ni into Cr_2O_3. Figure 2.15 shows that the segregated metal particles preferentially react with CO and N_2 molecules providing an effective barrier against permeation of carbon. They also observed that subsequent addition of SO_2 to the environment may facilitate carbon permeation through the Cr_2O_3 scale as SO_2 is adsorbed by Fe and Ni segregated in Cr_2O_3 in expense of CO.

Finally, Rouillard et al. [28] exposed Alloy 230 samples pre-oxidized in He containing 80 - 100 molppm H_2O, to a dry He mixture containing 50 molppm CO composed of ^{13}C and ^{18}O radiotracers at 850 °C. As can be seen from Figure 2.16, Secondary Ion Mass Spectrometry (SIMS) and Glow Discharge Mass Spectroscopy (GDMS) results indicate that ^{13}C and ^{18}O penetrated the Cr_2O_3 layer and reached deeper in the alloy beneath the alloy/oxide interface. Considering that elemental carbon is insoluble in Cr_2O_3, it was concluded that CO permeated the

surface oxide in its molecular form through fast diffusion paths, such as nanopores/channels or grain boundaries to reach the alloy/oxide interface.

2.5.5. Summary

The classical theory assumes that internal oxidation of an alloy is governed by oxygen dissolution at the alloy surface (or metal-oxide interface) and oxygen diffusion through the alloy matrix surrounding the spherical internal oxide particles. However, the internal oxidation kinetics of Ni-Al based alloys appear to be much faster than that predicted by the theory due to formation of rod-like shaped internal Al_2O_3 precipitates which facilitate inward oxygen diffusion. Furthermore, sufficient evidence has been shown that surface Cr_2O_3 film is gas permeable, which can increase the oxygen solubility at the alloy - oxide interface of the alloys oxidized in multicomponent gas mixtures. Therefore, these two effects can greatly increase the driving force for internal oxidation in Ni-Cr-Al based alloy systems.

2.6. Oxidation of Al in Ni-Al and Ni-Cr-Al based alloys

This section reviews the oxidation of Ni-Al and Ni-Cr-Al based alloys with the focus on understanding the alloy composition and temperature effects on the transition from internal to external Al oxidation of an alloy.

Figure 2.17 presents an “oxide map” which outlines the oxidation regimes of Ni-Al alloys as a function of Al composition and temperature [46]. The figure shows three major regions that characterize the oxidation behavior of the alloy separated by wide cross-hatched borders where a variation between the two major oxidation regimes can be observed. Region I indicates that alloys containing up to 13 at.% Al exhibit internal penetration of α-Al_2O_3 and formation of surface NiO and Ni-Al based spinels. Region II shows the Al composition range (13 - 31 at.%) where the alloys initially form surface α-Al_2O_3 which is subsequently replaced by surface NiO

and Ni-Al spinel due to insufficient Al supply from the base metal over prolonged exposures. Note that 25 at.% Al containing Ni_3Al intermetallic falls into this category and is likely to form sustainable surface Al_2O_3 scale at temperatures below 1200 °C. Alloy compositions that fall into Region III (> 31 at.% Al) can form sustainable external Al_2O_3 scales. Formation of slow growing α-Al_2O_3 is very desirable for long-term oxidation resistance; however it requires very high Al concentrations in the alloy.

It has been shown that addition of Cr as the "third-element" in a Ni-Al alloy promotes formation of surface Al_2O_3 scales on alloys containing lower Al than that is indicated in Figure 2.17 [81]. The "third-element" effect was first observed by Wagner [82], who suggested that the element having intermediate stability between the base metal and the most noble elements acts as an oxygen getter reducing oxygen solubility and flux into the base metal. Guan and Smeltzer [83] Cr addition to Ni-Al alloy can effectively decrease oxygen solubility. Nesbitt and Heckel [84] showed that Cr addition increases the Al flux in Ni-Cr-Al system. These observations indicated that Cr addition to Ni-Al system effectively reduces the driving force for internal Al oxidation and can even facilitate formation of surface Al_2O_3 scales.

Figure 2.18 shows the oxide maps for Ni-Cr-Al alloys oxidized in 0.1 atm oxygen at 1000 - 1200 °C [85]. Different from the Ni-Al system, Region II in these maps designates the group of alloys which form both surface Cr_2O_3 and internal Al_2O_3. Comparison of Figure 2.18 with Figure 2.17 confirms that the minimum concentration of Al required for surface Al_2O_3 formation is reduced. For instance, at 1200 °C an alloy containing 11 at.% Cr and as low as 6 at.% Al exhibited surface Al_2O_3 formation whereas a binary Ni-Al alloy requires around 30 at.% Al.

Figure 2.19 shows that the oxidation kinetics observed in each region indicated in Figure 2.15 differ from each other approximately by 1 order of magnitude and the measured weight gain rate constants follow the trend: Region I > Region II > Region III. Figure 2.16 also compares the oxidation kinetics of Region I, Region II and Region III alloys with those measured in pure Ni, Ni-30Cr and Ni-25Al, respectively. Region I alloys exhibited greater weight gains than that did pure Ni, which can be attributed to the formation of Ni, Cr and Al based spinels in addition to NiO. Region II alloys, on the other hand, exhibited slightly lower weight gain kinetics than did Ni-30Cr alloys. This could be attributed to the increase in the Cr flux in the alloy due to Al presence [84]. Finally, Region III alloys exhibited slightly greater weight gains than did Ni-25Al. Considering that the surface oxidation kinetics of both types of alloys is controlled via diffusion through the Al_2O_3 scale, slight difference in the measured weight gain kinetics may be due to the possible differences in the structure of Al_2O_3 formed on each alloy.

The candidate nickel based superalloys for IHX application fall into Region II shown in Figure 2.18 based on their composition (Cr: 20-24 wt.%, Al: 0.1 - 1.5 wt.% [9]). Therefore, it is not surprising that they exhibit substantial internal Al oxidation beneath a surface Cr_2O_3 in IHX equivalent helium environments. In addition, the "third-element effect" associated with the high Cr content of the alloys is likely to be countered by the processes which are likely to increase the inward oxygen flux in the alloys as described in Section 2.5.4. Unfortunately, previous oxidation studies were mainly concerned with describing the general corrosion behavior of these alloys in low oxygen partial pressure environments and internal Al oxidation of these alloys have not been studied by systematically varying the environment oxygen partial pressure, temperature and Al concentration in the alloys. Therefore, there are no data available in the literature to describe the

mechanism of internal oxidation in these alloys and predict the minimum aluminum concentration required to prevent internal Al oxidation.

2.7. Objective and approach

The objective of this dissertation is to characterize the surface and internal oxidation behavior and determine the oxygen transport mechanisms that govern the internal Al oxidation of Alloy 617 in helium environments containing ppm levels of CO and CO_2 at 750 - 850 °C. It is hypothesized that accelerated oxygen diffusion along the Al_2O_3 - alloy interfaces and enhanced oxygen solubility at the alloy - Cr_2O_3 interface due to gas permeability of Cr_2O_3 are the two mechanisms that result in severe internal Al oxidation of Alloy 617.

To test this hypothesis, the following approach was followed. First, internal Al oxidation kinetics of Alloy 617 were measured at fixed oxygen solubility at the alloy surface established by an ambient oxygen activity equal to the dissociation oxygen partial pressure of Cr_2O_3 in a Rhines pack experiment [86] at 850 °C. Next, the oxygen diffusion coefficient corresponding to the measured internal oxidation kinetics was determined. Then the internal Al oxidation kinetics of Alloy 617 beneath a growing Cr_2O_3 film were measured in two He-CO-CO_2 environments with CO/CO_2 ratios 9 and 1320 at 850 °C. The internal oxidation rate constants measured in He-CO-CO_2 environments and the oxygen diffusion coefficient values determined from the Rhines pack exposure were used to determine the oxygen solubility values established at the alloy - Cr_2O_3 interface in each environment. The oxygen solubility values at the alloy-Cr_2O_3 interface determined in He-CO-CO_2 environments are compared to that established at the surface of the Alloy in Rhines pack exposure to assess the gas permeability of Cr_2O_3. The significance of the oxygen diffusion coefficients determined in the Rhines pack exposure is discussed in terms of

the influence of easy diffusion paths and in comparison with the values reported in pure Ni and binary Ni alloys in the literature.

The mechanisms of internal Al oxidation in Alloy 617 are further substantiated by determining the Arrhenius parameters (activation energy and pre-exponential coefficient) of the oxygen solubility and diffusion coefficient values based on the internal Al oxidation kinetics measured in He-CO-CO_2 environments in the temperature range of 750 - 850 °C. Finally, the oxygen solubility and diffusion coefficients were used to determine the critical concentration of Al required to mitigate internal Al oxidation of Alloy 617.

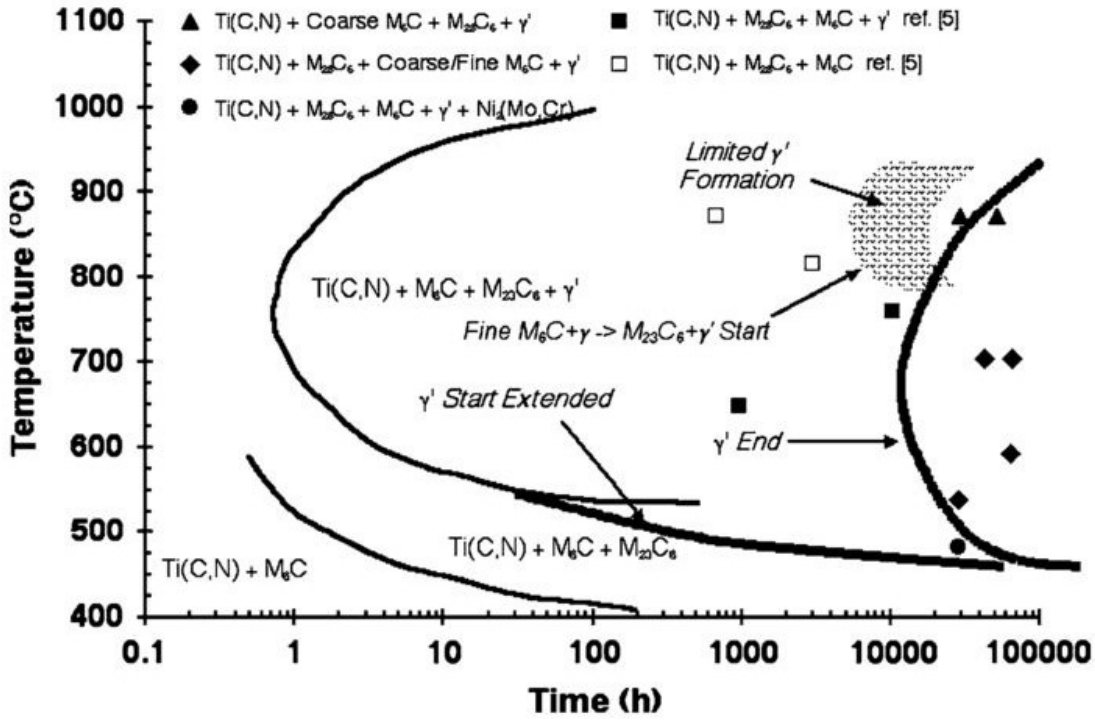

Figure 2.1 T-T-T diagram of Alloy 617 [36]

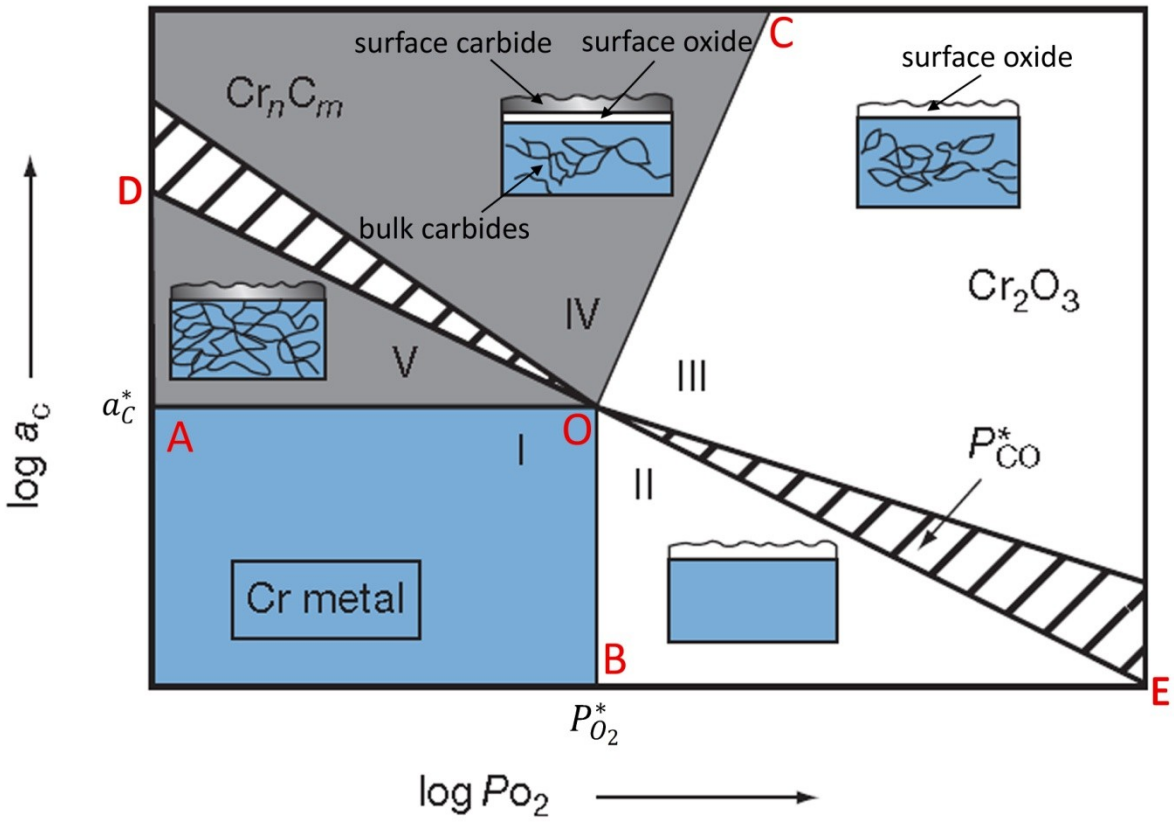

Figure 2.2 Cr - C - O stability diagram and the schematic representation of the corrosion regimes expected to be observed in each condition.

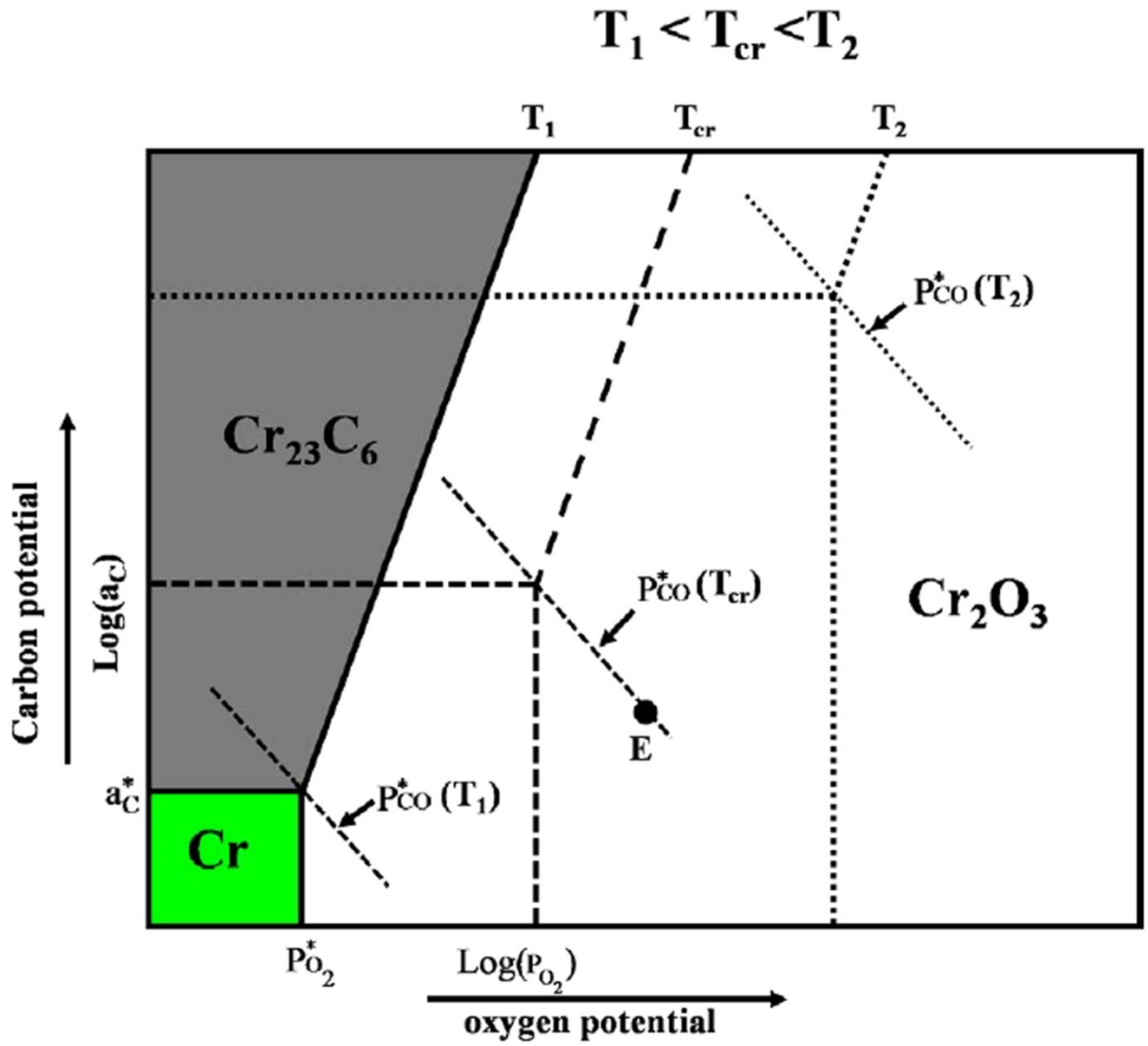

Figure 2.3 Description of the temperature dependence of P_{CO}^{*} on a Cr - C - O stability diagram. The graph is reproduced from Kumar [38].

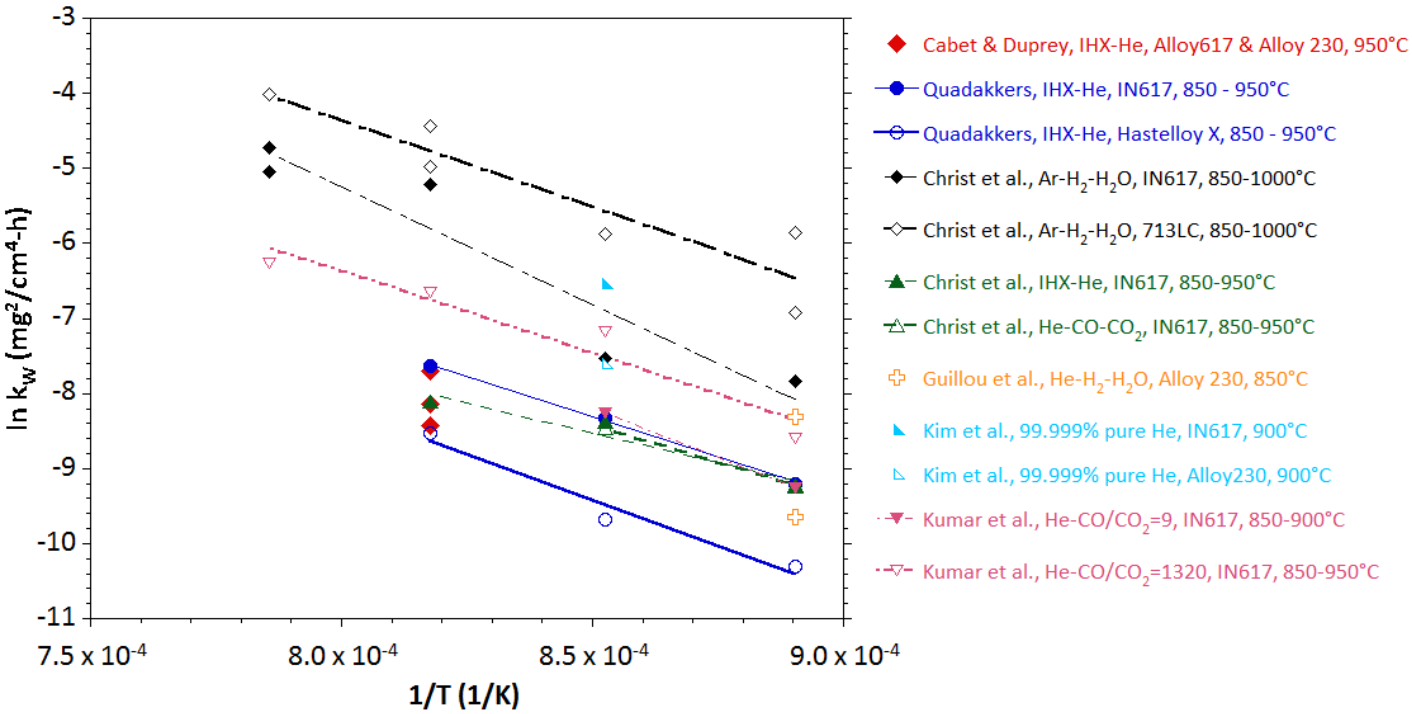

	ln (k_w°)	Q/R	Q (kJ/mol)	R^2
Christ et al., Ar-H_2-H_2O, IN617	19.7	31122	258.8	0.90
Christ et al., Ar-H_2-H_2O, 713LC	14.1	23114	192.2	0.86
Quadakkers, IHX - He, IN617	10.0	21528	179.0	0.99
Quadakkers, IHX - He, Hastelloy X	11.2	24292	202.0	0.96
Christ et al., IHX - He, IN617	4.8	15675	130.3	0.94
Christ et al., He-CO-CO_2, IN617	8.8	20185	167.8	1.00
Kumar et al., He-CO/CO_2=9, IN617	14.0	26147	217.4	1.00
Kumar et al., He-CO/CO_2=1320, IN617	11.1	21783	181.1	0.92

Figure 2.4 Parabolic weight gain rate constants of the most common Ni-Cr based candidate alloys in simulated IHX helium or equivalent low oxygen partial pressure environments at 850 - 1000 °C.

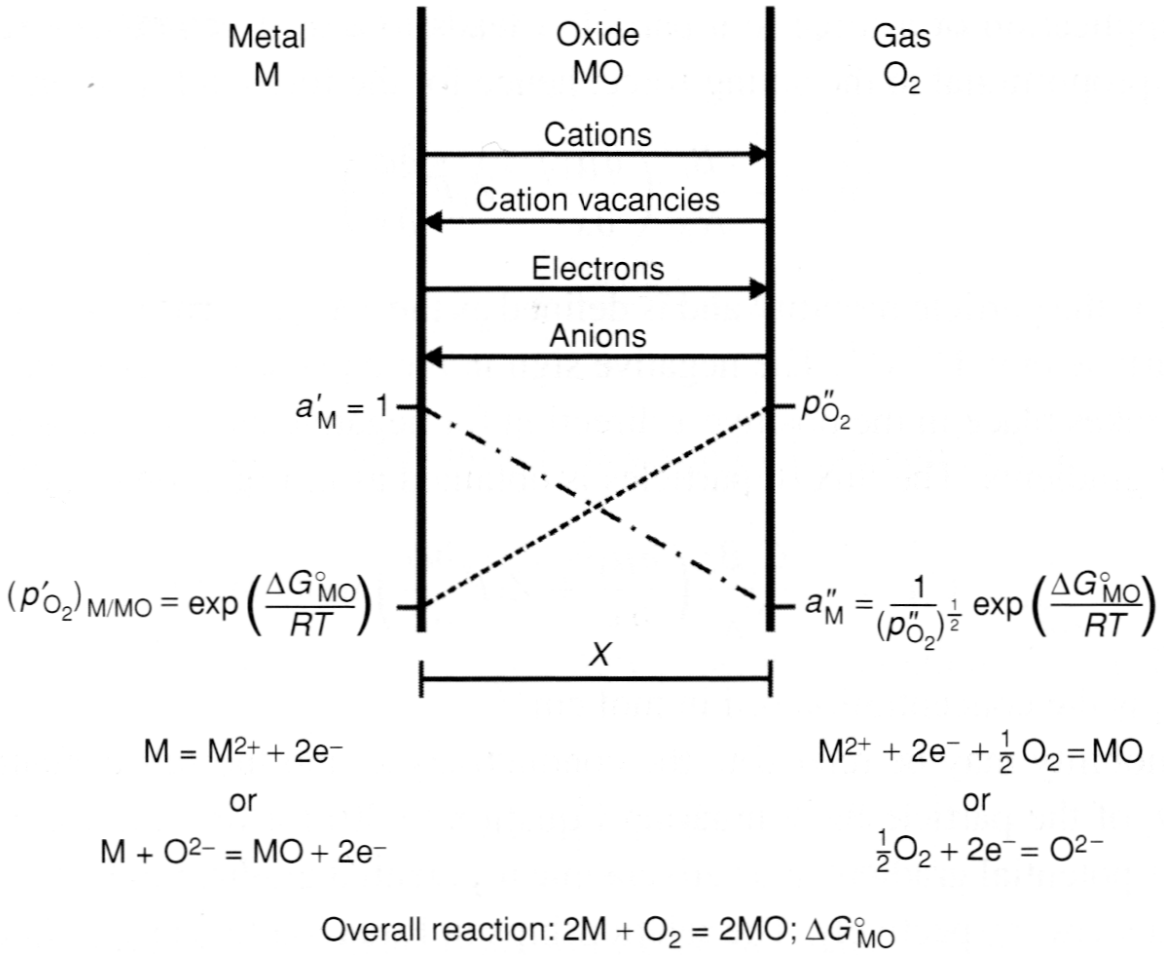

Figure 2.5 Schematic representation of oxide growth according to Wagner's theory of oxidation [46].

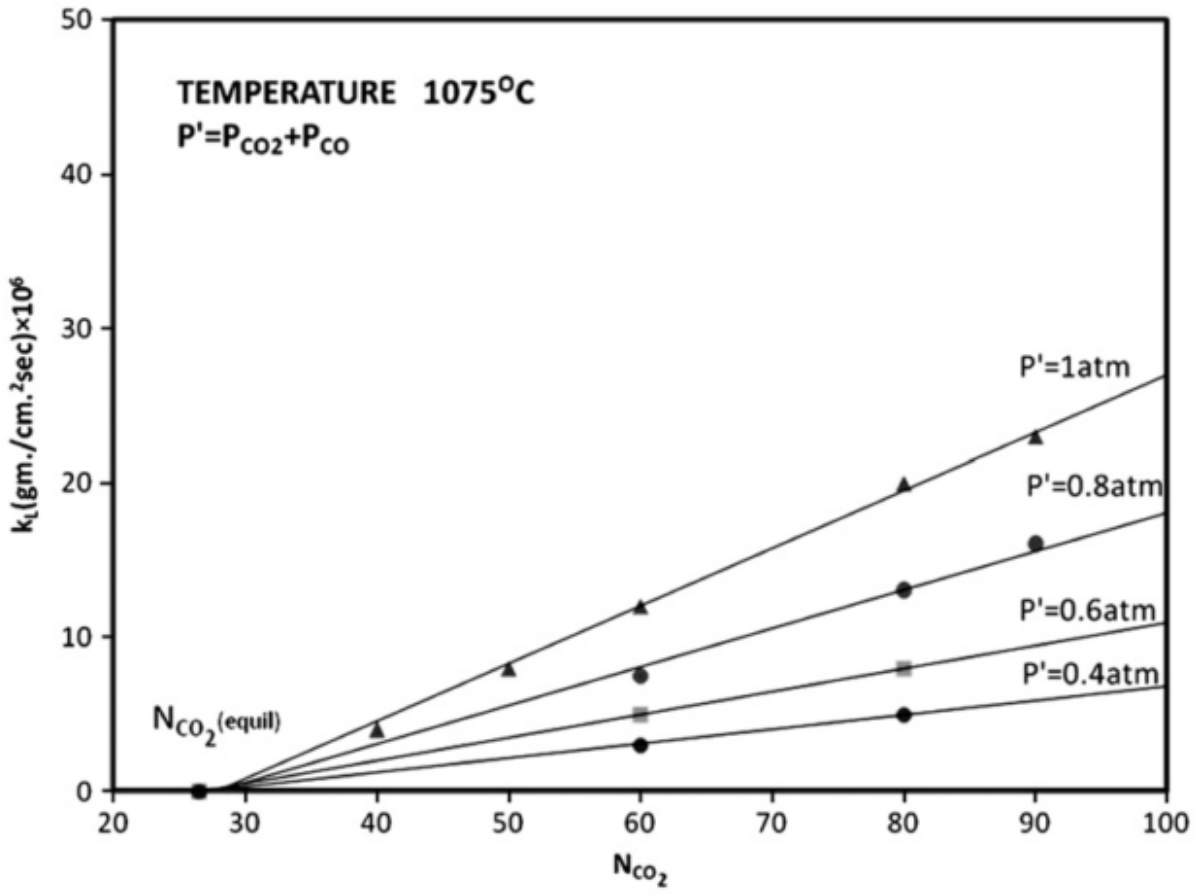

Figure 2.6 Variation of the oxidation rate of iron in CO-CO_2 as a function of CO_2 mole fraction at 1075 °C [48].

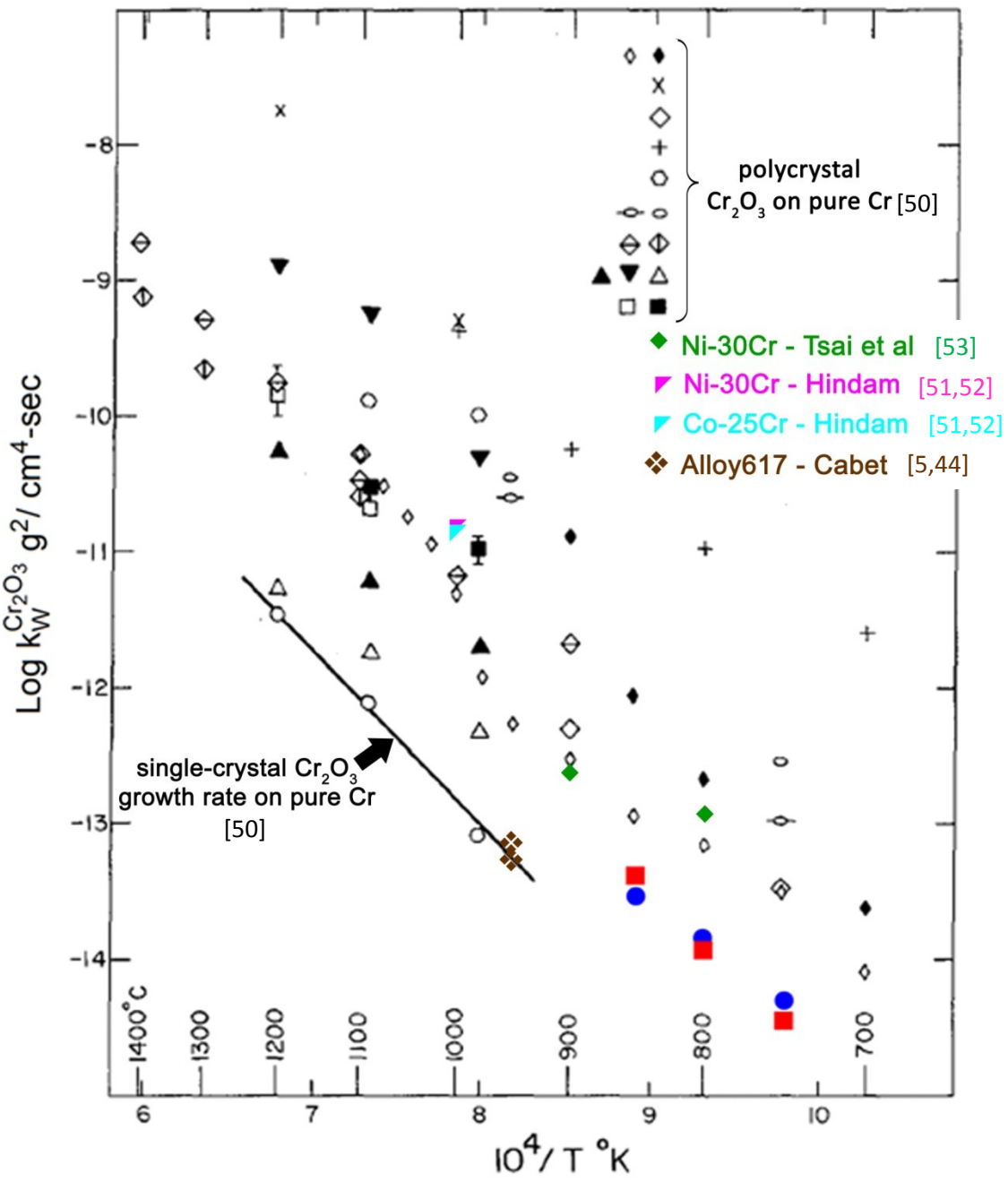

Figure 2.7 Kinetics of Cr_2O_3 growth reported in the literature pure Cr and chromia forming alloys. The plot is reproduced from Caplan and Sproule [50].

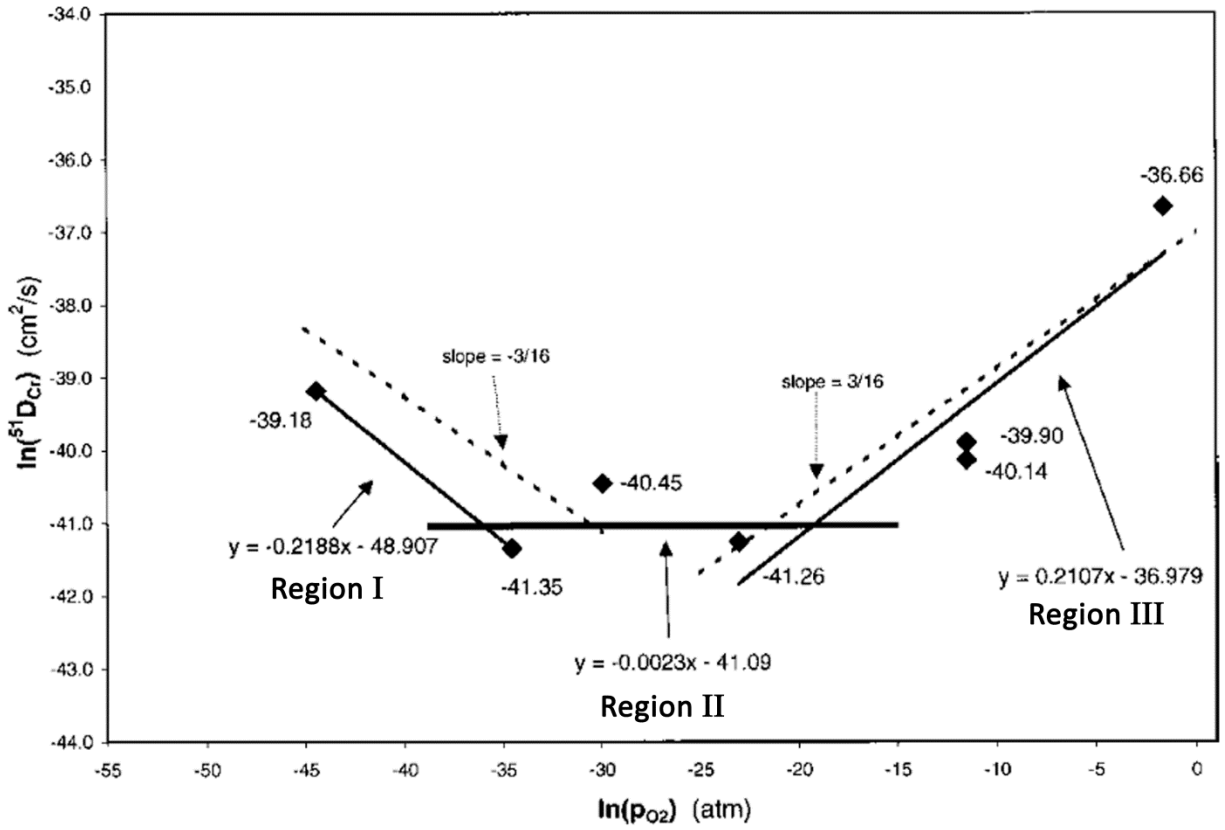

Figure 2.8 Plot of Cr tracer self-diffusion coefficients in the bulk of Cr_2O_3 measured as a function of ambient oxygen partial pressure at 1100 °C [68]. Plot is reproduced from England and Virkar [69].

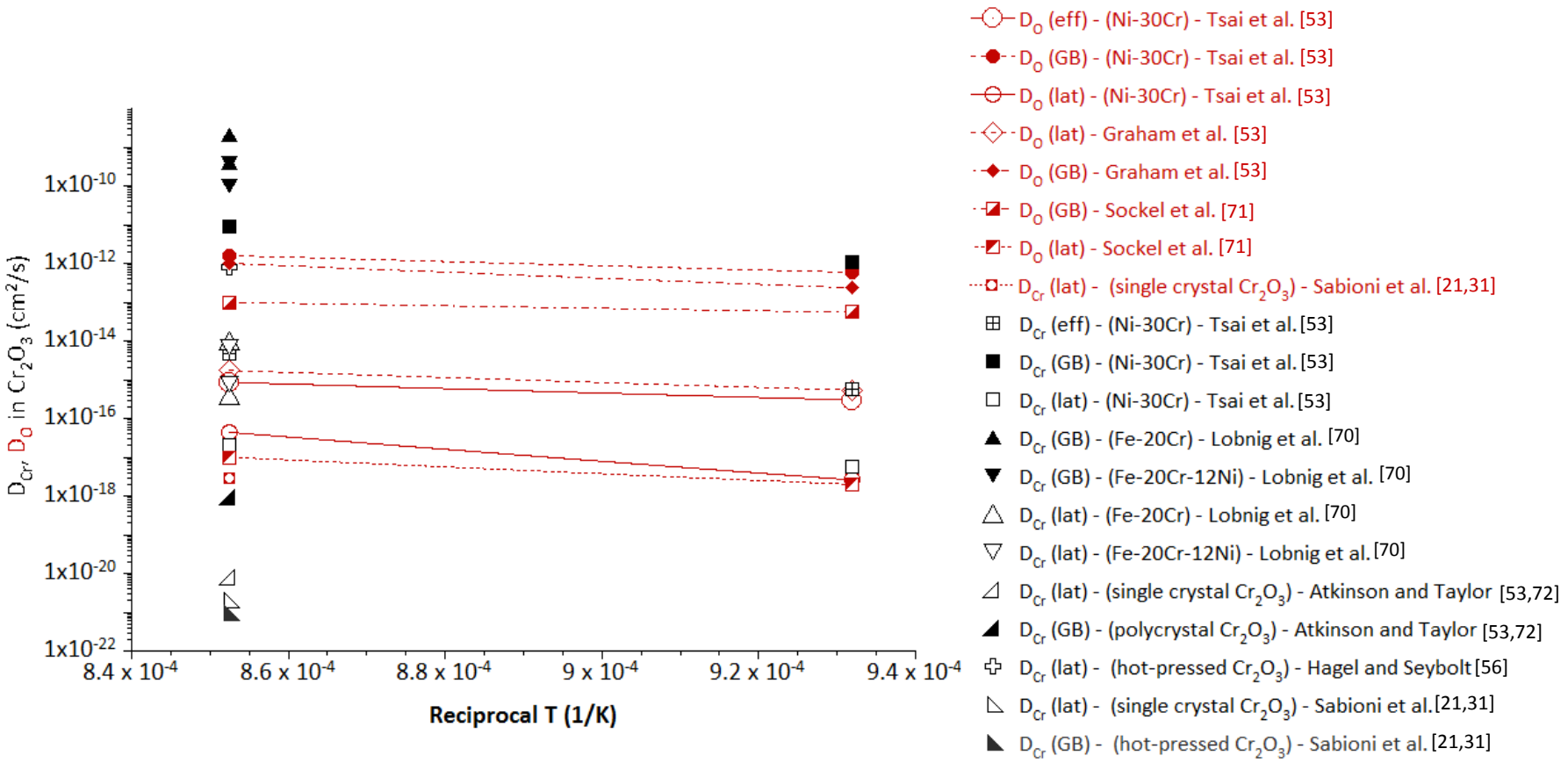

Figure 2.9 Comparison of the lattice, grain boundary and effective diffusion coefficients of oxygen (red) chromium (black) in Cr_2O_3. Oxygen diffusion coefficient data points are connected with lines to distinguish them from the chromium diffusion coefficient data points. The plot is reproduced from Tsai et al. [53].

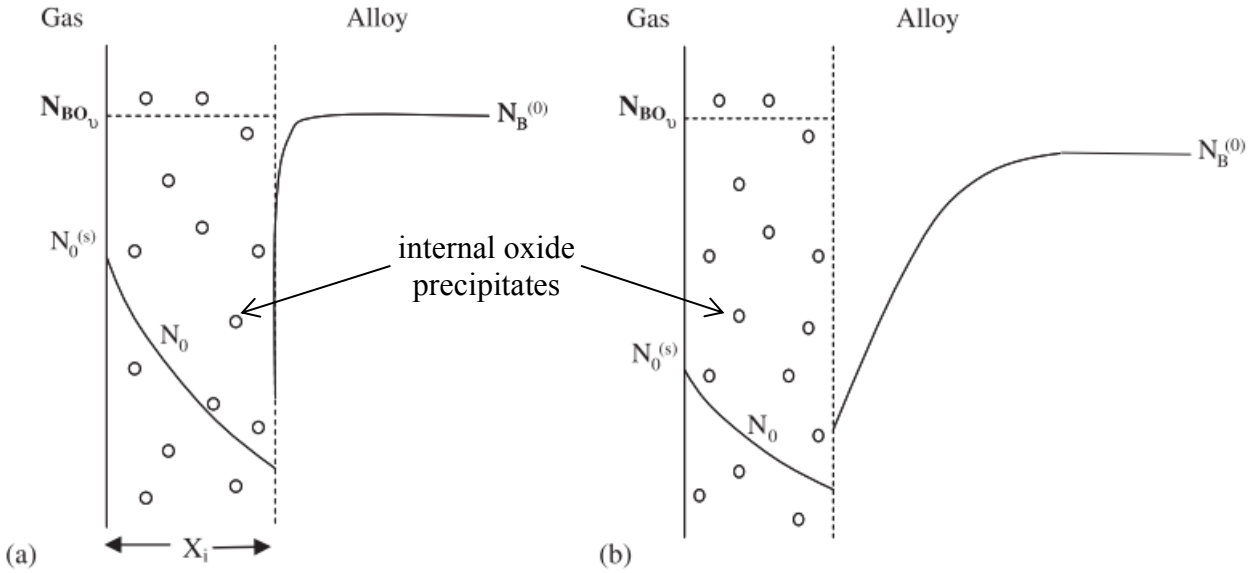

Figure 2.10 Schematic representation of the internal oxidation reaction front and the reactant concentration profiles when: a) solute element B is immobile, b) both oxygen and B diffuse. The schematics are reproduced from Young [21].

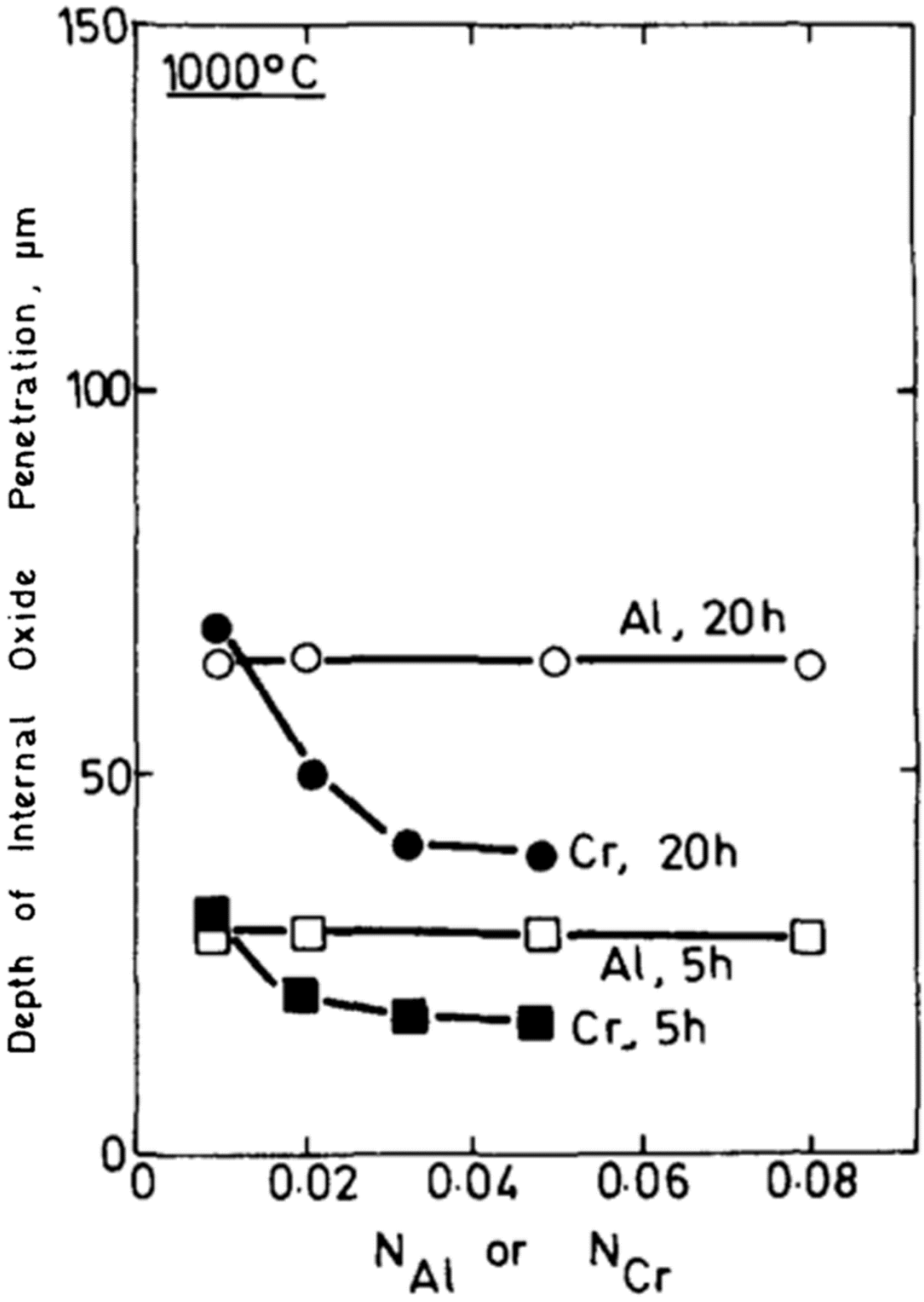

Figure 2.11 The depths of internal oxide penetration of Ni-Cr and Ni-Al alloys oxidized in Ni/NiO Rhines packs at 1000 °C. Graph is reproduced from Stott et al. [30].

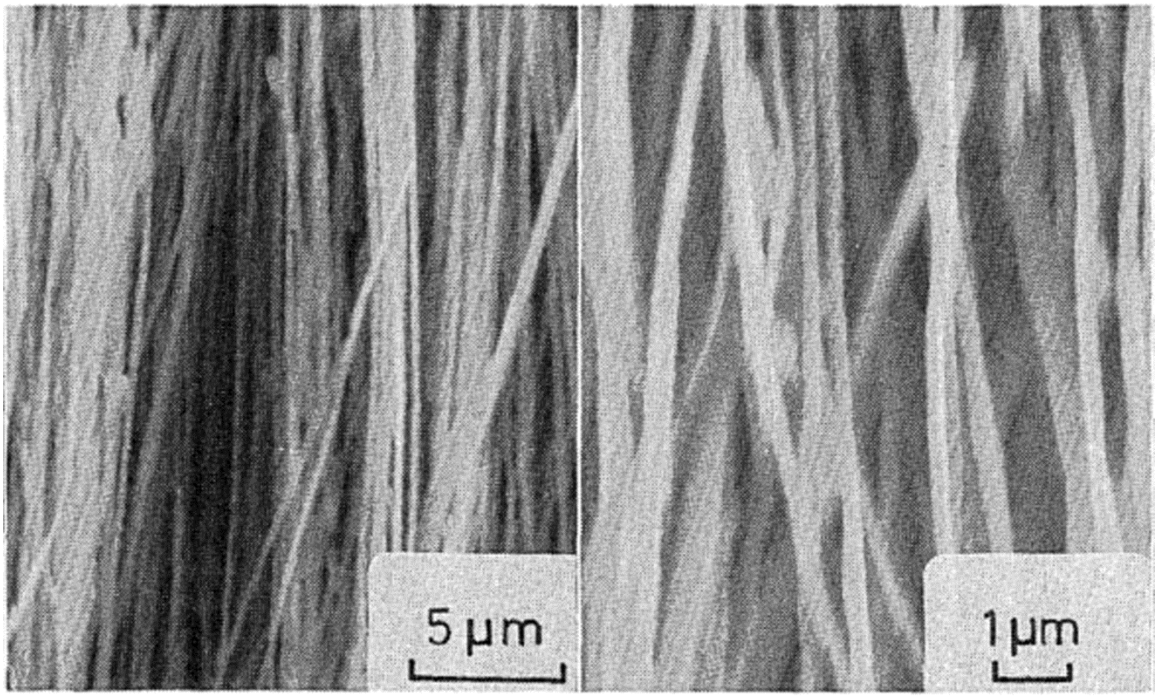

Figure 2.12 Morphology of the internal Al_2O_3 precipitates in the etched cross-sections of Ni-Al alloys after oxidation in Ni/NiO Rhines packs at 1000 - 1100 °C [31].

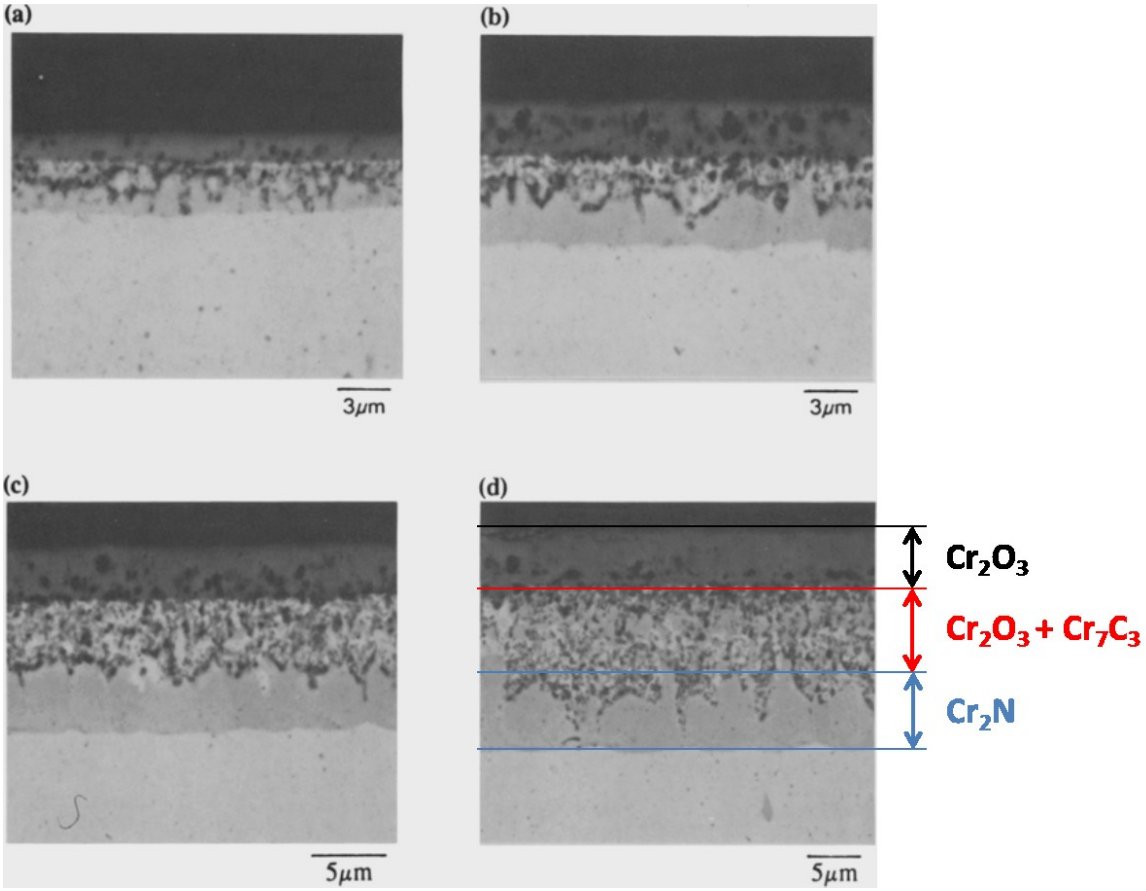

Figure 2.13 Cross-section of pure Cr samples exposed to CO - CO_2 - N_2 at 900 °C for a) 35min, b) 2h, c) 5h, d) 15h [27].

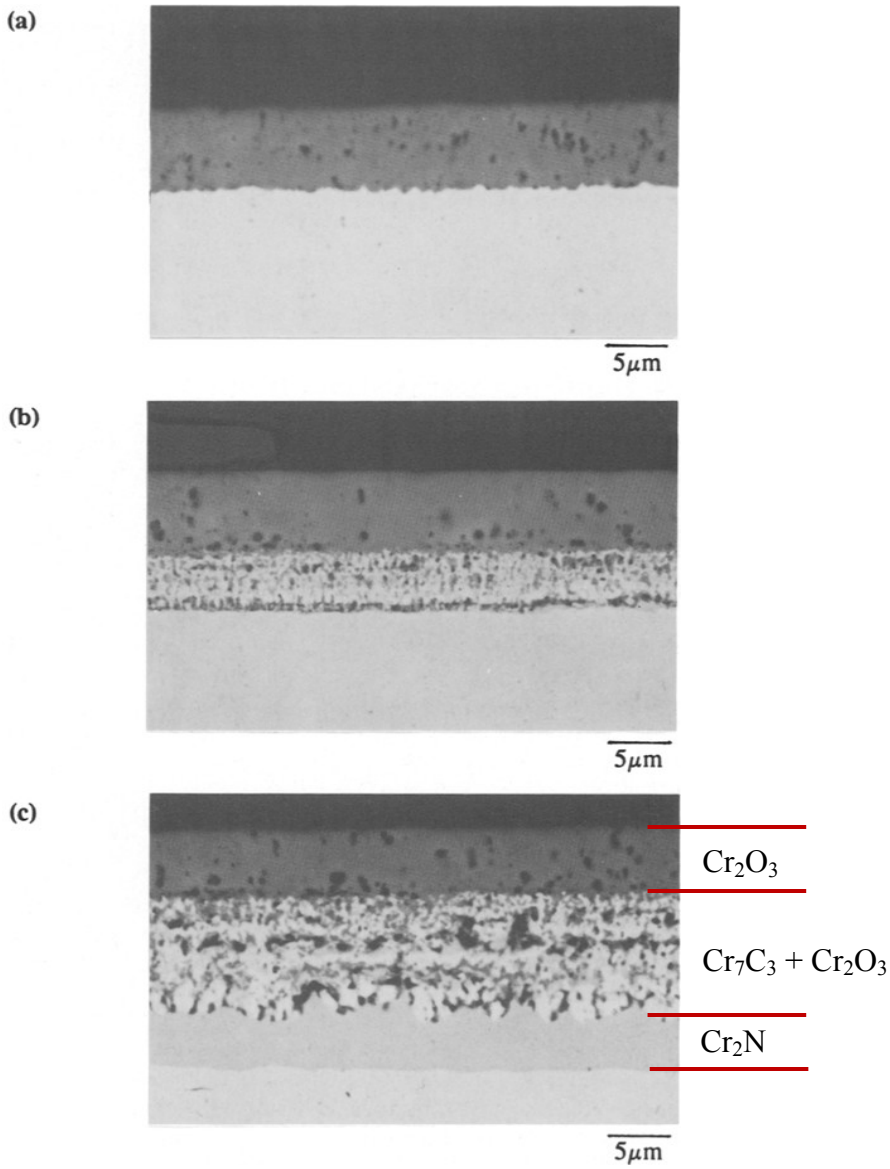

Figure 2.14 Cross-section of pure Cr samples exposed to exposed to a) H_2 - H_2O - N_2 (no internal oxidation), b) CO - CO_2 (internal carbides and oxides formed), c) CO - CO_2 - N_2 (internal carbides, oxides and nitrides formed) for 22h at 900 °C [27].

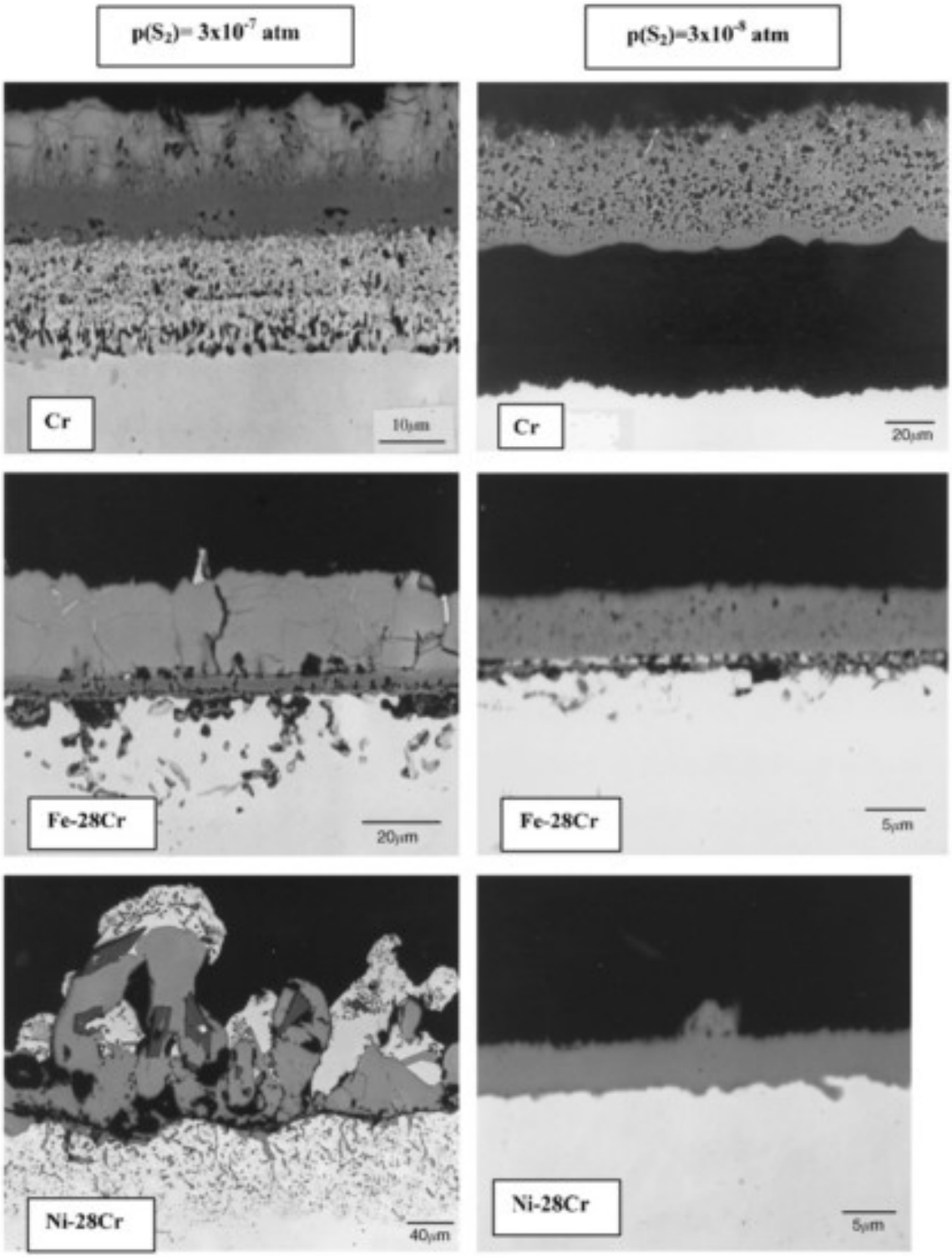

Figure 2.15 Cross-sections of pure Cr, Fe-Cr and Ni-Cr samples after 2h pre-oxidation in CO - CO_2 - N_2 followed by exposure to CO - CO_2 - N_2 - SO_2 gas mixtures at 900 °C with $P_{S_2} = 3 \times 10^{-7}$ and $P_{S_2} = 3 \times 10^{-8}$ for 18h and 35h, respectively [24,26].

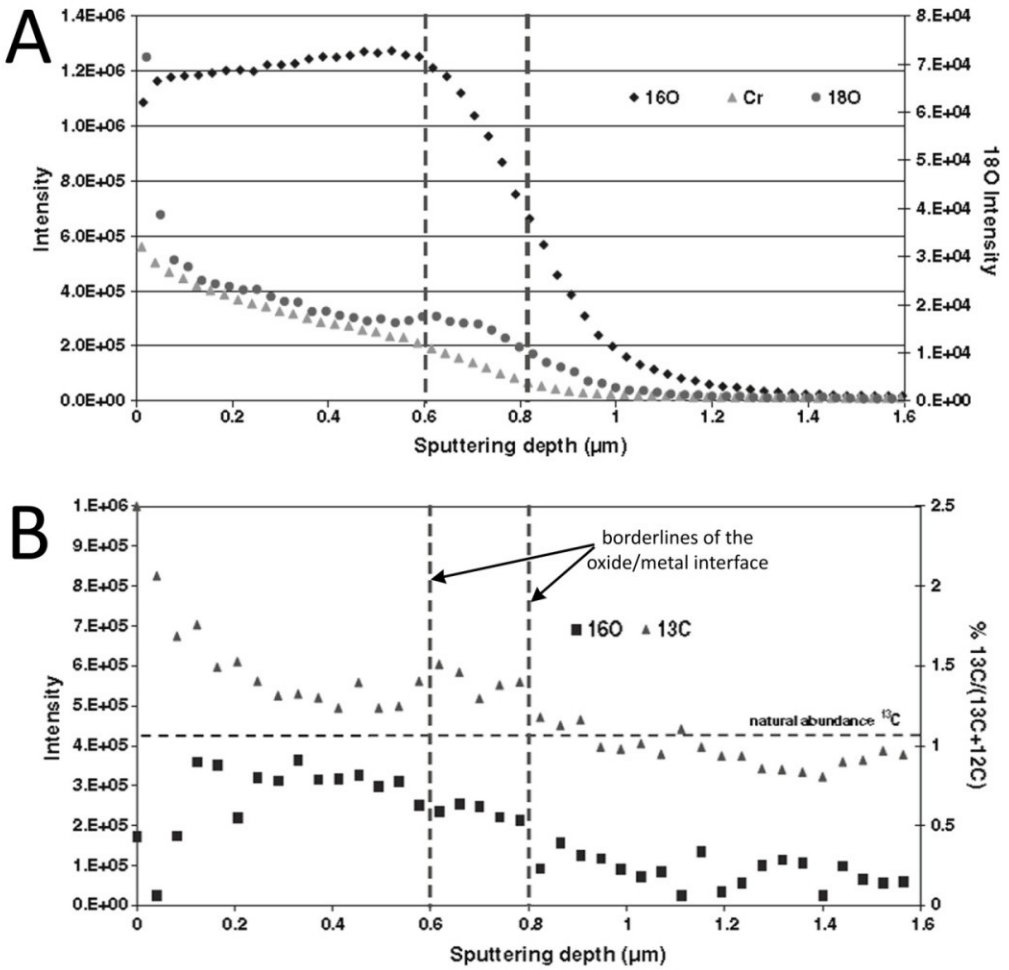

Figure 2.16 SIMS and GDMS analyses indicated that a) ^{18}O isotope and b) ^{13}C isotope reached penetrated through the surface Cr_2O_3 and reached to the metal-oxide interface [28].

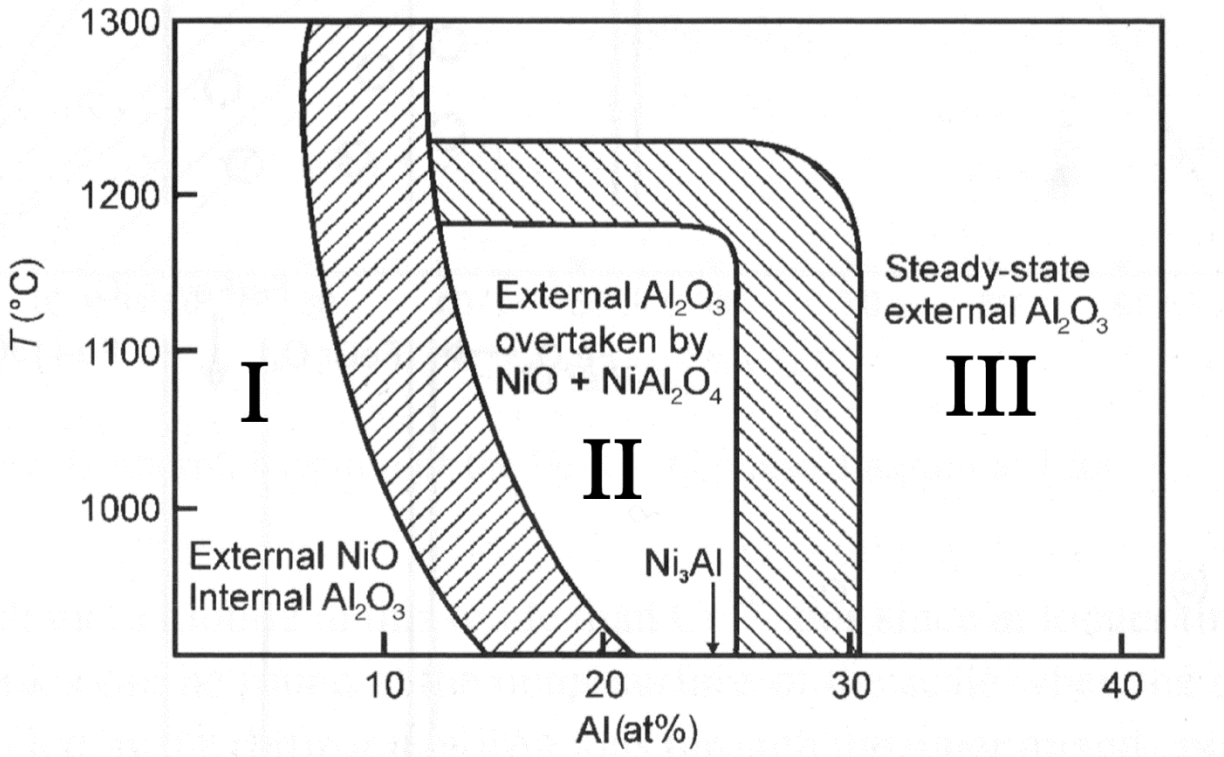

Figure 2.17 Oxide map for the Ni-Al system showing the effects of Al concentration and temperature on the oxidation regime [46].

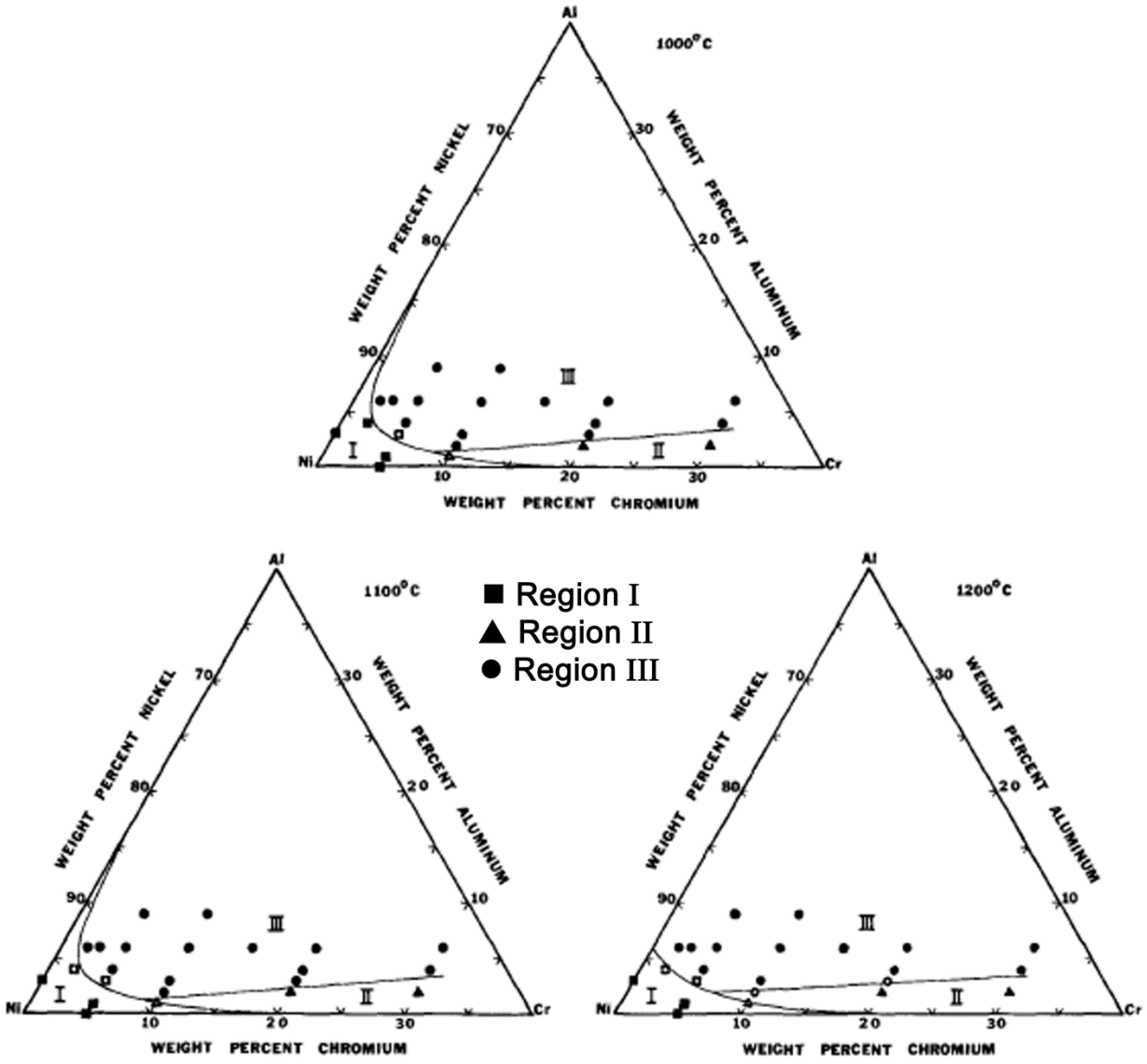

Figure 2.18 Oxide maps for the Ni-Cr-Al system in the temperature range 1000 - 1200 °C [85].

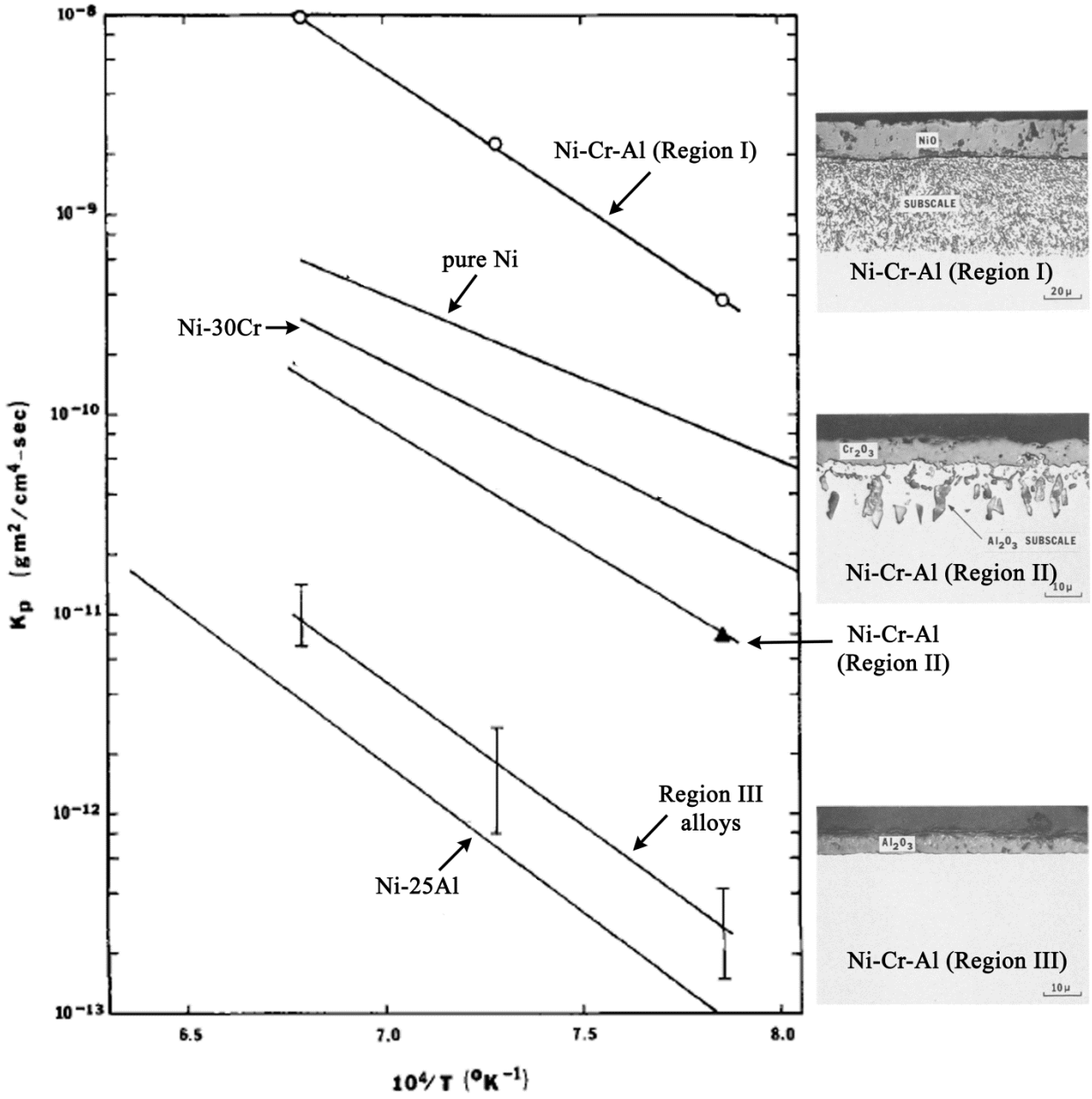

Figure 2.19 Weight gain kinetics of Region I, Region II and Region III alloys in comparison with that of Pure Ni, Ni-30Cr and Ni-25Al alloys [85].

CHAPTER 3

EXPERIMENTAL PROCEDURE

This chapter describes the experimental and measurement techniques used in this dissertation work in five sections. Section 3.1 describes the properties of the two different heats of Alloy 617 studied in this dissertation. Section 3.2 describes the controlled impurity helium flow loop system used for exposures in He-CO-CO_2 in detail and optimization of certain experimental variables to improve the consistency of the exposures. He-CO-CO_2 and Rhines pack exposure parameters and procedures are covered in Section 3.3. Section 3.4 covers the post-exposure characterization techniques to determine the oxidation rates and to analyze the microstructures of the samples. Finally, Section 3.5 provides a summary of the error analysis procedure employed for weight gain measurements and post-exposure X-ray based spectroscopy techniques.

3.1 Alloy description

In this study, two different heats of Alloy617 were investigated. First heat, provided by the Special Metals Corporation, Inc. (Huntington, WV), is designated as IN617 (heat number: XXX2323UK). The other heat was obtained from Thyssen Krupp VDM USA (Calvert, AL) and it is designated as Nicrofer 5520Co (heat number: 314626). IN617 is the primary heat subjected

to all temperature-environment conditions and Nicrofer5520Co samples are only exposed to one temperature-environment condition to investigate the possible heat-to-heat variation in the oxidation of Alloy 617 in impure He.

IN617 plate was 12mm in thickness and solution annealed at 1175°C followed by subsequent air cooling. Kumar [38] characterized the as-received microstructure of IN617, determined the grain size and verified the compliance of the chemical composition of the alloy with the manufacturer specifications and the ASTM standards. The as-received microstructure contained globular intergranular and transgranular $M_{23}C_6$ and M_6C type carbides aligned along the rolling direction (Figures 3.1a and b). Area fraction of the carbides was 2.9 ± 0.4%. Average grain size of the alloy was determined as 65μm by using the linear intercept method, designated in the ASTM E112 − 12 Standard [87]. Table 3.1 summarizes the chemical composition of IN617 provided by the manufacturer [88], which is independently verified by Sherry Laboratories and by Electron Probe Microanalysis (EPMA).

Nicrofer5520Co plate was 38.1 mm in thickness and solution annealed at 1175°C followed by subsequent water quenching. Figure 3.2 shows the as-received microstructure of the alloy etched in waterless Kalling's reagent (5g $CuCl_2$, 100ml ethanol and 100 ml HCl). The microstructure of the alloy contained extremely small amounts of Mo rich M_6C carbides and Ti(C,N) precipitates. The average grain size of this heat was 129 μm, significantly larger than that of IN617 [89]. The chemical composition of Nicrofer5520Co as provided by the manufacturer is given in Table 3.2.

3.2 Controlled impurity helium flow system

High temperature exposures in controlled He-CO-CO_2 environments were conducted in controlled impurity helium flow system (CIHFS). It is composed of a helium purification system,

gas mixing, exposure and gas analysis sections as schematically shown in Figure 3.3. Helium purification system is composed of three filtering cartridges which further dilute the impurities present in the initial helium stream of 99.9995% purity. After passing through the purification system, helium stream is supplied to the gas mixing section consisted of a series of mass-flow controllers. Mass-flow controllers are arranged to split the main helium stream up to six sub-streams and to mix controlled amounts of CO and CO_2 into each individual sub-stream. Each He-CO-CO_2 stream is fed to the exposure section which is composed of a multi-quartz tube furnace. The furnace keeps the desired temperature steady along a sufficiently long section of each tube and the metering valves at the inlet of each tube enable precise control of the flow rate during the exposures. The inlet and outlet of each tube is connected to a discharge ionization detector gas chromatograph (DIDGC), which establishes the gas analysis section of the whole system. DIDGC can analyze the CO and CO_2 concentrations in the helium stream both at the inlets and outlets of each tube, sequentially. This enables precise control of the inlet CO and CO_2 concentrations established in each tube and the analysis of the amount of consumption of each molecule by the samples being tested in the exposure section. Each section of the CIHFS is described in more detail in the following sub-sections of this text.

3.2.1. Helium purification section

Helium purification section is composed of a Perkin Elmer Three-Cartridge Gas Purification System and a manual gas stream changeover system connected to two 8 m^3 size 99.9995% pure helium cylinders. Helium inside the cylinders is further diluted through a series of moisture, hydrocarbon and oxygen removal cartridges. The triple cartridge system can process 152 m^3 of high purity helium (99.997%). Manual gas stream changeover system enables switching the stream coming from the cylinder about to be depleted to the full one without

interrupting the helium flow. This arrangement enables unlimited supply of pure helium (> 99.9999% in purity) to the CIHFS during the experiments and the lifetime of the triple cartridge system is elongated.

3.2.2. Gas mixing section

The gas mixing section is consisted of 18 electronic mass-flow controllers manufactured by Omega, Inc. (part number: FMA-A2402-SS). The mass flow controllers have an accuracy of 1ml/min with a full scale operation range of 0-100 ml/min. The stainless steel body enables safe operation up to 500 psig pressure at the inlet of each mass-flow controller. Calibration of each device was performed by the manufacturer at 30 psig helium pressure at the inlet in compliance with the calibration standards set by the National Institute of Standards and Technology standards.

Mass flow controllers are connected to each other in groups of three to split the helium stream coming from the helium purification section into six sub-streams. Two mass-flow controllers in each group adjust the flow rates of the gas supplied by the certified He-CO and He-CO_2 pre-mixed cylinders attached to them. The third mass-flow controller adjusts the flow rate of the pure helium to dilute the He-CO-CO_2 mixture until the desired concentrations are achieved. Each individual He-CO-CO_2 stream is the fed to the exposure section by using 316 stainless steel tubing.

3.2.3. Exposure section

Exposures are conducted in a 30” long, horizontal, three-zone, Mellen split-tube furnace, rated for temperatures up to 1200°C. The temperature in each zone is controlled independently by OMEGA brand temperature controllers, each featuring a resolution of 1°C. Each temperature controller receives feedback from the S-type thermocouples located in the middle of each zone to

keep the temperature at the desired set point. The desired temperature can be maintained along at least 6” long segment of each zone. During exposures, samples are positioned in each quartz tube corresponding to the middle portion of the 6” long segment of the middle zone.

Furnace housing contains seven quartz tubes with an outer diameter of 0.5” and 50-52” in length. Two discs containing seven holes on both sides of the furnace housing hold the tubes in a honeycomb arrangement. Six holes are located along the periphery of the process diameter of each disc and are symmetrically arranged around the seventh hole located at the center of the disc, as shown in Figure 3.4. The length of each quartz tube extends the length of the furnace housing on both ends at least by 8”. Samples are kept in these extended regions of the quartz tubes almost at room temperature before the exposures, while sealing and purging the quartz tubes with the gas mixtures. However, an apparatus is needed in each quartz tube to manipulate the samples between the cold zone and the hot zone without breaking the seals of the tubes during exposures.

Push-rods made of quartz rods, 0.1” in diameter and 18” in length, also have encapsulated steel fork heads and five equally spaced hooks, designed to manipulate samples in each tube (Figures 3.5 a-b) [38,90]. A U-shaped aluminum bracket containing two rare-earth metal magnets on each side of the inner walls is used to externally manipulate the pushrods (Figure 3.5c). Samples in the cold zone of the quartz tubes are always positioned ahead of the first hook of the push-rod, leaving at least one-third of the rod inside the furnace. Each hook is used to push the samples by 3 - 4” before the next hook is engaged by retracting the push-rod without touching the samples. Same practice is applied to push the samples into the middle portion of the furnace or to pull out the exposed samples to the cold zone of the quartz tubes without breaking the seals.

The major advantages of the exposure section are setting the furnace temperature without exposing the samples to the exposure temperature and manipulating the samples without breaking the seals of the quartz tubes. The latter design feature further enables continuous analysis of the gas compositions sustained both at the inlets and outlets of each tube connected to the DIDGC. A detailed description of the gas analysis section is given in the following sub-section.

3.2.4. Gas analysis section

Gas analysis section is consisted of the DIDGC, capable of analyzing H_2, Ar, O_2, N_2, CH_4, CO and CO_2 molecules in a helium stream with a resolution of 0.1 molppm. Main parts of the DIDGC are pulse discharge ionization detector (PDID), an oven, three capillary columns located in the oven, sampling loops, a valve system which connects the columns to the PDID, a carrier helium gas of purity 99.9999% further purified down to a total impurity level less than 10 ppb by a Vici-Valco HP2 brand heated helium purifier, and a multi-port stream selection valve (MPV).

MPV had 12 ports connected to the inlets and the outlets of the six quartz tubes available for the exposures in He-CO-CO_2 environments. MPV was designed to sequentially deliver the gas mixtures flowing through each port to the sampling loops. A representative volume of the gas mixture filled the sampling loops and the gas molecules were transfer to the columns by the carrier helium gas. Columns are designed to selectively adsorb the molecules and chronologically release them to the PDID for quantification of their relative amounts in the sampled gas mixture. Configuration and the operation principles of the DIDGC are described in more detail in the following sub-section.

3.2.4.1. DIDGC configuration and operation principles

Figure 3.6 schematically shows the valve plumbing diagram of the DIDGC as well as the flow paths of the gas mixture filing the sampling loops and the carrier helium gas transporting molecules to the PDID. The analysis sequence starts with sampling a representative volume of the gas stream delivered through the MPV. Initially the pressure-relieve valve, valve 5 is off, which allows the gas stream to fill the two 0.25cc sampling loops as shown by the green flow path in Figure 3.6a. The sample loops are filled for about 0.2 mins to ensure that both loops contain the identical compositions of the gas mixture being sampled. Then valve 5 is turned off to vent the gas stream being sampled so that the pressure inside the sample loops can equilibrate with the atmospheric pressure. Next, valve 1 (8-port valve) and valve 2 (6-port valve) are turned on to introduce the carrier helium gas into the sampling loops. The carrier helium gas follows the blue and the orange gas flow paths, shown in Figure 3.6b, to flush the sample loops 1 and 2, respectively. The carrier gas following the orange path transports the constituents of sample loop 2 to the PDID much faster than the blue path does those of sample loop 1.

The orange path carries the gas molecules in sample loop 2 to a Porous Layer Open Tubular (PLOT) column designated as "column 3", which selectively adsorbs and separates CO_2 from the rest of the molecules. The remaining molecules collectively pass through the column almost immediately and are ionized by the PDID, forming the first peak of the representative chromatogram shown in Figure 3.7. CO_2 molecules start eluting from column 3 after about 1.15 mins and are ionized by the PDID to form the second peak of the chromatogram. This concludes the quantification of CO_2 present in the sampled gas and the carrier helium gas keeps flushing sample loop 2 while the molecules in sampling loop 1 are transported to the PDID through columns 1 and 2 following the blue gas flow path.

The molecules in sample loop 1 are initially carried through column 1, another PLOT column identical to column 3. Likewise column 3, column 1 selectively adsorbs and retains CO_2 molecules in the mixture for at least 1.15 mins while the rest of the molecules are transported to column 2. Column 2 is a molecular sieve which adsorbs and sequentially releases H_2, O_2, Ar, N_2, CH_4 and CO according to their sizes. However, CO_2 molecules poison column 2 and should not be introduced into it. To avoid that, valve 1 is shut off after 1.25mins to back-flush the carrier helium gas into column 1 and vent the CO_2 molecules retained in the column, as shown by the red flow path in Figure 3.6a. H_2, O_2, Ar, N_2, CH_4 and CO molecules elute from column 2 after reasonably different times and are ionized by the PDID forming the rest of the peaks shown in Figure 3.7. Column 2 can completely release H_2, O_2 and Ar at the default temperature setting of the oven (50°C); however the elution of N_2, CH_4 and CO requires temperatures greater than 50°C. This is achieved by ramping up the oven temperature to 120°C at a rate of 7°C/min. The increase in the oven temperature results in elevated background signal after the 5^{th} minute as shown in Figure 3.7. After all the molecules reach to the PDID, valve 2 is shut off and MPV is turned by one port to allow the next gas stream to be sampled and analyzed.

Quantification of the chromatogram is performed by the TotalChrom™ software. The software integrates the peaks associated with each of the molecules to determine their relative compositions in a given gas mixture. The accuracy of the measurements relies on the proper calibration performed by using certified helium based gas compositions.

3.2.4.2. Calibration of the DIDGC

The DIDGC is calibrated for CO_2, H_2, O_2, CH_4, and CO each time after the carrier helium gas cylinder is replaced. For this purpose, four certified helium based gas cylinders prepared by

Cryogenic Gases, Inc. are used. The cylinders contain at least four different gas molecules in ppm levels and the certified concentrations of each cylinder are listed in Table 3.3.

Each cylinder composition is analyzed twenty times at a flow rate of 200ml/min. Last five measurements are averaged to obtain the mean response of the DIDGC (area under each peak in the chromatogram) corresponding to the certified concentrations of each gas molecules analyzed. Calibration curves for each molecule are obtained by linear regression fit of at least 2 data points, as shown in Figures 3.8 a - e.

3.2.5. Characterization of the CIHFS

The consistency of the He-CO-CO_2 experiments relies on how well the experimental variables are controlled during each exposure. These variables include the temperature uniformity inside the exposure section, physical interaction of CO and CO_2 molecules with the quartz tubes, precise control of the environment compositions throughout an exposure, gas flow rate and sample dimensions. This subsection describes characterization of the experimental setup and optimization of each of these variables to improve the consistency of the exposures.

3.2.5.1. Temperature uniformity inside the quartz tubes under flowing He gas

The purpose of measuring the temperature uniformity along each quartz tube is to determine the location to place corrosion coupons in each quartz tube, along which the temperature is sustained at the desired experiment temperature with an error of ± 1°C.

The measurements were performed at three different experiment temperatures of 750, 800 and 850°C by inserting a K-type thermocouple from the outlet side of each quartz tube while pure helium gas was flowing at a rate of 200 ml/min. Figure 3.9 shows the measured temperature profiles in each quartz tube at the target experiment temperatures. The measured temperatures were within the ± 1°C error margin, along a distance between 12-18 inches from the right end of

the furnace. The exact experiment temperature was sustained within the distance of 15 ± 0.5 inches for each tube except Tube 6. Therefore, during the exposures corrosion coupons are placed at a distance approximately 15 inches from the right end of the furnace. Samples to be exposed in Tube 6 are positioned at a distance of 12 inches from the right end of the furnace.

3.2.5.2. Analysis of the thermal adsorption and desorption of CO and CO_2 molecules by the quartz tubes

Exposures are conducted in quartz tubes due to their chemical inertness to the He-CO-CO_2 environments to be sustained at high temperatures. However, quartz has a tendency to adsorp gas molecules such as H_2O, CO and CO_2. To release any of these physically adsorbed molecules, quartz tubes were baked at 1000°C for at least 24 hours before starting an exposure. After completing the bake-out process, it was still necessary to monitor the thermal adsorption/desorption of the CO and CO_2 molecules with the quartz tubes and verify that no significant change in the gas composition occurs at the experiment temperature. Figures 3.10 a - d summarize the changes in the CO and CO_2 molecule concentrations measured as a function of time at the outlet of the quartz tubes due to the interactions with He - 1.3 molppm CO_2 -1980 molppm CO and He - 1.3 molppm CO_2 - 13.5 molppm CO gas mixtures at 850°C. In general, the deviations in CO and CO_2 concentrations between the outlets and the inlets of the tubes reached to a steady-state after at least 40-50 hours. It is evident that the environment containing 1980 molppm CO results in greater variations in the inlet and outlet CO and CO_2 concentrations. In addition, CO_2 molecules are consistently desorbed when this environment is sustained in the quartz tubes (Figure 3.10a).

The average steady-state deviations in the CO and CO_2 concentrations due to the interactions of He - 1.3 molppm CO_2 -1980 molppm CO with the quartz tubes at 850°C did not

exceed 0.1% and 6.8%, respectively. On the other hand, average steady-state deviations in the CO and CO_2 concentrations due to He - 1.3 molppm CO_2 - 13.5 molppm CO were less than 2.4% and 3.7%, respectively. Results showed that baking out the quartz tubes at 1000°C proved to be essential to minimize the physical interactions between the He-CO-CO_2 environments and the quartz tubes. However, to attain the smallest possible deviations in the CO and CO_2 concentrations between the inlet and outlets of the tubes, a minimum of 60 hours long pre-treatment of the quartz tubes with the He-CO-CO_2 gas mixtures at the exposure temperature is necessary before inserting the samples in to the furnace.

3.2.5.3. Variance in the inlet gas composition during an exposure

Consistency of the oxidation experiments conducted at different temperatures relies on the accuracy of the desired He-CO-CO_2 compositions achieved in each quartz tube and the deviation from the target CO and CO_2 concentrations. Figures 3.11 a and b summarize the CO_2 and CO concentrations achieved at the inlet of a quartz tube over the course of a 500h exposure in He - 1.3 molppm CO_2 -1980 molppm CO.

As shown in Figure 3.11a, the average CO_2 concentration achieved in the exposure was 1.5 molppm (blue line) with a maximum deviation of 7.4% (~0.1 molppm, red line). Therefore, the standard deviation in the inlet CO_2 concentration did not exceed 3.0% of the mean concetration achieved during the exposure. Figure 3.11b shows that an average CO concentration of 1972.8 molppm was maintained, only 0.4% different than the target CO concentration (green line). The standard deviation was 1.1% of the mean CO concentration established throughout the exposure.

The results show that CO and CO_2 concentrations in a desired He-CO-CO_2 environment can be controlled with a standard deviation of 3.0% or less over a sufficiently long exposure time.

3.2.5.4. Optimization of the gas flow rate and sample geometry to improve the consistency of the exposures

As discussed previously in section 2.4.2, reaction of an inert environment containing very small amounts of oxidizing molecules with a metal surface results in rapid depletion of the reactive molecules at the gas-metal interface. To achieve a steady state flux of these molecules on the metal surface for a given environment, two experimentally controlled variables should be optimized: gas flow rate and the longitudinal dimension of the metal surface parallel to the gas flow direction.

Kumar [47, 50] carried out an experiment to determine the minimum gas flow rate to avoid depletion of the CO and CO_2 molecules in the gas mixture by more than 10% of their inlet concentrations upon reaction with the corrosion coupons. Seven IN617 corrosion coupons, each 6.25mm x 6.25mm x 1.5mm in dimensions were exposed to He - 0.7molppm CO_2 -70molppm CO at 950°C by varying the gas flow rate between 24 ml/min and 106 ml/min. Corrosion coupons were located inside the quartz tube as shown in Figure 3.12. The experiment established that a flow rate of 70 ± 10 ml/min should sustain sufficient flux of both gas molecules on the surfaces of each corrosion coupon to avoid significant depletion of them. However, according to the equations 2.85 and 2.86, the flux of a reactant molecule in an inert gas stream depends on the partial pressure of the reactant molecule and the temperature. For environments containing relatively lower concentrations of CO and CO_2, 70 ± 10 ml/min flow rate may not be sufficient enough to avoid significant depletion of those reactant species. In addition, no information was

provided concerning the uniformity of oxidation in each corrosion coupon or the variation in the oxidation rates among the different corrosion coupons placed in the same quartz tube. Therefore, additional short term exposures were conducted at 850°C to optimize the gas flow rate and the sample geometry with the following specific aims:

1. To avoid significant starvation of CO and CO_2 molecules in any given time during the exposure,

2. To achieve identical oxidation rates at the top and bottom surfaces of a corrosion coupon in a quartz tube,

3. To achieve uniform oxidation over the longitudinal dimensions of all the corrosion coupons inserted in quartz tubes,

4. To verify that corrosion coupons exposed to the same environment in different quartz tubes exhibit identical oxidation rates over a given exposure time.

First exposure was conducted in He - 1.5molppm CO_2 - 13.5 molppm at a flow rate of 85 ml/min. Six IN617 corrosion coupons, each 6.5mm x 6.5mm x 1.5mm in dimensions, were placed in the quartz tube as depicted in Figure 3.12. Depletion in CO_2 and CO concentrations between the inlet and outlet of the tubes are plotted as a function of exposure time in Figures 3.13a and 3.13b, respectively. The maximum depletion in CO_2 and CO molecules was measured as 15% and 35%, respectively. These values were much greater than Kumar's criterion for the onset of starvation of the molecules. Therefore, additional short term exposures in the same environment and at the same temperature were conducted by raising the gas flow rate to a range of 150-200 ml/min.

Figures 3.14a and 3.14b show the net and percent depletion in CO_2 and CO concentrations between the inlet and outlet of the tubes at two different flow rates of 150 ml/min

and 200 ml/min. At both flow rates, the maximum depletion in CO_2 and CO molecules did not exceed 4% and 8%, respectively. Even though the minimum flow rate to avoid significant starvation of the CO and CO_2 molecules was identified as 150 ml/min, it was still necessary to determine if the corrosion coupons exhibited identical weight gains at both flow rates.

Figure 3.15 summarizes the weight gain results obtained from the coupons exposed to He - 1.5molppm CO_2 - 13.5 molppm at flow rates of 150 ml/min and 200 ml/min with respect to their locations in the quartz tubes. At a given location, both flow rates resulted in almost identical weight gains. However, weight gains measured for the samples positioned behind the first sample, located closest to the inlet of the tube, gradually decreased. This, at first, was attributed to lack of flow rate to sustain equal fluxes of CO and CO_2 molecules at the surface of each sample, along a total length of approximately 39 mm. A quick qualitative analysis of the surface oxide layers using an optical microscope revealed that the top surfaces of all the coupons are covered almost completely by a surface oxide layer. However, the bottom surfaces of all the samples did not oxidize completely. It was concluded that the gas flow was not splitting evenly between the top and bottom surfaces of the coupons, in dimensions 6.5mm x 6.5mm x 1.5mm, as the coupons were situated almost in the bottom of the tube. Due to insufficient flow rate, CO and CO_2 molecules were starved at the bottom of the samples resulting in incomplete oxidation. To overcome this problem, the width of the corrosion coupons were extended to allow them to fit almost in the middle of the quartz tubes, as shown in Figure 3.16.

Two corrosion coupons with new dimensions of 4.0mm x 9.85mm x 1.5mm were exposed to He - 1.5molppm CO_2 - 13.5 molppm at a flow rate of 200 ml/min at 850°C. Both corrosion coupons exhibited almost identical weight gains, which were almost 75% greater than that did the 6.5mm x 6.5mm x 1.5mm coupons located closest to the inlet of the quartz tubes

(Figure 3.17). In addition, both the top and bottom surfaces of the coupons were homogeneously oxidized. Therefore, the optimum flow rate and the sample dimensions are determined as 200ml/min and 4.0mm x 9.85mm x 1.5mm, respectively.

As a final sanity check, four corrosion coupons, in dimensions 4.0mm x 9.85mm x 1.5mm, were placed in four different quartz tubes to verify that each coupon would exhibit identical weight gains upon exposure to He - 1.5molppm CO_2 - 13.5 molppm, at a flow rate of 200ml/min for a very short exposure duration of 25h at 850°C. Weight gain results summarized in Figure 3.18 verified that each corrosion coupon exhibited almost identical weight gains. Hence, the corrosion experiments in this dissertation are conducted at a flow rate of 200ml/min and by placing only one corrosion coupon, in dimensions 4.0mm x 9.85mm x 1.5mm, per quartz tube.

3.3 Exposure Parameters and Procedures

3.3.1. He-CO-CO_2 exposures

3.3.1.1. Exposure parameters

In this dissertation work, the primary candidate IHX material Alloy 617 was exposed to two HTGR helium equivalent environments in the temperature range of 750 - 850°C. Three major considerations were taken when deciding the compositions of the selected environments. First, the environments should reproduce the degradation modes predicted for the real HTGR helium chemistry. Second, the environment compositions should systematically be varied to understand the effect of environment chemistry on the driving force for oxidation. Third, the environment chemistry should be kept simple to understand the mechanism of oxidation in impure helium without introducing the complex kinetic competition between different varieties of oxidizing molecules.

The HTGR helium chemistry was simplified to He-CO-CO_2 mixtures and two environments were selected. First environment contained 1.5 molppm of CO_2 and 13.5 molppm of CO which complied with the upper limits of the CO and CO_2 concentrations reported for the helium chemistries of the previous HTGRs listed in Table 1.1. Second environment was composed of the same CO_2 concentration; but contained two orders of magnitude greater CO concentration of 1980 molppm. To verify that both environments reproduce the predicted degradation modes in HTGR helium, the oxygen and carbon activities of both environments were superimposed on a representative Cr - C - O stability diagram, as shown in Figure 3.19. The construction of the stability diagram was described in Section 2.2.2. The oxygen activity of the environment was calculated according to the following reaction of CO_2 at the alloy surface:

$$\mathrm{CO_2} \rightleftarrows \mathrm{CO} + 1/2\mathrm{O_2}\ . \tag{3. 1}$$

The equilibrium oxygen activity of the environment is equal to:

$$P_{O_2}^{eq} = \left(K_{(3.1)} \times P_{CO_2}/P_{CO}\right)^{1/2}\ , \tag{3. 2}$$

where

$$K_{(3.1)} = \exp(-\Delta G_{(3.1)}^{f}/RT). \tag{3. 3}$$

The equilibrium carbon activity of the environment can be calculated according to the following reaction:

$$2\mathrm{CO} \rightleftarrows \mathrm{CO_2} + [\mathrm{C}]\ . \tag{3. 4}$$

The equilibrium carbon activity is equal to:

$$a_C^{eq} = K_{(3.4)} \times (P_{CO})^2/P_{CO_2}\ , \tag{3. 5}$$

where

$$K_{(3.4)} = \exp(-\Delta G_{(3.4)}^{f}/RT). \tag{3. 6}$$

Note that the environment oxygen and carbon activities in Figure 3.19 were calculated by assuming equilibrium conditions, which is not the case in IHX helium as described in Section 2.2.1. The steady state activities for He-CO-CO_2 mixtures could not be calculated due to the lack of published data for the reaction rate constants of CO and CO_2 molecules on the surface of Alloy 617, at temperatures 750 - 850°C. Nevertheless, the calculated equilibrium oxygen and carbon activities are expected to be close to the steady-state values as the environments do not contain other major oxidizing and carburizing molecules such as H_2O and CH_4. Figure 3.19 shows that both environments remain the oxidizing - carburizing regime as predicted for the HTGR helium chemistry.

Within the scope of this dissertation work, samples of IN617 were exposed to environments He - 1.5molppm CO_2 - 13.5 molppm and He - 1.5molppm CO_2 - 1980 molppm in the temperature range of 750 - 850°C for up to 500h. In addition, an IN617 equivalent alloy, Nicrofer 5520Co, was exposed to He - 1.5molppm CO_2 - 1980 molppm only at 850°C, for 225 h in an effort to investigate the possible effects of heat-to-heat variation. The parameters of the exposures are tabulated in Table 3.4. Note that, the environments in the table are designated by their CO/CO_2 ratios to adopt a concise nomenclature when referring to the selected environments throughout the rest of the dissertation. Henceforth, He - 1.5molppm CO_2 - 13.5 molppm and He - 1.5molppm CO_2 - 1980 molppm will be referred as Env. 9 and Env. 1320, respectively.

3.3.1.2. Exposure procedure

IN617 and Nicofer 5520Co coupons of size 4.5mm x 10mm x 1.5mm were machined by electrical discharge machining (EDM), ground starting with a grit 400 SiC paper and polished down to 1 μm diamond finish until an optically scratch free surface is obtained. Afterwards, the dimensions of the coupons were measured by a digital micrometer with 0.01mm accuracy to

calculate the total surface areas of each sample. Each dimension was measured three times. Then as-polished samples were weighed by a Mettler Toledo brand microbalance featuring an accuracy of 0.02mg. Sample preparation was finalized by cleaning and degreasing the samples ultrasonically in an ethanol-acetone mixture for 15 min with a subsequent cleaning in distilled water for another 15 min.

Before inserting the samples into the cold zones of the quartz tubes, the tubes were baked at 1000°C under flowing pure helium at a rate of 85 ml/min, for at least 24 hours. This allows removal of the residual moisture adsorbed by the quartz tubes at room temperature. It is important to note that during baking process the outlets of the quartz tubes should not be connected to the GC. After baking the tubes, furnace temperature was brought down to the experiment temperature and samples were inserted into the cold zones of the quartz tubes. As long as the furnace door is kept closed, samples located in the cold zone should not be exposed to temperatures above 45 °C. Then, quartz tubes were sealed and connected to the DIDGC. Tubes were purged with the He-CO-CO_2 mixtures at a flow rate of 200 ml/min, while the inlet sampling lines were purged at a flow rate of 70 ml/min. As soon as the oxygen and nitrogen concentrations measured at the inlet sampling lines of each tube dropped below the detection limit of the DIDGC, the target concentrations were established. It usually takes 4 - 6 h to adjust the desired concentrations at the inlet of each tube.

After setting the target concentrations, flow rate in each quartz tube was checked by connecting a gas flow meter to the sample vent of the DIDGC to ensure that the flow rate was 200 ± 5 ml/min. Then, CO and CO_2 concentrations at the inlet and outlet of each quartz tube were measured for up to 75 h until the variation between the inlet and outlet concentrations reached to a steady-state value.

Finally, samples were inserted into the designated reaction zone in the furnace. The samples were pushed into the furnace by using the push-rods described in Section 3.2.3. At this point the furnace door was kept open to watch the samples while pushing them into the reaction zone. It is important to wear all the fire resistant, refractory personal-protective equipment to avoid any personal damage. It nominally takes 1-2 minutes to insert one sample into a quartz tube.

After the exposures were completed, samples were pulled out of the hot zone and placed in the cold zone. Samples were kept in the cold zone for at least 40 - 50 h after the exposures while the CO and CO_2 concentrations at the inlet and outlet of each quartz tube were measured to verify that the steady-state variation between the inlet and outlet concentrations did not significantly deviate from the values measured before the samples were pushed in to the reaction zone. As a final step, quartz tube seals were broken and oxidized samples were taken out to conduct post-exposure analyses on them.

3.3.2. Rhines pack exposures

Rhines pack [86] is an evacuated dumbbell shaped capsule, which contains a mixture of powdered metal A mixed with its most stable oxide on one side of the capsule, and the alloy which is composed of A and a more reactive element B, on the other side. Rhines packs are useful to study the internal oxidation kinetics of B in an alloy AB which is still reactive at the dissociation oxygen partial pressure of the oxide of A. Within the scope of this dissertation work, four Rhines pack samples of IN617 were prepared using Cr and Cr_2O_3 powder mixtures to study the internal oxidation kinetics of Al in IN617 at 850°C. Pure Cr coupons were also placed in the capsules to verify that the ambient oxygen partial pressure in the capsule was brought down to the dissociation oxygen partial pressure of Cr_2O_3.

IN617 coupons of size 10.5 mm x 6.5 mm x 1.5 mm and pure Cr coupons of size 6.75 mm x 3.25 mm x 1.5 mm were machined by electrical discharge machining (EDM), ground starting with a grit 400 SiC paper and polished down to 1 μm diamond finish until optically scratch free surfaces are obtained. Afterwards, the dimensions of IN617 coupons were measured by a digital micrometer with 0.01mm accuracy to calculate the total surface area of each coupon. Each dimension was measured three times. Then as-polished IN617 samples were weighed by a Mettler Toledo brand microbalance featuring an accuracy of 0.02mg. Preparation of both IN617 and pure Cr coupons were finalized by cleaning and degreasing the samples ultrasonically in an ethanol-acetone mixture for 15 min with a subsequent cleaning in distilled water for another 15 min.

Rhines pack capsules were initially dumbbell shaped cylindrical quartz tubes with only one end sealed. The length of a capsule was around 50cm and the outer diameter of each capsule was small enough to fit into the quartz tubes of the furnace described in Section 3.2.3. One side of each quartz capsule was filled with approximately 2.5 g of 55 wt.% Cr - 45 wt.% Cr_2O_3 powder mixture. Both Cr and Cr_2O_3 powders were of 99% purity and sieved down to size 325 mesh. Then, one of each Cr and IN617 coupons were inserted to the other side of the capsule. The bottleneck between the two sides was blocked with silica wool, which was gas permeable yet tight enough to avoid direct contact of the powder mixture with the IN617 and Cr coupons. Four capsules were prepared and mounted on the setup described in Figure 3.20 to be evacuated.

The setup was composed of a quartz manifold of 1.5” in inner diameter, which had graded seals on both sides to 2.75” diameter CF stainless steel flanges. One side of the quartz manifold was attached to a turbomolecular pump backed up with a mechanical pump. The other side of the manifold was connected to a rough vacuum gauge and a 99.9995% pure Helium

cylinder via a tee flange. Pure titanium chips were placed in the manifold to getter the impurities when the 266 W cord heater heated the manifold. The manifold and the capsules were initially evacuated only by the mechanical pump while the cord heater was kept on and reached to a temperature of 275°C. This temperature was sufficient enough for the titanium chips to getter the moisture, all the volatiles and oxygen present inside the manifold. When the pressure was reduced to 10^{-6} atm the manifold was purged with 99.9995% pure helium gas further purified by a Perkin Elmer all-in-one moisture, oxygen and hydrocarbon cartridge system, until the pressure inside the manifold reached just below the atmospheric pressure. This cycle was repeated 10 times before the turbomolecular pump was turned on. The turbomolecular pump further reduced the pressure inside the manifold and the capsules down to $4x10^{-9}$ atm, measured by an ion gauge attached to the inlet of the pump. Quartz capsules were sealed one by one by heating the necked connections with an oxyacetylene torch. The turbomolecular pump was kept operational while sealing the capsules and no major change in the ion gauge pressure reading was observed.

Before pushing the capsules in to the furnace, only powder containing portion of each capsule was inserted into the multi-quartz tube furnace, while the other side of the capsule containing the coupons remained approximately at room temperature. Powder mixture in each capsule was heated up to 550°C for up to 100h. This way the remaining volatiles inside the capsules were gettered and the ambient oxygen partial pressure inside each capsule was stabilized. Afterwards, capsules were inserted in to the core of the furnace to be exposed to 850 °C. After the target exposure durations of 150h, 500h, 750h and 1000h, capsules were removed from the furnace. At the conclusion of the experiment, each quartz capsule was carefully broken and IN617 and Cr coupons were removed to conduct post-exposure analysis on them.

3.4 Post-exposure sample characterization procedures

3.4.1. Measurement of weight change in the samples

Samples were weighed before and after the exposures using a Mettler Toledo brand microbalance with an accuracy of 0.02mg. Three measurements were taken each time the samples were weighed. These measurements were averaged and divided by the average surface area to determine the specific weight of a sample. Assuming that the change in the dimensions of the sample is negligible after the exposures, the weight gain of the sample is calculated according to the following equation:

$$\Delta \mathrm{W/S} = \left(W_{bfr}^{avg} - W_{aft}^{avg}\right)/\mathrm{S}\,, \tag{3. 7}$$

where S is the average surface area of the sample and W_{bfr}^{avg} and W_{aft}^{avg} are the average of three weight measurements taken before and after the exposures, respectively. S is calculated as follows:

$$\mathrm{S} = 2 \times (\ell \times w + \ell \times t + w \times t)\,, \tag{3. 8}$$

where ℓ, w and t are the average length, width and thickness of the corrosion coupons, each measured three times prior to starting an exposure.

3.4.2. Scanning Electron Microscopy (SEM)

SEM was employed to characterize the morphology and distribution of the features at the surface and cross-sections of the samples exposed to He-CO-CO_2 environments and the Rhines pack samples. Cross-section characterization of the samples required proper metallographic preparation. First, the region of interest in a particular sample was sectioned using a Buehler ISOCUT wafering blade. Then, if the sectioned part had fragile surface features to be characterized, such as surface oxide scales, then electroless nickel plating was employed to protect these features. Electroless nickel plating required sample surfaces to be sufficiently

conductive, thus samples featuring continuous surface oxide layers were gold sputtered. Nickel plating solution was prepared in a beaker by adding 50ml of MacDermid Elnic 101-C5 solution composed of nickel sulfate and sodium hypophosphate to 250ml of DI water. Gold coated samples were placed in the beaker which was, then, heated in a water bath up to 90°C. Electroless plating lasted 1-2 hours until a protective nickel coating is obtained. After plating, samples were mounted on a 1" stub using crystal bond (South Bay Technology Quickstick 135). Sufficient amount of crystal bond is used the cover the surface of the sample. Mounts were successively ground using 800, 2400 and 4000 grit SiC paper and then polished by 3μm and 1μm diamond polishing slurries. The surface of interest was finished by 0.05 μm Al_2O_3 polishing. Mounts were kept in an acetone bath until the entire crystal bond was dissolved. As a final step, samples were briefly rinsed in acetone and cleaned in DI water and became ready for SEM characterization.

The instruments typically used for the SEM analysis were a tungsten filament JEOL JSM-6480 SEM in Irradiated Materials Testing Laboratory (IMTL) and a Schottky Field Emission filament FEI Nova 200 Nanolab SEM/FIB located at the University of Michigan Electron Microbeam Analysis Laboratory (EMAL). Both instruments were capable of performing secondary electron (SE) imaging, backscatter electron (BSE) imaging and energy dispersive X-ray spectroscopy. SE imaging is preferred for retaining topographical information from the surface features. BSE imaging offers a distinct advantage of achieving a clear contrast between different phases present in a sample. Phases that contain atoms with large atomic numbers (Z) have brighter BSE intensity; whereas areas those appear dark are composed of lower Z atoms. BSEs also encounter multiple scattering events, which creates a deeper interaction volume within the sample being analyzed. As such, BSE imaging provides more in-

depth information in expense of topographical detail. Figures 3.21a and b show the micrographs taken from the same region over a sample using SE and BSE imaging, respectively. The topographical details in the SE image are sharp and distinct; whereas the BSE image reveals a better Z-contrast and provides information from the subsurface of the sample (dark areas indicate presence of subsurface oxide structure).

Within the context of this dissertation work, time evolution of the characteristic dimensions of surface Cr_2O_3 and internal Al_2O_3 phases in IN617 was characterized as a function of temperature and environment chemistry. For this purpose, JEOL JSM-6480 SEM was mainly used in backscattered imaging mode to clearly reveal the Z-contrast between IN617 matrix, surface Cr_2O_3 and internal Al_2O_3. Figure 3.22a shows the BSE image of an IN617 sample exposed to environment 1320 at 850 °C for 500h. Surface Cr_2O_3, internal Al_2O_3, sub-surface and surface carbides were clearly distinguished from each other. The characterization of the micrograph involved calculating the average thickness of the Cr_2O_3 scale and measuring the depths of intergranular Al_2O_3 scales. Depths of the Al_2O_3 scales were measured by using the ImageJ software. Area associated with the Cr_2O_3 scale was delineated using the "magic wand tool" feature of the Adobe Photoshop software. Then the selected area was saved as a separate layer and painted in black using the "curves" feature. The total area was calculated using Image J after converting the image to binary mode and using the "analyze particles" feature. Area calculated was divided into the length of the micrograph to determine the average thickness of the scale. Specific weight gain due to oxygen pick-up during Cr_2O_3 formation can also be calculated from the average Cr_2O_3 scale thickness:

$$\left(\frac{\Delta W}{A}\right)^{oxygen} = t_{Cr_2O_3} \times \rho_{Cr_2O_3} \times \frac{(AW)^{oxygen}}{(MW)^{Cr_2O_3}} \times 3, \quad (3.9)$$

where $\rho_{Cr_2O_3}$ is the density of the Cr_2O_3 scale, $(AW)^{oxygen}$ is the atomic weight of elemental oxygen and $(MW)^{Cr_2O_3}$ is the molecular weight of Cr_2O_3.

3.4.3. X-Ray Diffraction (XRD)

XRD was employed to characterize the features that form at the surfaces of Rhines pack samples and IN617 samples exposed to He-CO-CO_2 environments. A Rigaku rotating anode and a Bruker D8 Discover Cu-Kα diffratometers were mainly used for XRD analysis.

Rigaku was operated at an X-ray beam voltage of 40kV and beam current of 100mA in "2Θ - Θ reflection" and "2Θ" modes. In 2Θ - Θ reflection mode, detector and the sample rotate simultaneously such that incident and reflecting beam angles remain the same. This mode is useful for bulk powder diffraction analysis. When analyzing exposed samples in 2Θ - Θ reflection mode, the incident beam angle usually remained large enough, so that more counts were collected from the base metal compared to that collected from the surface features. To better resolve the peaks associated with the surface features, 2Θ mode was adopted. In this mode the incident X-ray angle was fixed to a value smaller than 5° so that diffraction was more surface sensitive. Rhines pack IN617 and pure Cr samples were analyzed in 2Θ mode. To enhance the intensities of the peaks and to better resolve peaks associated with different phases, a very slow scan rate of 0.05°/min was used in the 2Θ range of 32°-45° at a fixed Θ angle of 1.5°.

Bruker D8 Discover can be used for grazing-incidence XRD and large detector window enabled much faster data collection speed than did the Rigaku rotating anode XRD. Bruker D8 was operated at a beam voltage and current of 40kV and 40mA, respectively. The incident beam angle (θ_1) and the detector angle (θ_2) were selected as 1.5° and 40°. The detector window was capable of covering a 2Θ range of 40°, which enabled an analysis window of 21.5° - 61.5°. The step size was usually kept around 0.25°/min.

3.4.4. Raman Spectroscopy

Raman spectroscopy uses intense laser beams to measure vibrational frequencies in a molecule to determine the crystal symmetry, orientation and stress/strain state of a crystal as well as structure and composition of a material. Incident laser beam both elastically and inelastically interacts with the sample resulting in Rayleigh and Raman scattering, respectively [91]. Rayleigh scattering has the same frequency as the incident beam. Raman scattering appear due to the energy difference between the incident and scattered photons. If the scattered photon has lower energy than the incident atom, the scattering event is called Stokes. On the other hand, if the scattered photon has more energy than the incident photon, the scattering event is called as Anti-stokes. In Raman spectroscopy, the shifts from the incident beam give characteristic information of the material being analyzed. Raman spectroscopy cannot be used to characterize pure metals and alloys.

Raman spectroscopy was employed to characterize the surface features on IN617 samples exposed to He-CO-CO_2 environments and compare them with those on IN617 samples oxidized in Cr- Cr_2O_3 Rhines packs. Prior samples are expected to exhibit surface Cr_2O_3 formation, therefore used as a standard to verify the peak locations of Cr_2O_3 (eskolaite). Raman was spectra obtained using a Renishaw inVia Raman microscope equipped with a 633nm He-Ne laser and confocal objective lenses with magnifications X5 - X100. Samples were excited with 633nm He-Ne laser source for up to 10s in a total number of three scans.

3.4.5. X-Ray Photoelectron Spectroscopy (XPS)

XPS is a highly surface-sensitive characterization technique that identifies the nature, composition, chemical and electronic states of the elements that exist at the surface of a sample. XPS uses X-rays to excite photoelectrons within 10 nm depth of the material and the number and

the kinetic energy of these electrons are measured. The kinetic energy of a photoelectron, E_K, is given as follows [92,93]:

$$E_K = h \times \upsilon - E_B - \phi_A, \quad (3.10)$$

where $h \times \upsilon$ is the incident photon energy, E_B is the binding energy of a photoelectron and ϕ_A is the work function of the analyzer. The instrument work function can be calibrated, so that ϕ_A is set to zero in Equation (3.10). XPS spectra are conventionally given by intensity (number of photoelectrons) as a function of E_B.

Any change in the bonding state of an element reflects to the binding energy, peak width and shape and valence band changes [93]. For instance, chemical bonding in a compound results in change of the binding energy of an element compared to that of its pure form. This is called as "chemical shift", which represents the structure of the compound being analyzed as well as identifies the valance band structure of the elements forming the compound.

In this dissertation work, XPS was mainly used to characterize the surface structure of the Rhines pack samples. In particular, XPS was utilized to prove that no surface Cr_2O_3 formed during the exposures at 850°C. For this purpose, a Kratos Axis Ultra XPS with a spectrometer resolution of 0.35 eV at 10 eV pass energy was used. The instrument work function was calibrated to give an Au $4f_{7/2}$ metallic gold E_B of 83.95 eV. The spectrometer dispersion was adjusted to give an E_B of 932.63eV for metallic Cu $2p_{3/2}$. The instrument is equipped with a monochromatic Al and dual Al and Mg sources. To characterize the surfaces of Rhines pack samples, monochromatic Al Kα radiation with a characteristic energy of 1486.6 eV was used. X-ray beam energy and the filament current were set to 14kV and 8mA. Several different apertures are available to confine the X-ray beam size to a designated area. In most of the analyses the

larges aperture size of *300μm x 700μm* was used. The instrument is also equipped with an Ar ion gun for performing surface cleaning or through-depth XPS analysis.

Before analyzing the Rhines pack samples, peak locations of pure *Cr* and Cr^{+3} (in association with formation of Cr_2O_3 phase) were determined using an as-polished pure Cr sample. Sample surface was prepared by grinding with 360 and 800 grit SiC papers and then successively polishing by 9, 3 and 1μm diamond polishing slurries. The surface of the samples was finished by 0.05 μm Al_2O_3 polishing. To confirm the peak locations of *Cr* and Cr^{+3}, first, the native oxide layer was sputtered away by operating the Ar ion gun at 3.8 eV over a *2mm x 2mm* area for 10 mins and then an XPS analysis was performed. The sample was then removed from the XPS instruments and oxidized at 750°C for 12h under pure helium flowing at a rate of 85 ml/min, followed by another XPS analysis. The XPS analyses were confined to a binding energy range of 595eV - 560eV and 10 sweep scans were performed each at a pass energy of 40eV, lasting for 120s. XPS spectra were analyzed using CasaXPS software [94]. Figure 3.23 shows the XPS spectra confined to the range of Cr $2p_{3/2}$ binding energy range, obtained from the as-polished pure Cr after sputtering (red curve) and after oxidation at 750°C (green curve) showing the peak positions of elemental Cr and Cr^{+3}, respectively. Cr^{+3} peak formed a double shoulder and was unusually wide to be represented by one peak. Biesinger et al. [95] attributed this wide peak formation to the multiplet structure of Cr^{+3} photoelectrons. Therefore, five synthetic peaks were introduced to represent the Cr $2p_{3/2}$ peak associated with Cr_2O_3. The peaks were fitted using Gaussian - 30% Lorentzian (GL30) mixed distribution. Peak areas were also calculated by introducing a Shirley background to each peak. Peak positions and areas are summarized in Table 3.5.

Due to the roughness of the Rhines pack samples, signal-to-noise ratio of the Cr $2p_{3/2}$ and Cr $2p_{1/2}$ peaks were considerably low. For the consistency of the analysis, collecting sufficient signal was more important than resolving the smallest chemical shifts in the electron binding energies. Hence, instead of using 10 eV pass energy, at which a very high energy resolution can be achieved, the detector pass energy was set to 40 eV. Cr 2p measurements were confined to a binding energy range of 595eV - 560eV and 20 sweep scans were performed each lasting for 300s. These parameters were set to collect at least 5000 counts from each peak measured, considering the statistical significance of the analyses (see Section 3.5).

3.4.6. Transmission Electron Microscopy (TEM)

Microstructure and microchemistry of the cross-sections of IN617 samples oxidized in Cr - Cr_2O_3 Rhines packs were analyzed using JEOL™ 2010F scanning transmission electron microscope located at the University of Michigan Electron Microbeam Analysis Laboratory (EMAL). The microscope has a zirconated tungsten thermal field emission gun which can be operated at a voltage of 200kV. The microanalysis techniques that can be performed with this microscope are X-ray energy dispersive spectroscopy (EDX) and electron energy loss spectroscopy. This subsection describes cross-sectional TEM sample preparation procedure, electron diffraction and imaging with TEM and the procedure of performing EDX at the cross-section of the samples.

3.4.6.1. TEM sample preparation by Focused Ion Beam (FIB)

This section describes the in-situ FIB lift-out procedure employed to prepare cross-sectional TEM samples from Rhines pack samples using FEI Nova 200 Nanolab SEM/FIB. Each step of the procedure is briefly summarized in Figure 3.24.

First, the sample surface was thoroughly examined in BSE imaging mode using the through lens detector (TLD) in high resolution mode, to find the grain boundary oxides which shows distinct Z-contrast compared to the matrix and the surface features (Figure 3.24a). Next, platinum, in dimensions 15µm x 2µm x 0.2µm, was deposited over the region of interest using the electron beam. To increase the deposition efficiency a very low beam voltage of 2 keV and the largest beam current that gives a decent quality secondary electron image was used. After depositing a thin layer of platinum, sample stage was gradually tilted to 52°, while maintaining the eucentric height at 5mm. At this tilt angle, the surface of interest is exposed to the ion beam at a right angle. Using the ion beam at 30 keV more platinum is deposited up to 2µm thickness. The ion beam current density for the deposition should not be significantly greater than 2.6 $pA/\mu m^2$. The next step is to make trenches at the front and back sides of the deposited platinum layer and reveal the cross-sectional features to be characterized under TEM. The initial trenches were made using the "cross-section cleaning" setting at a beam voltage of 30keV and beam current of 7nA. To make an undercut below the deepest feature of interest, the length of the trench was set to be three times of the depth of the cut. Figure 3.24b shows the trench made at the front side of the platinum layer. After both trenches were made, the front and back faces of the lift-out sample were cleaned using a beam current of 1nA. At this point, it is a common practice to the thin the lift-out sample down to 1-1.5µm. Then, the sample stage was tilted back to 7°, so that two side cuts and an undercut can be made with the ion beam milling the back surface of the lift-out sample at 45°. These three cuts were made in parallel and the sample was suspended from both sides as shown in Figure 3.24c. Thereafter, the stage was tilted back to 0° and the Omniprobe tip was attached to the top surface of the suspended sample by depositing platinum with 30keV ion beam at a current of 50pA. At this angle, the ion beam images the lift-

out sample upside down, which can be reverted by a scan rotation of 180°. After the Omniprobe tip is successfully attached, the lift-out sample was cut loose by milling away the connection points (Figure 3.24d). Next, the Omniprobe tip was retracted to move the stage and find an available post on the copper TEM grid. The lift-out sample was attached to the post as shown in Figure 3.24e and the Omniprobe tip was detached from the sample by milling away the platinum weld.

The final step involved gradually thinning the lift-out sample until it becomes transparent to the electrons and removing the ion beam damage from the sample surfaces. The stage was tilted to 54°, while maintaining the eucentric height at 5mm. The front surface of the lift-out sample was milled gradually using 30 keV ion beam at beam currents of 0.5nA, 0.1nA and 50pA. Once the front surface is finished the stage was tilted back to 50°. The back surface was milled using the same beam settings used to mill the front surface of the sample. During the milling of both front and back surfaces of the lift-out sample, secondary electron beam imaging was kept online using a beam voltage of 5keV and beam current of 1.6nA. Milling the back surface of the lift-out sample at 50pA beam current should be ceased before the surface platinum layer is completely milled away. At this point, the sample should already be less than 150nm thick and electron transparent. Finally, the ion beam damage was removed from both front and back surfaces using 5keV ion beam voltage and 70pA ion beam current by tilting the stage to 57° and 47°, respectively. During this very final step, the front surface of the sample should be imaged using electron beam voltage of 5keV and beam current of 1.6nA. The sample becomes ready for TEM imaging, when the electron transparency of the sample is verified by the secondary electron images (Figure 3.24f).

3.4.6.2. Electron diffraction patterns

Collective scattering of an incident electron beam by an arrangement of atoms is called diffraction [96]. Diffraction is influenced by the angle of incident electron beam, the spacing between the planes and the interatomic distances within the planes. Electron diffraction in TEM is of paramount importance to determine the crystallographic structure of the specimen being analyzed.

Figures 3.25 a-c show the electron diffraction patterns of a pure Si specimen taken at three different camera lengths (L) of 30cm, 40cm and 50cm. The most noticeable difference between each image is the increase in the distance between a diffraction spot to the transmitted spot, R, with increasing L. L is the distance of the recording plane from the diffraction pattern (Figure 3.26). R can be related to L as follows:

$$Rd = \lambda L, \tag{3. 11}$$

where d is the interatomic spacing and λ is the wavelength of the 200keV electron beam (0.0251Å). λL is also called as camera constant, in units $\text{Å} - cm$. The unit of R is in *pixels*, if a digital image of the diffraction pattern is obtained. However, R indeed represents the spacing of each plane of atoms in the reciprocal space and is inversely proportional to d according to Equation (3.11). Therefore, the unit of R in the reciprocal space is in nm^{-1}. It is a common practice to calibrate pixel-to-nm^{-1} ratio for a given camera constant, so that the measured R values on a diffraction pattern can accurately represent the d-spacings of each plane. This process is called as camera length calibration.

The diffraction patterns shown in Figure 3.25 serve for two purposes. First, each of the silicon diffraction patterns is used as a standard to perform the camera length calibration. Second, the procedure followed to index the electron diffraction patterns to identify the crystal

structure of the certain features of interest within the context of this dissertation work is described.

To perform the camera length calibration, first, R values for the three closest diffraction spots to the transmitted beam are measured (Figure 3.25a). Then, these diffraction spots should be indexed with the purpose of relating the *d* values with the measured R values. Determining the d value requires knowledge of the crystal structure of silicon, which is face centered cubic (fcc). To index the diffraction spots, the diffraction pattern is compared with the indexed single crystal diffraction patterns of the fcc crystal in different orientations [97]. Each diffraction pattern in Figure 3.25 resembles that of the fcc crystal oriented along [110] direction. The diffraction spots of interest are indexed, as shown in Figure 3.25a. Next step is to calculate the *d* value for each diffraction spot and relate them with the measured *R* values according to the Equation (3.11). For cubic structures, *d* is given as follows [98]:

$$d = a/\sqrt{h^2 + k^2 + l^2}, \tag{3. 12}$$

where a is the lattice parameter of the silicon crystal (0.543nm) and h, k, l are the Miller indices of each plane. Afterwards, λ, L and d are inserted in Equation (3.11) to determine the corresponding *R* values with units nm^{-1}. Note that the unit of camera constant, $\text{Å} - cm$, is neglected in this calibration. Finally the values of *R* in nm^{-1} are divided by the corresponding values measured in *pixels* to determine the *pixel-to-*nm^{-1} ratio for each diffraction pattern taken at each camera length. The results are tabulated in Tables 3.6 - 3.8 and the camera length calibration is graphically shown in Figure 3.27.

To index the electron diffraction patterns of the unidentified phases and features, first, the electron diffraction pattern obtained is matched with one of the single crystal electron diffraction patterns for fcc, bcc, dc and hcp crystal structures given by Fultz and Howe [97]. Then, each

diffraction spot is indexed accordingly and R values of at least three closest diffraction spots from the transmitted beam are measured. The measured R values are converted into the units of nm^{-1} by using the *pixel-to-*nm^{-1} ratio corresponding with the camera length used to take the electron diffraction pattern and the *d* values for each diffraction spots is calculated according to Equation (3.11). Thereafter, the lattice parameter of the structure is calculated, for instance, if the structure is cubic according to Equation (3.12). The relationship between the interplanar spacings, *d*, and the lattice parameter for other crystal systems is given by Andrews et al. [98]. To verify that the electron diffraction pattern is indexed accurately, the angles between the diffraction spots are measured and compared with the calculated values. For example, if the indexed electron diffraction pattern is associated with a cubic structure, the angle between two diffraction spots, representing two crystallographic planes, is given as follows [98]:

$$\cos\phi = (h_1h_2 + k_1k_2 + l_1l_2)/\sqrt{(h_1^2 + k_1^2 + l_1^2)(h_2^2 + k_2^2 + l_2^2)}. \quad (3.13)$$

The angle between the two crystallographic planes of the other crystal systems are also given by Andrews et al. [98]. Once the accuracy of the measured angles is proved and the consistency of the indexing is proved, the crystal structure and the calculated lattice parameter reveals the identity of the feature analyzed.

3.4.6.3. TEM imaging conditions

Imaging operations in TEM can be performed by first projecting the SAD pattern [96]. Both the transmitted electron beam and diffracted beams can be selected to create images. Bright field image is obtained by introducing the objective aperture, blocking out most of the diffraction pattern and selecting the transmitted electron beam. The image can be obtained by retracting the SAD aperture and can be focused with the objective lens. The dark field image can be obtained by following the same routine but by selecting a specific diffracted beam.

Apart from conventional TEM imaging, scanning transmission electron microscopy (STEM) imaging techniques were also used. STEM image can be obtained by focusing and converging the beam at the specimen [96]. The convergent beam indeed reduces the image contrast. To see an image, the convergent beam should be scanned and move parallel to the optic axis. The major advantage of STEM imaging is that, detectors are used to form the images, not the lenses. Therefore, images are not subject to the defects such as chromatic aberration.

The probe is first aligned by setting the magnification higher than X1,000,000 and switching to the spot mode. Then an amorphous area, preferentially the thinnest part of the platinum overlayer, is found and the image is focused to see the "Ronchigram". Ronchigram is a shadow image, which looks like a defocused diffraction pattern as shown in Figure 3.28 [99]. After finding the Ronchigram, the condenser stigmatism should be corrected and the illumination beam alignment should be performed. To form an STEM image, a detector is inserted either above or below the viewing screen to intercept the scattering or direct electron beam. A bright field STEM image can be obtained by inserting a bright field detector which intercepts the direct electron beam. Dark field STEM image is formed by inserting an annular dark field detector that picks up the scattered electrons.

3.5 Error analysis

3.5.1. Weight gain measurements

Each weight gain measurement is reported with an error equal to the propagation of the standard deviations of the weight and surface area measurements. Equations to determine specific weight gain of each sample are given in Section 3.4.1. In total, five parameters were measured three times to obtain the specific weight gain values. Standard deviation for each measurement, σ_i, is given according to the following equation:

$$\sigma_i = \sqrt{\sum_{i=1}^{N}(x_i - \mu)^2 / (N-1)}, \quad (3.\ 14)$$

where x_i is the measured value, μ is the average value of N set of measurements.

Errors associated with weigh and surface area measurements are, first, propagated separately and then combined to calculate the total error in the specific weight gain measurement. The standard deviation of the weight change in a sample, $\sigma_{\Delta W}$, is propagated according to the following equation:

$$\sigma_{\Delta W} = \sqrt{\left(\sigma_{W_{bfr}}\right)^2 + \left(\sigma_{W_{aft}}\right)^2}, \quad (3.\ 15)$$

where $\sigma_{W_{bfr}}$ and $\sigma_{W_{aft}}$ are the standard deviation of the weight measurements performed before and after the exposures, respectively.

The standard deviation of the surface area measurements, σ_{S}, is propagated as follows:

$$\sigma_{\mathrm{S}} = 2 \times \sqrt{(\sigma_{\ell \times w})^2 + (\sigma_{\ell \times t})^2 + (\sigma_{w \times t})^2}, \quad (3.\ 16)$$

where:

$$\sigma_{\ell \times w} = (\ell \times w) \times \sqrt{(\sigma_\ell / \ell)^2 + (\sigma_w / w)^2}, \quad (3.\ 17)$$

$$\sigma_{\ell \times \mathrm{t}} = (\ell \times \mathrm{t}) \times \sqrt{(\sigma_\ell / \ell)^2 + (\sigma_{\mathrm{t}} / \mathrm{t})^2}, \quad (3.\ 18)$$

$$\sigma_{w \times \mathrm{t}} = (w \times \mathrm{t}) \times \sqrt{(\sigma_w / w)^2 + (\sigma_{\mathrm{t}} / \mathrm{t})^2}. \quad (3.\ 19)$$

Finally, the total error in the specific weight gain measurement of a sample, $\sigma_{\Delta W/S}$, is given by:

$$\sigma_{\Delta W/S} = \Delta W/S \times \sqrt{(\sigma_{\Delta W}/\Delta W)^2 + (\sigma_{\mathrm{S}}/\mathrm{S})^2}. \quad (3.\ 20)$$

3.5.2. Error propagation in X-ray based spectroscopy techniques

In any X-ray based spectroscopy technique, generation of the peaks obeys Gaussian statistics. The standard deviation, σ, associated with a single each peak collection process is given as follows:

$$\sigma = \sqrt{N}, \tag{3. 21}$$

where N is the peak number of counts above the background. The probability of the measured value N to remain within $\pm 1\sigma$ of its true value is 67%. The probability increases to 95% for $\pm 2\sigma$ and 99.7% for $\pm 3\sigma$. If the measurement is desired to remain in the 99.7% confidence interval, then the relative error for a single measurement becomes:

$$Relative\ error\ (\%) = 3\sqrt{N}/N \times 100. \tag{3. 22}$$

Table 3.1 Chemical composition of IN617 as reported by Special Metals Inc. [88], Sherry Labs, and obtained from EPMA [38].

	Element concentration (wt. %)										
	Ni	Cr	Co	Mo	Al	Ti	Fe	Mn	Cu	Si	C
Special Metals Inc.	54.6	21.8	11.5	9.7	1.1	0.3	0.79	0.03	0.02	0.07	0.09
Sherry Labs	55.1	21.6	11.5	9.4	0.9	0.3	0.68	0.06	0.03	0.08	0.09
EPMA	54.8	21.4	11.5	9.2	1.1	0.3	0.78	0.02	0.02	0.08	N/A

Table 3.2 Chemical composition of Nicrofer5520Co as reported by Thyssen Krupp VDM.

	Element concentration (wt. %)										
	Ni	Cr	Co	Mo	Al	Ti	Fe	Mn	Cu	Si	C
Thyssen Krupp VDM	54.1	22.2	11.6	8.6	1.1	0.4	1.6	0.1	0.04	0.1	0.05

Table 3.3 Composition of the calibration gases provided by Cryogenics Inc.

	Molecule concentration (molppm)						
	CO_2	H_2	O_2	N_2	CH_4	CO	He
Calibration Gas 1	3.2	-	-	-	-	14.5	Base
Calibration Gas 2	-	482.0	47.5	147.0	480.0	-	Base
Calibration Gas 3	-	46.3	7.3	27.6	50.0	-	Base
Calibration Gas 4	13.1	-	-	-	-	1876.0	base

Table 3.4 Summary of the parameters of the He-CO-CO_2 exposures.

Environment			Alloy	Temperature (°C)	Flow Rate (ml/min)	Exposure times (h)
P_{CO} (molppm)	P_{CO_2} (molppm)	Designation				
13.5	1.5	Env. 9	IN617	750 - 850	200 ± 5	25, 75, 150, 225, 375, 500
1980	1.5	Env. 1320	IN617	750 - 850	200 ± 5	25, 75, 150, 225, 375, 500
1980	1.5	Env. 1320	Nicrofer 5520Co	850	200 ± 5	225

Table 3.5 Summary of the Cr $2p_{3/2}$ peak positions and areas shown in Figure 3.23.

Sample	Element (Valence)	Peak 1		Peak 2		Peak 3		Peak 4		Peak 5	
		E_B (eV)	% Area	E_B (eV)	% Area	E_B (eV)	% Area	E_B (eV)	% Area	E_B (eV)	% Area
Sputter cleaned pure Cr	Cr (0)	574.41	-	-	-	-	-	-	-	-	-
Oxidized pure Cr at 750°C	Cr (+3)	575.15	55.78	575.15	18.04	576.95	8.46	578.02	13.93	579.11	3.80

Table 3.6 *Pixel-to-nm^{-1}* calibration for the Si [110] diffraction pattern taken at L = 30cm.

	distance (pixel)	plane	$h^2+k^2+l^2$	d (nm)	a (nm)	λL (Å-cm)	*pixel - nm^{-1}* ratio
R1	145.003	(002)	4	0.272	0.543	0.753	0.019
R2	123.810	(-111)	3	0.314	0.543	0.753	0.019
R3	201.347	(-220)	8	0.192	0.543	0.753	0.019
						Average *pixel - nm^{-1}* ratio:	0.019

Table 3.7 *Pixel-to-nm^{-1}* calibration for the Si [110] diffraction pattern taken at L = 40cm.

	distance (pixel)	plane	$h^2+k^2+l^2$	d (nm)	a (Å)	λL (Å-cm)	*pixel - nm^{-1}* ratio
R1	210.010	(002)	4	0.272	0.543	1.004	0.018
R2	178.807	(-111)	3	0.314	0.543	1.004	0.018
R3	290.007	(-220)	8	0.192	0.543	1.004	0.018
						Average *pixel - nm^{-1}* ratio:	0.018

Table 3.8 *Pixel-to-nm^{-1}* calibration for the Si [110] diffraction pattern taken at L = 50cm.

	distance (pixel)	plane	$h^2+k^2+l^2$	d (nm)	a (Å)	λL (Å-cm)	*pixel - nm^{-1}* ratio
R1	264.008	(002)	4	0.272	0.543	1.255	0.014
R2	227.622	(-111)	3	0.314	0.543	1.255	0.014
R3	368.005	(-220)	8	0.192	0.543	1.255	0.014
						Average *pixel - nm^{-1}* ratio:	0.014

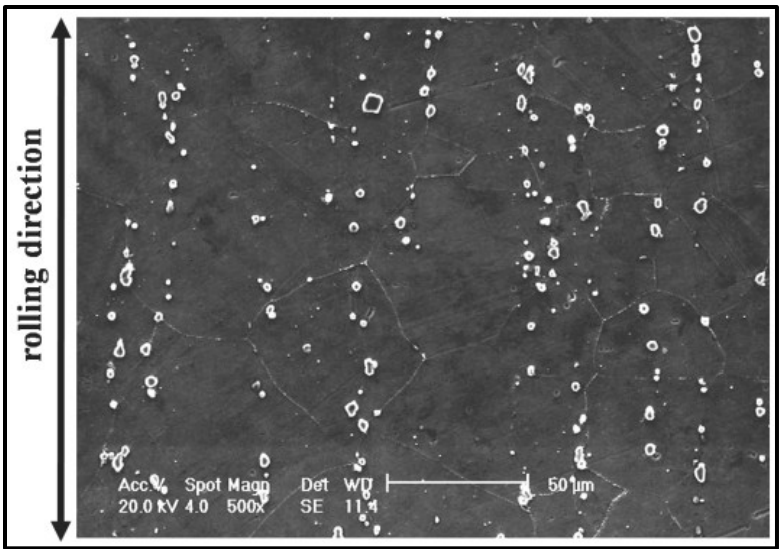

a)

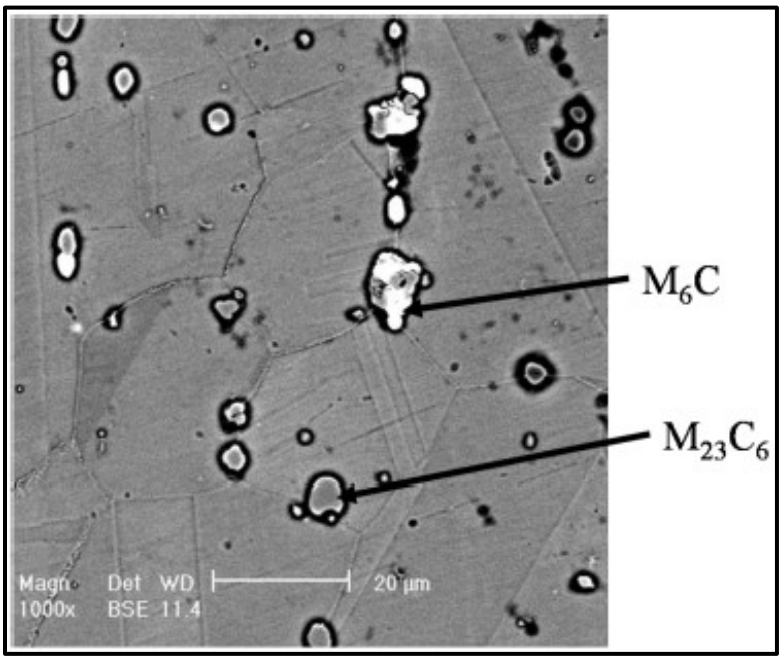

b)

Figure 3.1 Microstructures of the as-received IN617 electro-etched in 10% oxalic acid solution at room temperature to reveal the carbides a) secondary electron image b) backscattered electron image [38].

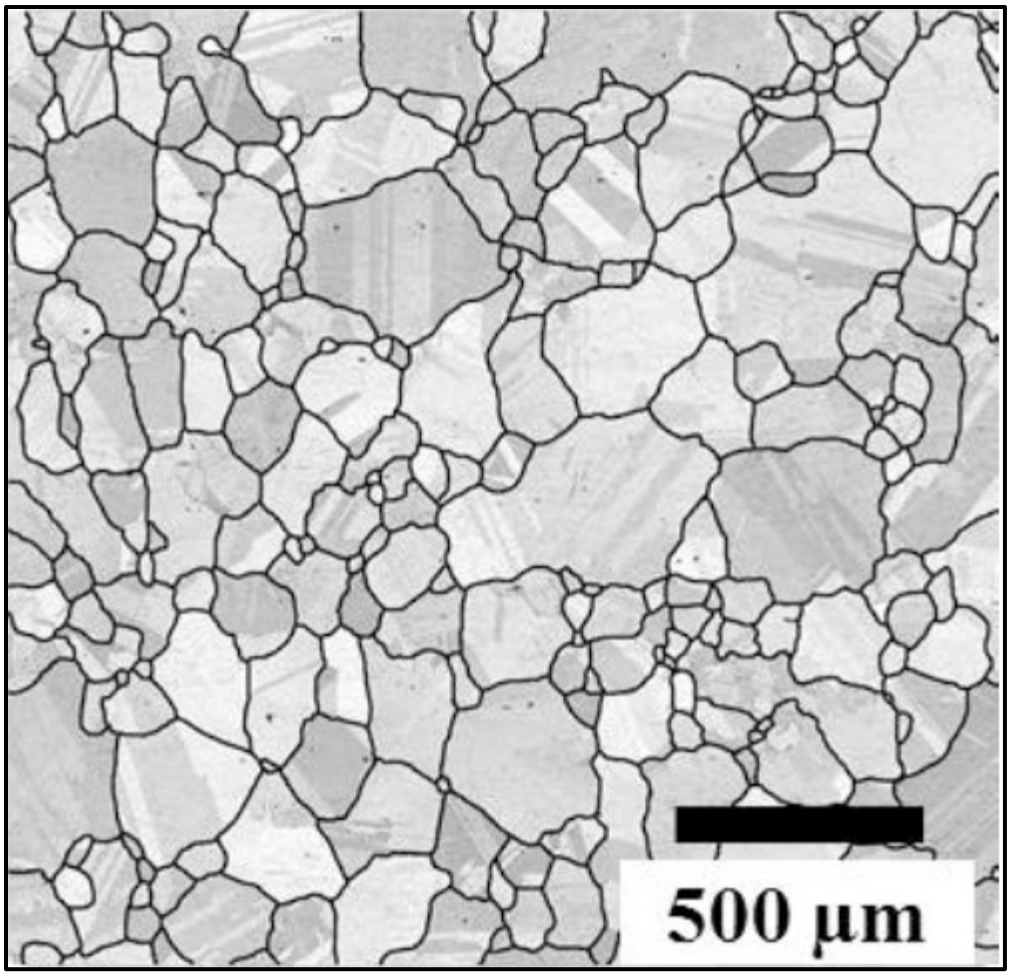

Figure 3.2 As -received microstructure of Nicrofer5520Co etched in Kalling's reagent (5g $CuCl_2$, 100ml ethanol and 100 ml HCl) [89].

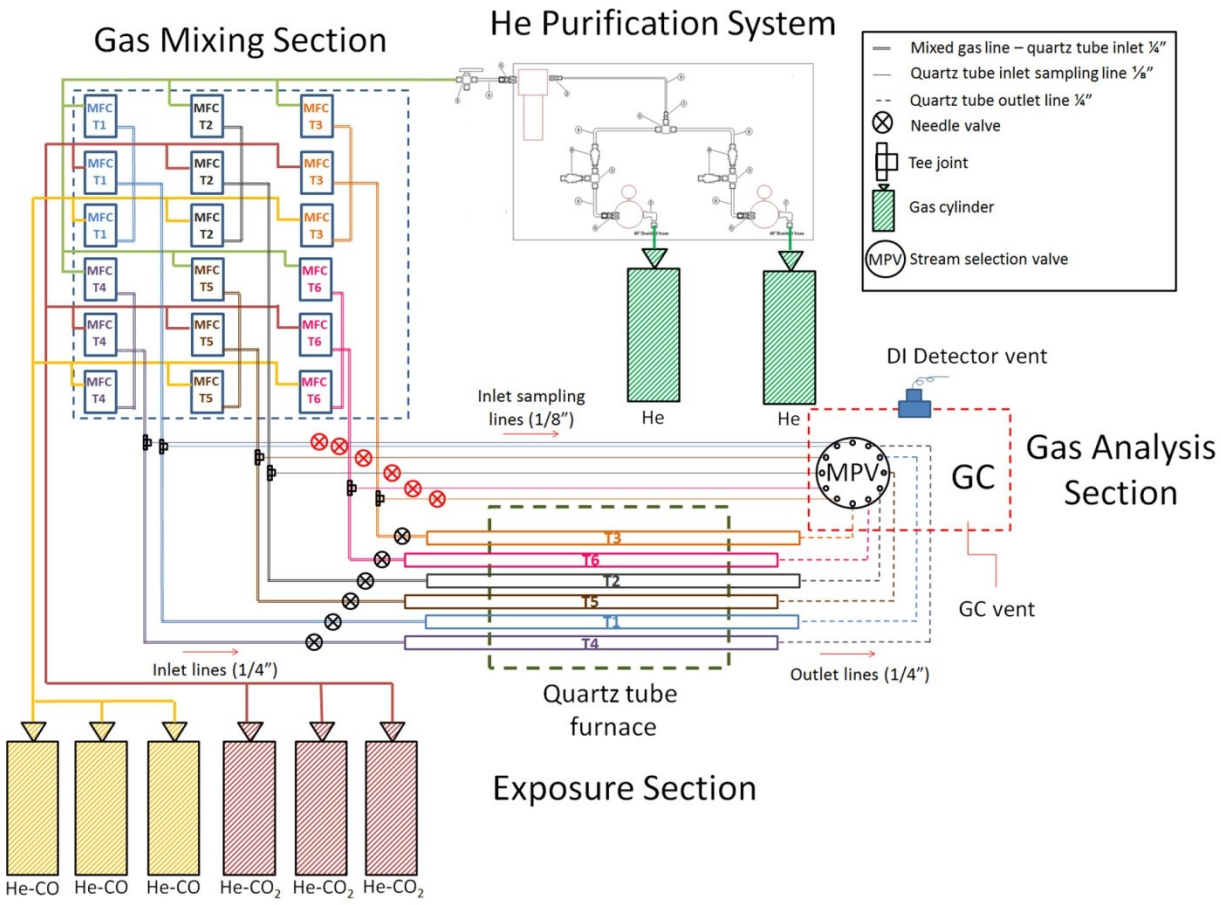

Figure 3.3 A schematic representation of the Controlled-impurity helium flow system.

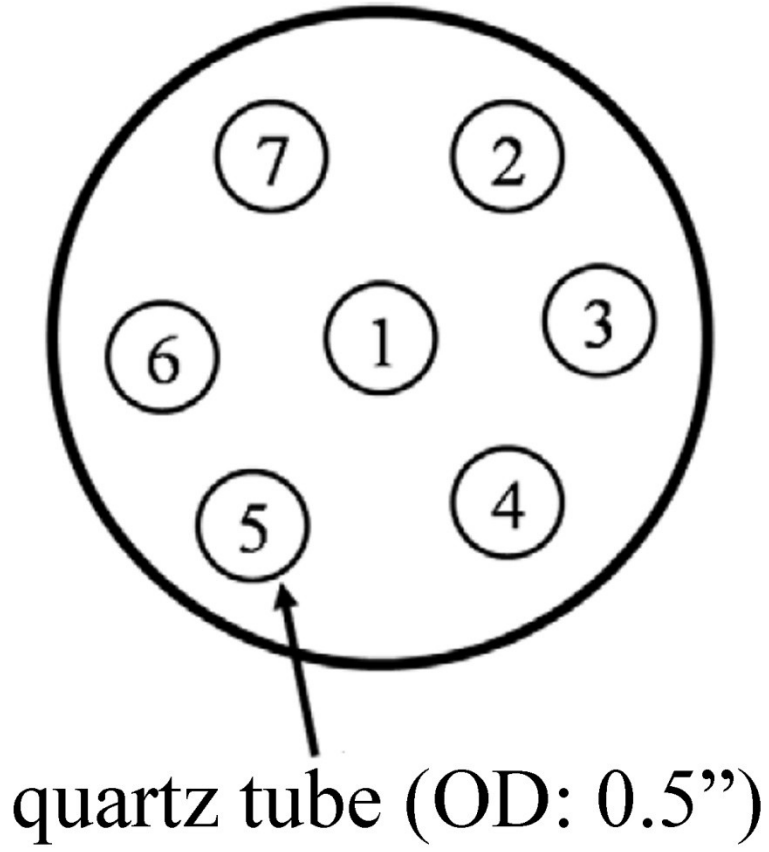

Figure 3.4 Side view of the discs holding seven quartz tubes in honeycomb arrangement.

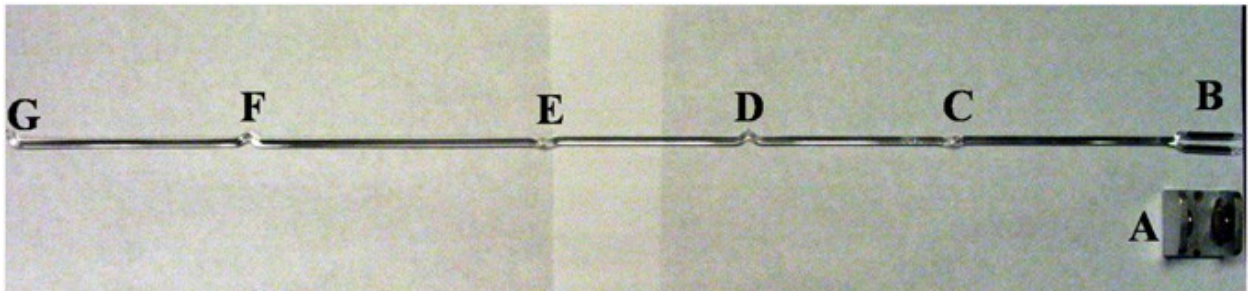

a)

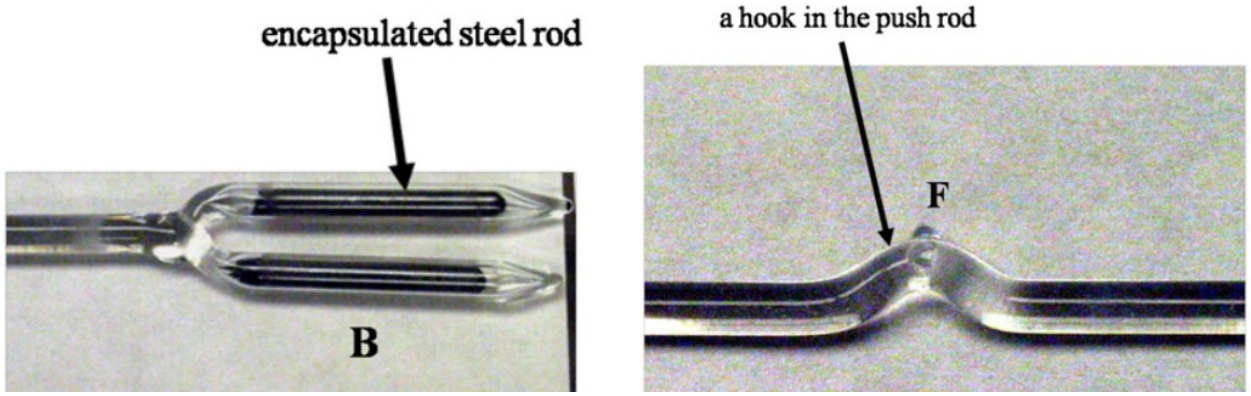

b)

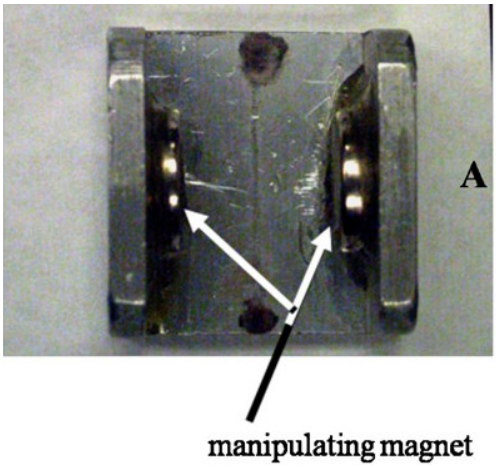

c)

Figure 3.5 Photographs of a) push-rod designed to manipulate samples in each tube without breaking the seals of the quartz tubes, b) the encapsulated steel fork head (B) and one of the hooks (C-G) that moves the sample, and c) the U-shaped manipulating magnet bracket (A) [38,90].

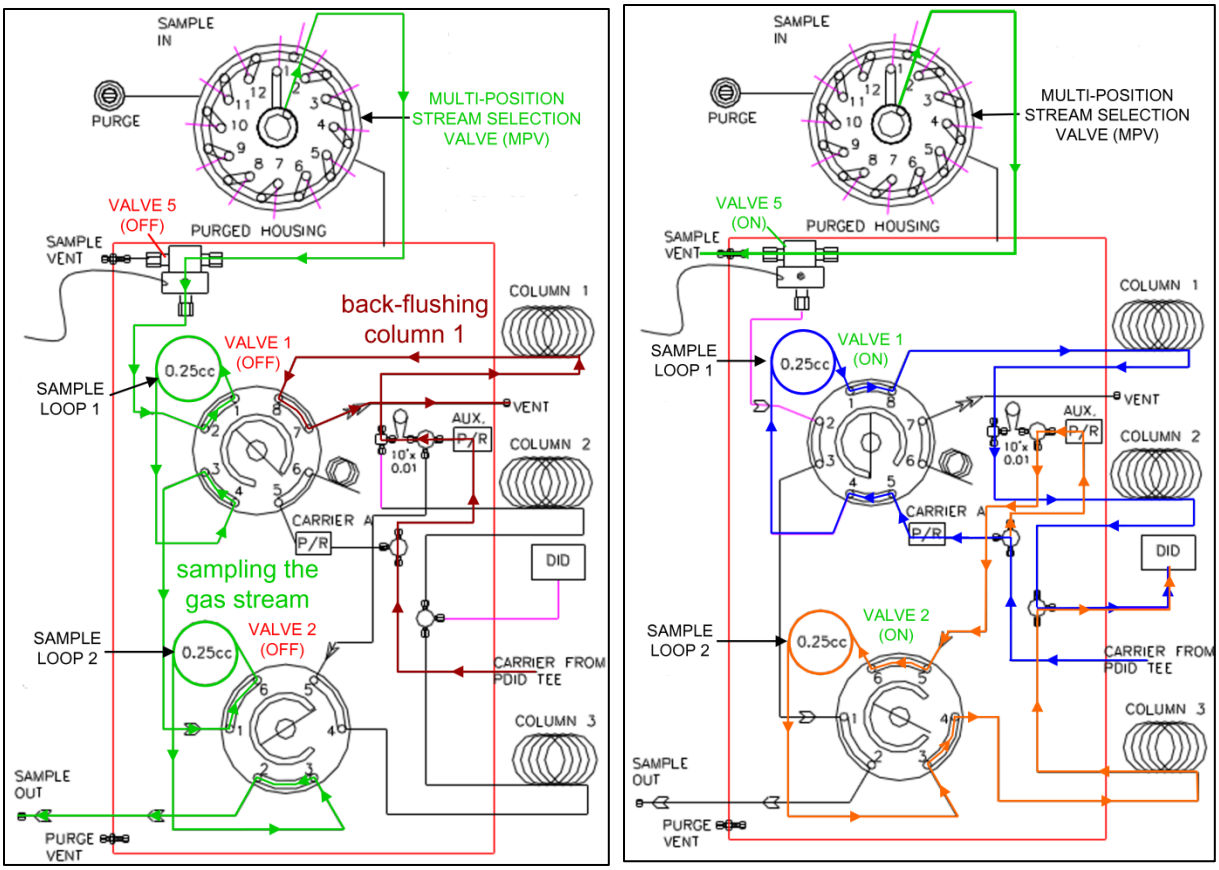

Figure 3.6 Schematic representation of the GC valve plumbing diagram and flow path of a) the sampled gas stream filling the two sample loops (green path) and the carrier gas is back-flushing Column1 (dark red path), and b) the career gas pushing the sampled gas from loop 1 (blue path) and loop 2 (orange path) for the analysis of H_2, Ar, O_2, N_2, CH_4, CO and CO_2 concentrations in the sampled gas.

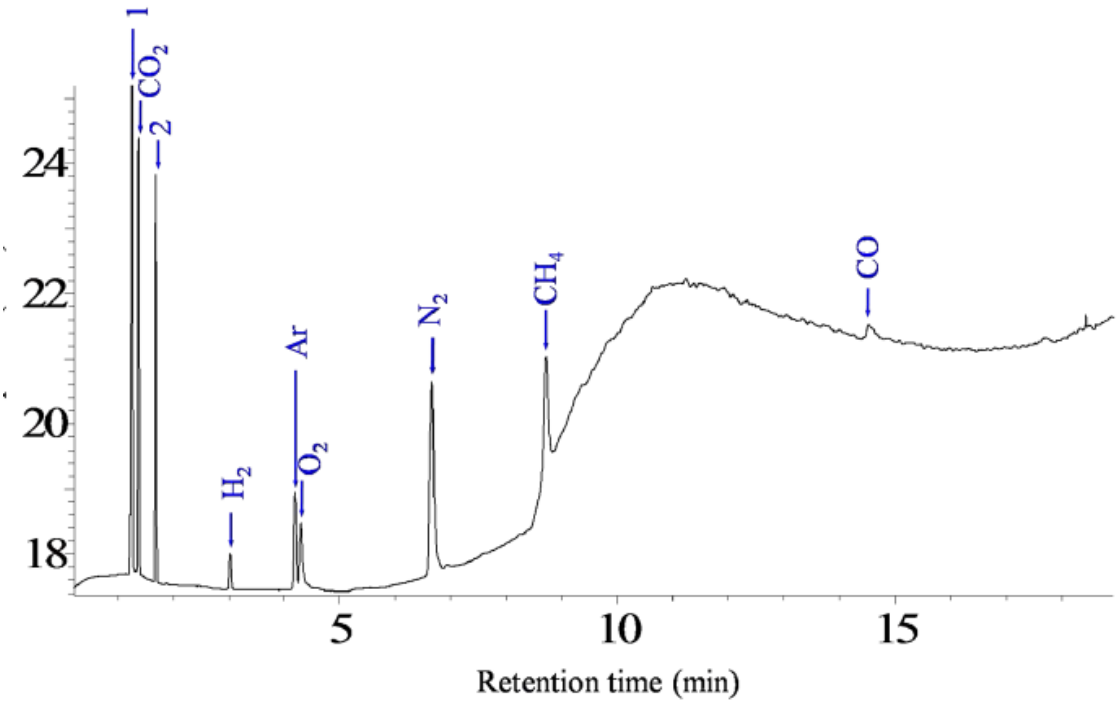

Figure 3.7 A representative chromatogram obtained from helium based gas mixture containing 2ppm of each H_2, Ar, O_2, N_2, CH_4, CO and CO_2 molecules.

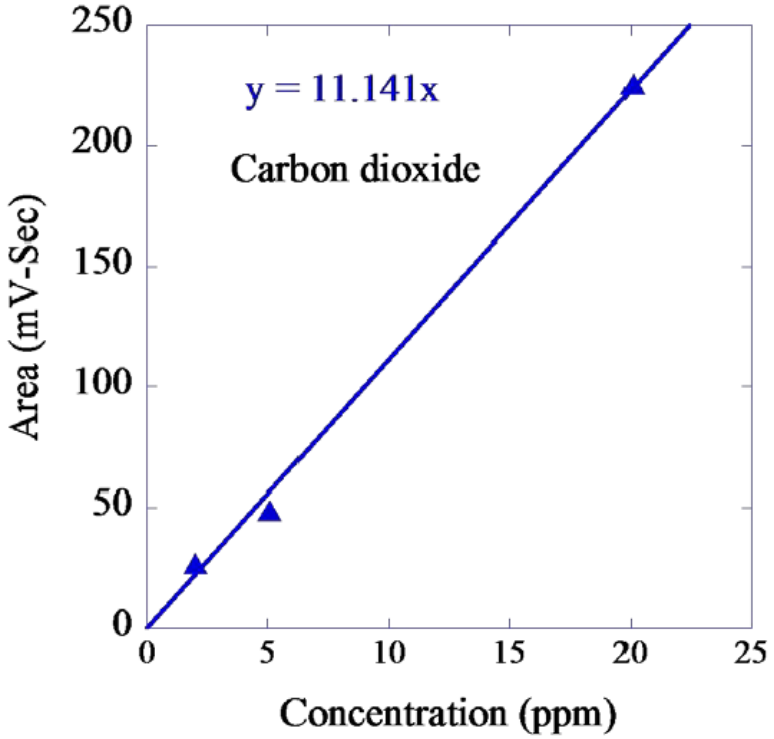
y = 11.141x
Carbon dioxide
Area (mV-Sec)
Concentration (ppm)
0
50
100
150
200
250
0
5
10
15
20
25

a)

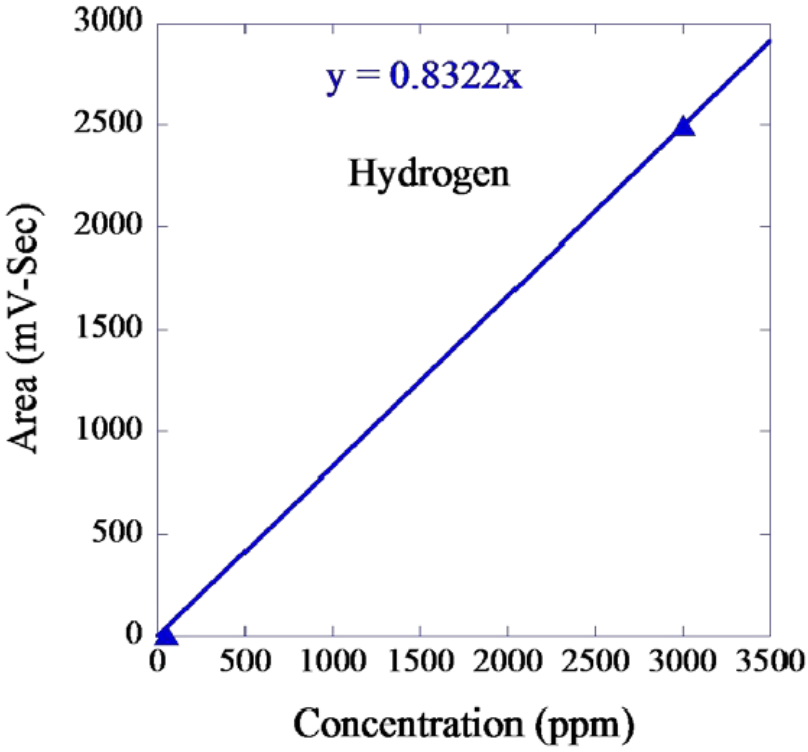
y = 0.8322x
Hydrogen
Area (mV-Sec)
Concentration (ppm)
0
500
1000
1500
2000
2500
3000
0
500
1000
1500
2000
2500
3000
3500

b)

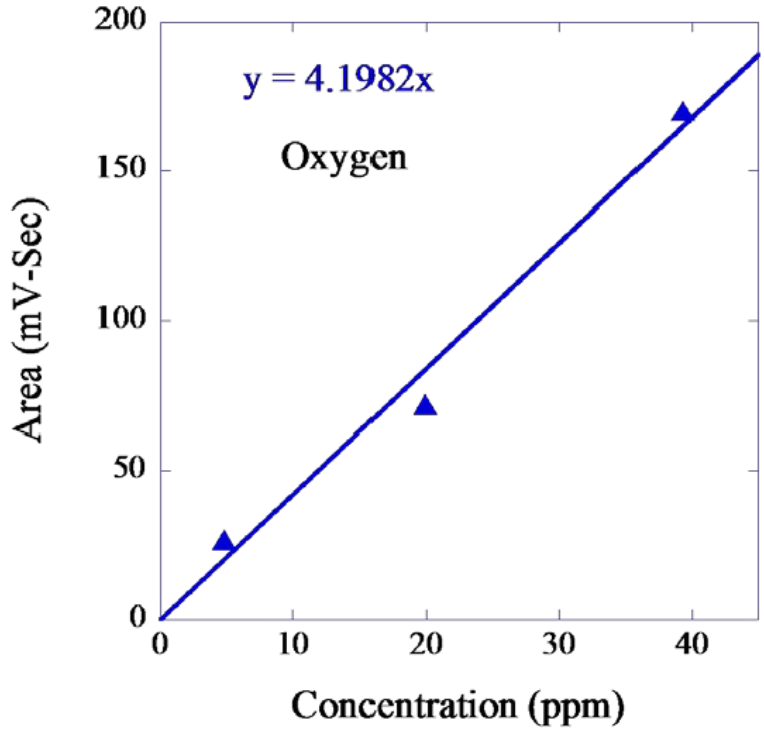
y = 4.1982x
Oxygen
Area (mV-Sec)
Concentration (ppm)
0
50
100
150
200
0
10
20
30
40

c)

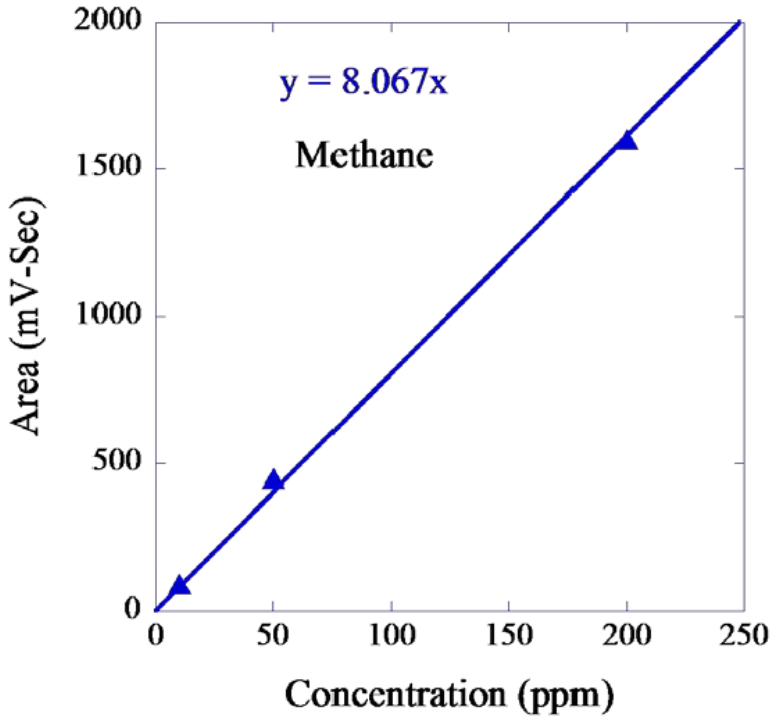
y = 8.067x
Methane
Area (mV-Sec)
Concentration (ppm)
0
500
1000
1500
2000
0
50
100
150
200
250

d)

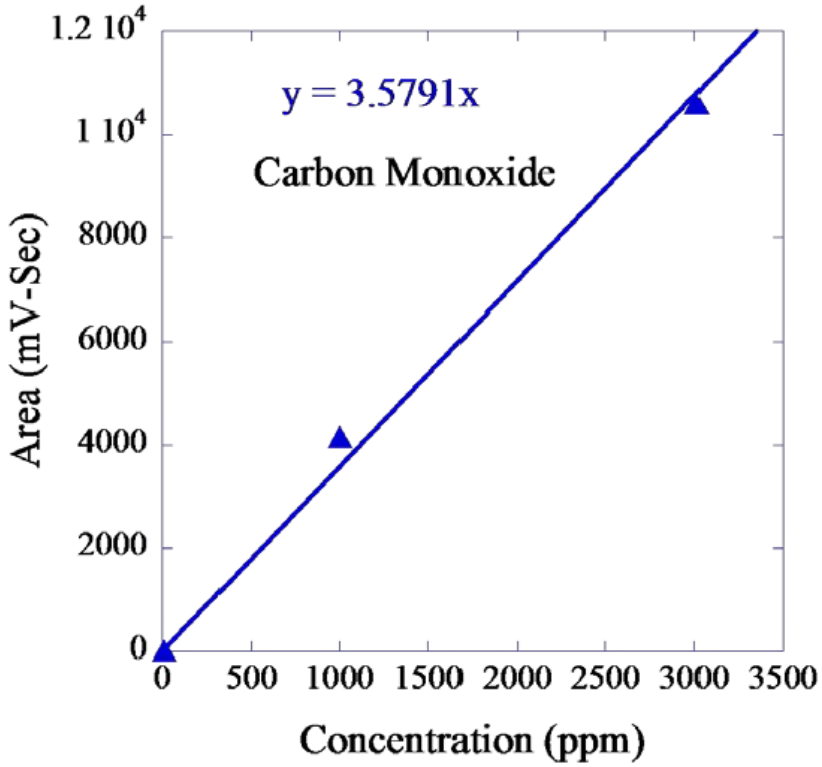

e)

Figure 3.8 Calibration curves obtained for a) carbon dioxide, b) hydrogen, c) oxygen, d) methane and e) carbon monoxide from the analysis of the of the calibration gas compositions indicated in Table 3.3.

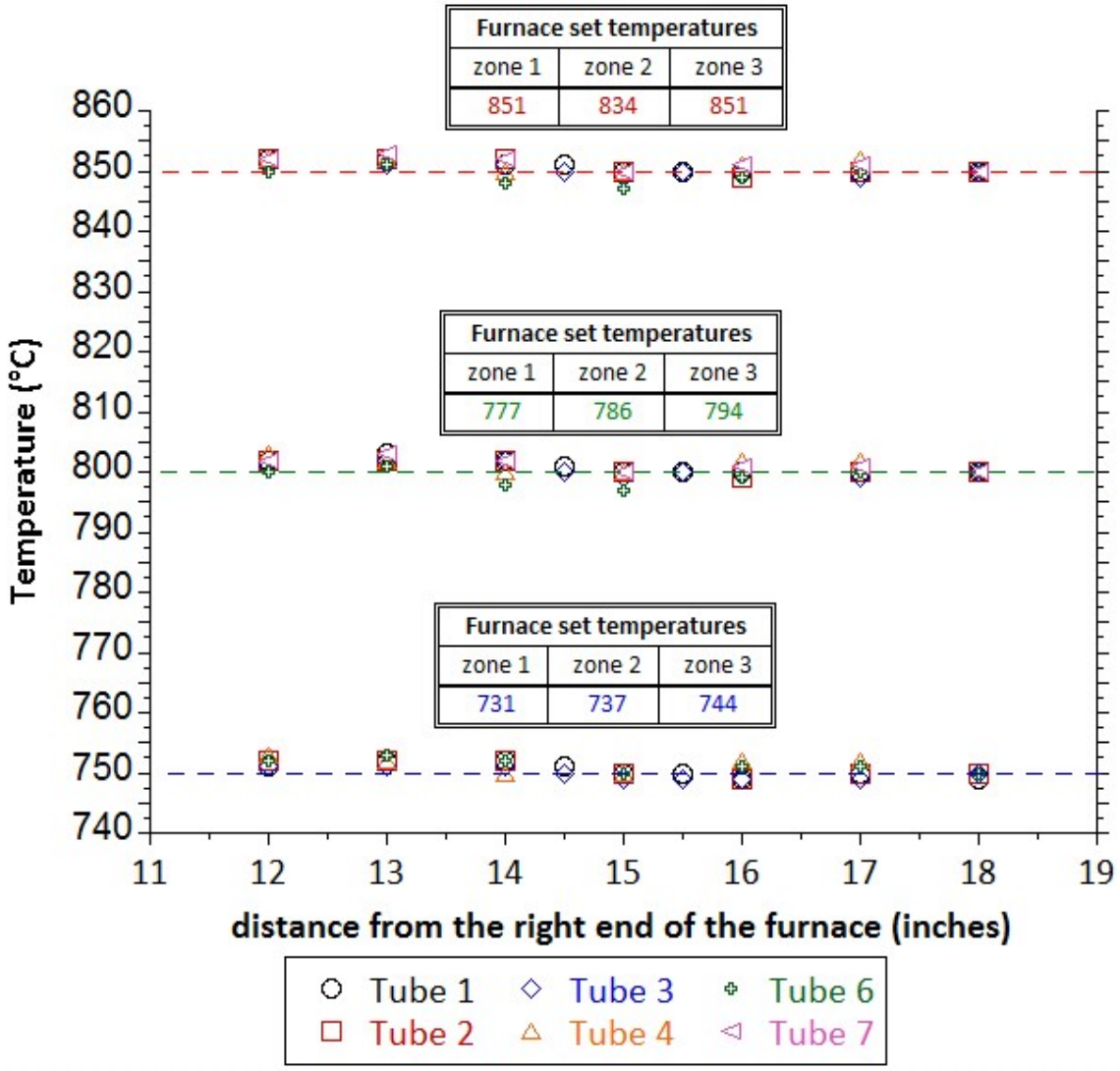

Figure 3.9 Temperature profiles obtained along each tube used for exposures at temperatures 750, 800 and 850 °C while pure helium gas was flowing at a rate of 200 ml/min. The error in each measurement was +/- 1 °C. Set temperatures for each zone of the furnace to achieve the measured temperature profiles are indicated in the tables overlaid to the figure.

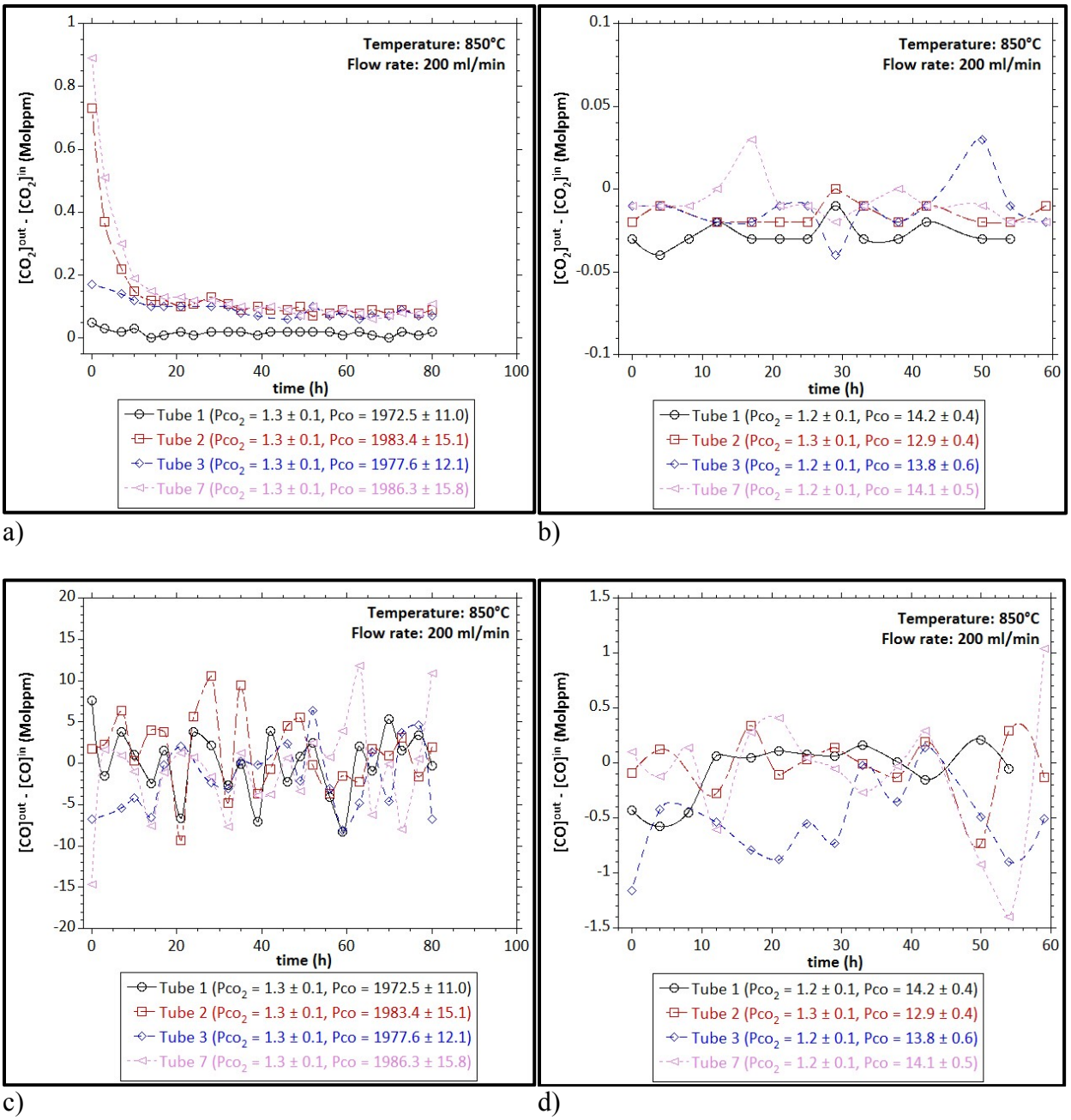

Figure 3.10 Differences in the inlet and outlet CO_2 (a, b) and CO (c, d) concentrations due to the interactions of He - 1.3 molppm CO_2 - 1980 molppm and He - 1.3 molppm CO_2 - 13.5 molppm CO gas mixtures with the quartz tubes at 850°C (flow rate is 200 ml/min).

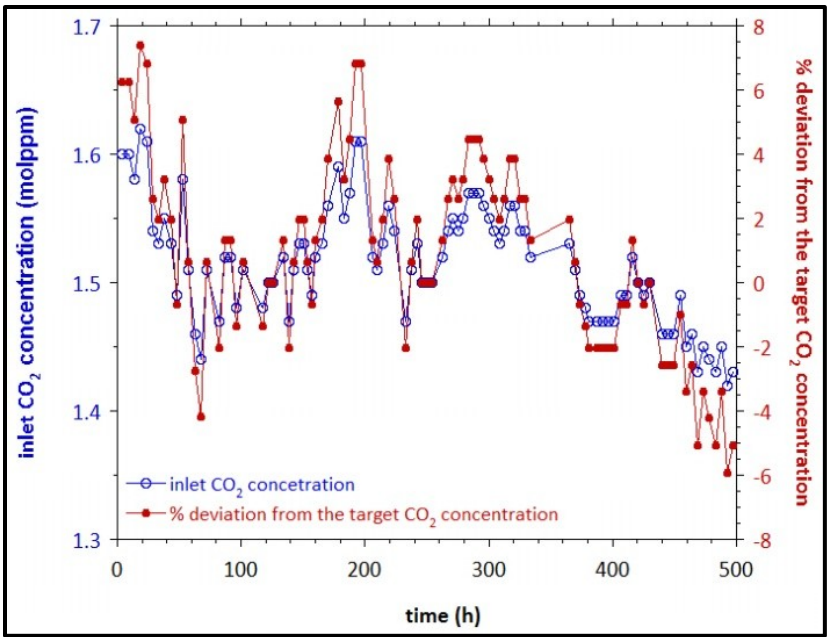

a)

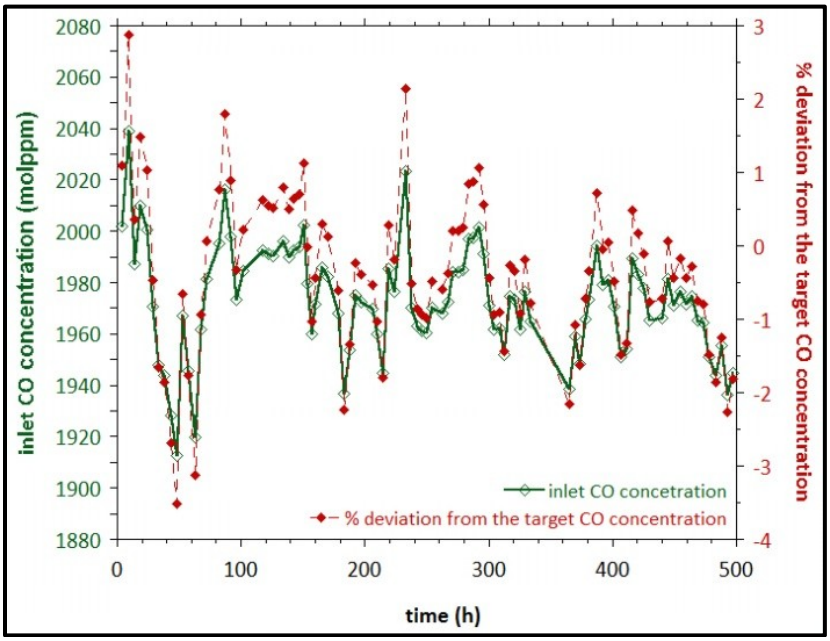

b)

Figure 3.11 Plots of a) the CO_2 concentrations maintained and the deviations from the target CO2 value and b) the CO concentrations maintained and the deviations from the target CO value when establishing He - 1.5 molppm CO_2 and 1980 molppm CO environment at the inlet of a quartz tube over 500h of exposure duration.

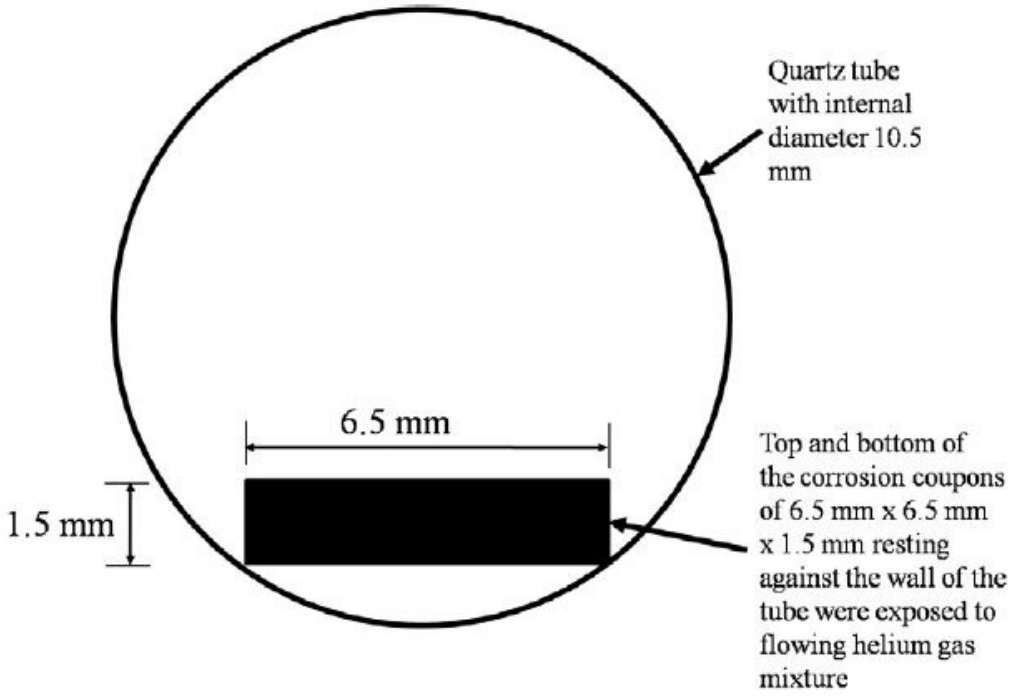

Figure 3.12 Cross-section view of a quartz tube showing the location of the corrosion coupons in dimensions 6.5mm x 6.5mm x 1.5mm [38].

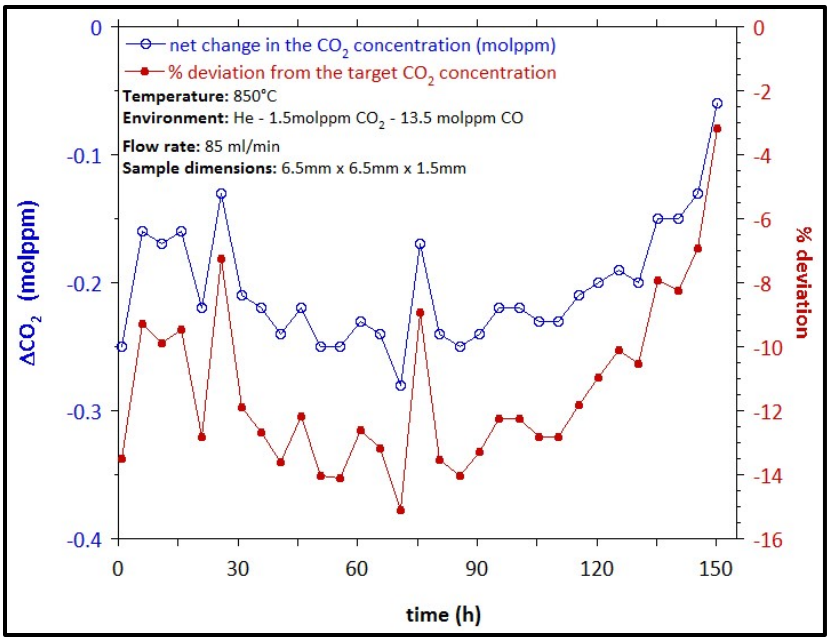

a)

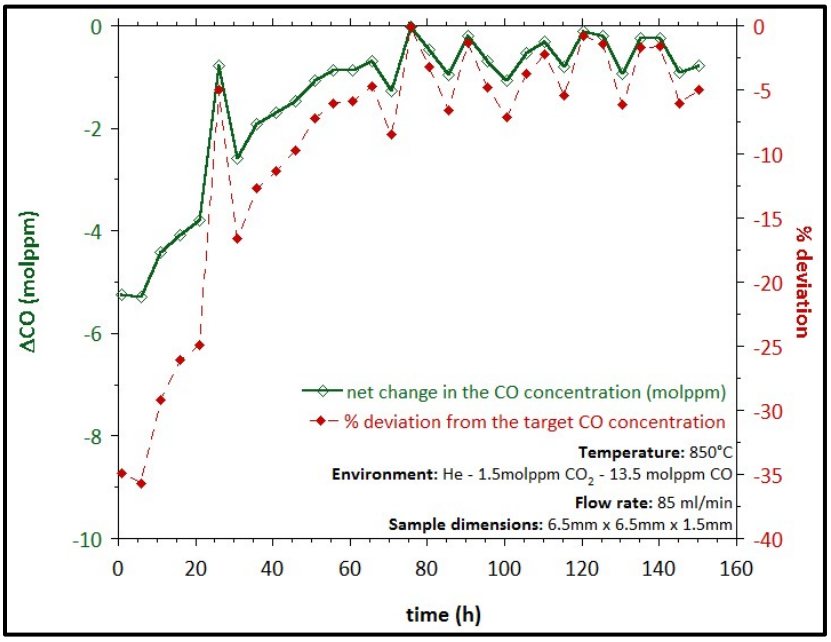

b)

Figure 3.13 Plots of a) the CO_2 concentrations maintained and the deviations from the target CO_2 value and b) the CO concentrations maintained and the deviations from the target CO value when environment He - 1.5 molppm CO_2 - 13.5 molppm CO is established at a flow rate of 85 ml/min.

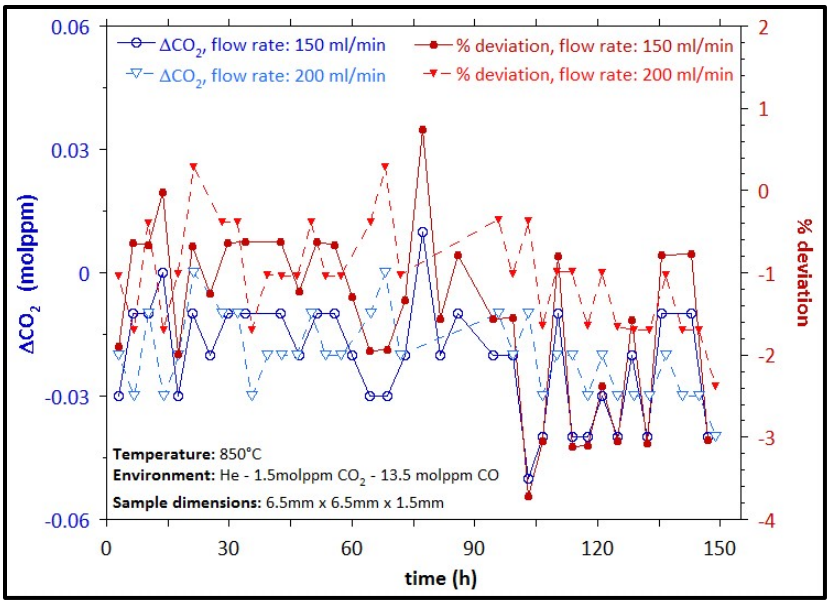

a)

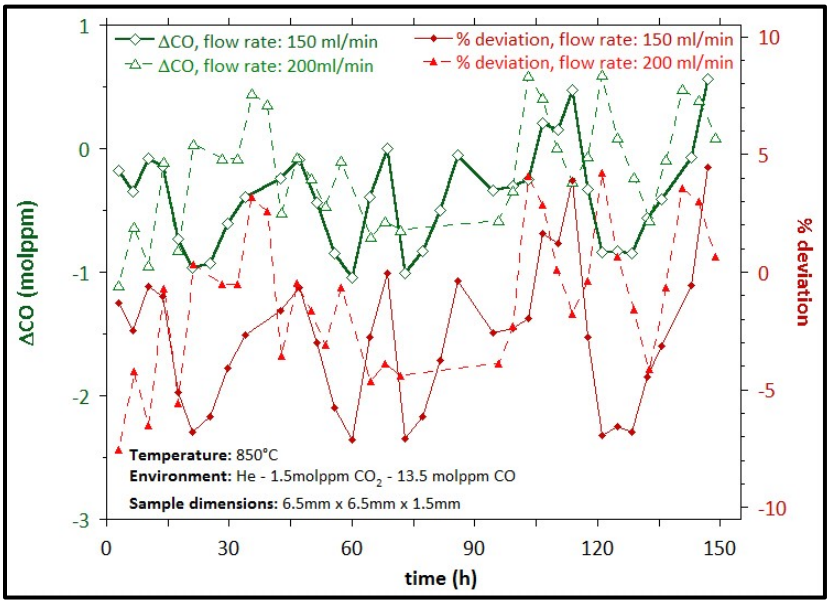

b)

Figure 3.14 Plots of a) the CO_2 concentrations maintained and the deviations from the target CO_2 value and b) the CO concentrations maintained and the deviations from the target CO value when environment He - 1.5 molppm CO_2 - 13.5 molppm CO is established at flow rates of 150 ml/min and 200 ml/min.

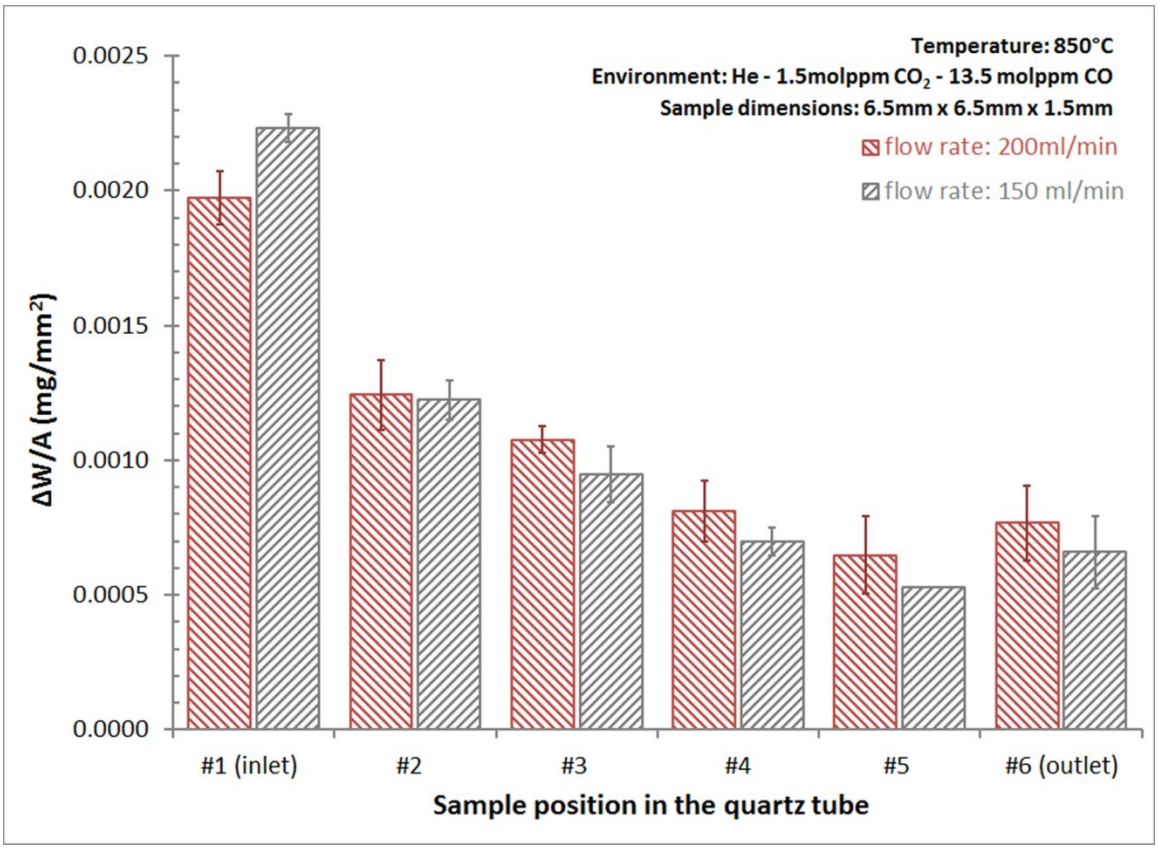

Figure 3.15 Specific weight gains measured for IN617 samples exposed to He - 1.5molppm CO_2 - 13.5 molppm at flow rates of 150 ml/min and 200 ml/min with respect to their locations in the quartz tubes. Sample dimensions were 6.5mm x 6.5mm x 1.5mm.

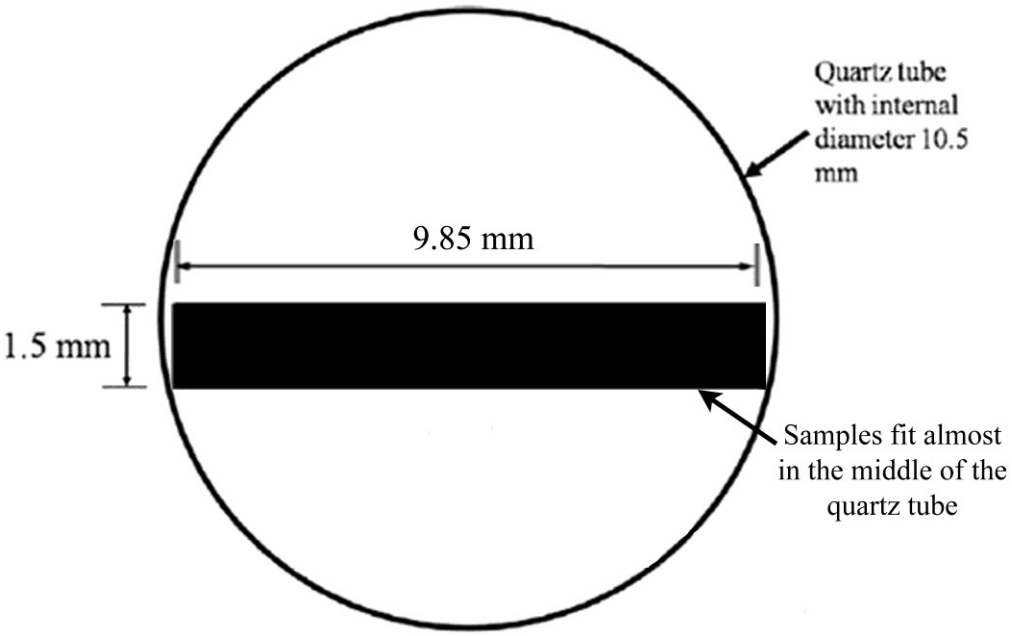

Figure 3.16 Cross-section view of a quartz tube showing the location of the corrosion coupons in dimensions 9.85mm x 4.00mm x 1.50mm.

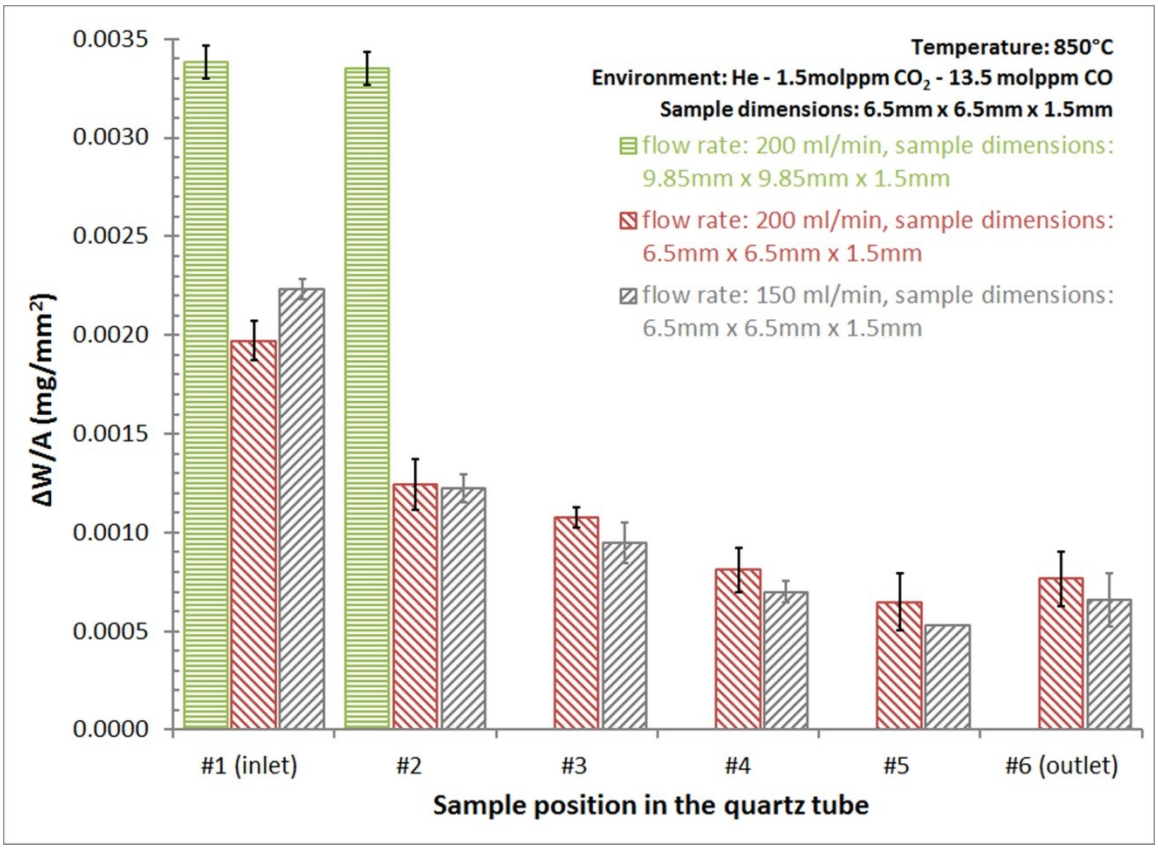

Figure 3.17 Comparison of the specific weight gains measured for IN617 samples, in dimensions 4.5mm x 10mm x 1.5mm, exposed to He - 1.5molppm CO_2 - 13.5 molppm at 850 °C, for 150h, at a flow rate of 200 ml/min with that measured for the samples, in dimensions 6.5mm x 6.5mm x 1.5mm, exposed to the same environment - temperature - exposure time at a flow rates of 150 ml/min and 200 ml/min.

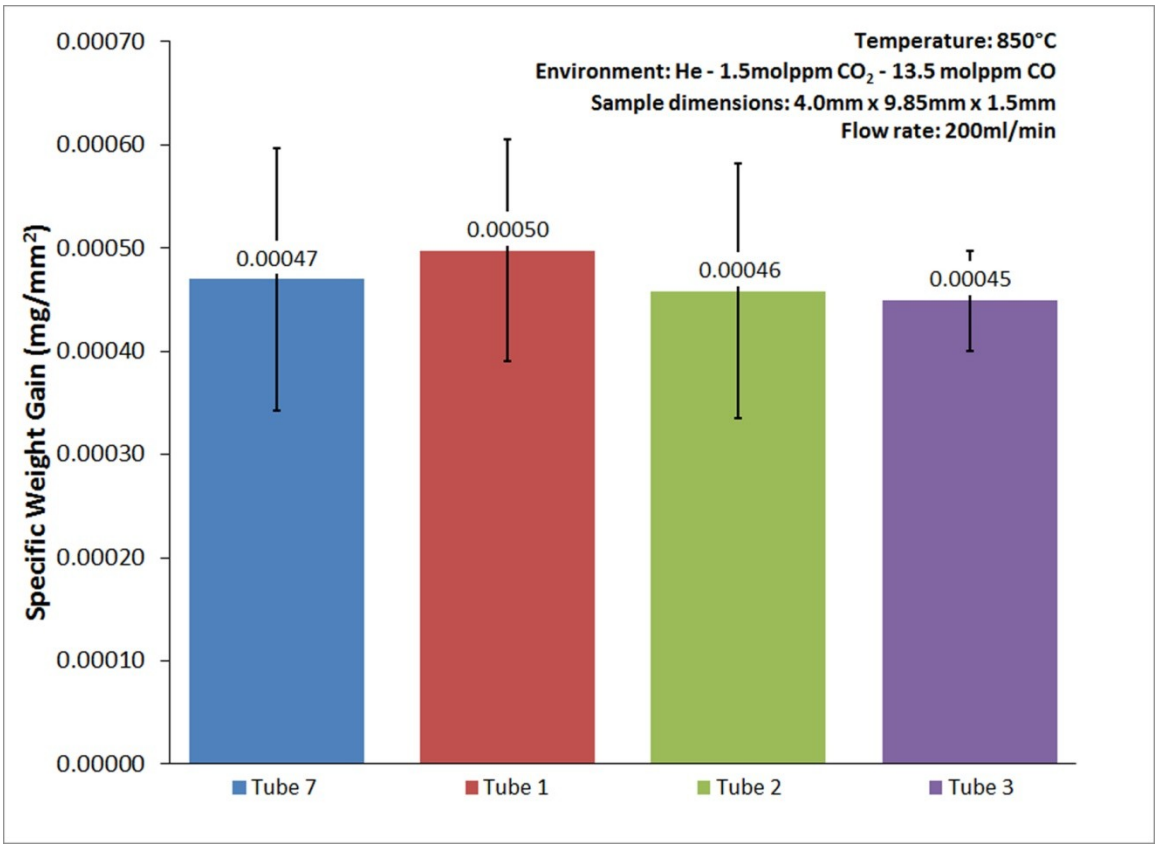

Figure 3.18 Specific weight gain values measured for four IN617 samples removed simultaneously after 25h of exposure to He - 1.5molppm CO_2 - 13.5 molppm at a flow rate of 200 ml/min, at 850 °C.

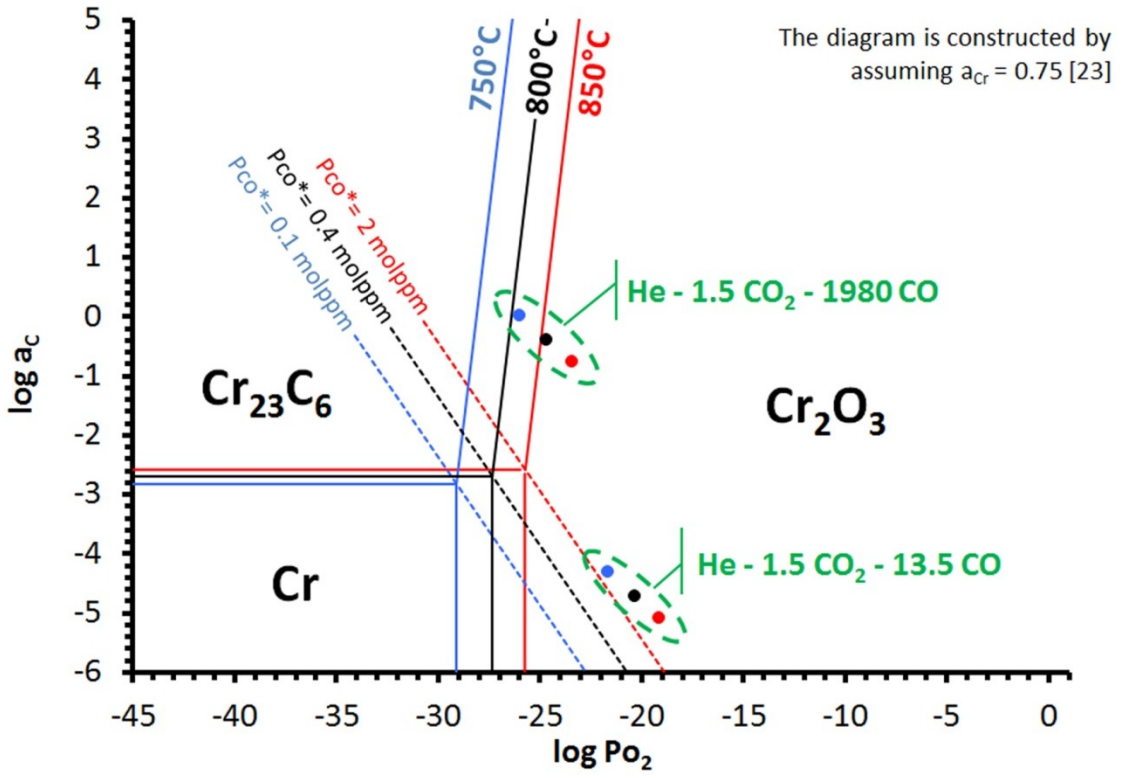

Figure 3.19 A representative Cr-C-O stability diagram showing the equilibrium oxygen partial pressure and carbon activities of environments He - 1.5molppm CO_2 - 13.5 molppm and He - 1.5molppm CO_2 - 1980 molppm at temperatures 750 - 850 °C.

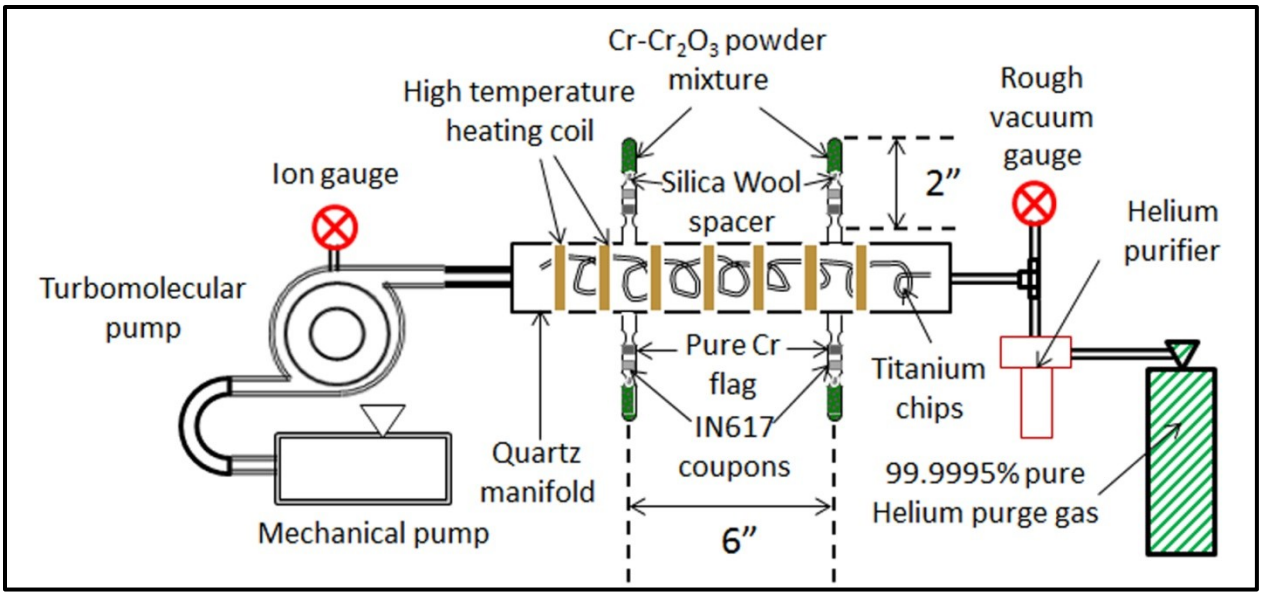

Figure 3.20 Schematics of the Rhines pack capsule preparation setup.

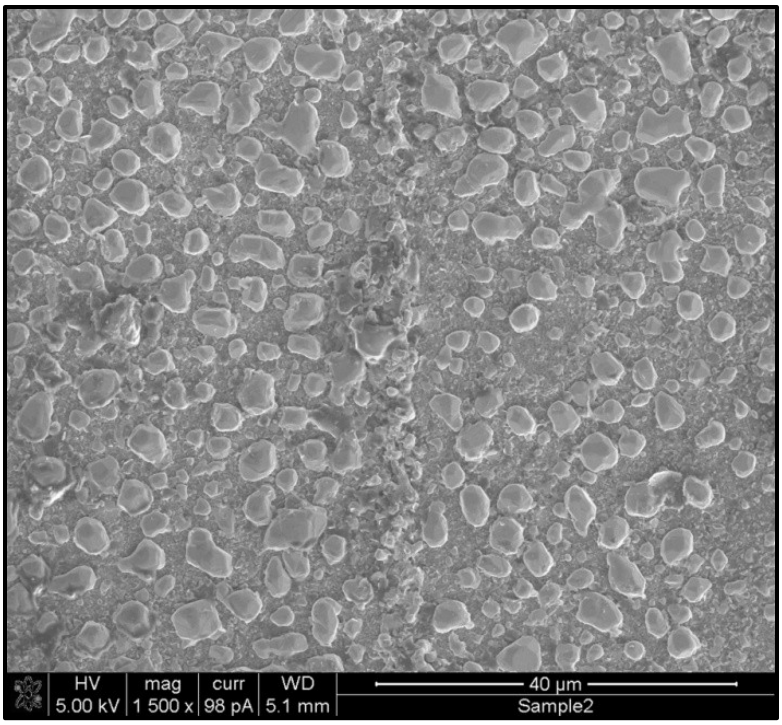

a)

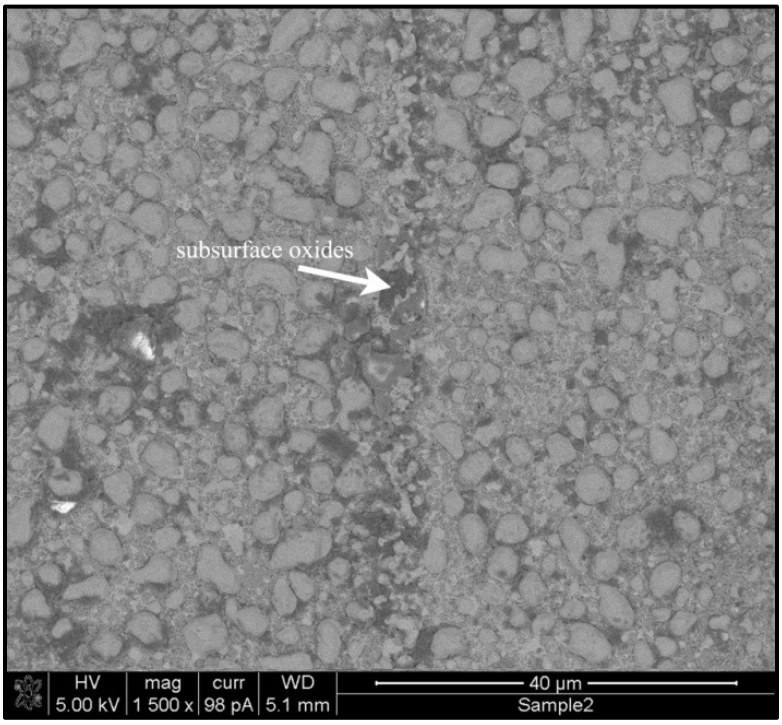

b)

Figure 3.21 Micrographs taken from the same region by a) secondary electron (SE) and b) backscattered electron (BSE) imaging, respectively. SE image reveals the surface features in greater detail; whereas BSE image provides much better Z-contrast and in-depth information.

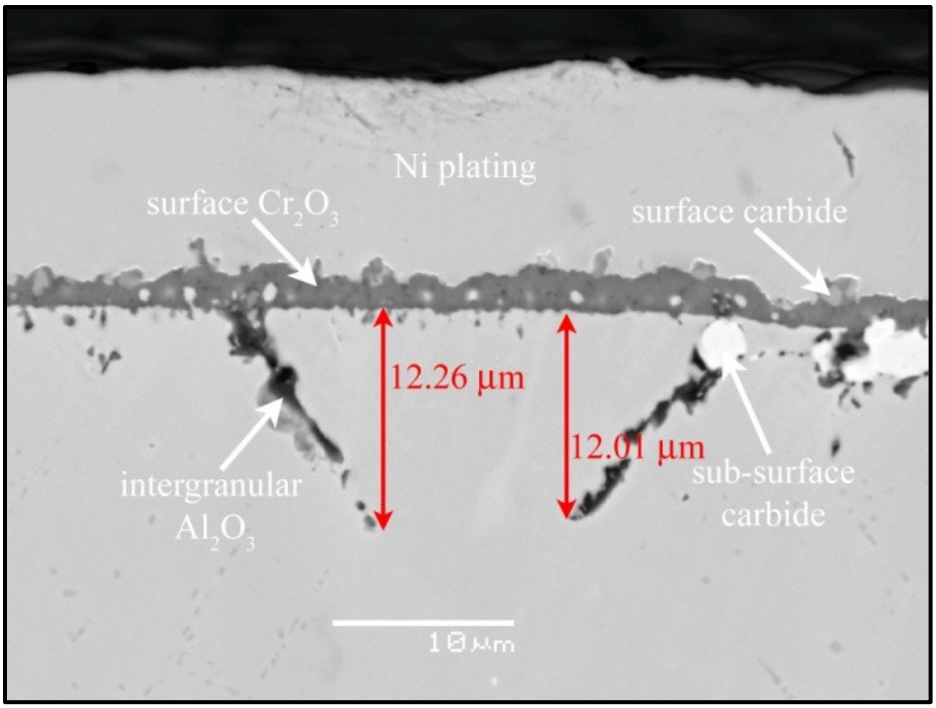

a)

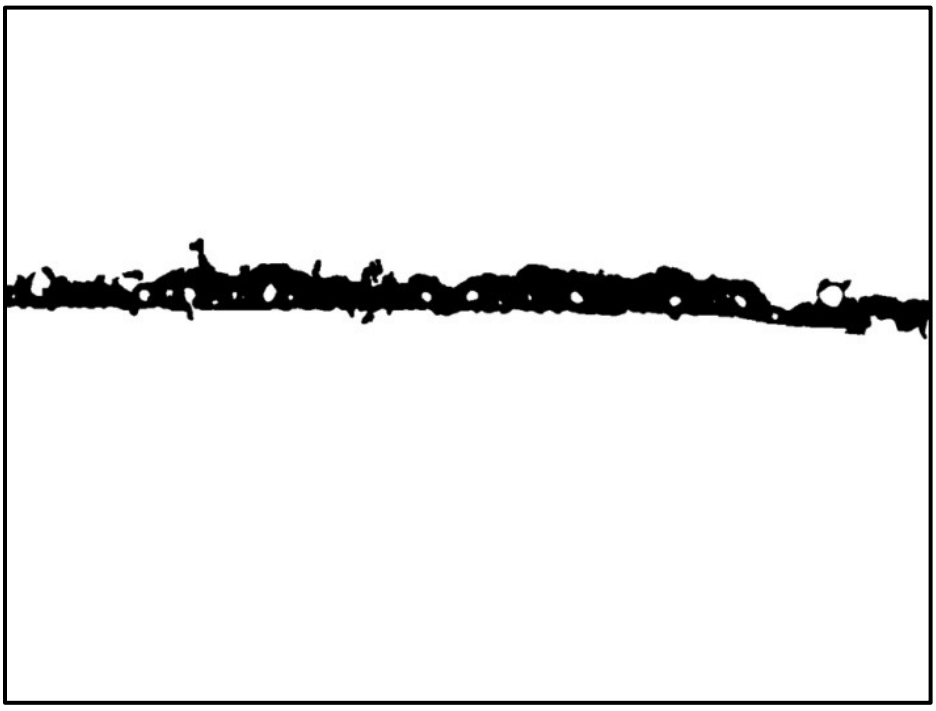

b)

Figure 3.22 a) BSE image of IN617 exposed to environment 1320 at 850 °C clearly revealing all the distinct features present at the cross-section of the sample. Depths of the Al_2O_3 scales were measured by using ImageJ software. b) Surface Cr_2O_3 was delineated using the magic wand tool feature of Adobe Photoshop software.

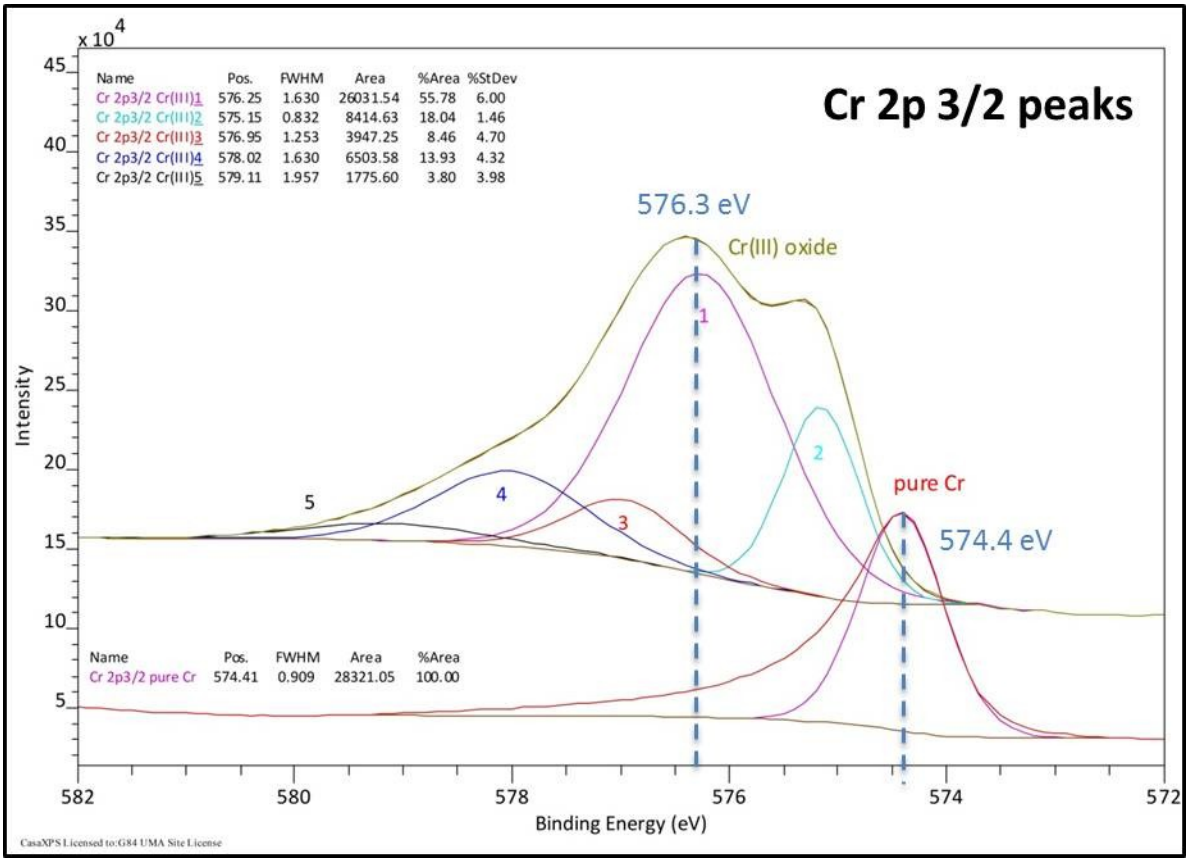

Figure 3.23 XPS spectra obtained from the as-polished pure Cr after sputtering (red curve) and after oxidation at 750 °C (green curve) showing the peak positions of elemental Cr and Cr^{+3}, respectively. Cr^{+3} peak formed a double shoulder and was wide enough to be represented by five different "synthetic" peaks, each representing Cr^{+3} photoelectrons emitted with slightly different energies due to multiplet splitting phenomenon.

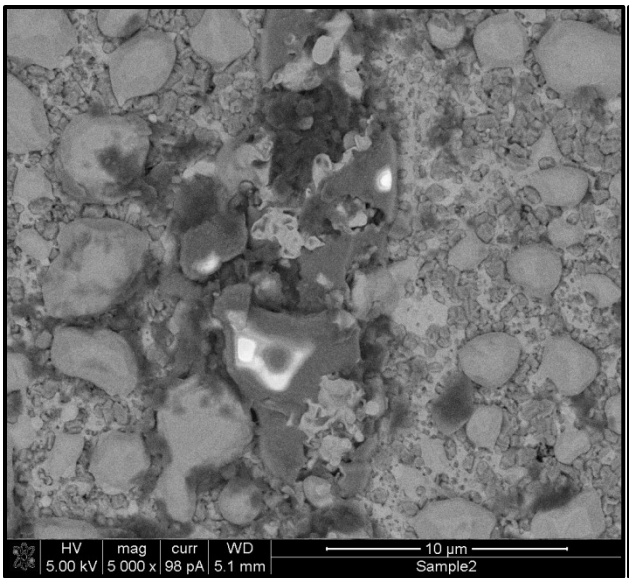
HV
5.00 kV
mag
5 000 x
curr
98 pA
WD
5.1 mm
10 µm
Sample2

a)

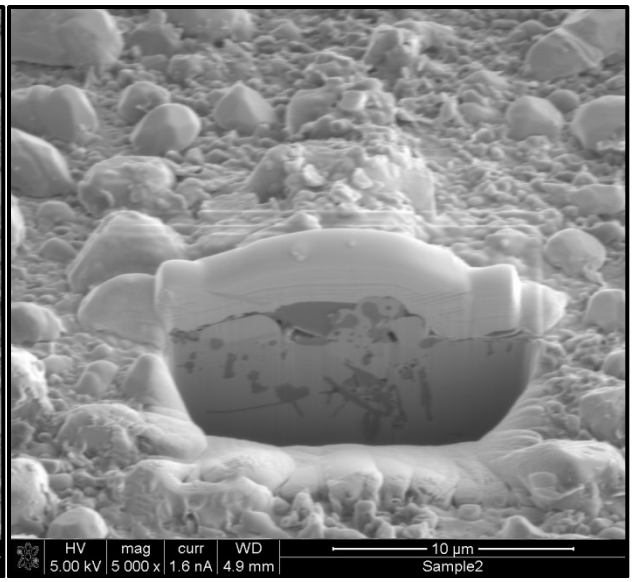
HV
5.00 kV
mag
5 000 x
curr
1.6 nA
WD
4.9 mm
10 µm
Sample2

b)

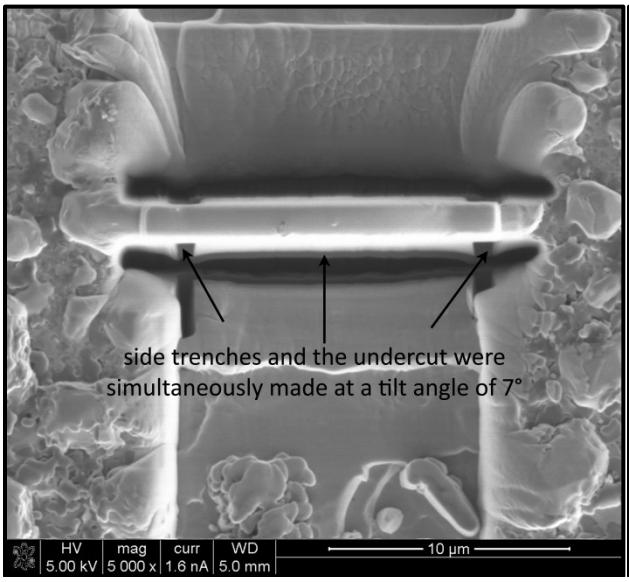
side trenches and the undercut were simultaneously made at a tilt angle of 7°
HV
5.00 kV
mag
5 000 x
curr
1.6 nA
WD
5.0 mm
10 µm

c)

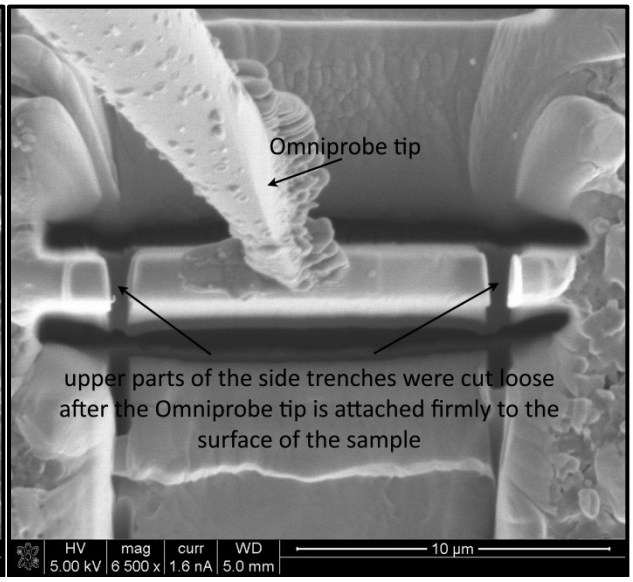
Omniprobe tip
upper parts of the side trenches were cut loose after the Omniprobe tip is attached firmly to the surface of the sample
HV
5.00 kV
mag
6 500 x
curr
1.6 nA
WD
5.0 mm
10 µm

d)

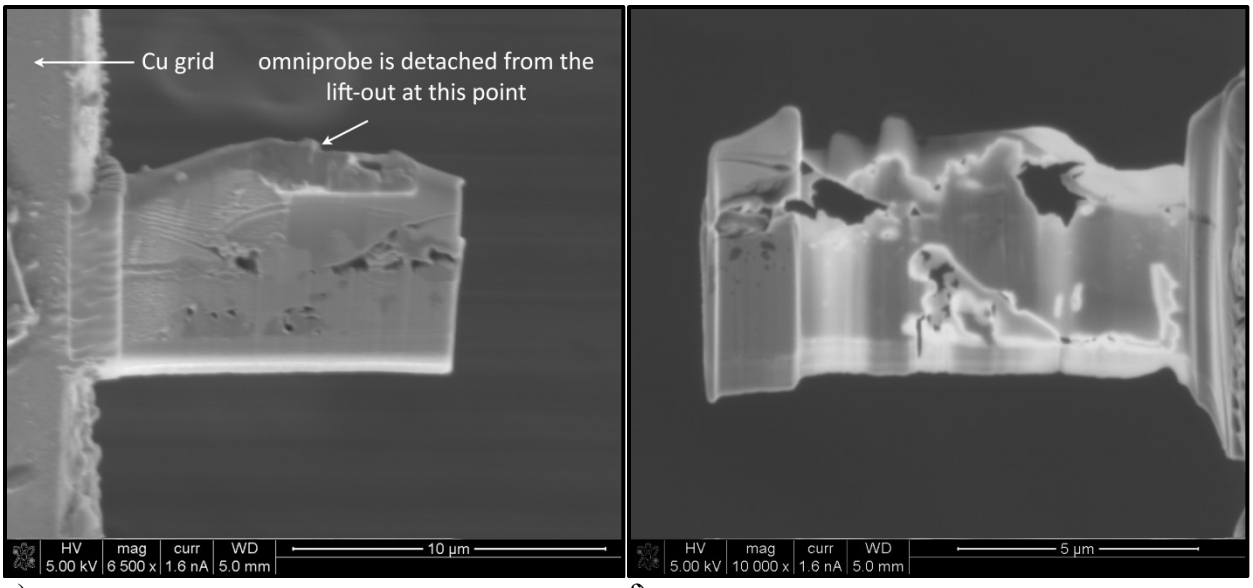

e) f)

Figure 3.24 The summary of the in-situ FIB lift-out procedure followed to prepare cross-sectional TEM samples: a) step 1: find the region of interest in BSE imaging mode using the through lens detector (TLD), b) step 2: deposit platinum over the surface of interest and make the trenches at the back and front sides of the platinum deposit, c) step 3: Suspend the lift-out sample by simultaneously making two side cuts and one undercut, d) step 4: Attach the Omniprobe tip and cut loose the lift-out sample, e) step5: Weld the sample to the TEM grid, f) Step 6: Thin the lift-out sample by both milling the front and back surfaces until the sample becomes electron transparent.

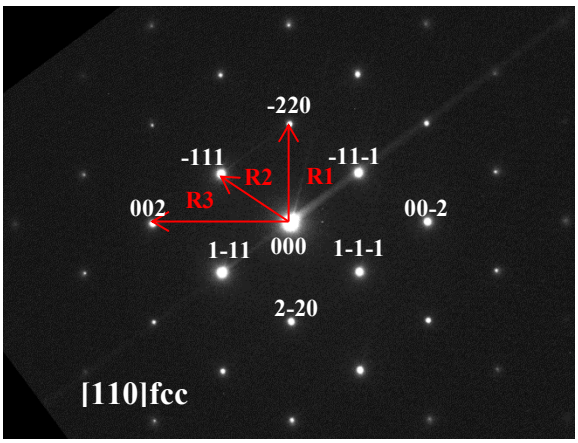

a)

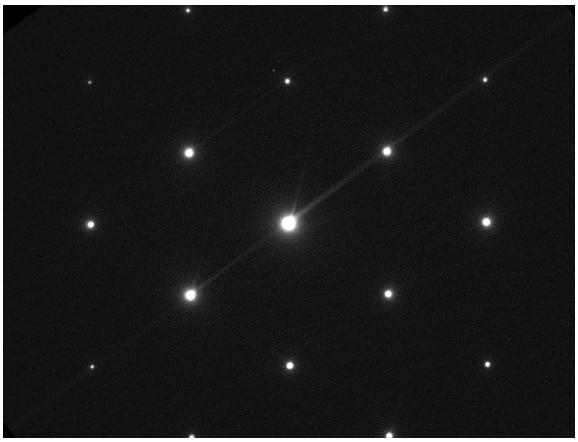

b)

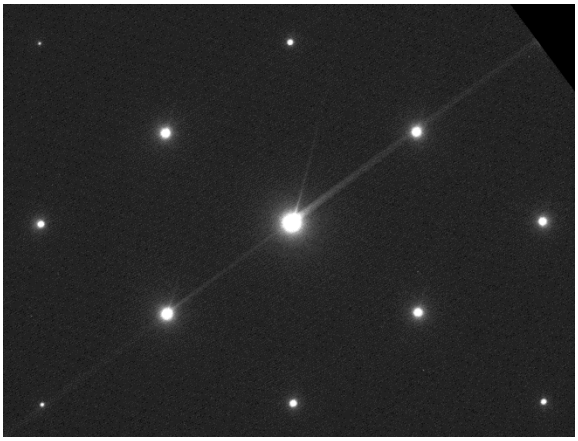

c)

Figure 3.25 Electron diffraction patterns of pure Si taken at camera lengths of a) 30 cm, b) 40 cm, c) 50cm. Number of pixels in each image are kept the same.

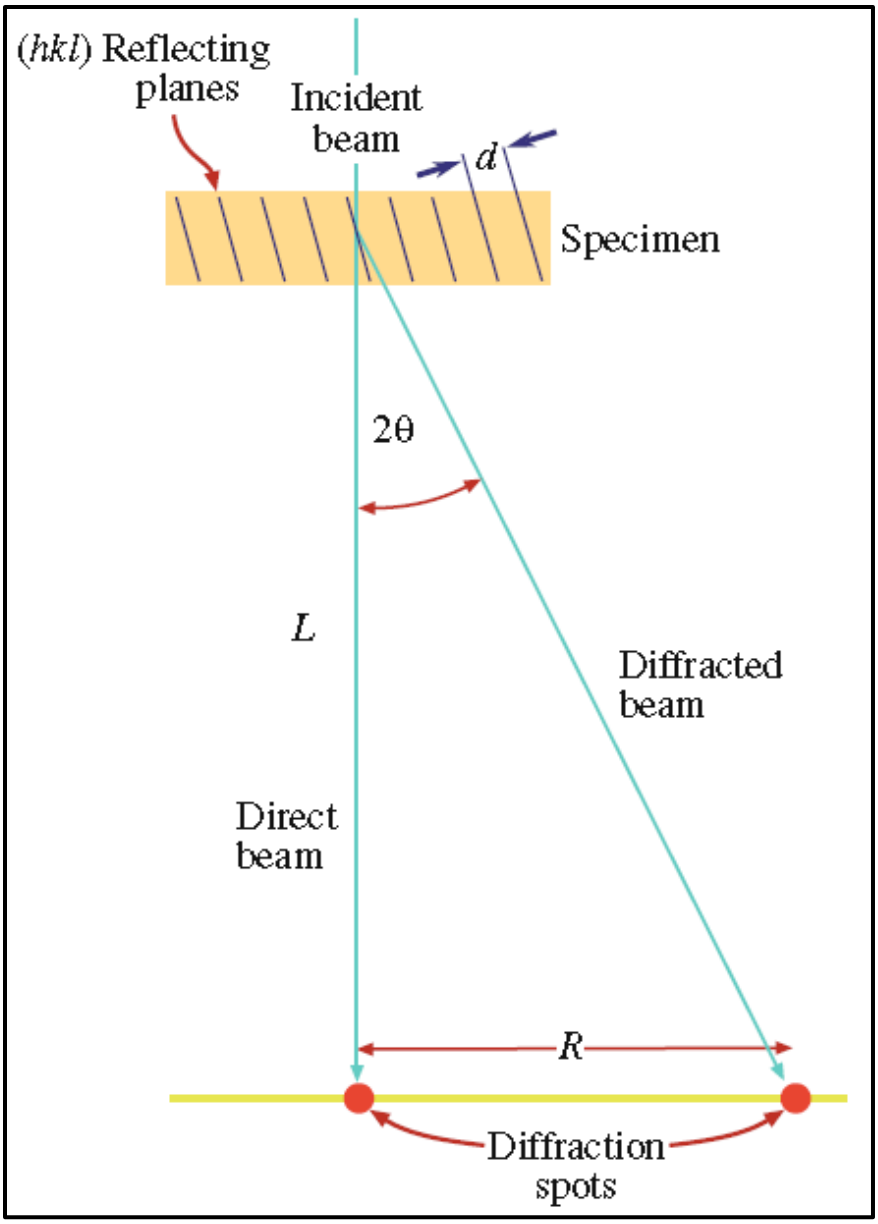

Figure 3.26 The spacing between the transmitted beam and the diffraction spot is related to the camera length, *L* [96].

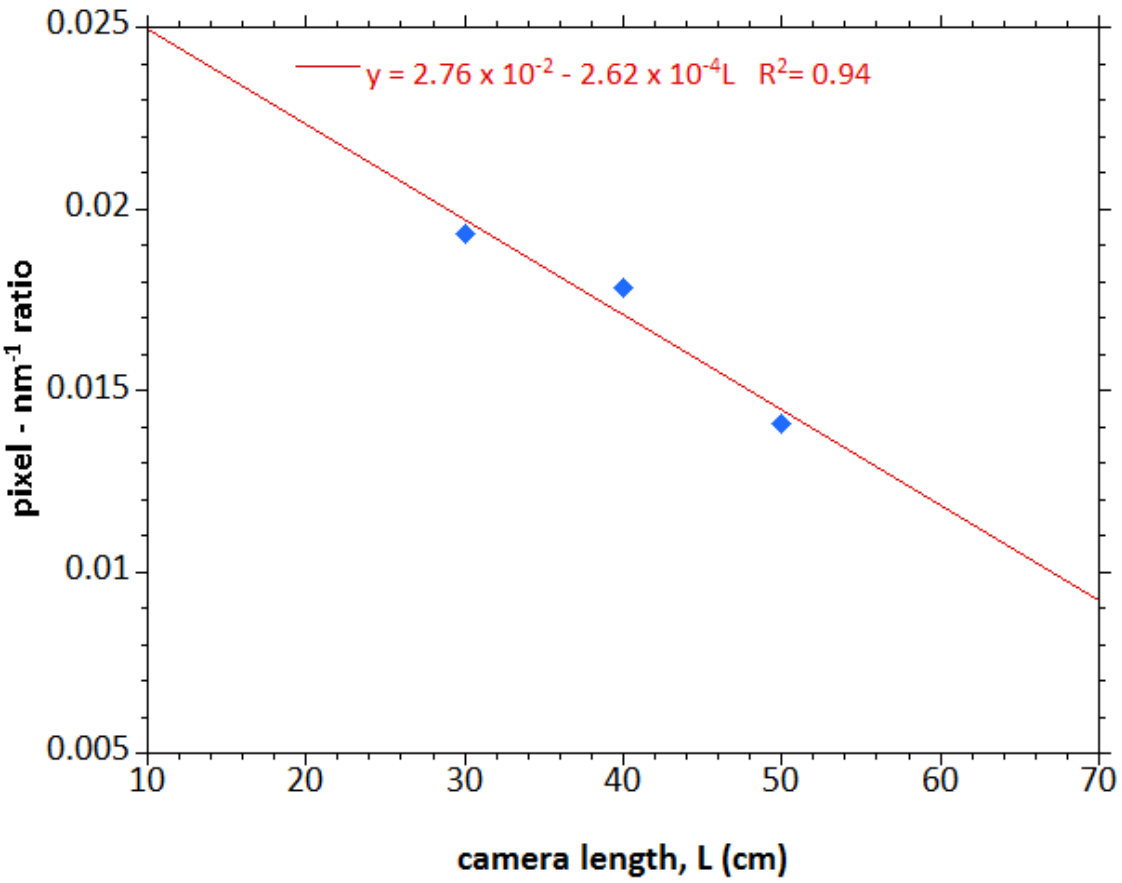

Figure 3.27 *Pixel-to-nm*$^{-1}$ ratio calibration as a function of the camera length.

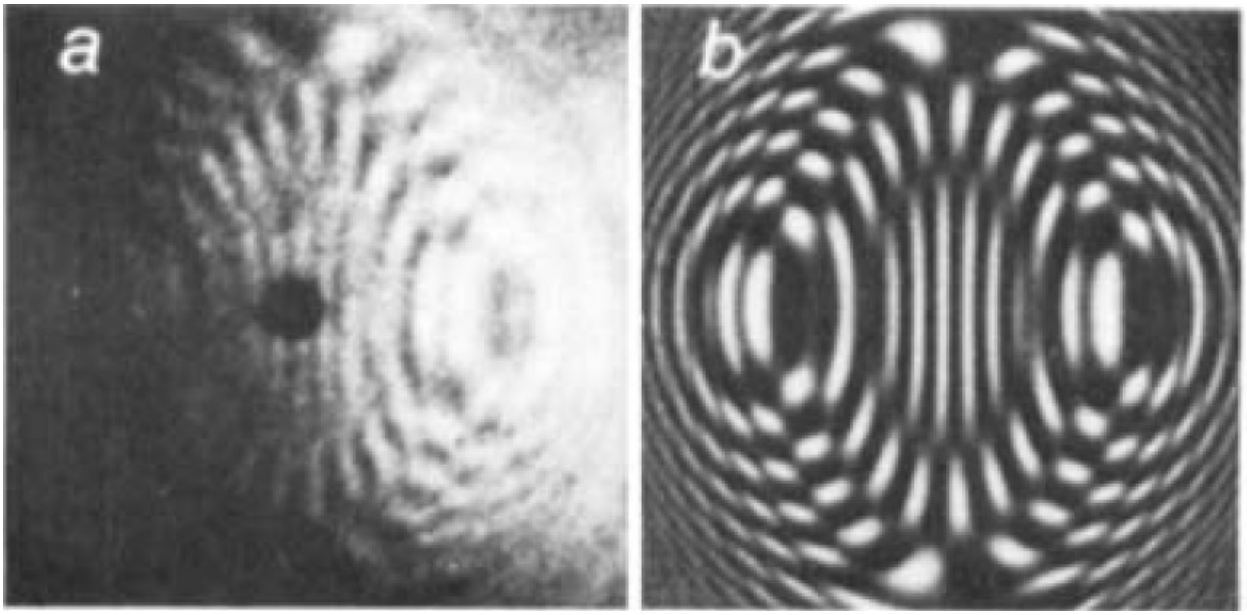

a) b)

Figure 3.28 a) Electron Ronchigram obtained from the (100) lattice planes (d = 8Å) of a thin beryllium crystal. b) Computed Ronchigram for C_s = 0.8mm and defocus = -4500Å [99].

CHAPTER 4

RESULTS

This chapter presents the results of the exposures conducted in the Cr-Cr_2O_3 Rhines pack and the He-CO-CO_2 environments in two parts. The first part summarizes the weight gain kinetics, microstructure characterization and internal Al oxidation kinetics of the IN617 samples oxidized in the Cr-Cr_2O_3 Rhines pack at 850 °C.

In the second part, an analysis of the He-CO-CO_2 compositions at the inlet and outlet of each quartz tube are presented. Next, the weight gain kinetics of the IN617 samples oxidized in Env. 9 and Env. 1320 in the temperature range of 750 - 850 °C are presented. These results are compared with the weight gains measured in a Nicofer 5520Co sample oxidized in Env. 1320 at 850 °C and that in IN617 samples oxidized in the Cr-Cr_2O_3 Rhines pack at 850 °C. After presenting the weight gain results, microstructure characterization of the samples exposed to the He-CO-CO_2 environments are presented to elucidate the effects of temperature, environment, exposure time and heat-to-heat variation on surface and internal oxidation. This chapter is concluded by presenting the surface and internal oxidation kinetics of the samples oxidized in H-CO-CO_2 environments in the temperature range of 750 - 850 °C.

4.1. Oxidation kinetics of IN617 Rhines packs at 850 °C

4.1.1. Weight gain kinetics

Figure 4.1 shows the weight gain of IN617 samples oxidized in the Cr - Cr_2O_3 Rhines pack as a function of exposure time. The error bars associated with each data point are calculated from Equation (3.20) and the specific weight gain measurements corresponding to each exposure time are summarized in Table 4.1. The weight gain rate constants, k_W, and the time exponents, n, were obtained from a linear regression fit of the logarithm of the specific weight gain values with respect to the logarithm of the exposure times, as follows:

$$\log \Delta W/A = \log k_W + n \times \log t. \quad (4.1)$$

The values of k_W and n were determined as 2.58×10^{-5} mg/mm^2-h and 0.57, respectively. The value of *n* indicated that the IN617 samples oxidized in the Cr - Cr_2O_3 Rhines packs exhibited near parabolic weight gain kinetics at 850 °C.

4.1.2. Microstructure characterization

Figures 4.2a-d and 4.3a-d show the representative microstructures of the surfaces and cross-sections of the IN617 samples oxidized in the Cr - Cr_2O_3 Rhines pack for 150, 500, 750 and 1000 h. The microstructures revealed severe penetration of internal Al_2O_3 precipitates, especially along the grain boundaries, which were also decorated with carbides beneath the internal oxidation zone. Carbide precipitates were also present in the bulk of the alloy. In addition, protrusions were observed on the surface of the samples. Formation of such surface features on the Ni-Al and Ni-Al-Si alloys oxidized in the Ni-NiO Rhines packs in the temperature range of 800-1000°C was previously reported by Yi et al. [100]. Their appearance was attributed to the outward transport of nickel by the Nabarro-Herring mechanism or by the pipe diffusion along the dislocations to accommodate the high level of stresses induced in the

base metal due to large volume expansion associated with the precipitation of internal oxides. Even though the evidence in the literature suggests that the exposures in the Rhines packs result in formation of metallic surface protrusions, XRD, Raman spectroscopy, TEM and XPS were employed to establish that the protrusions observed in this study were not associated with formation of a surface oxide phase.

Figure 4.4 shows grazing incidence angle XRD diffraction patterns ($\theta = 1.5°$) of the two IN617 samples exposed in Cr-Cr_2O_3 Rhines packs for 750 and 1000h at 850 °C. The XRD analysis revealed only the base metal peaks and showed no indication of Cr_2O_3 presence on the surfaces of both samples.

Figure 4.5 shows the Raman spectra obtained from an IN617 sample exposed in the Cr-Cr_2O_3 Rhines pack at 850 °C for 1000h, an as-polished IN617 sample and another IN617 sample exposed to Env. 9 at 850 °C for 375h using Renishaw inVia Raman microscope equipped with a 633nm He-Ne laser and a confocal objective lens with magnification X100. The sample oxidized in Env. 9 showed distinct Cr_2O_3 peaks at locations reported by Farrow et al. [101]. Raman spectroscopy did not reveal Cr_2O_3 formation on the surface of the IN617 sample oxidized in the Cr-Cr_2O_3 Rhines pack.

Figure 4.6a shows a more magnified microstructure of an IN617 sample exposed in the Cr-Cr_2O_3 Rhines pack sample at 850 °C for 1000 h, which further reveals the extent of surface rumpling and internal Al_2O_3 penetration. A cross-section TEM sample was prepared by in-situ FIB liftout technique and a bright field image was obtained as shown in Figure 4.6b. Selected area electron diffraction (SAED) patterns recorded from the surface protrusion, the protrusion-base metal interface and the base metal indicated that each feature had identical face-centered-cubic crystal structure (Figures. 4.7a-c). The lattice parameters calculated from each pattern

using Equation (3.12) were in the range of 0.363 - 0.364 nm, which was slightly larger than that of pure nickel (0.352 nm). This could be attributed to the presence of Cr, Mo and Co in the solid solution of γ-Ni in Alloy 617, which can increase the lattice parameter of pure γ-Ni from 0.352 nm up to 0.360 nm according to the X-ray diffraction studies conducted by Mishima et al. [102]. Therefore, the SAED patterns confirmed that the surface protrusions are metallic in content with an FCC crystal structure and lattice parameter similar to that of the alloy matrix.

An electron diffraction pattern was also recorded from the internal Al_2O_3, as shown in Figure 4.7d. Comparison of this diffraction pattern with the single crystal electron diffraction patterns computed for Al_2O_3 by Lee and Lagerlof [103] indicated that the internal oxide was α-Al_2O_3 with a hexagonal unit cell structure. Hexagonal unit cell parameters can be calculated according to the following equation:

$$d_{hkl} = \sqrt{(4/3a^2(h^2 + hk + k^2) + l^2/c^2)^{-1}}. \quad (4.2)$$

From Equation (4.2), the basal (a) and height lattice parameters (c) were calculated as 0.463 nm and 1.320 nm, respectively.

As a final attempt, a surface sensitive XPS technique was employed to investigate the very near surface chemistry of the Rhines pack sample. XPS spectra, shown in Figure 4.8, revealed peaks associated with both pure Cr and Cr_2O_3 phases after applying the peak identification and fitting procedure described in Section 3.4.5. The co-existence of both Cr_2O_3 and pure Cr peaks indicated that the thickness of Cr_2O_3 on the Rhines pack sample was less than the depth resolution of XPS, which is approximately equal to three times of the inelastic mean free path of Cr photoelectrons. Following Strohmeier's [104] methodology, the thickness of Cr_2O_3 was estimated using the following equation:

$$t_{Cr_2O_3} = \lambda_{Cr_2O_3} \times sin\theta \times ln\left[(\rho_{Cr}^{Cr} \times \lambda_{Cr} \times I_{Cr})/\left(\rho_{Cr}^{Cr_2O_3} \times \lambda_{Cr_2O_3} \times I_{Cr_2O_3}\right) + 1\right], \quad (4.3)$$

where λ_{Cr} and $\lambda_{Cr_2O_3}$ are the inelastic mean free paths of Cr photoelectrons in Cr and Cr_2O_3, respectively; θ is the photoelectron takeoff angle with respect to the sample surface; ρ_{Cr}^{Cr} and $\rho_{Cr}^{Cr_2O_3}$ are the volume densities of Cr atoms in pure Cr and Cr_2O_3, respectively; and finally, I_{Cr} and $I_{Cr_2O_3}$ are the total areas of Cr and Cr_2O_3 peaks, respectively. λ_{Cr} and $\lambda_{Cr_2O_3}$ were calculated based on the TPP model established by Tanuma et al. [105] as 1.15nm and 1.31nm, respectively. After substituting all the values in to Equation (4.3), $t_{Cr_2O_3}$ was estimated as 1.27nm. Therefore, the Cr_2O_3 film on the surface of the sample oxidized in the Cr - Cr_2O_3 Rhines pack detected by XPS was likely to be a native oxide, formed after removing the sample from the quartz capsule.

XRD, Raman spectroscopy, TEM and XPS analyses verified that the samples oxidized in the Cr - Cr_2O_3 Rhines pack exhibited only internal Al oxidation at an ambient oxygen activity equal to the dissociation oxygen partial pressure of Cr_2O_3. The next section reports on the internal oxidation kinetics of IN617 oxidized in the Cr - Cr_2O_3 Rhines pack using measurements of the internal Al_2O_3 penetration depths with time.

4.1.3. Internal oxidation kinetics

Figure 4.9 shows the intergranular and transgranular Al_2O_3 penetration depth measurements as a function of exposure time in IN617 samples oxidized in the Cr - Cr_2O_3 Rhines pack at 850°C. The data is plotted according to Equation (2.102) and the error bars are equal to $\sqrt{2}\sigma$, where σ is the standard deviation of as many as 157 depth measurements taken from each sample. The statistics of the measured depths of intergranular and transgranular Al_2O_3 penetrations at each exposure time are also summarized in Table 4.2.

The intergranular and transgranular oxidation rate constants $k_I^{Al_2O_3}(RP)$ and $k_T^{Al_2O_3}(RP)$, determined by simple linear regression fit of the Al_2O_3 penetration depth data, were summarized in Table 4.3. The magnitude of $k_I^{Al_2O_3}(RP)$ was approximately 10 times that of

$k_T^{Al_2O_3}(RP)$, supporting the microstructure observations, which indicated that the internal Al oxidation preferentially occurred along the grain boundaries.

Internal oxidation kinetics of IN617 oxidized in the Cr - Cr_2O_3 Rhines pack will be further assessed in Chapter 5 to determine D_O^{617} using the analysis presented in Section 2.5.1.

4.2. Oxidation kinetics of IN617 in He-CO-CO_2 at 750 - 850 °C

4.2.1. GC results

CO and CO_2 concentrations at the inlet and outlet of each tube were closely monitored using the DIDGC during each He-CO-CO_2 exposure conducted in the temperature range of 750-850°C. The average inlet concentrations established during each exposure are summarized in Table 4.4. The differences in the inlet and outlet CO_2 and CO concentrations during the oxidation of the samples in both Env. 9 and Env. 1320 at each temperature are shown in Figures 4.10 and 4.11, respectively. To provide a long term summary of environment-alloy interactions, only the data obtained from the 500h exposures are included in the figures. The error bars shown on these plots correspond to the standard deviation of the average steady-state difference measured between the outlet and inlet CO and CO_2 concentrations, due to the interactions of the quartz tubes with Env. 9 and Env. 1320 at each temperature (refer to Section 3.2.5.2). Exposures to Env. 1320 generally exhibited greater scatter in the CO and CO_2 consumption data than that observed in Env. 9. Oxidation of IN617 in Env. 1320 at 800 and 850°C resulted in evolution of CO_2, which was probably an artifact of the CO_2 desorption observed in the empty quartz tubes interacting with Env. 1320, as shown in Figure 3.10a in Chapter 3.

Overall, the change in the CO and CO_2 concentrations due to the reactions with the samples oxidized in both environments at each temperature remained below the detection limit of the DIDGC. This could possibly be attributed to the presence of only one sample in each

quartz tube; therefore the alloy-environment interaction volume, in which significant changes in the outlet CO and CO_2 concentrations occurred, was very small. Therefore, the selected flow rate was sufficiently high to maintain steady state CO and CO_2 concentrations in the tubes during exposure of samples to Env. 9 and Env. 1320.

4.2.2. Weight gain kinetics

Figure 4.12 shows the logarithm of the weight gains measured as a function of exposure time in samples oxidized in Env. 9 and Env. 1320 at temperatures 750 - 850°C in comparison with those did in samples exposed to Cr-Cr_2O_3 Rhines packs at 850°C. The specific weight gain values corresponding to each exposure time in Env. 9 and Env. 1320 are summarized in Tables 4.6 and 4.7, respectively. Table 4.8 shows the values of k_W and n determined from the linear regression fit according to the Equation (4.1).

Weight gains measured in both Env. 9 and Env. 1320 increased with the exposure time and temperature. Based on the values of n, samples exposed to Env. 1320 exhibited parabolic-like weight gain kinetics; whereas samples exposed to Env. 9 showed noticeable deviations from parabolic kinetics in the temperature range of 750-850°C. It appears that the samples oxidized in Env. 9 exhibited lower weight gains than those oxidized in Env. 1320 during the first 150h of exposure at each temperature. This initial 150h period corresponds to a transient oxidation regime in He-CO-CO_2 environments, during which the oxidation kinetics are sensitive to the environment composition.

The effect of heat-to-heat variation on the oxidation kinetics of Alloy 617 was also investigated by oxidizing a sample of Nicofer 5520Co in Env. 1320 at 850°C for 225 h and comparing the measured weight gain with that of an IN617 sample oxidized in the same

conditions. IN617 and Nicofer 5520Co samples exhibited almost identical weight gains, which indicated that the effect of heat-to-heat variation was negligible.

Finally, IN617 samples exposed to Env. 9 and Env. 1320 exhibited greater weight gains than those oxidized in the Cr-Cr_2O_3 Rhines pack at 850°C. Given that the time exponents for the Rhines pack and Env. 1320 exposures are identical; the weight gain rate constants measured in both environments can be compared directly. The results showed that the rate constant measured in Env. 1320 was 5 times faster than that did in the Cr-Cr_2O_3 Rhines pack at 850°C.

Weight gain measurements reflected the combined contributions of surface and internal oxidation, as well as possible carburization of IN617 in He-CO-CO_2 environments. Therefore, it is necessary to distinguish the kinetics of surface oxidation from the internal oxidation kinetics established in Env. 9 and Env. 1320 in the temperature range of 750 - 850°C by characterizing the cross-sections of each sample exposed to both environments.

4.2.3. Microstructure characterization

The SEM characterization of the cross-sections of IN617 samples exposed to Env. 9 and Env. 1320 in the temperature range of 750 - 850 °C served two fundamental purposes. First, the corrosion features developed in each environment-temperature combination were identified to verify that the He-CO-CO_2 environments mimicked the degradation modes in the IHX helium. Second, the characteristic dimensions of the surface and internal oxides formed in each sample were measured as a function of time to determine separately, the surface and internal oxidation kinetics of IN617 in the He-CO-CO_2 environments at temperatures 750 - 850 °C.

Figure 4.13a and b show the representative microstructures of the samples exposed to Env. 9 and Env. 1320 at 850 °C for 500h that captured all the corrosion features encountered in He-CO-CO_2 environments in the temperature range of 750 - 850 °C. Both samples exhibited

formation of surface Cr_2O_3, intergranular and transgranular Al_2O_3 and carbide denuded zone in the subsurface regions. In addition, the sample oxidized in Env.1320 for 500h exhibited formation of discrete surface particulates embedded in the Cr_2O_3 film, which were identified as Cr_7C_3 precipitates in a previous work [16,38] (Figure 4.13b).

Figure 4.14 shows a more magnified image and EDX maps of the cross-section of the sample oxidized in Env. 1320 at 850°C for 500h. The elemental maps clearly distinguished the intergranular and transgranular Al_2O_3 from the surface Cr_2O_3 film. In addition, two different types of metallic nodules (M1, M2) and the M_7C_3 type surface carbide (C3) were revealed in the Cr_2O_3 film. M2 type nodule and C3 type carbide were distinguished from each other and from the Cr_2O_3 film using the Cr and O elemental maps as well as the Z contrast achieved in the backscatter electron imaging mode. Nodules designated as M1 were rich in Ni, Co and Mo. M2 type nodules were rich in Cr and probably formed by Cr transport out of the grain boundaries above the original alloy interface. Formation of these nodules is most likely associated with the internal oxidation of the alloy and driven by a mechanism similar to the formation of the protrusions on the surface of the sample oxidized in the Cr-Cr_2O_3 Rhines pack. C3 type carbides were revealed as an extra bright region in the Cr elemental map. Furthermore, the Mo-rich M_6C type carbides (C2) were clearly distinguished from the Cr-rich $M_{23}C_6$ type carbides (C1) by comparing the Cr and Mo elemental maps.

Figures 4.15 and 4.16 show the microstructures of the IN617 samples oxidized in Env. 9 and Env. 1320, respectively, at 850 °C. The samples oxidized in Env. 9 formed surface Cr_2O_3 film of thickness 0.82 ± 0.21 μm after 75 h of exposure, which gradually increased to 1.69 ± 0.26 μm and 2.56 ± 0.26 μm after 375 h and 500 h, respectively (Table 4.9). Cr_2O_3 film formed in Env. 9 was continuous but highly non-uniform especially during the first 225 h of exposure.

Surface Cr_2O_3 was noticeably thicker over the grain boundaries above the original alloy interface compared to that over the grains. This could be attributed to the faster outward transport of Cr along the alloy grain boundaries, which caused the non-uniformity of the Cr_2O_3 film. The samples oxidized in Env. 1320; however exhibited thicker and more uniform surface Cr_2O_3 film than did the samples exposed to Env. 9 during the first 225h of exposure. The thickness of the surface Cr_2O_3 film on the sample oxidized in Env. 1320 was 0.93 ± 0.21 μm after 75h. The thickness of the film increased to 2.09 ± 0.20 μm after 375h of oxidation; however it dropped to 1.63 ± 0.16 μm after 500h of exposure (Table 4.10). This discrepancy was primarily attributed to the formation of discrete, irregular shaped surface carbides, as can be seen from Figures 4.13b and 4.14. The area fractions of these carbides were excluded from that of the surface Cr_2O_3 film to determine the average Cr_2O_3 film thickness according to the procedure described in Section 3.4.2. Kumar [16,38] observed that these precipitates formed over the surface Cr_2O_3 film and grew to a significant volume fraction during the first few hundred hours of exposure before dissolving over longer exposure times at 900°C. The dissolution of these carbides created large scale voids in the continuously growing surface Cr_2O_3 film, possibly distorting its integrity and resulting in spallation.

Table 4.9 shows that the penetration depth of Al_2O_3 along the grain boundaries of the sample oxidized in Env. 9 at 850°C was 3.53 ± 0.95 μm after 75 h of exposure, which gradually increased to 13.21 ± 2.80 μm after 500h of exposure. The average depth of the transgranular Al_2O_3 precipitates was 1.16 ± 0.40 μm after 75 h of oxidation, which extended to 4.20 ± 0.70 μm after 500h of exposure. As can be seen in Table 4.10, The average depth of the intergranular Al_2O_3 precipitates after 75 h exposure to Env. 1320 was 5.15 ± 1.13 μm, which extended further deeper to 11.18 ± 2.52 μm after 500 h of exposure. The average depths of the transgranular

Al_2O_3 precipitates measured in these samples were less than that of the intergranular Al_2O_3 precipitates and were in the range of 1.04 ± 0.54 - 3.58 ± 1.04 μm over 75 h - 500 h long exposure (Table 4.10).

Figure 4.17 compares the microstructures of Nicrofer 5520Co and IN617 samples oxidized in Env. 1320 at 850°C, for 225h. Both heats of Alloy 617 exhibited identical corrosion features despite the slight differences in their chemistry (Tables 3.1 and 3.2) and as-received microstructures (Figures 3.1 and 3.2). The average surface Cr_2O_3 thickness, intergranular Al_2O_3 and transgranular Al_2O_3 penetration depths measured in the Nicrofer 5520Co sample were 1.53 ± 0.23 μm, 7.46 ± 1.74 μm and 2.15 ± 0.80 μm, respectively. These measurements were very similar to those summarized in Table 4.10 for the IN617 sample. Thus, heat-to-heat variation is not significant enough to influence the oxidation of Alloy 617 in Env. 1320 at 850°C.

Figure 4.18 summarizes the microstructures of the IN617 samples oxidized in Env. 9 and Env. 1320 in the temperature range of 750 - 850 °C for 375 h. The thickness of the surface Cr_2O_3 film and the depth of the internal Al_2O_3 precipitates decrease with decreasing temperature in both environments. This is expected as both surface and internal oxidation are thermally-activated and diffusion-controlled processes. The microstructures showed that as the exposure temperature decreases, the Al_2O_3 penetration along the grain boundaries becomes more prominent than that within the grains. This suggests that the short-circuit diffusion processes governing the internal oxidation of IN617 become more dominant at lower temperatures.

Section 4.2.4 reports on the surface and internal oxidation kinetics of IN617 samples oxidized in Env. 9 and Env. 1320 in the temperature range of 750 - 850 °C based on the surface Cr_2O_3 thickness, intergranular and transgranular Al_2O_3 depth measurements summarized in Tables 4.9 - 4.14.

4.2.4. Surface and internal oxidation kinetics

Figure 4.19 shows the parabolic plots of the surface chromium oxide thickness measured as a function of exposure time on IN617 samples exposed to Env. 9 and Env. 1320, in the temperature range of 750 - 850 °C. The error bars assigned to each data point are equal to √2σ, where σ is the standard deviation of the Cr_2O_3 thickness measurements summarized in Tables 4.9 - 4.14. Table 4.15 shows the parabolic surface Cr oxidation rate constants, $k_S^{Cr_2O_3}$, in each environment and at each temperature determined from the slopes of the linear regression lines shown in Figure 4.19. Only 500 h exposure data obtained from the samples oxidized in Env. 9 and Env. 1320 at 850 °C were excluded from the linear regression fit due to their significant deviations from the general trends of the previous data points. The reason for the discrepancy in the data measured in Env. 1320 was explained in the previous section; however the sudden increase in the surface Cr_2O_3 thickness of the sample oxidized in Env. 9 for 500 h remained unclear.

The $k_S^{Cr_2O_3}$ values determined from the linear regression analysis revealed the temperature and environment dependence of the IN617 surface oxidation kinetics. The rate of surface Cr oxidation at 850 °C was almost 10 times that measured at 750 °C. In addition, the surface oxidation rate constant in Env. 1320 was slightly greater than that in Env. 9 at 850 °C; however this trend was reversed in exposures at lower temperatures. In general, $k_S^{Cr_2O_3}$ values determined in both environments were very similar at each temperature, which indicated that the IN617 surface oxidation kinetics was independent of the He-CO-CO_2 composition.

Figures 4.20 and 4.21 show the parabolic plots of the intergranular and transgranular Al oxide penetration depths measured in IN617 samples exposed in Env. 9 and Env. 1320 at 750 - 850 °C, in comparison with those did in the samples oxidized in Cr-Cr_2O_3 Rhines packs at

850°C. The error bars are equal to √2σ, where σ is the standard deviation of the intergranular and transgranular penetration depth measurements summarized in Table 4.2 for the Rhines pack exposure and in Tables 4.9 - 4.14 for the He-CO-CO_2 exposures. Table 4.15 summarizes the rate constants for intergranular oxidation, $k_I^{Al_2O_3}$, and transgranular oxidation, $k_T^{Al_2O_3}$, of the samples oxidized in Env. 9 and Env. 1320.

In general, the values of $k_I^{Al_2O_3}$ and $k_T^{Al_2O_3}$ measured in both Env. 9 and Env. 1320 are very similar at each exposure temperature. The observed differences in the measurements are not statistically significant to account for a possible dependence of the IN617 internal oxidation kinetics on the He-CO-CO_2 composition at a given temperature. On the other hand, both intergranular and transgranular oxidation kinetics of IN617 measured in the He-CO-CO_2 environments exhibited strong temperature dependence, as expected. The rate of internal Al oxidation along the grain boundaries at 850°C was 10 times greater than that measured at 750 °C; whereas the rate of transgranular oxidation was almost a factor of 40 lower at 750 °C than that at 850°C. This greater drop in the rate of transgranular oxidation with decreasing temperature revealed that grain boundary diffusion becomes more important at lower temperatures. Furthermore, the $k_I^{Al_2O_3}/k_T^{Al_2O_3}$ ratio increased from 10 to 36 when the exposure temperature decreased from 850 °C to 750 °C. This also confirmed the microstructure observations that internal Al oxidation occurs preferentially along the grain boundaries at any given temperature and grain boundary diffusion becomes more important at lower temperatures.

The severity of the intergranular Al oxidation kinetics becomes more apparent when the values of $k_I^{Al_2O_3}$ are compared to those of $k_S^{Cr_2O_3}$ in each environment. The value of $k_I^{Al_2O_3}$ was as high as 40 times that of $k_S^{Cr_2O_3}$ at 850°C. Extrapolation of the fastest surface and intergranular oxidation kinetics measured at 850°C ($k_S^{Cr_2O_3}$*(Env. 1320)* = 1.53 × 10^{-14} cm^2/s and $k_I^{Al_2O_3}$*(Env. 9)*

= 3.94 × 10^{-13} cm^2/s), to the expected service lifetime of the intermediate heat exchanger (~60 years) calls for formation of surface Cr_2O_3 layer in thickness 76.1 μm and penetration of Al_2O_3 precipitates to a depth of 386.3 μm along the grain boundaries of IN617.

Finally, the measured rates of intergranular Al oxidation in Env. 9 and Env. 1320 were 8 times as high as that measured in the Cr-Cr_2O_3 Rhines pack at 850°C. Similarly, transgranular Al oxidation kinetics in the He-CO-CO_2 environments were approximately 7 times faster than those in the Cr-Cr_2O_3 Rhines pack. The causes of increased oxidation rate in He-CO-CO_2 environments will be examined in Chapter 5.

Table 4.1 Specific weight gains of the Rhines Pack samples exposed to 850 °C.

Exposure time (h)	$\Delta W/A$ **(×10^{-3} mg/mm^2)**
150	0.47 ± 0.07
500	0.76 ± 0.05
750	1.07 ± 0.05
1000	1.50 ± 0.05

Table 4.2 Statistics of the depths of intergranular and transgranular Al_2O_3 penetrations measured in Rhines pack samples at 850 °C.

Rhines Packs, 850°C	**intergranular Al_2O_3 depth**				**transgranular Al_2O_3 depth**			
Exposure time (h)	150	500	750	1000	150	500	750	1000
# of measurements[4]	66	116	104	64	88	157	76	34
Max. value (µm)	4.76	6.53	8.02	9.76	1.61	1.81	2.77	3.24
Min value (µm)	2.17	2.56	3.21	3.62	0.64	0.58	1.23	1.30
Mean value (µm)	**3.70**	**4.23**	**5.16**	**6.01**	**0.97**	**1.22**	**1.82**	**2.08**
Standard Dev. (µm)	**0.58**	**0.86**	**0.96**	**1.32**	**0.21**	**0.23**	**0.32**	**0.43**

Table 4.3 The intergranular and transgranular Al oxidation rate constants obtained from the linear regression fits of the internal oxidation kinetics data presented in Figure 4.7.

	$k_I^{Al_2O_3}$ **(cm^2/s)**	$k_I^{Al_2O_3}$ **(cm^2/s)**
Rhines Pack	5.08×10^{-14}	5.83×10^{-15}

[4] The number of measurements taken at each exposure time does not necessarily represent the number density of the associated Al_2O_3 penetrations.

Table 4.4 Inlet CO and CO_2 concentrations established during exposures to Env. 9 at temperatures 750 - 850 °C.

Exposure time (h)	**Environment**			**Alloy**	**Temperature (°C)**	**Flow Rate (ml/min)**
	P_{CO} (molppm)	P_{CO_2}(molppm)	P_{CO}/P_{CO_2} ratio			
25	13.4 ± 0.3	1.2 ± 0.1	11.2 ± 1.0	IN617	850	200 ± 5
25	12.8 ± 0.5	1.2 ± 0.1	10.7 ± 1.0	IN617	850	200 ± 5
25	12.9 ± 0.3	1.2 ± 0.1	10.8 ± 0.4	IN617	850	200 ± 5
25	13.0 ± 0.7	1.2 ± 0.1	10.8 ± 1.1	IN617	850	200 ± 5
75	13.6 ± 0.6	1.2 ± 0.1	11.3 ± 1.1	IN617	850	200 ± 5
150	13.6 ± 0.4	1.3 ± 0.1	10.5 ± 0.9	IN617	850	200 ± 5
225	13.7 ± 0.6	1.3 ± 0.1	10.5 ± 0.9	IN617	850	200 ± 5
375	13.7 ± 0.6	1.3 ± 0.1	10.5 ± 0.9	IN617	850	200 ± 5
500	13.5 ± 0.4	1.3 ± 0.1	10.4 ± 0.7	IN617	850	200 ± 5
25	13.7 ± 0.3	1.4 ± 0.1	9.8 ± 0.4	IN617	800	200 ± 5
75	13.9 ± 0.8	1.8 ± 0.1	7.7 ± 0.5	IN617	800	200 ± 5
150	13.4 ± 0.4	1.3 ± 0.1	10.3 ± 0.4	IN617	800	200 ± 5
225	13.4 ± 0.3	1.3 ± 0.1	10.3 ± 0.3	IN617	800	200 ± 5
375	13.2 ± 0.4	1.4 ± 0.1	9.4 ± 0.5	IN617	800	200 ± 5
500	13.3 ± 0.5	1.4 ± 0.2	9.5 ± 1.1	IN617	800	200 ± 5
25	13.2 ± 0.3	1.8 ± 0.1	7.3 ± 0.2	IN617	750	200 ± 5
75	14.1 ± 0.5	1.5 ± 0.1	9.4 ± 0.5	IN617	750	200 ± 5
150	13.6 ± 0.6	1.6 ± 0.1	8.5 ± 0.5	IN617	750	200 ± 5
225	13.8 ± 0.6	1.6 ± 0.1	8.6 ± 0.6	IN617	750	200 ± 5
375	13.5 ± 0.6	1.4 ± 0.1	9.6 ± 0.5	IN617	750	200 ± 5
500	13.7 ± 0.5	1.4 ± 0.1	9.8 ± 0.6	IN617	750	200 ± 5

Table 4.5 Inlet CO and CO_2 concentrations established during exposures to Env. 1320 at temperatures 750 - 850 °C.

Exposure time (h)	Environment			Alloy	Temperature (°C)	Flow Rate (ml/min)
	P_{CO} (molppm)	P_{CO_2}(molppm)	P_{CO}/P_{CO_2} ratio			
25	1982.9 ± 0.3	1.3 ± 0.1	1525.3 ± 10.0	IN617	850	200 ± 5
75	1981.6 ± 9.3	1.4 ± 0.1	1415.4 ± 53.9	IN617	850	200 ± 5
150	1984.1 ± 13.2	1.3 ± 0.1	1526.2 ± 63.5	IN617	850	200 ± 5
225	1975.4 ± 12.2	1.3 ± 0.1	1519.5 ± 58.9	IN617	850	200 ± 5
225	1982.8 ± 13.3	1.5 ± 0.1	1321.9 ± 38.2	Nicofer 5560 Co	850	200 ± 5
375	1981.0 ± 15.9	1.4 ± 0.1	1415.0 ± 26.4	IN617	850	200 ± 5
500	1983.6 ± 16.8	1.3 ± 0.1	1525.8 ± 49.6	IN617	850	200 ± 5
25	2005.7 ± 5.0	1.8 ± 0.1	1114.3 ± 21.4	IN617	800	200 ± 5
75	1974.6 ± 18.0	1.7 ± 0.1	1161.5 ± 21.0	IN617	800	200 ± 5
150	1980.1 ± 14.7	1.8 ± 0.1	1100.1 ± 30.5	IN617	800	200 ± 5
225	1988.8 ± 16.8	1.8 ± 0.1	1104.9 ± 27.9	IN617	800	200 ± 5
375	1982.2 ± 16.3	1.5 ± 0.1	1321.5 ± 53.1	IN617	800	200 ± 5
500	1981.7 ± 15.9	1.5 ± 0.1	1321.1 ± 90.9	IN617	800	200 ± 5
25	2001.8 ± 10.7	2.0 ± 0.1	1000.9 ± 22.7	IN617	750	200 ± 5
75	1977.7 ± 32.0	1.9 ± 0.1	1040.9 ± 36.7	IN617	750	200 ± 5
150	1972.3 ± 38.8	2.0 ± 0.1	986.2 ± 32.9	IN617	750	200 ± 5
225	1974.2 ± 25.1	1.7 ± 0.1	1161.3 ± 48.1	IN617	750	200 ± 5
375	1973.8 ± 25.0	1.7 ± 0.1	1161.1 ± 42.4	IN617	750	200 ± 5

Table 4.6 Specific weight gains of the samples exposed to Env. 9 at temperatures 750 - 850 °C.

Exposure time (h)	Alloy	Temperature (°C)	$\Delta W/A$ ($\times 10^{-3}$ mg/mm^2)	Error ($\times 10^{-3}$ mg/mm^2)
25	IN617	850	0.45	0.05
25	IN617	850	0.46	0.12
25	IN617	850	0.50	0.11
25	IN617	850	0.47	0.13
75	IN617	850	1.19	0.07
150	IN617	850	2.15	0.05
225	IN617	850	2.57	0.07
375	IN617	850	3.78	0.10
500	IN617	850	5.94	0.07
25	IN617	800	0.31	0.07
75	IN617	800	0.57	0.11
150	IN617	800	1.14	0.10
225	IN617	800	1.21	0.11
375	IN617	800	2.15	0.10
500	IN617	800	2.96	0.07
25	IN617	750	0.26	0.04
75	IN617	750	0.41	0.06
150	IN617	750	0.65	0.12
225	IN617	750	1.02	0.12
375	IN617	750	1.02	0.06
500	IN617	750	1.67	0.08

Table 4.7 Specific weight gains of the samples exposed to Env. 1320 at temperatures 750 - 850 °C.

Exposure time (h)	Alloy	Temperature (°C)	$\Delta W/A$ ($\times 10^{-3}$ mg/mm^2)	Error ($\times 10^{-3}$ mg/mm^2)
25	IN617	850	0.83	0.12
75	IN617	850	1.78	0.07
150	IN617	850	2.11	0.10
225	IN617	850	3.42	0.07
225	Nicofer 5560 Co	850	3.40	0.05
375	IN617	850	5.32	0.12
500	IN617	850	3.82	0.07
25	IN617	800	0.62	0.07
75	IN617	800	1.03	0.09
150	IN617	800	1.16	0.12
225	IN617	800	1.39	0.11
375	IN617	800	2.10	0.05
500	IN617	800	3.03	0.07
25	IN617	750	0.34	0.09
75	IN617	750	0.49	0.09
150	IN617	750	0.68	0.09
225	IN617	750	1.13	0.12
375	IN617	750	1.16	0.12

Table 4.8 Values of k_W and n obtained from the weight gain kinetics data presented in Figure 4.10 for IN617 samples exposed to Env. 9 and Env. 1320 at temperatures 750 - 850 °C.

Environment	Temperature (°C)	k_W (mg/mm^2-h)	n
9	850	3.47×10^{-5}	0.81
	800	2.51×10^{-5}	0.75
	750	3.39×10^{-5}	0.60
1320	850	1.35×10^{-4}	0.58
	800	1.20×10^{-4}	0.48
	750	6.76×10^{-5}	0.49

Table 4.9 Statistics of the surface Cr_2O_3 thickness and internal Al_2O_3 penetration measurements of IN617 samples oxidized in Env. 9 at 850 °C.

Env. 9, 850 °C	**surface Cr_2O_3 thickness**				**intergranular Al_2O_3 depth**				**transgranular Al_2O_3 depth**			
Exposure time (h)	75	225	375	500	75	225	375	500	75	225	375	500
# of measurements	50	90	43	75	108	171	63	61	41	107	55	55
Max. value (µm)	1.32	2.13	2.34	3.00	5.61	14.09	16.27	20.20	2.16	4.66	5.50	7.98
Min value (µm)	0.50	0.28	0.74	2.04	1.36	2.28	4.84	7.50	0.50	0.73	1.32	2.51
Mean value (µm)	**0.82**	**1.31**	**1.69**	**2.56**	**3.53**	**5.85**	**9.05**	**13.21**	**1.16**	**1.92**	**2.86**	**4.20**
Standard Dev. (µm)	**0.21**	**0.39**	**0.26**	**0.26**	**0.95**	**2.11**	**2.29**	**2.80**	**0.40**	**0.86**	**0.82**	**0.70**

Table 4.10 Statistics of the surface Cr_2O_3 thickness and internal Al_2O_3 penetration measurements of IN617 samples oxidized in Env. 1320 at 850 °C.

Env. 1320, 850 °C	**surface Cr_2O_3 thickness**				**intergranular Al_2O_3 depth**				**transgranular Al_2O_3 depth**			
Exposure time (h)	75	225	375	500	75	225	375	500	75	225	375	500
# of measurements	72	57	45	62	109	93	63	45	49	49	105	23
Max. value (µm)	1.24	1.78	2.56	2.01	7.86	12.54	20.47	19.63	2.89	3.22	4.42	5.92
Min value (µm)	0.69	0.91	1.75	1.40	2.96	2.32	4.70	6.72	0.43	0.82	1.22	1.84
Mean value (µm)	**0.93**	**1.46**	**2.09**	**1.63**	**5.15**	**6.91**	**11.42**	**11.18**	**1.04**	**1.88**	**2.67**	**3.58**
Standard Dev. (µm)	**0.11**	**0.15**	**0.20**	**0.16**	**1.13**	**2.31**	**3.10**	**2.52**	**0.54**	**0.56**	**0.74**	**1.04**

Table 4.11 Statistics of the surface Cr_2O_3 thickness and internal Al_2O_3 penetration measurements of IN617 samples oxidized in Env. 9 at 800 °C.

Env. 9, 800 °C	**surface Cr_2O_3 thickness**			**intergranular Al_2O_3 depth**			**transgranular Al_2O_3 depth**		
Exposure time (h)	75	225	500	75	225	500	75	225	500
# of measurements	25	54	44	29	40	56	-	42	41
Max. value (µm)	0.39	1.01	2.00	2.57	7.66	13.81	-	1.40	3.52
Min value (µm)	0.23	0.34	1.03	1.09	1.91	3.02	-	0.38	0.73
Mean value (µm)	**0.30**	**0.57**	**1.55**	**1.69**	**3.34**	**8.10**	**-**	**0.58**	**1.38**
Standard Dev. (µm)	**0.05**	**0.15**	**0.23**	**0.39**	**1.10**	**2.51**	**-**	**0.20**	**0.51**

Table 4.12 Statistics of the surface Cr_2O_3 thickness and internal Al_2O_3 penetration measurements of IN617 samples oxidized in Env. 1320 at 800 °C.

Env. 1320, 800 °C	**surface Cr_2O_3 thickness**			**intergranular Al_2O_3 depth**			**transgranular Al_2O_3 depth**		
Exposure time (h)	75	225	500	75	225	500	75	225	500
# of measurements	59	54	49	34	37	53	18	39	49
Max. value (µm)	0.54	1.15	1.77	2.89	5.14	13.77	0.93	1.32	2.27
Min value (µm)	0.19	0.35	0.96	1.19	1.89	0.00	0.16	0.25	0.80
Mean value (µm)	**0.35**	**0.57**	**1.29**	**2.26**	**3.74**	**8.50**	**0.35**	**0.55**	**1.32**
Standard Dev. (µm)	**0.07**	**0.12**	**0.18**	**0.43**	**0.83**	**3.12**	**0.25**	**0.25**	**0.31**

Table 4.13 Statistics of the surface Cr_2O_3 thickness and internal Al_2O_3 penetration measurements of IN617 samples oxidized in Env. 9 at 750 °C.

Env. 9, 750 °C	**surface Cr_2O_3 thickness**			**intergranular Al_2O_3 depth**			**transgranular Al_2O_3 depth**		
Exposure time (h)	150	375	500	150	375	500	150	375	500
# of measurements	64	87	179	85	66	166	15	18	33
Max. value (µm)	0.66	0.90	1.50	5.00	6.94	7.14	1.06	0.97	1.58
Min value (µm)	0.33	0.36	0.58	1.02	1.43	1.05	0.17	0.26	0.28
Mean value (µm)	**0.43**	**0.60**	**0.87**	**2.21**	**3.17**	**3.40**	**0.31**	**0.47**	**0.60**
Standard Dev. (µm)	**0.06**	**0.13**	**0.15**	**0.72**	**1.13**	**0.97**	**0.23**	**0.19**	**0.33**

Table 4.14 Statistics of the surface Cr_2O_3 thickness and internal Al_2O_3 penetration measurements of IN617 samples oxidized in Env. 1320 at 750 °C.

Env. 1320, 750 °C	**surface Cr_2O_3 thickness**			**intergranular Al_2O_3 depth**			**transgranular Al_2O_3 depth**		
Exposure time (h)	150	225	375	150	225	375	150	225	375
# of measurements	59	37	52	63	68	35	-	14	27
Max. value (µm)	0.36	0.85	0.88	2.41	6.75	7.64	-	0.87	1.28
Min value (µm)	0.19	0.33	0.28	0.75	1.14	1.18	-	0.16	0.22
Mean value (µm)	**0.25**	**0.51**	**0.60**	**1.54**	**2.92**	**2.90**	-	**0.40**	**0.51**
Standard Dev. (µm)	**0.03**	**0.14**	**0.16**	**0.36**	**1.37**	**1.30**	-	**0.24**	**0.25**

Table 4.15 Surface and internal oxidation rate constants determined in He-CO-CO_2 exposures in the temperature range of 750 - 850 °C.

Environment	**Temperature (°C)**	$k_S^{Cr_2O_3}$ **(cm^2/s)**	$k_C^{Cr_2O_3}$ **(cm^2/s) [Eq. 2.75]**	$k_I^{Al_2O_3}$ **(cm^2/s)**	$k_T^{Al_2O_3}$ **(cm^2/s)**
Env. 9	850	1.06×10^{-14}	2.59×10^{-15}	3.94×10^{-13}	3.97×10^{-14}
	800	5.17×10^{-15}	1.27×10^{-15}	1.61×10^{-13}	4.79×10^{-15}
	750	1.82×10^{-15}	1.82×10^{-15}	3.46×10^{-14}	9.33×10^{-16}
Env. 1320	850	1.53×10^{-14}	3.75×10^{-15}	3.86×10^{-13}	3.08×10^{-14}
	800	4.39×10^{-15}	1.08×10^{-15}	1.80×10^{-13}	4.32×10^{-15}
	750	1.32×10^{-15}	1.32×10^{-15}	3.52×10^{-14}	9.70×10^{-16}

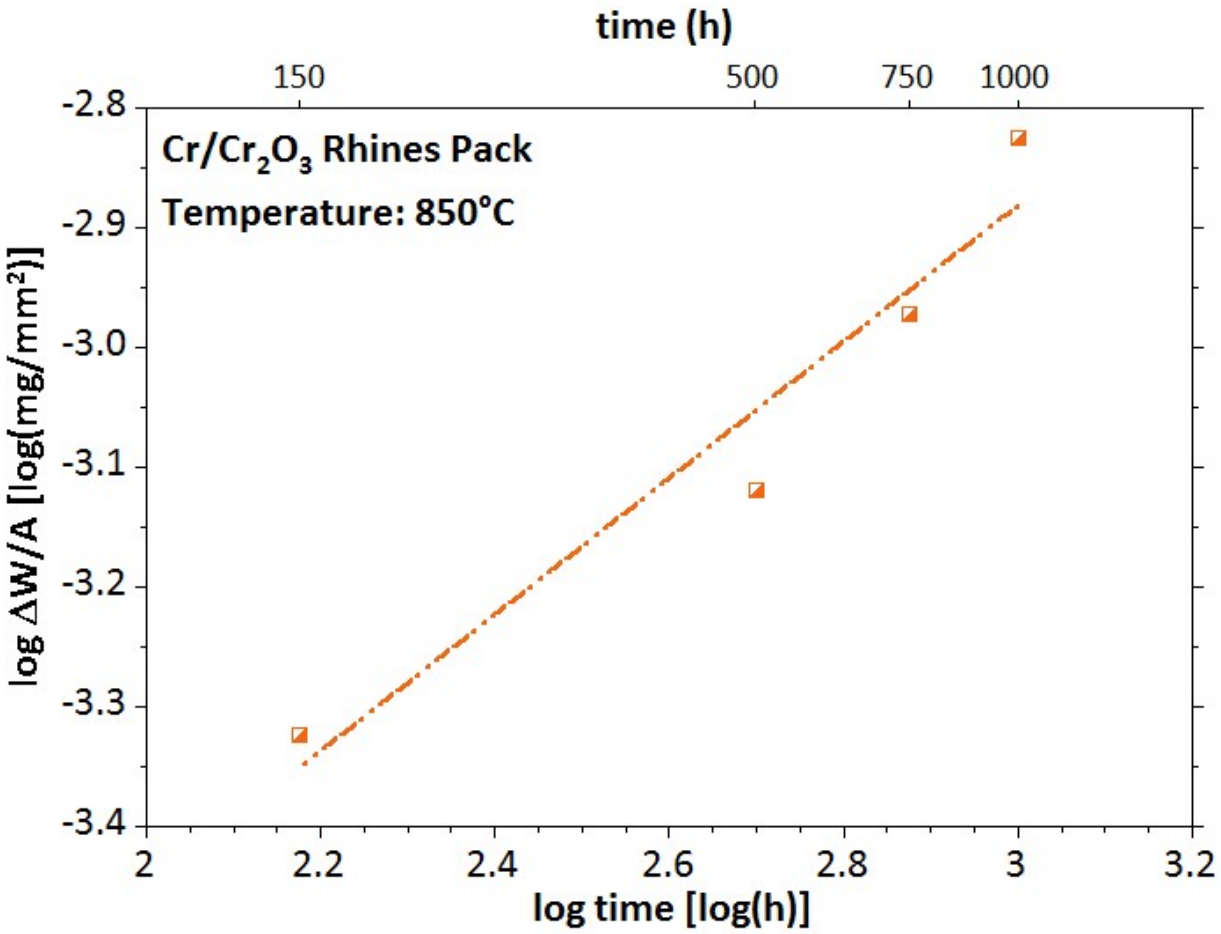

Figure 4.1 Logarithmic plot of the weight gains measured for the IN617 samples exposed in Cr-Cr_2O_3 Rhines packs as function of exposure time at 850 °C.

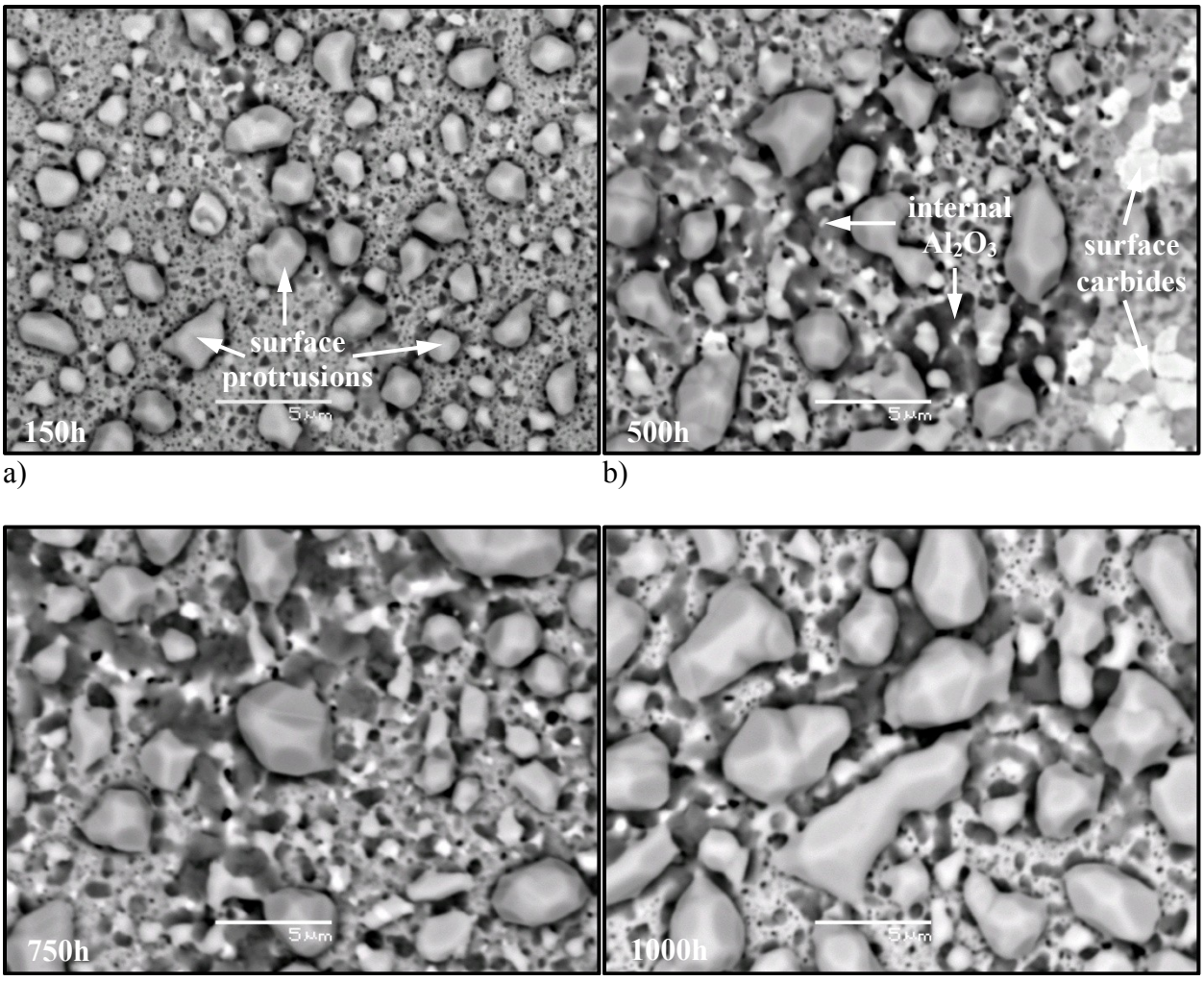

a) b)

c) d)

Figure 4.2. Backscattered electron images of the surfaces of the Rhines pack IN617 samples exposed to 850 °C for a) 150h, b) 500h, c) 750h, d) 1000h.

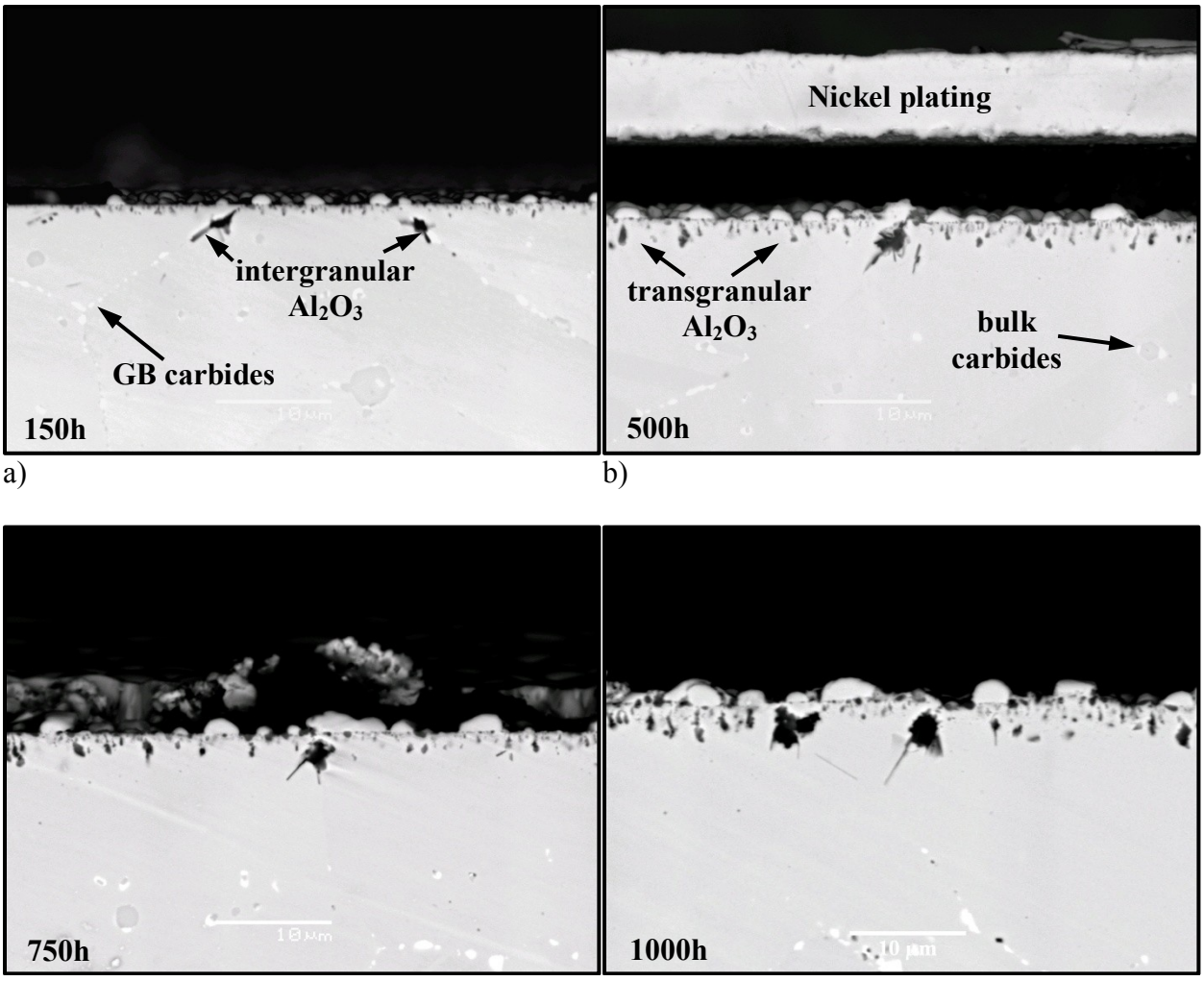

Figure 4.3. Backscattered electron images of the cross-sections of the Rhines pack IN617 samples exposed to 850 °C for a) 150h, b) 500h, c) 750h, d) 1000h.

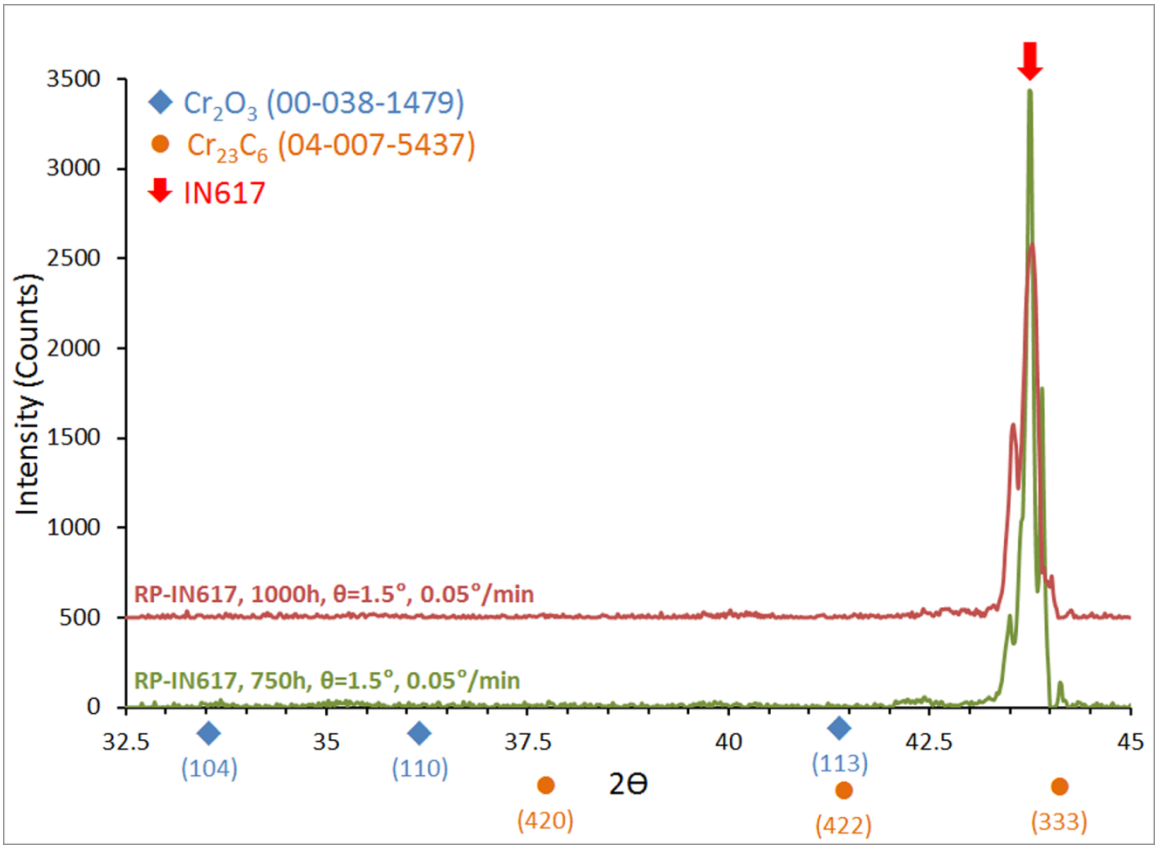

Figure 4.4. Grazing incidence angle X-Ray diffraction pattern (θ = 1.5°) of the IN617 samples exposed in Cr-Cr_2O_3 Rhines packs at 850 °C for 750h and 1000h. Blue diamond markers mark the peak positions of Cr_2O_3 phase (PDF#: 00-038-1479). Orange circles mark the peak positions of $Cr_{23}C_6$ phase (PDF#: 04-007-5437). Red arrow indicates the position of the primary peak of the γ matrix of IN617. The pattern was obtained using Cu-Kα radiation with a characteristic wavelength of 1.5406Å.

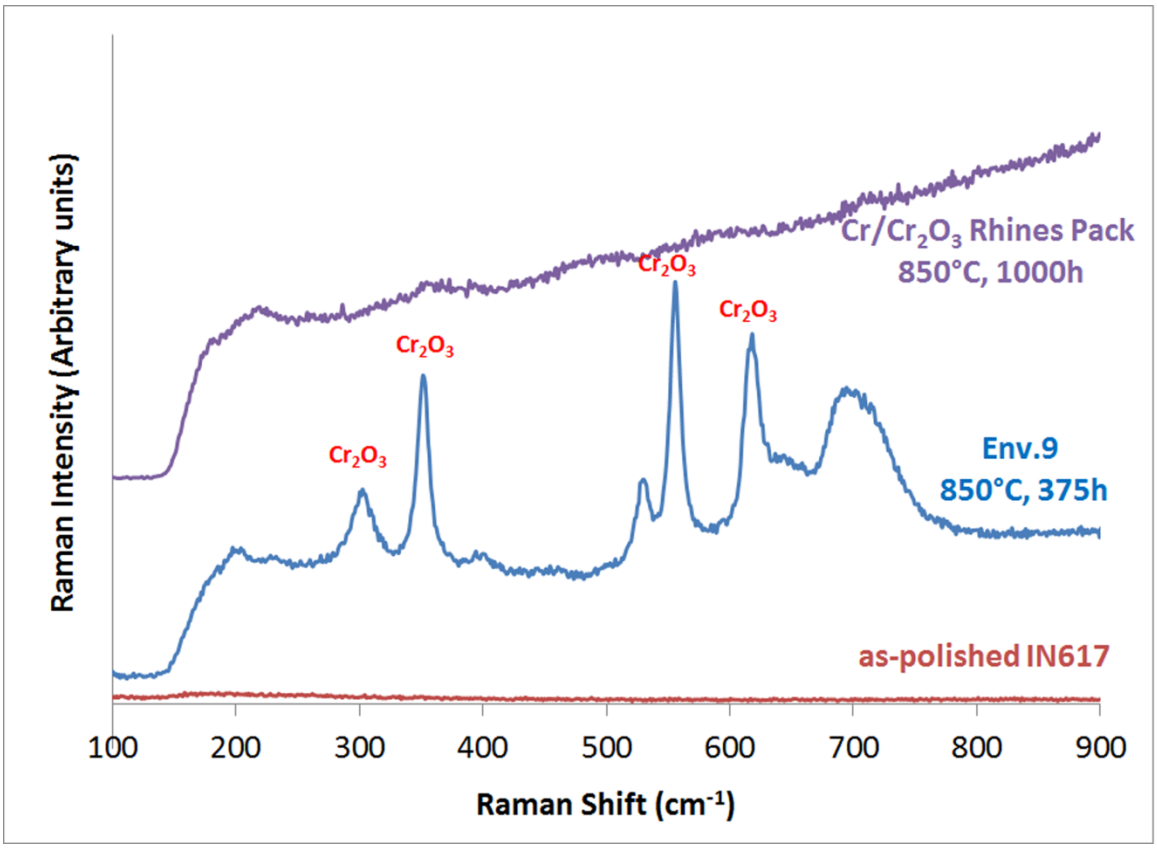

Figure 4.5. Comparison of the Raman spectra of an as-polished IN617 sample, an IN617 sample exposed to Env. 9 at 850 °C for 375 and an IN617 sample exposed in a Cr-Cr_2O_3 Rhines pack at 850 °C for 1000h. Spectra were obtained by exciting the surfaces of the samples using a 633nm He-Ne laser. The peak locations of the Cr_2O_3 phase were reported by Farrow et al. [101].

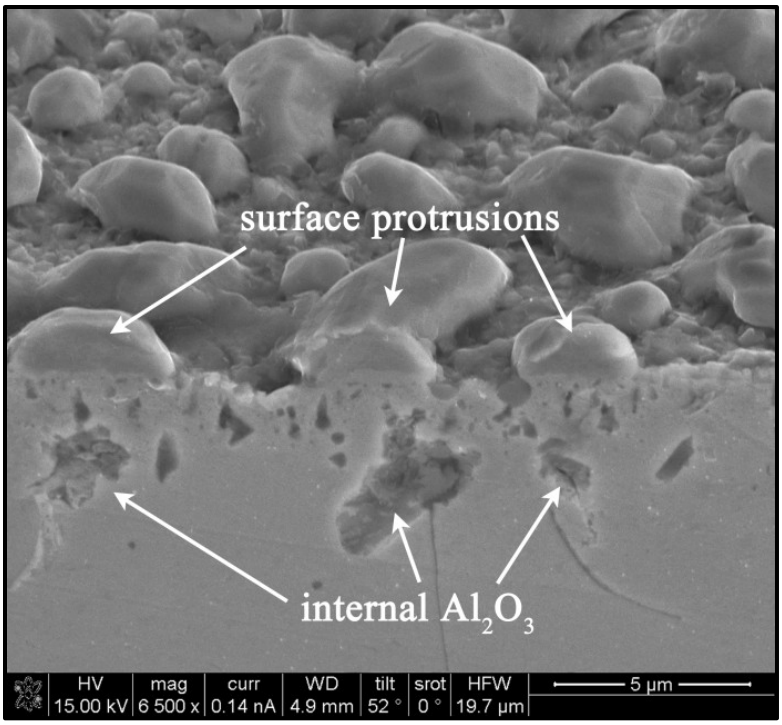

a)

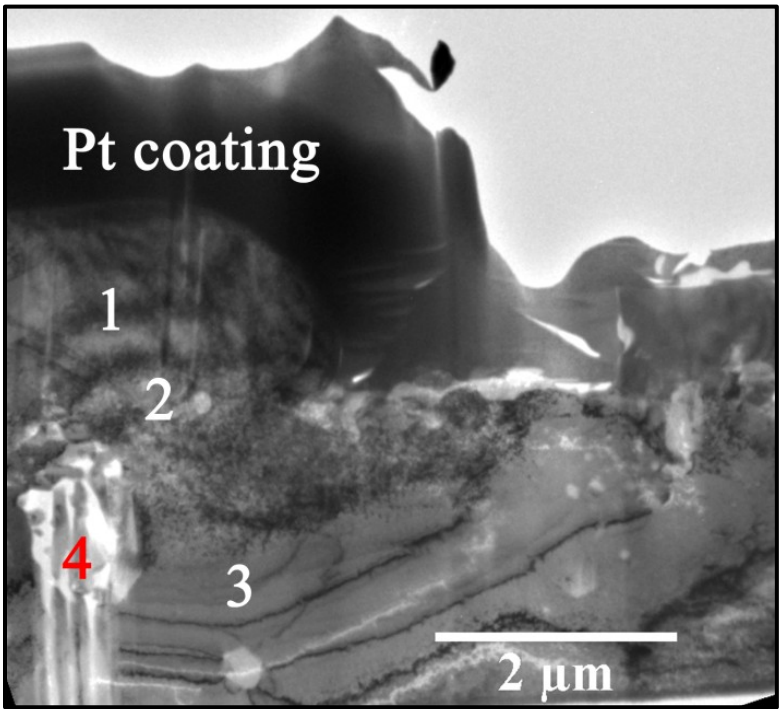

b)

Figure 4.6. a) Secondary electron image and b) bright field STEM image of Rhines pack IN617 sample exposed to 850 °C for 1000h.

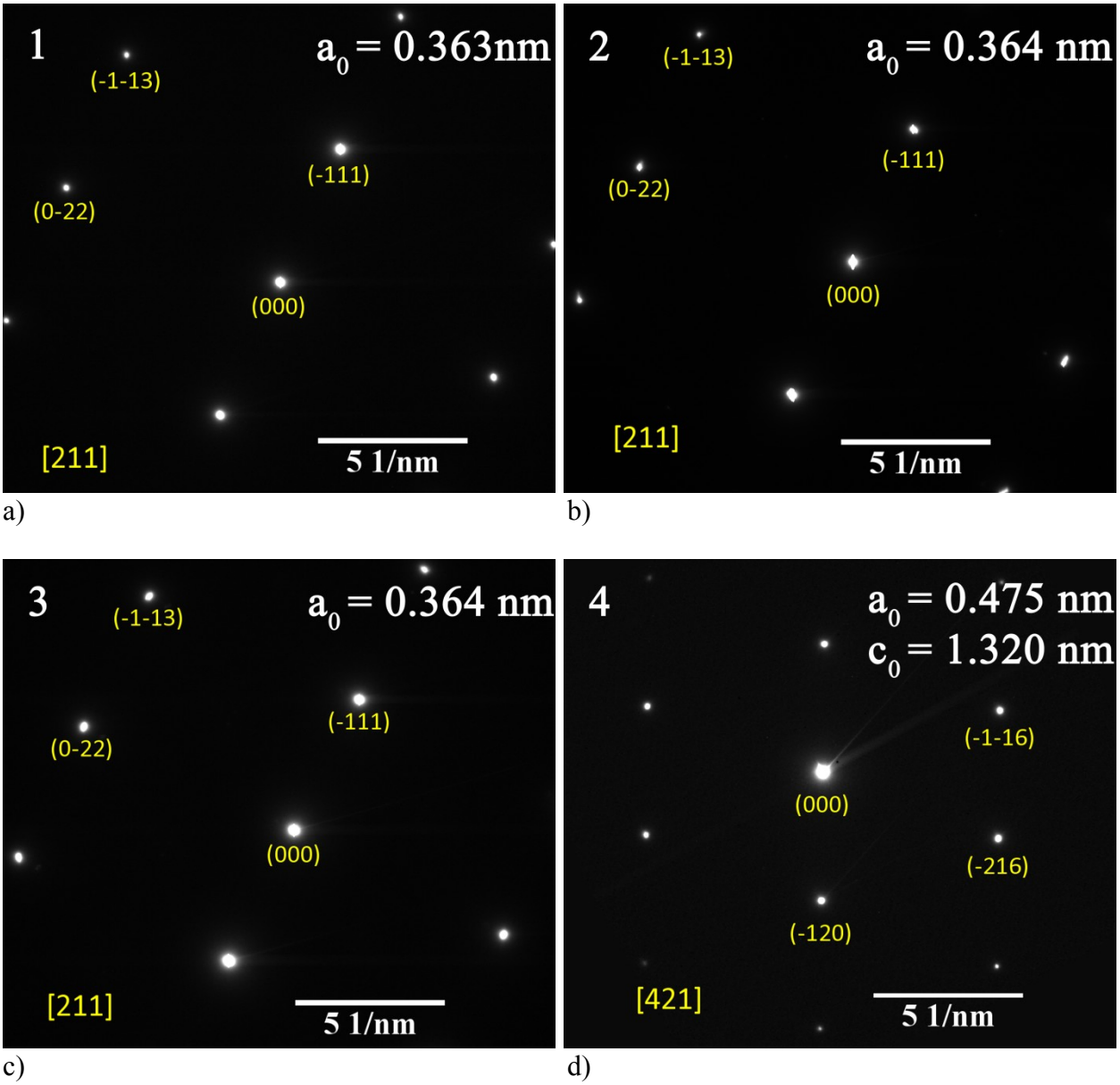

a) b)

c) d)

Figure 4.7. Selected area electron diffraction (SAED) patterns recorded at a) the surface protrusion, b) the protrusion-base metal interface, c) the base metal and d) the internal Al_2O_3 penetration.

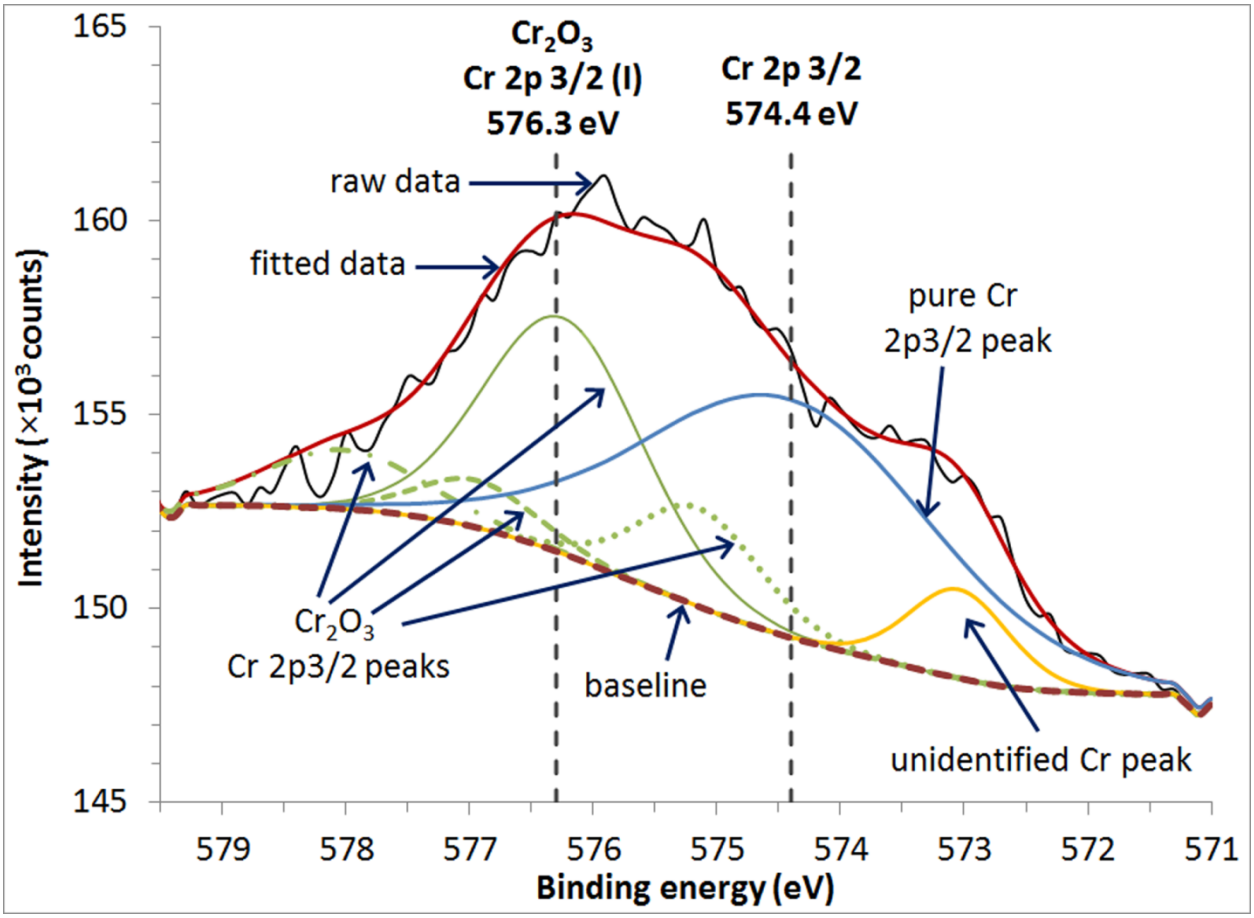

Figure 4.8. XPS spectrum recorded from the surface of the IN617 sample exposed in a Cr-Cr_2O_3 Rhines pack at 850 °C for 1000h.

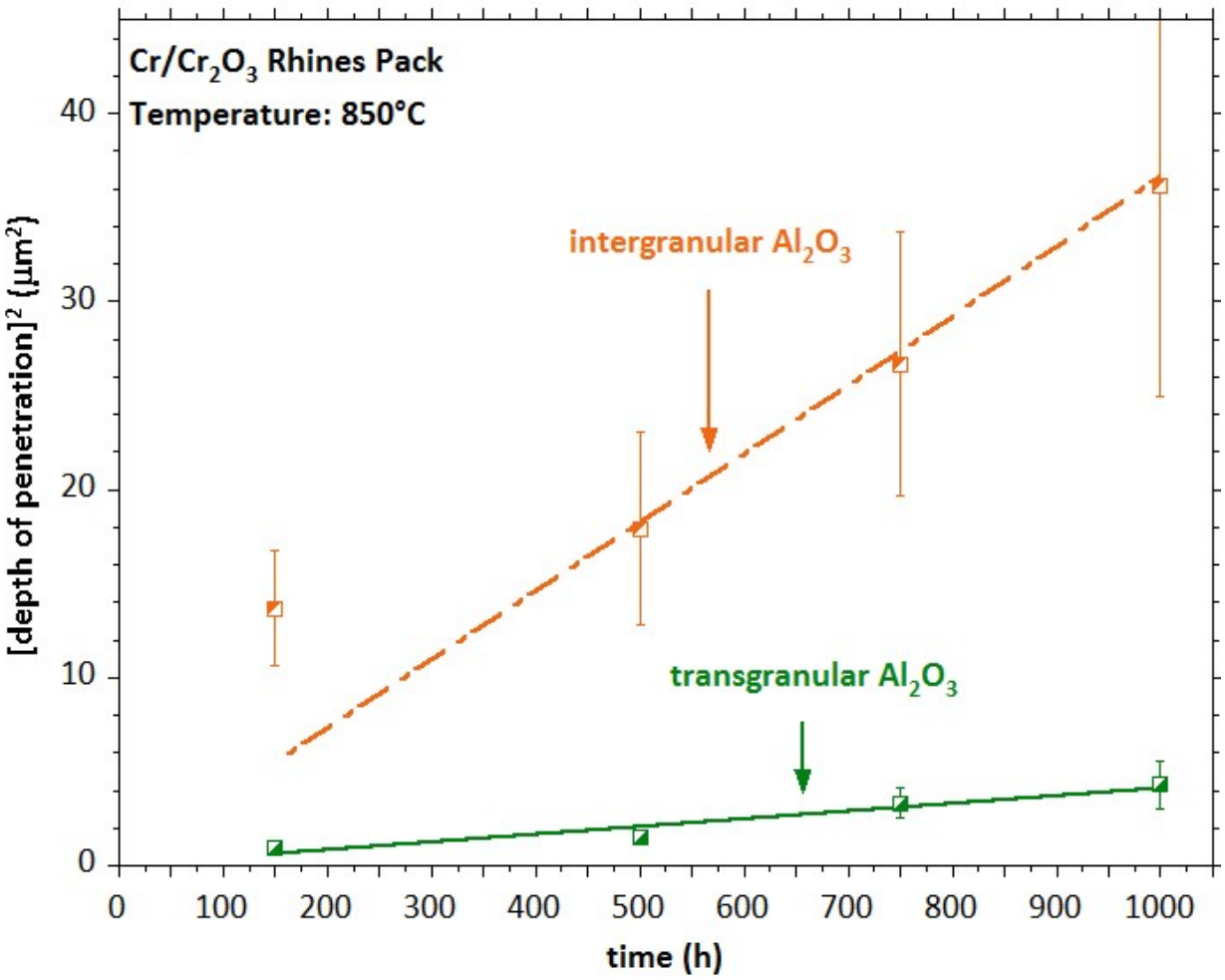

Figure 4.9. Parabolic plots of intergranular and transgranular aluminum penetration depths in IN617 samples oxidized in Cr-Cr_2O_3 Rhines packs at 850 °C.

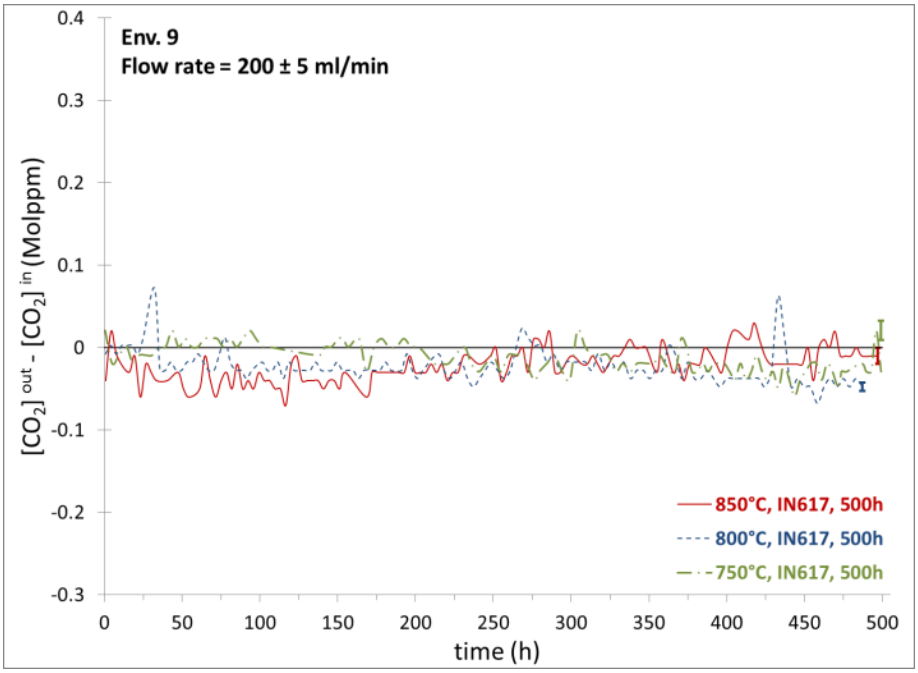

a)

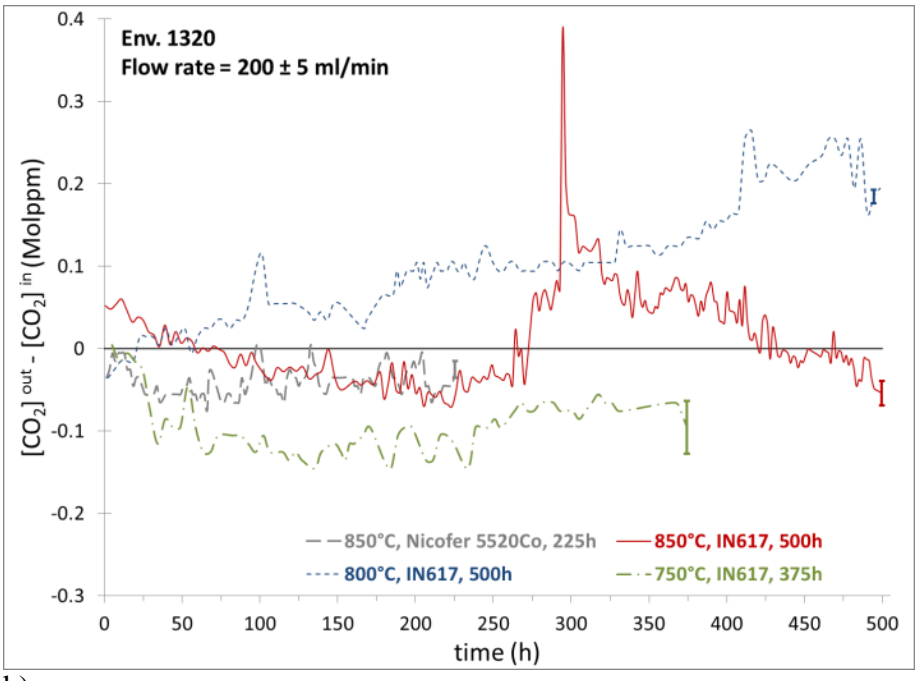

b)

Figure 4.10. Difference in the outlet and inlet CO_2 concentrations during the exposure of IN617 samples to a) Env. 9 and b) Env. 1320 at temperatures 750 - 850 °C (Flow rate 200 ± 5 ml/min). [5] For clarity, only one error bar is shown for each set of measurements.

[5] Nicrofer 5520Co sample was exposed only to Env. 1320 at 850°C for 225h

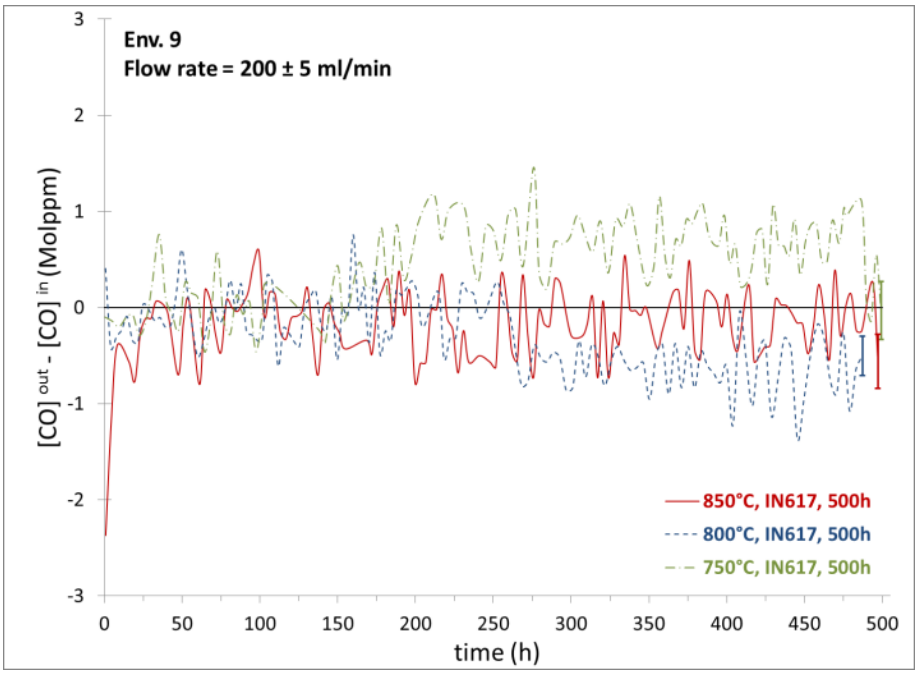

a)

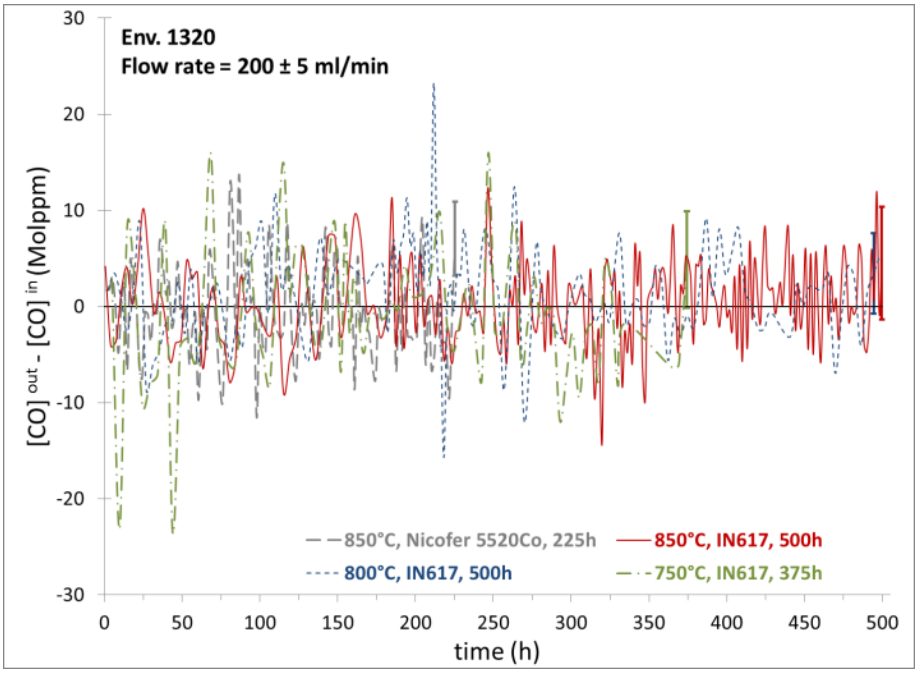

b)

Figure 4.11. Difference in the outlet and inlet CO concentrations during the exposure of IN617 samples to a) Env. 9 and b) Env. 1320 at temperatures 750-850 °C (Flow rate 200 ± 5 ml/min).[6] For clarity, only one error bar is shown for each set of measurements.

[6] At 750 °C IN617 samples were exposed to Env. 1320 for up to 375h

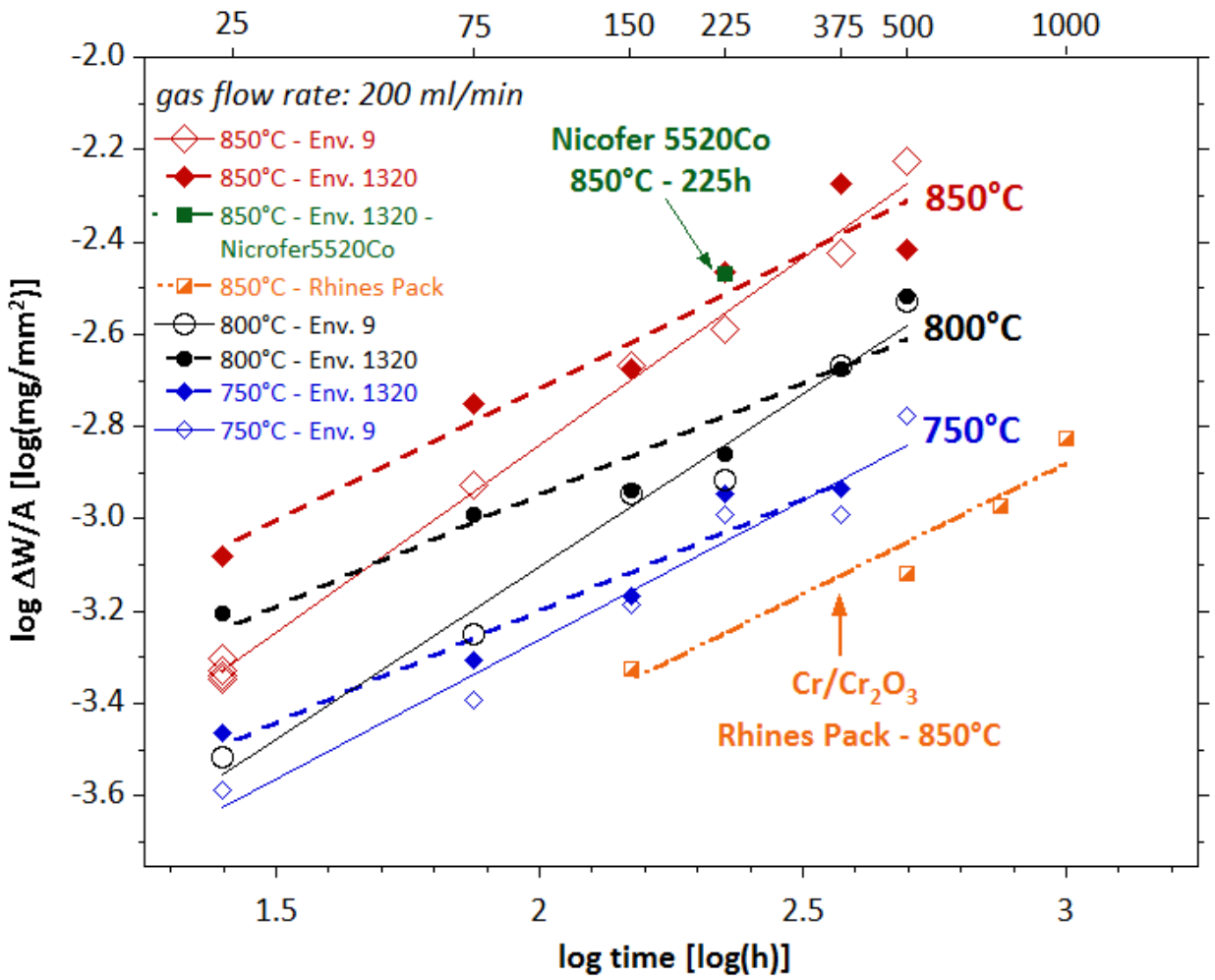

Figure 4.12. Logarithmic plots of the weight gains measured as a function of exposure time in IN617 samples exposed in Env. 9 and Env. 1320 at 750 - 850 °C in comparison with that of the weight gain measured in IN617 samples exposed in Cr-Cr_2O_3 Rhines packs as a function of exposure time at 850 °C.

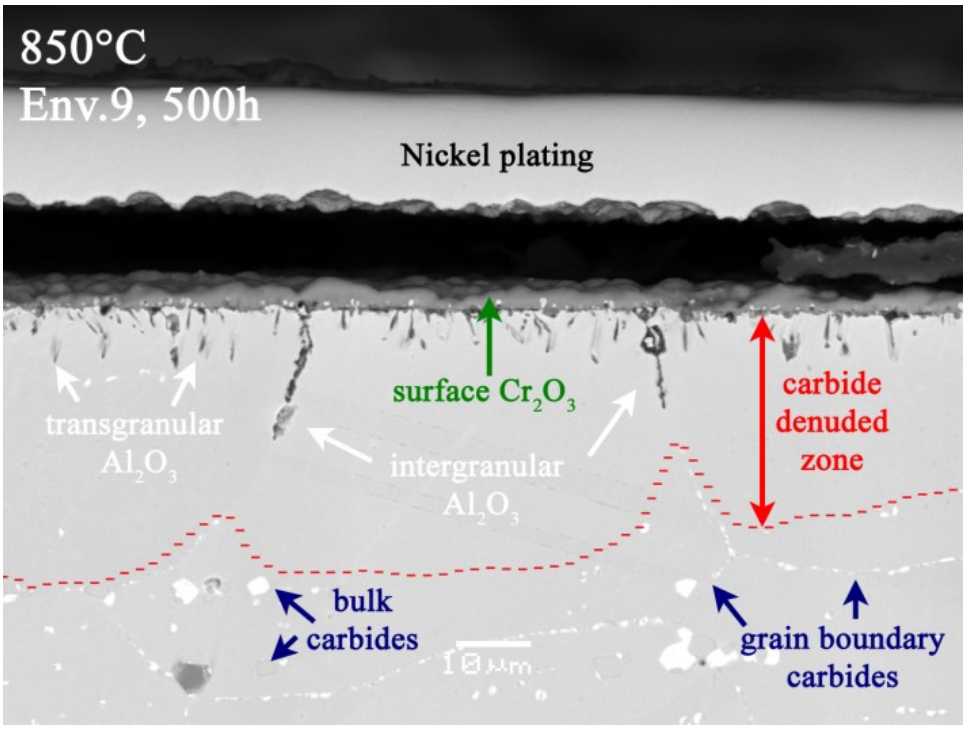

a)

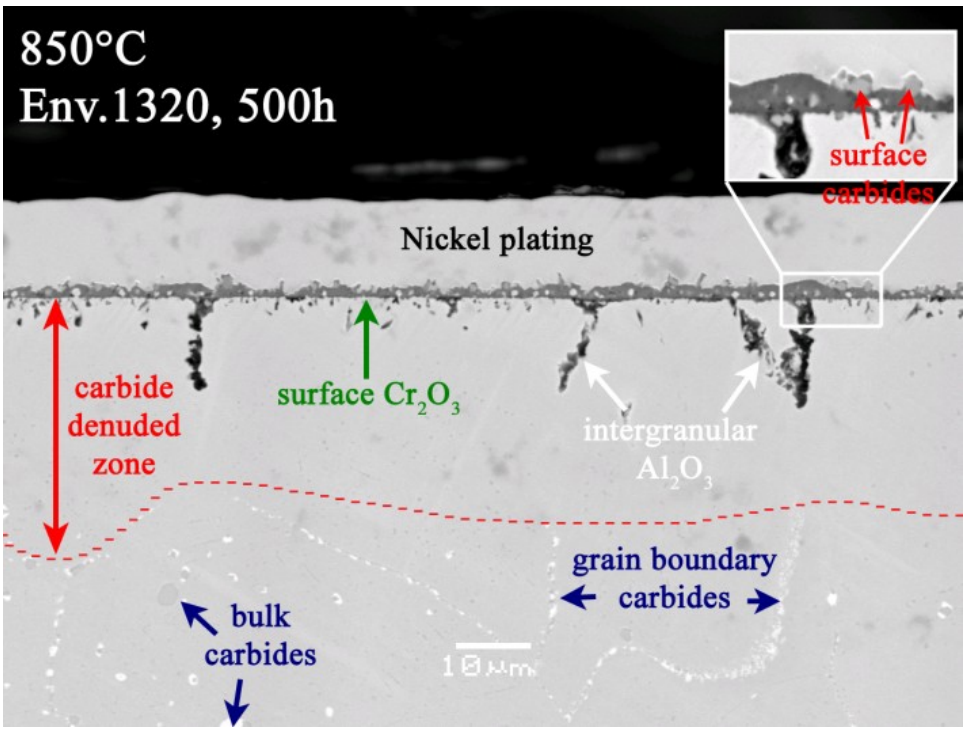

b)

Figure 4.13. Backscattered electron images of the IN617 samples exposed to a) Env.9 and b) Env.1320 at 850 °C for 500 h.

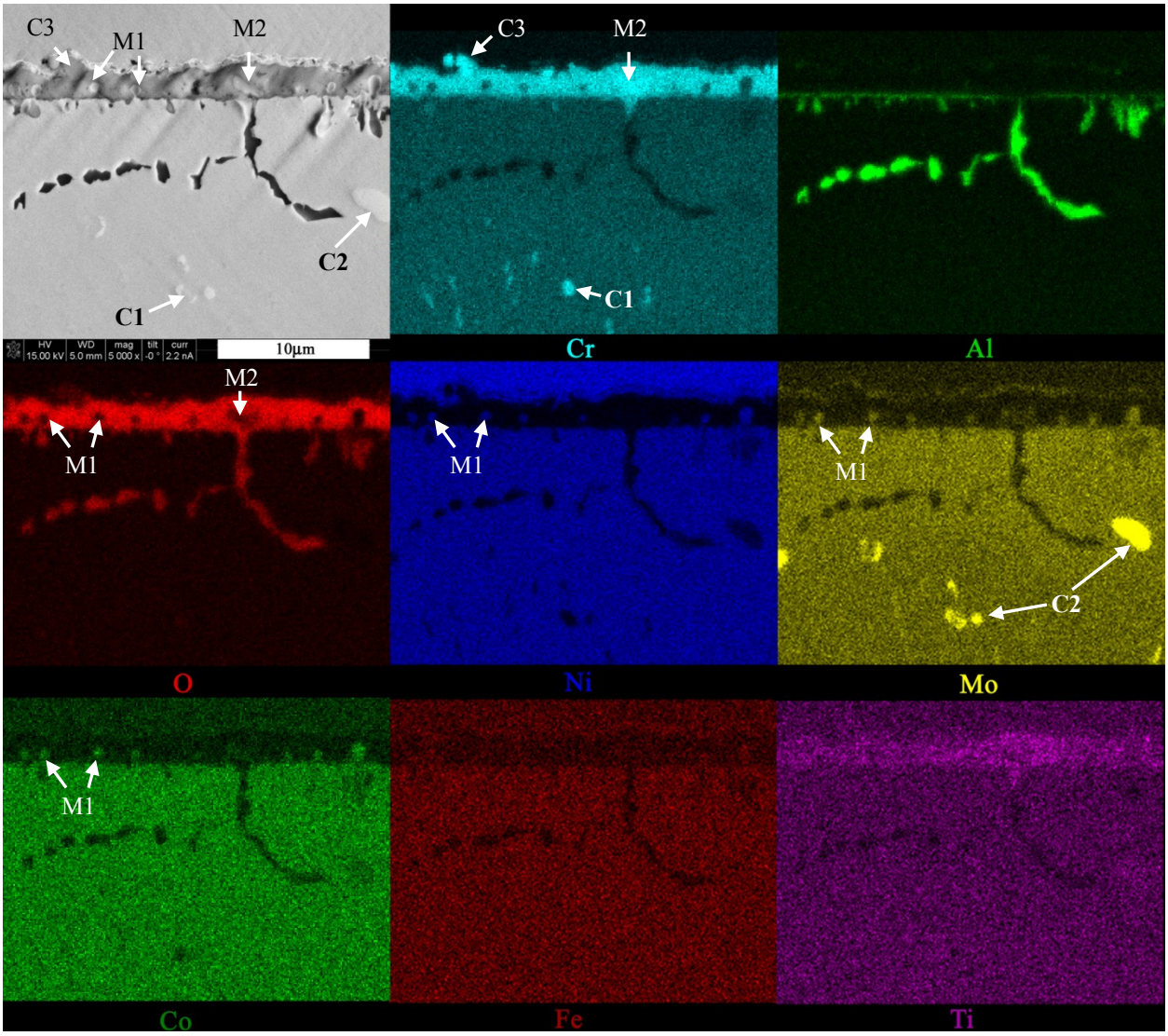

Figure 4.14. EDX mapping of the microstructure of IN617 exposed to Env.1320 at 850 °C for 500h. The annotations made in the SEM image stand for: M1 - Ni, Mo, Co rich surface nodule, M2 - Cr rich surface nodule, C1 - Cr rich $M_{23}C_6$ type carbide, C2 - Mo rich M_6C type carbide, C3 - Cr rich M_7C_3 type carbide.

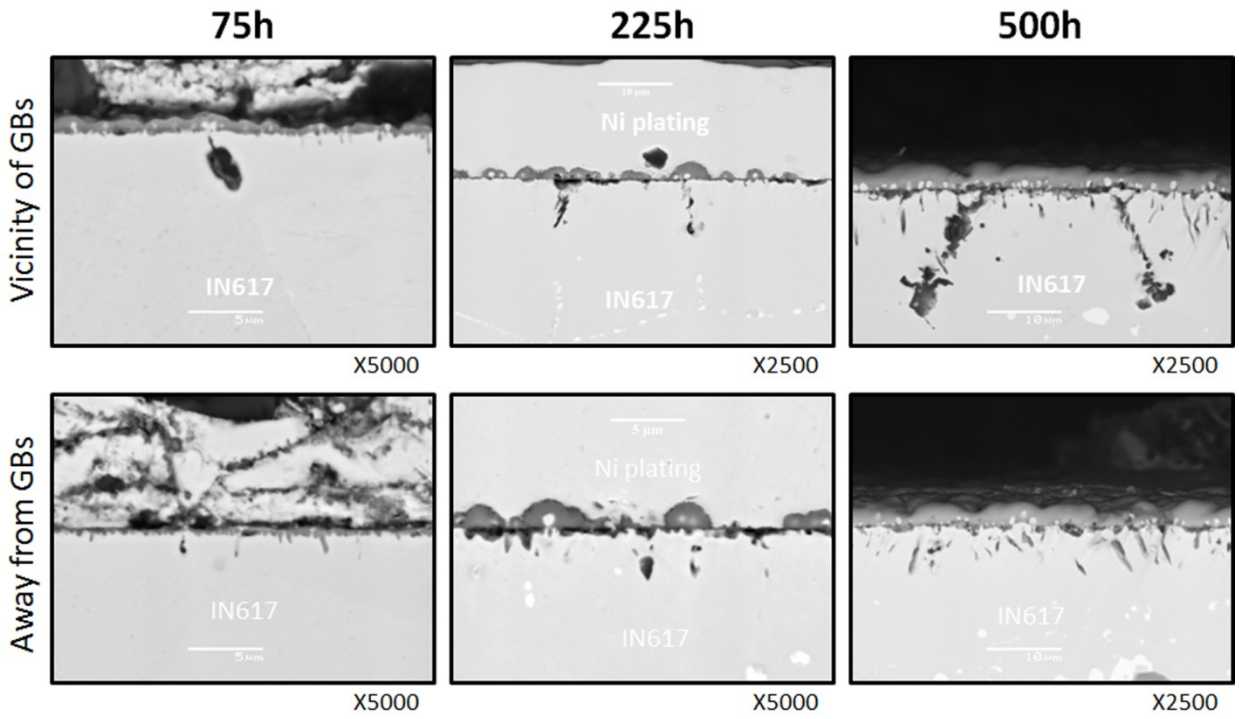

Figure 4.15. Backscattered electron images of the cross-sections of IN617 samples exposed to He-CO/CO_2 = 9 at 850 °C for 75, 225 and 500h taken from regions in the vicinity of grain boundaries and away from the grain boundaries. Image magnification is indicated below each microstructure.

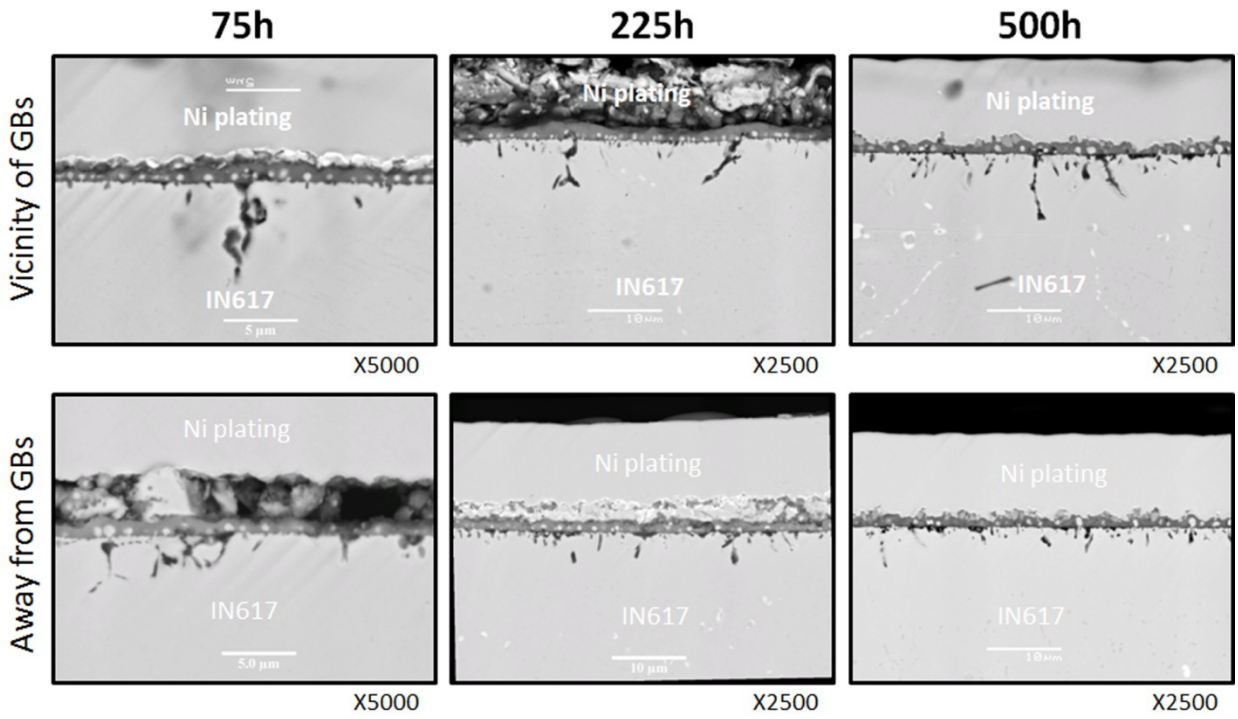

Figure 4.16. Backscattered electron images of the cross-sections of IN617 samples exposed to He-CO/CO_2 = 1320 at 850 °C for 75, 225 and 500h taken from regions in the vicinity of grain boundaries and away from the grain boundaries. Image magnification is indicated below each microstructure.

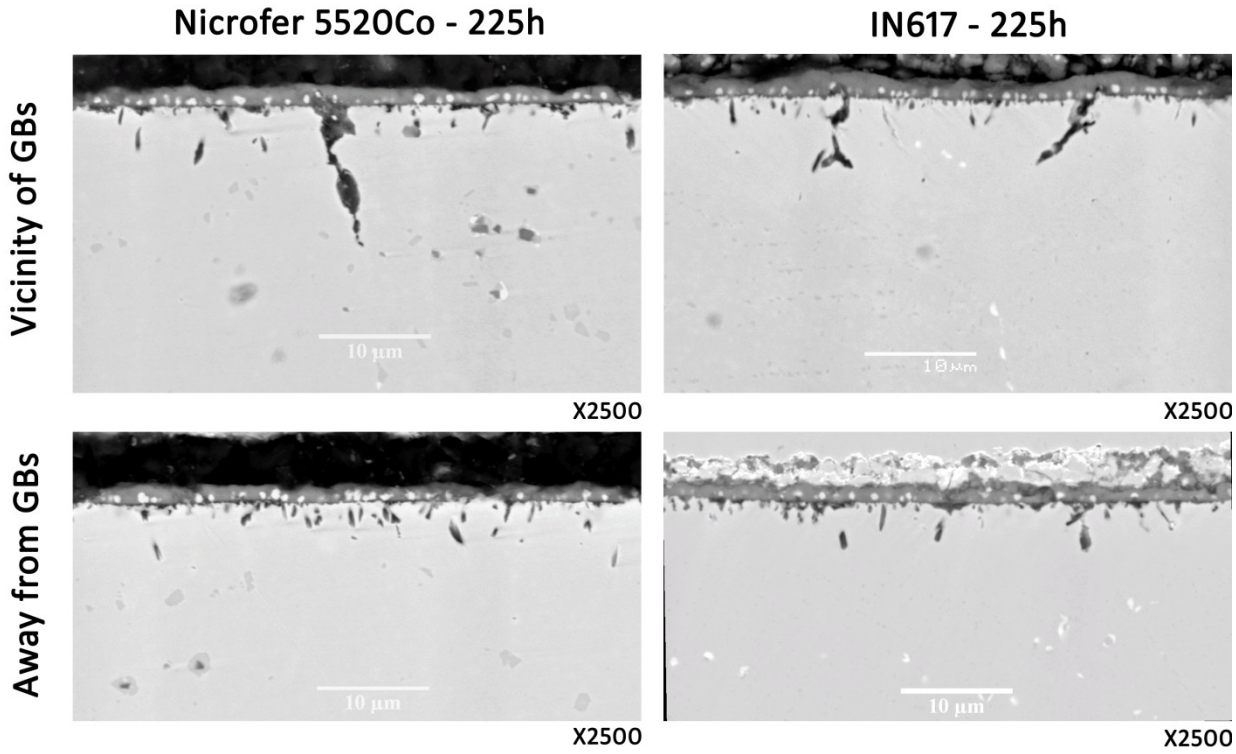

Figure 4.17. Backscattered electron images of the cross-sections of Nicrofer 5520Co and IN617 samples exposed to He-CO/CO_2 = 1320 at 850 °C for 225h taken from regions in the vicinity of grain boundaries and away from the grain boundaries. Image magnification is indicated below each microstructure.

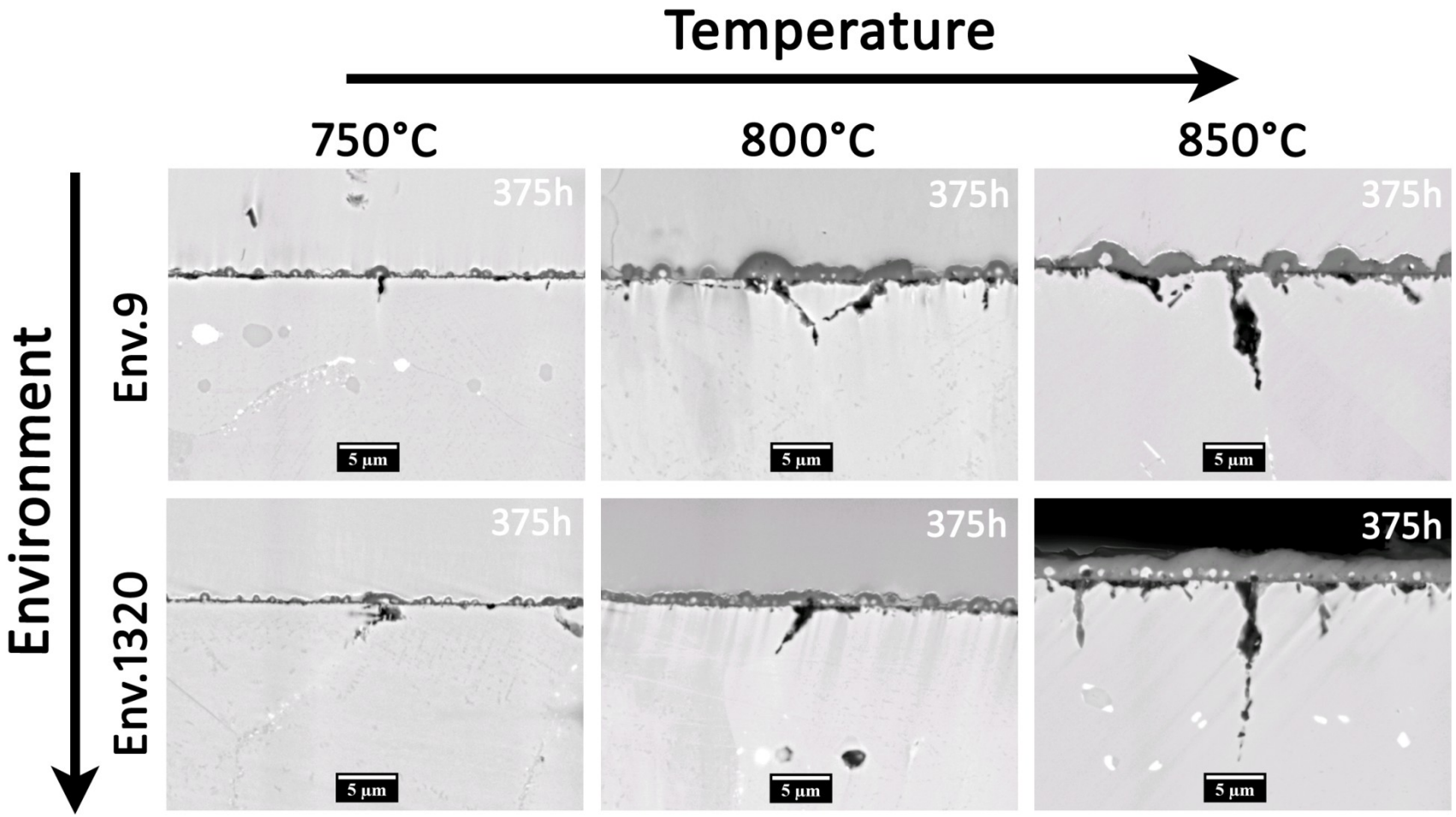

Figure 4.18. Backscattered electron images of IN617 samples oxidized in Env. 9 and Env. 1320 in the temperature range of 750 - 850 °C for 375h.

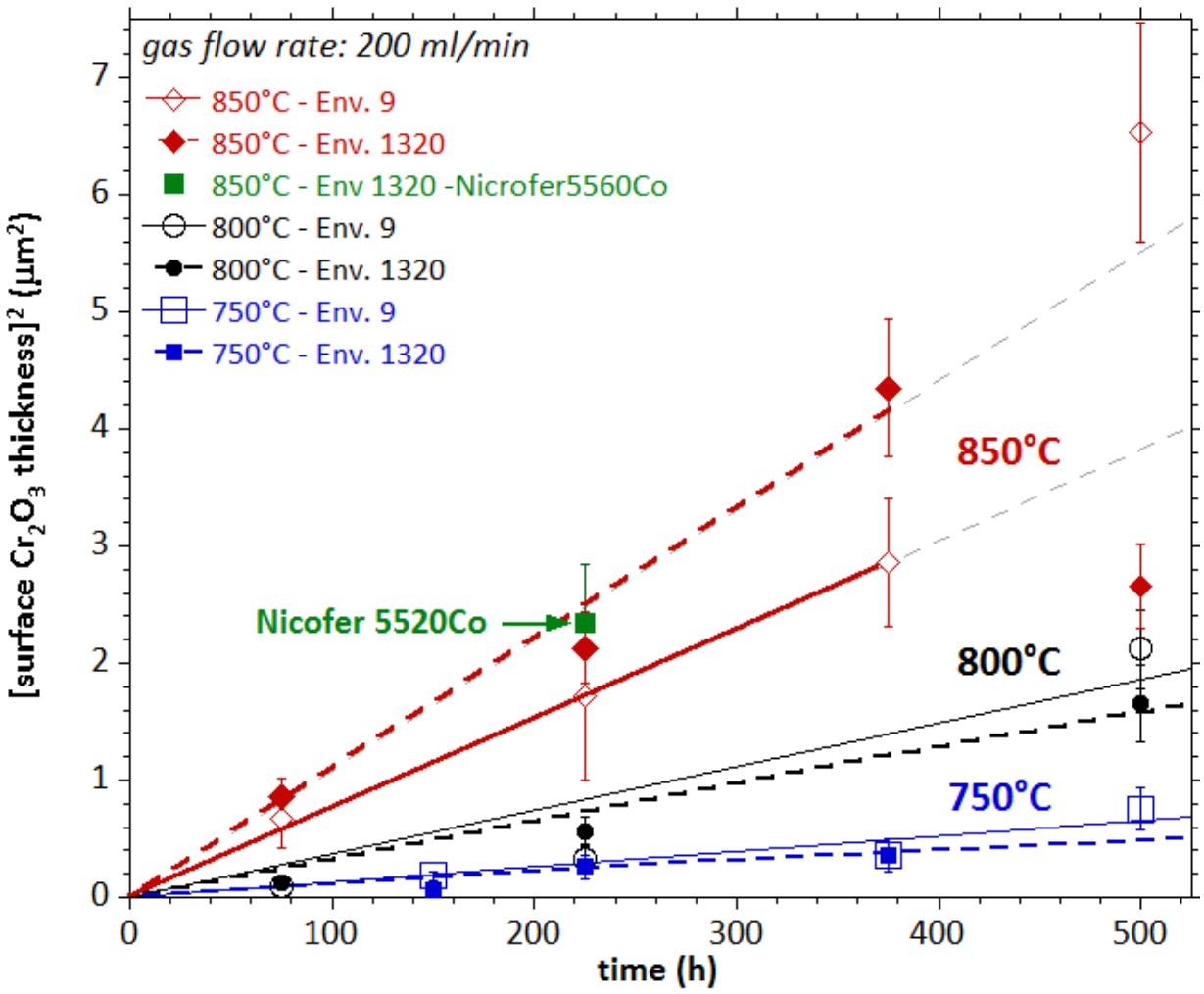

Figure 4.19. Parabolic plots of the surface Cr_2O_3 thickness measured as a function of exposure time on IN617 samples oxidized in Env.9 and Env.1320 at 750 - 850 °C. Light gray dashed lines show the extension of the linear regression lines of the oxide thickness data obtained in Env. 9 and Env. 1320 at 850 °C excluding the 500h data points.

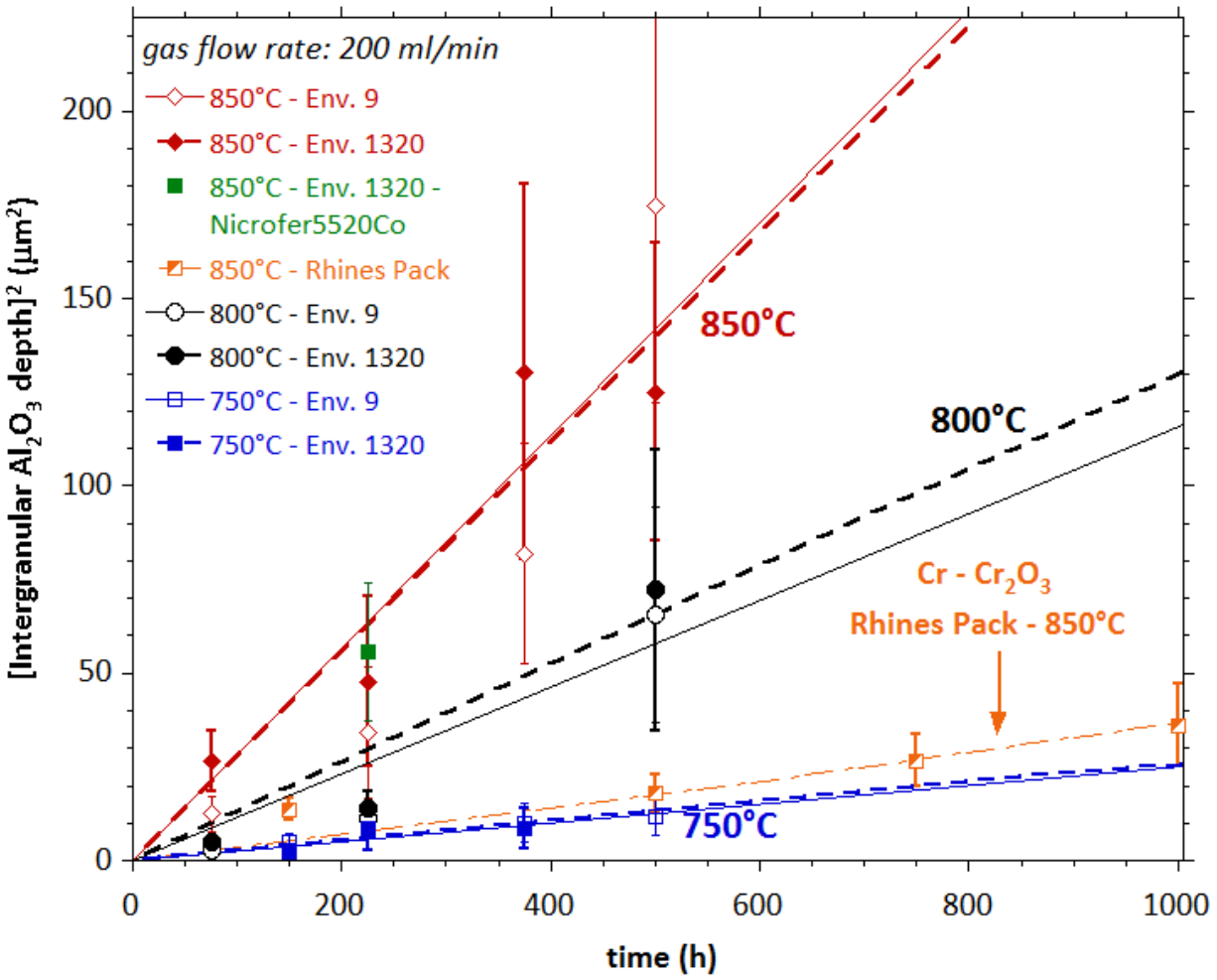

Figure 4.20. Parabolic plots of intergranular Al_2O_3 penetration depths in samples oxidized in the Cr-Cr_2O_3 Rhines pack, Env.9 and Env.1320 as a function of exposure time at 750 - 850 °C.

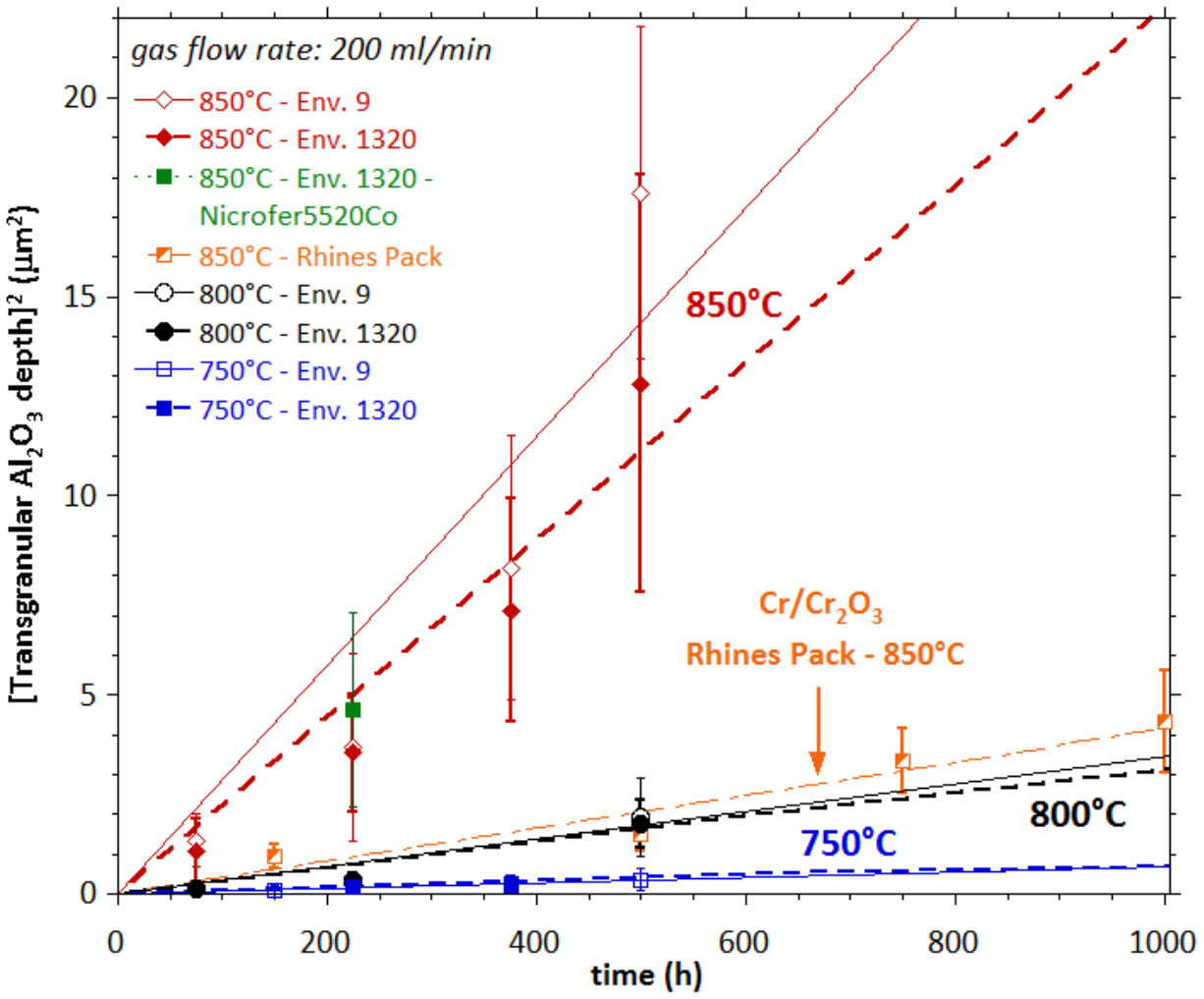

Figure 4.21. Parabolic plots of transgranular Al_2O_3 penetration depths in samples oxidized in the Cr-Cr_2O_3 Rhines pack, Env.9 and Env.1320 as a function of time at 750 - 850 °C.

CHAPTER 5

DISCUSSION

In this chapter, the oxygen transport mechanism(s) governing the internal aluminum oxidation kinetics of IN617 in He-CO-CO_2 and in Cr-Cr_2O_3 Rhines pack exposures are identified using classical internal oxidation theory. The oxygen diffusion coefficient in the internal oxidation zone of IN617, D_O^{617}, is determined first from Equation (2.105). The oxygen diffusion coefficient is then used to determine the oxygen solubility at the alloy-oxide interface, driving the internal oxidation kinetics in He-CO-CO_2 environments, from Equation (2.114). The significance of the calculated oxygen diffusion coefficient and oxygen solubility values are then discussed in terms of easy diffusion paths for oxygen in the internal oxidation zone and gas permeability of surface Cr_2O_3 film, respectively.

Afterwards, the temperature and environment dependence of surface Cr and internal Al oxidation kinetics of IN617 in He-CO-CO_2 environments are discussed. First, the mechanism of surface Cr oxidation is described based on the activation energy and effective Cr diffusion coefficient in Cr_2O_3 determined from the surface chromium oxidation rate constant measurements in the temperature range of at 750 - 850 °C. Next, the processes that accelerate the

internal Al oxidation kinetics are discussed based on the Arrhenius parameters (activation energy and pre-exponential coefficient) of the oxygen solubility and diffusion coefficients as well as the morphology of the intergranular and transgranular Al_2O_3 precipitates, which form interfaces that facilitate oxygen diffusion.

Finally, the oxygen solubility and diffusion coefficient values determined in IN617 are used to calculate the minimum amount of aluminum concentration in the alloy required to mitigate the internal oxidation of IN617 in He-CO-CO_2 environments at 850 °C.

5.1. The mechanisms of internal oxidation of IN617

The internal oxidation mechanism(s) of IN617 is determined by calculating D_O^{617} from the measured internal oxidation kinetics in the Cr - Cr_2O_3 Rhines pack exposure by using Equation (2.105):

$$N_O^{(s)}/N_B^{(o)} = [\nu \times erf\gamma \times exp(\gamma^2)]/\left[\phi^{1/2}exp(\gamma^2\phi)erfc(\gamma\phi^{1/2})\right]. \quad (5.1)$$

However, this calculation requires knowledge of the oxygen solubility at the surface of the alloy, $N_O^{617}(RP)$, exposed in the Cr-Cr_2O_3 Rhines pack to be known. Due to the lack of solubility data in IN617, $N_O^{617}(RP)$ was approximated using the solution thermodynamics model developed by Guan and Smeltzer [83] that takes thermodynamic interaction coefficients, $\mathcal{E}_i^j$[7] [106], into account to calculate the oxygen solubility in Ni-Cr-Al-O system from the oxygen solubility in pure Ni:

$$N_O^{Cr_2O_3} ln N_O^{617}(RP) - \left[(1+\mathcal{E}_O^{Cr})N_{Cr}^{617} + 2\left(1+\mathcal{E}_O^{Al}\right)N_{Al}^{617}\right]N_O^{617}(RP) = (N_{Al}^{617})^2\left(1+\mathcal{E}_{Al}^{Al}\right)/2 + \left(1+\mathcal{E}_{Cr}^{Al}\right)\left(N_{cr}^{617} - N_{Cr}^{Cr_2O_3}\right)N_{Al}^{617} - \left(1+\mathcal{E}_{Al}^{Al}\right)N_O^{Cr_2O_3}N_{Al}^{617} + N_{Al}^{617} + N_O^{Cr_2O_3}\, ln N_O^{Ni}(RP), \quad (5.2)$$

[7] $\mathcal{E}_i^j$ is a measure of the change in the activity coefficient of *i* as a function of the concentration of *j* in a solid solution [106].

where N_{Al}^{617} and N_{Cr}^{617} are the atomic fractions of Al and Cr in IN617, respectively; $N_O^{Cr_2O_3}$ and $N_{Cr}^{Cr_2O_3}$ are the atomic fractions of O and Cr in stoichiometric Cr_2O_3; $\mathcal{E}_O^{Cr}$, $\mathcal{E}_O^{Al}$, $\mathcal{E}_{Al}^{Al}$, $\mathcal{E}_{Cr}^{Al}$ are the dimensionless thermodynamic interaction coeffcients in nickel melts at 1600 °C [83]; and $N_O^{Ni}(RP)$ is the oxygen solubility in pure nickel at the dissociation oxygen partial pressure of Cr_2O_3. To determine $N_O^{Ni}(RP)$, Sievert's constant, S_O^{Ni}, relating the oxygen solubility in nickel to the ambient oxygen partial pressure, was calculated from the following equation:

$$N_O^{Ni}(Ni/NiO)[at.fr.] = S_O^{Ni} \times \sqrt{P_{O_2}(Ni/NiO)}, \tag{5.3}$$

where $N_O^{Ni}(Ni/NiO)$ is the terminal oxygen solubility in pure nickel reported by Park and Altstetter [107] at the dissociation oxygen partial pressure of NiO, $P_{O_2}(Ni/NiO)$:

$$N_O^{Ni}(Ni/NiO)[at.fr.] = 8.3 \times exp(-55000/RT \ \ [J/mol]). \tag{5.4}$$

Using the published data for the free energy of formation of NiO ($\Delta G° = -473600 + 175.6T\ [J/mole\ O_2]$ [107]), $P_{O_2}(Ni/NiO)$ was calculated as 1.4×10^{-13} *atm* at 850 °C. Inserting this value into Equation (5.3) yields the value of $615.1\ at.fr./\sqrt{atm}$ for S_O^{Ni} at 850 °C.

Next, $N_O^{Ni}(RP)$ was determined using the dissociation oxygen partial pressure of Cr_2O_3, $P_{O_2}(Cr/Cr_2O_3)$, in Equation (5.3):

$$N_O^{Ni}(RP)[at.fr.] = S_O^{Ni} \times \sqrt{P_{O_2}(Cr/Cr_2O_3)}, \tag{5.5}$$

where $P_{O_2}(Cr/Cr_2O_3)$ is equal to 2.0×10^{-26} *atm* at 850 °C based on the free energy of formation of Cr_2O_3 ($\Delta G° = -740635 - 163.5T\ [J/mole\ O_2]$ [108]). Inserting $N_O^{Ni}(RP)$ into Equation (5.2) yields the value of $N_O^{617}(RP)$, which is approximately one order of magnitude smaller than that of $N_O^{Ni}(RP)$ at 850 °C, as can be seen from Table 5.1.

The oxygen diffusion coefficients associated with the intergranular and transgranular oxidation of IN617, $D_O^{617,IGO}$ and $D_O^{617,TGO}$, were determined by using $N_O^{617}(RP)$ and the ternary

interdiffusion coefficient for Al in γ phase of the Ni-Cr-Al system, ($\widetilde{D}_{Al}^{Ni\text{-}Cr\text{-}Al} = 4.07 \times 10^{-13} cm^2/s$ *at 850 °C* [109]**,** in Equation (2.105). Table 5.2 summarizes the calculated values of $D_O^{617,IGO}$ and $D_O^{617,TGO}$ which are approximately 5 orders of magnitude greater than those reported for pure nickel, D_O^{Ni}, at 850 °C by Park and Altstetter [107]. Similar observations were made by Stott et al. [30,31] and Whittle et al. [29] in binary Ni-Al alloys oxidized in Ni-NiO Rhines packs in the temperature range of 800 - 1100 °C. They reported oxygen diffusion coefficients in Ni-Al alloys that are up to 4 orders of magnitude greater than that in pure nickel, which was attributed to the formation of incoherent boundaries between the internal Al_2O_3 precipitates and the alloy matrix.

Whittle et al. [29] and Stott et al. [30,31] assumed that the internal oxidation kinetics is governed by an effective oxygen flux, which is the sum of oxygen fluxes through the metal lattice and along the internal oxide-metal interfaces. Based on this assumption, they developed a model which predicted an effective oxygen diffusion coefficient as a function of the lattice and interfacial oxygen diffusion coefficients in the internal oxidation zone. Referring to the internal oxidation kinetics data shown in Figures 4.18 and 4.19 for the IN617 samples oxidized in the Cr-Cr_2O_3 Rhines pack according to their model described in Section 2.5.4.1, the interfacial oxygen diffusion coefficient is calculated to be 0.13 cm^2/s. This value, however, is so high that it seems improbable for oxygen diffusion coefficient in IN617 at 850 °C. High values of $D_O^{617,IGO}$ and $D_O^{617,TGO}$, shown in Table 5.2, can be attributed to the enhanced oxygen diffusion along the alloy matrix - intergranular Al_2O_3 and alloy matrix - transgranular Al_2O_3 interfaces. Considering that the lattice diffusion coefficient of oxygen in a nickel based matrix is too low to sustain the measured rates of Al_2O_3 penetration in IN617 at 850 °C, it is concluded that accelerated oxygen

diffusion along the incoherent Al_2O_3-alloy boundaries resulted in rapid internal Al oxidation of IN617.

The values of $D_O^{617,IGO}$ and $D_O^{617,TGO}$ were then used to determine the oxygen solubility at the alloy - Cr_2O_3 interface in Env.9 and Env. 1320 using Equation (2.114):

$$\frac{N_O^{(s)}}{N_{Al}^{(o)}} = \frac{\nu\left[erf\gamma - erf\left(1/2\sqrt{k_C^{Cr_2O_3}/D_O}\right)\right]exp(\gamma^2)}{\left[\phi^{1/2}exp(\gamma^2\phi)erfc(\gamma\phi^{1/2})\right]}, \tag{5.6}$$

where the values of $k_C^{Cr_2O_3}$ in Equation (2.114) are reported in Table 4.15. Table 5.1 shows that the oxygen solubility at the alloy - Cr_2O_3 interface in He-CO-CO_2 environments is more than 4 times that at the alloy surface in the Cr-Cr_2O_3 Rhines pack exposure. Therefore, the oxygen partial pressure at the alloy - Cr_2O_3 interface in He-CO-CO_2 environments is greater than the equilibrium dissociation oxygen partial pressure of Cr_2O_3 established in the Rhines pack, indicating that the surface Cr_2O_3 film is gas permeable. This result is the first to provide quantitative evidence for the gas permeability of surface Cr_2O_3 film, which apparently establishes the mechanism for enhanced oxygen solubility at the alloy - Cr_2O_3 interface.

The Rhines pack and He-CO-CO_2 exposures conducted at 850 °C established that the governing oxygen transport mechanisms of rapid internal oxidation kinetics of IN617 are gas permeability of the surface Cr_2O_3 film resulting in increased oxygen solubility at the alloy - Cr_2O_3 interfaces and enhanced oxygen diffusion along the incoherent Al_2O_3 - alloy interfaces.

5.2. Oxidation of IN617 in He-CO-CO_2 environments in the temperature range of 750 - 850 °C

Surface and internal oxidation rate constants reported in Table 4.15 (Section 4.2.4) are compiled in an Arrhenius plot, as shown in Figure 5.1, to determine the activation energies associated with each oxidation process in the temperature range of 750 - 850 °C as a means to identify their mechanisms. Table 5.3 shows the activation energies determined for surface Cr oxidation of IN617 as 169.0 ± 13.2 and 234.4 ± 8.9 kJ/mol, for intergranular Al oxidation as 233.1 ± 29.3 and 358.1 ± 14.4, and for transgranular Al oxidation as 229.8 ± 41.7 and 330.2 ± 23.7 in Env.9 and Env. 1320, respectively. These activation energy values are used to extrapolate the rate constants measured in this work to 950 °C to compare with those reported in the literature for the oxidation of IN617 in a simulated IHX helium environment.

Cabet et al. [5,44] oxidized IN617 samples in a simulated IHX helium environment at 950 °C for up to 5000h. This environment consisted of 160 molppm H_2, 16 molppm CH_4, 40 molppm CO and 1.6 molppm H_2O in helium. The gas flow rate was maintained in the range of 833-1667 ml/min, which is much higher than that is used in this study (200 ml/min). Figure 5.1 shows that the extrapolation of the surface Cr, intergranular and transgranular Al oxidation rate constants measured in this study to 950 °C agreed well with those reported by Cabet et al. [5,44]. This agreement in the surface and internal oxidation kinetics measured in both studies can be further substantiated if the oxygen and carbon activities established in Env. 9 and Env. 1320 are also in agreement with those established in the simulated IHX helium environment. The oxygen and carbon activities of Env. 9 and Env. 1320 can be calculated using the following equations:

$$P_{O_2}^{He\text{-}CO\text{-}CO_2} = \left(P_{CO_2}/P_{CO}\right)^2 \times \left[\exp[(-282400 + 86.81T)/RT]\right]^2, \quad (5.7)$$

and

$$a_C^{He\text{-}CO\text{-}CO_2} = \left(P_{CO}^2/P_{CO_2}\right)/\exp[(-170700 + 174.5T)/RT]. \quad (5.8)$$

Table 5.4 shows that the oxygen and carbon activities reported for the simulated IHX environment at 950 °C [5] are very similar to those established in Env. 9 and Env. 1320. Therefore, the composition of the He-CO-CO_2 environments and the gas flow rate selected in this work successfully reproduced the expected surface and internal oxidation kinetics of IN617 in a simulated IHX environment in the temperature range of 750 - 850 °C.

Sections 5.2.1 and 5.2.2 will discuss the mechanisms of surface Cr and internal Al oxidation of IN617 in relation to the oxidation rate constants and activation energies reported in this section.

5.2.1. Mechanism of surface Cr oxidation of IN617 in He-CO-CO_2 environments at 750 - 850 °C

To understand the growth mechanism of Cr_2O_3 on IN617, the following approach is used. First, the growth direction of Cr_2O_3 is observed by microstructure characterization to determine the predominantly mobile species in Cr_2O_3. Next, the defect structure of Cr_2O_3 growing on IN617 in He-CO-CO_2 environments is identified by examining the oxygen partial pressure dependence of the Cr oxidation rate constants determined in this study in comparison with those reported for similar alloys in a wide oxygen partial pressure and temperature range. Finally, the diffusion coefficient of the predominantly mobile species in Cr_2O_3 is calculated and compared with the literature values to determine the mechanism that govern Cr oxidation kinetics of IN617 in He-CO-CO_2 environments.

Figure 5.2 shows the microstructures of IN617 samples exposed to Env. 9 and Env.1320 at 800 °C for 225h. The bright phases seen in the sub-surface regions of both microstructures are M_6C type carbides, which presumably remained stable throughout the exposure. Smooth top

surfaces of the carbides indicate that the precipitates were present at the surface of the as-polished samples. Considering that the carbides mark the original alloy surface, the growth direction of the surface Cr_2O_3 film appears to be outward. No significant cracking or blistering of the Cr_2O_3 film is observed; therefore nucleation of new oxide particles within the existing scale due to possible inward oxygen diffusion is ruled out. These observations indicated that Cr_2O_3 grows predominantly by outward diffusion of chromium cations.

The diffusion mechanism of chromium cations can be determined if the defect structure of Cr_2O_3 growing in He-CO-CO_2 environments is known. Atkinson and Taylor [68] showed that at low oxygen partial pressures (< 10^{-15} atm) Cr_2O_3 is an n-type semiconductor containing cation interstitials as the dominant defects; whereas at high ambient oxygen partial pressures Cr_2O_3 becomes a p-type semiconductor containing fully ionized cation vacancies. Referring to the oxygen activities of Env. 9 and Env. 1320 summarized in Table 5.4, Cr_2O_3 should grow on IN617 predominantly by the interstitial diffusion of Cr cations in He-CO-CO_2 environments at 750 - 850 °C. As such, the oxidation rate constant should have a very weak negative dependence on the environment oxygen partial pressure according to the Equation (2.62). To verify this, the surface Cr oxidation rate constants of IN617 in He-CO-CO_2 environments are compared with those reported in the literature for Ni-based superalloys [69,110] in a wide range of ambient oxygen partial pressures at temperatures 700-1100 °C.

Figure 5.3 shows that the values of $k_S^{Cr_2O_3}$ values determined for IN625, IN718, Hastelloy X and Haynes 230 in air were lower than those did in H_2-H_2O environments especially at temperatures below 900 °C [69,110]. In the temperature range of 750 - 850 °C, the values of the surface Cr oxidation rate constants of IN617 in He-CO-CO_2 environments obtained in this study fall in between those reported for the rest of the superalloys oxidized in air and in H_2-H_2O

environments. Furthermore, the activation energy for surface Cr oxidation of IN617 (169.0 - 234.4 kJ/mol) in He-CO-CO_2 environments determined in this study was in close agreement with the range of activation energies reported for the rest of the superalloys in H_2-H_2O environments (148 - 240 kJ/mol [69]). However, these values were much lower than the range of the activation energy values reported for the oxidation of IN625, IN718, Hastelloy X and Haynes 230 in air (314 - 340 kJ/mol [69,110]). This suggests that the dominant transport mechanism in Cr_2O_3 forming on the surface of nickel based superalloys changes at an intermediate range of oxygen partial pressures.

The ambient oxygen partial pressure dependence of the surface Cr oxidation rate constants of IN617 and the other Ni-based superalloys is investigated at 850 °C because the data presented in Figure 5.3 exhibited the least scatter, which can be attributed to alloy effects, at this temperature. Figure 5.4 shows the ambient oxygen partial pressure dependence of the surface Cr oxidation rate constants of IN617 measured in this work and those reported for the rest of the Ni-based superalloys at 850 °C. The trendline shown on the figure indicates a slightly negative ambient oxygen partial pressure dependence of the rate constants over a wide range between 3.6×10^{-24} - 0.21 atm. Referring to Section 2.3.1, this trend indicates that Cr_2O_3 growing on the Ni-based superalloys in low oxygen partial pressure environments cannot exhibit p-type behavior, which rules out vacancy diffusion to be the primary growth mechanism. On the other hand, the activation energy values reported for the oxidation of IN625, IN718, Hastelloy X and Haynes 230 in air (314 - 340 kJ/mol [69,110]) are much greater than those reported for the same alloys in H_2-H_2O environments (148 - 240 kJ/mol [69]) and for the interstitial diffusion mechanism of Cr in Cr_2O_3 (230 - 245) kJ/mol reported by Kofstad and Lillerud [57,58,63,66,67]. Therefore, in high oxygen partial pressure environments, Cr_2O_3 growing on nickel-based superalloys may

show p-type behavior containing cation vacancies as the primarily mobile species. These observations agree with Atkinson and Taylor's work [68] and it is likely that Cr_2O_3 exhibits n-type semiconductor behavior at very low oxygen partial pressure environments. As such, chromium interstitials are likely to be the primary mobile species in Cr_2O_3 growing on IN617 in He-CO-CO_2 environments.

The diffusion coefficients of Cr cations that correspond to the surface Cr oxidation kinetics of IN617 in Env. 9 and Env. 1320 can be determined by examining the point defect equation for Cr interstitials in Cr_2O_3:

$$3/2O_O^X + Cr_{Cr}^X = Cr_i''' + 3e' + 3/4O_2(g), \tag{5.9}$$

where O_O^X and Cr_{Cr}^X designate the normal lattice positions of O and Cr in the Cr_2O_3 lattice, e' is electrons and Cr_i''' represents the triple charged Cr interstitials. The surface oxidation rate constants summarized in Table 4.15, $k_S^{Cr_2O_3}$, can be related to the diffusion coefficient of Cr interstitials in Cr_2O_3, $D_{Cr,i}^{Cr_2O_3}$, as follows:

$$k_S^{Cr_2O_3} = 4 \times D_{Cr,i}^{o,Cr_2O_3} \times \left[\left(P_{O_2}^{int}\right)^{-3/16} - \left(P_{O_2}^{ext}\right)^{-3/16}\right], \tag{5.10}$$

where $D_{Cr,i}^{o,Cr_2O_3}$ is the self-diffusion coefficient of Cr interstitials in Cr_2O_3 at P_{O_2}= 1atm. Self-diffusion coefficients of Cr interstitials in Cr_2O_3 at the equilibrium oxygen activities of Env. 9 and Env. 1320, $D_{Cr}^{Cr_2O_3}$, can be calculated as follows:

$$D_{Cr,i}^{Cr_2O_3} = D_{Cr,i}^{o,Cr_2O_3} \times \left[\left(P_{O_2}^{int}\right)^{-3/16} - \left(P_{O_2}^{ext}\right)^{-3/16}\right], \tag{5.11}$$

where $P_{O_2}^{int}$ and $P_{O_2}^{ext}$ are the oxygen partial pressures at the alloy-oxide and oxide-gas interfaces, respectively. $P_{O_2}^{int}$ values at 750 - 850 °C are calculated by considering the increase in the oxygen activity at the metal-oxide interface due to gas permeability of the Cr_2O_3 film. The details of this calculation will be given in Section 5.2.2. The values of $P_{O_2}^{ext}$ in the temperature range of 750 -

850 °C are given in Table 5.4. It is important to note that the CO and CO_2 molecules in a flowing helium stream do not reach equilibrium on the alloy surface. The steady-state oxygen activities of Env. 9 and Env. 1320 could not be calculated because the reaction rate constants of CO and CO_2 molecules on the surface of IN617 at 750 - 850 °C have not been reported in the literature. Nevertheless, the anticipated difference between the steady state oxygen partial pressures and the $P_{O_2}^{ext}$ values given in Table 5.4 has no effect on the diffusion coefficients calculated using Equation (5.10). Tables 5.5 and 5.6 summarize the values of $D_{Cr,i}^{o,Cr_2O_3}$ and $D_{Cr,i}^{Cr_2O_3}$ calculated using Equations (5.10) and (5.11) based on the surface Cr oxidation rate constants of IN617 measured in Env. 9 and Env.1320 at at 750 - 850 °C.

The values of $D_{Cr,i}^{Cr_2O_3}$ calculated from Equation (5.11) are also plotted in Figure 5.5 in comparison with the lattice, grain boundary and effective diffusion coefficients of Cr in Cr_2O_3 reported in the literature using SIMS and radiotracer techniques. In general, $D_{Cr,i}^{Cr_2O_3}$ values calculated in this work are greater than the lattice diffusion coefficients of Cr in polycrystalline Cr_2O_3 measured by Tsai et al. (5.9×10^{-18} cm^2/s at 800 °C and 2×10^{-17} at 900 °C) [53], by Lobnig et al. (4×10^{-16} - 1×10^{-14} at 900 °C) [70], by Sabioni et al. (2×10^{-21} at 900 °C) [61,73,74] and Atkinson et al. (8×10^{-21} at 900 °C) [68]. On the other hand, the $D_{Cr,i}^{Cr_2O_3}$ values corresponding to the oxidation kinetics of IN617 in Env. 9 and Env. 1320 appears to be in very good agreement with the effective diffusion coefficient of Cr in Cr_2O_3 reported by Tsai [53] both at 800 and 900 °C. This indicates that the growth kinetics of Cr_2O_3 is likely to be facilitated by the grain boundary diffusion of Cr cations in Cr_2O_3 in addition to the lattice diffusion of Cr interstitials. This hypothesis can further be supported by considering that the activation energy values measured for the surface Cr oxidation of IN617 in Env. 9 and Env. 1320 (169.0 - 234.4

kJ/mol) are lower than those reported for the interstitial diffusion Cr in Cr_2O_3 lattice (230 - 245 kJ/mol) [57,58,63,66,67].

In conclusion, surface Cr oxidation of IN617 in He-CO-CO_2 environments is primarily controlled by the outward diffusion of Cr cations. Cr_2O_3 film appears to exhibit n-type behavior where Cr interstitials are the predominantly mobile species. Since the lattice diffusion coefficients of Cr in Cr_2O_3 reported in the literature are at least an order of magnitude lower than the diffusion coefficients determined in this work using Equation (5.11), it is concluded that the grain boundary diffusion of Cr in Cr_2O_3 facilitates the surface Cr oxidation kinetics of IN617.

5.2.2. Internal Al oxidation of IN617 in He-CO-CO_2 environments at 750 - 850 °C

According to the classical theory of oxidation [19–23], internal oxidation is governed by the dissolution of oxygen at the alloy surface and oxygen diffusion through the alloy matrix surrounding the discrete spherical shaped internal oxide precipitates, which are assumed to block inward oxygen diffusion. On the other hand, internal Al_2O_3 precipitates with plate-like morphologies in the internal oxidation zone of IN617 facilitate inward oxygen diffusion due to the formation of continuous incoherent alloy/oxide interfaces. Referring to Section 5.1, the oxygen diffusion coefficients ($D_O^{617,IGO}$ and $D_O^{617,TGO}$) along these interfaces are more than 5 orders of magnitude greater than those reported in pure nickel at 850 °C. Therefore, internal Al oxidation of IN617 is governed by an interfacial oxygen diffusion mechanism rather than oxygen diffusion along the alloy matrix. This section aims to further substantiate this hypothesis by determining the Arrhenius parameters (activation energy and pre-exponential coefficient) of $D_O^{617,IGO}$ and $D_O^{617,TGO}$ in He-CO-CO_2 environments at temperatures 750 - 850 °C and comparing with those of the oxygen diffusion coefficients reported in pure nickel and binary nickel based alloys.

To determine the Arrhenius parameters of the oxygen diffusion coefficients along the alloy-Al_2O_3 interfaces, first their values at 800 and 750 °C must be known. These values can be calculated from the measured intergranular and transgranular oxidation rate constants at each temperature using Equation (2.114). To carry out this calculation, it is necessary to extrapolate the oxygen solubility values reported in Table 5.1 ($N_O^{617,IGO}$ and $N_O^{617,TGO}$) to 800 and 750 °C using the activation energy for oxygen solubility in IN617. The activation energy for oxygen solubility in IN617 was determined by calculating the values of $N_O^{617}(RP)$ at 750 and 800 °C using Equation (5.1) which also requires $N_O^{Ni}(RP)$ values to be known at both temperatures. $N_O^{Ni}(RP)$ values were calculated using Equation (5.5) and the values of the Sievert's constants, S_O^{Ni}, determined from Equation (5.3) as $261.6\ at.fr./\sqrt{atm}$ and $96.6\ at.fr./\sqrt{atm}$ at 750 and 800 °C, respectively.

The logarithm of the $N_O^{617}(RP)$ values calculated at 750 - 850 °C was plotted against the reciprocal temperature in Figure 5.6 in comparison with the values of $N_O^{Ni}(RP)$ and $N_O^{Ni}(Ni/NiO)$ calculated according to the solubility data reported by Park and Altstetter [107] and Seybolt [111,112] in pure nickel. It is important to note that Seybolt's data exhibits opposite temperature dependence, which is not expected from the metal-oxygen systems. The linear regression fit of $N_O^{617}(RP)$ values gave an activation energy of 94.4 kJ/mol for oxygen solubility in IN617, which is greater than that for $N_O^{Ni}(Ni/NiO)$ (55 kJ/mol [107]) as shown in Table 5.7. The increase in the activation energy is mainly due to the presence of Cr in IN617, since the free energy of formation for Cr_2O_3 is more negative than that for NiO. Figure 5.6 also shows the logarithm of the extrapolated values of $N_O^{617,IGO}$ and $N_O^{617,TGO}$ in Env. 9 and Env. 1320 (given in Table 5.1) to 750 and 800 °C using the activation energy for oxygen solubility in IN617. These values are greater than $N_O^{617}(RP)$ by an order of magnitude due to the gas permeability of the

Cr_2O_3 film. On the other hand, they are consistently lower than $N_O^{Ni}(RP)$ mainly due to the lower oxygen solubility in IN617 in association with the presence of Cr in IN617.

After calculating the oxygen solubility values in Env. 9 and Env. 1320 at 750 and 800 °C, the values of the oxygen diffusion coefficients corresponding to the intergranular and transgranular oxidation of IN617 were determined using Equation (2.114) and following the same approach described in Section 5.1. $\widetilde{D}_{Al}^{Ni-Cr-Al}$ values to be substituted in Equation (2.114) were also extrapolated to 750 and 800 °C using the activation energy value of 288 kJ/mol, reported by Nesbitt and Heckel [109]. The logarithm of the $D_O^{617,IGO}$ and $D_O^{617,TGO}$ values plotted against reciprocal temperature in Figure 5.7 in comparison with the oxygen diffusion coefficients in nickel and binary Ni-X alloys (X = Si, Cr, Be, Al) determined by experimental studies [30,31,107,113–119] and by atomistic modeling [120,121]. The linear regression fit of the $D_O^{617,IGO}$ and $D_O^{617,TGO}$ values in the temperature range of 750 - 850 °C yielded the activation energy values to be 149.9 - 154.4 kJ/mol and 244.8 - 284.0 kJ/mol, respectively. Table 5.8 summarizes the pre-exponential coefficients and the activation energies of all the oxygen diffusion coefficients plotted in Figure 5.7.

As can be seen from Figure 5.7, the magnitudes and the activation energies of $D_O^{617,IGO}$ and $D_O^{617,TGO}$ are in agreement with the oxygen diffusion coefficients along the Al_2O_3 - alloy interfaces measured in the internal oxidation zone of binary Ni-2Al and Ni-8Al alloys by Whittle et al. [29] and Stott et al. [30,31]. This confirms that the internal Al oxidation of IN617 is also facilitated by enhanced diffusion along the Al_2O_3 - alloy interfaces. The difference between the magnitudes of the interfacial oxygen diffusion coefficients in Ni-Al alloys and IN617 can be attributed to the different chemistry and crystallographic properties of the matrix surrounding the

Al_2O_3 precipitates, which can largely influence the atomic structure and the chemical composition of these interfaces [122].

The unique rod-shaped morphology of the Al_2O_3 precipitates yields the interfacial oxygen diffusion coefficients both Ni-Al alloys and in IN617 to be several orders of magnitude greater than those determined by the internal oxidation measurements on other binary Ni based alloy systems, such as Ni-V [31], Ni-Si [114], Ni-Cr [115], and Ni-Be [116,117]. Figure 5.8 shows the microstructures of the Ni - V and Ni - Cr alloys internally oxidized in Ni - NiO Rhines packs in comparison with the microstructure of IN617 oxidized in Env. 1320 at 850 °C. Discrete, globular shaped oxide precipitates were formed in the sub-surface region of both Ni-V and Ni-Cr alloys [31], whereas continuous, rod-shaped Al_2O_3 precipitates extending along the direction of inward oxygen diffusion formed in the sub-surface region of IN617. The oxygen diffusion is greatly enhanced along these continuous and incoherent Al_2O_3 - alloy interfaces, whereas the discrete and globular Cr and V oxide particles do not facilitate the same effect even though they may also form incoherent interfaces with the base metal. This could be attributed to two possible reasons: First, the interfaces along the discrete oxide particles most probably fail to sustain continuous oxygen flux along the direction that the internal oxidation front advances. Second, the interfacial area - to - volume ratio for the spherical precipitates are smaller than that for the continuous rod-shaped precipitates assuming that the precipitates in both morphologies have identical volumes [29]. Considering that the enhancement in the oxygen diffusion is proportional to the area fraction of the incoherent interfaces between the precipitates and the alloy matrix, the enhancement effect would be less significant along the interfaces of the spherical precipitates. Furthermore, the increase in oxygen flux is enhanced along the interfaces of the spherical oxide precipitates is probably much less than the overall decrease in the inward oxygen flux achieved

due to the blocking effect of the bulk volume of these precipitates. As such, internal oxidation in alloy systems other than Ni-Al based alloys is mainly governed by the diffusion of oxygen along the alloy matrix surrounding the oxide precipitates.

Whittle et al. [29] and Stott et al. [30,31] assumed that the inward diffusion of oxygen through the Ni matrix (depleted in Al) surrounding the Al_2O_3 precipitates still remained significant. According to their model described in Section 2.5.4.1, an effective oxygen diffusion coefficient, which is the weighted average of D_O^{Ni} and $D_O^{Ni-Al}(int)$, governed the internal oxidation kinetics in Ni-Al alloys. However, this assumption does not apply for internal Al oxidation of IN617. As can be seen from Figure 5.7, the values of D_O^{Ni} are several orders of magnitude lower than those of $D_O^{617,IGO}$ and $D_O^{617,TGO}$ in the temperature range of 750 - 850 °C. Therefore, the lattice diffusion coefficients of oxygen in pure nickel are too low to sustain the observed internal aluminum oxidation kinetics in IN617. This leaves the enhanced oxygen diffusion along the Al_2O_3-alloy interfaces to be the mechanism of both intergranular and transgranular Al oxidation of IN617. This enhancement of the oxygen diffusion coefficients can be attributed to the crystallographic properties and chemical composition of the Al_2O_3-alloy interfaces as well as the chemical composition of the alloy matrix surrounding the precipitates.

As a final remark, the activation energy for oxygen diffusion along the intergranular Al_2O_3 - alloy interfaces is lower and the magnitude of oxygen diffusion coefficient is greater than that along the transgranular Al_2O_3 - alloy interfaces in the temperature range of 750 - 850 °C. This suggests that the grain boundaries of IN617 facilitate nucleation and growth of the Al_2O_3 precipitates. This hypothesis can be substantiated by the observations of Perusin et al. [123–125] and Shida et al. [126] which indicate that vacancy injection along the grain boundaries of pure nickel and binary Ni-Cr alloys results in formation of micro voids. The voids

can act as vacancy sinks enhancing oxygen flux along the grain boundaries and thereby promoting intergranular diffusion. Based on this understanding, oxygen diffusion occurs preferentially along the grain boundaries of IN617 facilitating intergranular Al oxidation, which appears to enhance oxygen diffusion along the intergranular Al_2O_3 - alloy interfaces.

In conclusion, the governing mechanism for rapid intergranular and transgranular Al oxidation of IN617 at 750 - 850 °C is enhanced oxygen diffusion along the incoherent Al_2O_3 - alloy interfaces. Oxygen diffusion through the alloy matrix appears to have negligible influence on both intergranular and transgranular Al oxidation. Greater values of the diffusion coefficients and lower activation energy values determined for the oxygen diffusion coefficients along the intergranular Al_2O_3 - alloy interfaces than those did along the transgranular Al_2O_3 - alloy interfaces indicate that the alloy grain boundaries facilitate intergranular Al_2O_3 precipitation.

5.3. Mitigation of the internal aluminum oxidation of Alloy 617 in He-CO-CO_2 environments

The collective impact of the oxygen transport mechanisms identified in this dissertation on the internal oxidation kinetics of IN617 can be used to determine the minimum amount of Al required in the alloy, $N_{Al}^{617,\min}$, above which the outward diffusion of Al is rapid enough to prevent internal oxidation. As described in Section 2.5.3, to sustain lateral growth of the internal oxide precipitates, the outward flux of Al should be sufficiently high for the volume fraction of internal precipitates to reach a critical value, $g_{Al_2O_3}^{crit}$. The degree of supersaturation of aluminum beneath the internal oxidation zone to achieve $g_{Al_2O_3}^{crit}$ is given by the solute enrichment factor, $\propto$, which can be calculated using Equation (2.117):

$$\propto = \left[\pi^{1/2}(\gamma\phi^{1/2})exp(\gamma^2\phi)erfc(\gamma\phi^{1/2})\right]^{-1}. \quad (5.12)$$

The enrichment factors calculated based on the measured intergranular and transgranular aluminum oxidation rate constants of IN617 at 850 °C are 1.54 and 3.22, respectively. Both values are greater than 1, which indicates that outward Al diffusion is not negligible and Al tends to enrich at the internal oxidation front. However, referring to the microstructures of the measured internal penetration depths of Al_2O_3 precipitates in IN617 samples oxidized in He-CO-CO_2 environments, Al enrichment does not seem to be sufficiently high to achieve the critical volume fraction of Al_2O_3 precipitates given by $g_{Al_2O_3}^{crit}$.

The critical concentration of aluminum required for the lateral growth of internal Al_2O_3 precipitates in the sub-surface region of IN617 can be calculated by using Equation (2.118):

$$N_{Al}^{\circ,crit} = \sqrt{\pi}\gamma\sqrt{\phi}exp(\gamma^2\phi)erfc\left(\gamma\sqrt{\phi}\right)g_{Al_2O_3}^{crit}V_{617}/V_{Al_2O_3}, \quad (5.13)$$

where $g_{Al_2O_3}^{crit}$ is equal to 0.3 [20], $V_{Al_2O_3}$ and V_{617} are 25.81 cm^3/mol and 6.67 cm^3/mol, respectively. Based on the greatest internal aluminum oxidation rate constant measured in this work ($k_S^{Cr_2O_3}(Env.9) = 3.94 \times 10^{-13}\ cm^2/sec$), the minimum Al concentration required to prevent rapid internal aluminum oxidation of IN617 in He-CO-CO_2 environments at 850 °C is 5.0 at. %.

Increasing the aluminum content of IN617 to 5.0 at. % (modified IN617 alloy) can greatly improve its corrosion resistance by promoting formation of continuous Al_2O_3 sub-oxide beneath the surface Cr_2O_3 film; however it is also necessary to predict the microstructure stability and mechanical properties of the modified IN617 for IHX service at high temperatures. For this purpose, the microstructure stability, creep-rupture and fatigue properties of two wrought nickel based superalloys containing 5.1 at.% Al (Udimet 710) and 6.2 at. % Al (Udimet 500) are investigated and compared with those of the original IN617 alloy. The compositions of these two higher Al containing alloys along with that of IN617 are given in Table 5.9.

Figure 5.9 shows the isothermal section of the ternary Ni - Cr - Al phase diagram at 850 °C [127] indicating that the solubility limit of aluminum in Ni - Cr - Al alloys at this temperature is 6.5 at.%. Hence, a modified IN617 alloy (Ni - 24Cr - 5Al) should remain in the single γ phase region at 850 °C and no secondary phases other than M_6C and $M_{23}C_6$ type carbides should be observed in its microstructure. However, the T-T-T diagram shown in Figure 2.1 indicates that γ' precipitation is observed even in the microstructure of the original IN617 alloy composed of only 2.4 at.% Al at 550 - 1000 °C. Furthermore, Udimet 710 (5.1 at.% Al) and Udimet 500 (6.2 at.% Al) are classified as precipitation-hardening alloys [32] and exhibit precipitation of γ', MC and $M_{23}C_6$ phases in the temperature range of 700 - 1100 °C [128,129]. Thus, the modified IN617 is expected to be a precipitation-hardening alloy in the temperature regime of 750 - 850 °C.

As shown in Figure 5.10, γ' - strengthened alloys Udimet 710 and Udimet 500 exhibit much higher creep-rupture strengths than that does the solid-solution hardened IN617 in the temperature range of 700 - 1000 °C. Furthermore, the low cycle fatigue strength of Udimet 720[8] [130] is much higher than that of IN617 [88], as shown in Figure 5.11. Improved fatigue strength of Udimet 720 can mainly be attributed to the microstructural effects such as grain size, grain orientation, dislocation substructure and grain boundary morphology; however it was also shown that uniform dispersion of fine γ' precipitates can improve fatigue life of an alloy by reducing the crack growth rate [32]. As such, the modified IN617 alloy has a potential to display an optimum combination of superior creep-rupture and fatigue properties owing to γ'-strengthening and closely controlled thermomechanical processing.

Perhaps a major concern for the high temperature mechanical properties of the modified IN617 alloy is to avoid coarsening of the γ' precipitates [32,129]. Lambert [129] reported that the size of γ' precipitates in Udimet 500 can increase by more than a factor of 2 after 3500h long

[8] Udimet 720 is very similar to Udimet 710 in composition and displays very similar mechanical properties.

creep exposure at 800 °C. Such coarsening of γ' precipitates can reduce the creep-rupture strength of the alloy approximately by 25% [32]. Furthermore γ' coarsening can result in depletion of Al from the alloy matrix as the driving force for γ' coarsening is the reduction of the γ' - γ interfacial area (Ostwald ripening), which is controlled mainly by aluminum diffusion [131–133]. If the concentration of Al in the alloy matrix is depleted below $N_{Al}^{\circ,crit}$ due to γ' coarsening, internal aluminum oxidation may occur in the subsurface region of the alloy. Addition of slow diffusing refractory elements such as Nb, Ta and Re, which can partition to the γ' phase, and increasing the Al/Ti ratio in the alloy composition have been reported to effectively retard γ' coarsening rates [132,133].

In summary, the modified IN617 alloy has a potential to display a combination of good oxidation resistance as well as improved creep-rupture and fatigue properties for long-term use in HTGR IHX environments at elevated temperatures. It is important to note that, precipitation and coarsening of γ' may result in substantial depletion of Al in the base alloy matrix. If the Al concentration in the subscale region of the modified IN617 alloy drops below the critical Al concentration of 5.0 at.% at 850 °C, then the lateral growth of continuous Al_2O_3 sub-oxide beneath the surface Cr_2O_3 film cannot be sustained and internal Al oxidation can occur during long term exposures in IHX helium equivalent environments. Therefore, it is recommended that the modified IN617 should contain more than 5 at.% Al to compensate Al depletion in the base alloy due to γ' precipitation and possible subsequent coarsening.

Table 5.1 Summary of the value of $N_O^{617}(RP)$ estimated from Equation (5.2), the oxygen solubility in pure nickel at the dissociation oxygen partial pressure of Cr_2O_3, $N_O^{Ni}(RP)$, and the oxygen solubility values determined at the alloy-Cr_2O_3 interfaces in the He-CO-CO_2 environments calculated from Equation (2.114) at 850 °C.

	RP	**Env. 9**	**Env. 1320**
$\boldsymbol{N_O^{Ni}(RP)}$ [107] **(at. fr.)**	8.78×10^{-11}	-	-
$\boldsymbol{N_O^{617}(RP)}$ **(at. fr.)**	5.57×10^{-12}	-	-
$\boldsymbol{N_O^{617,IGO}}$ **(at. fr.)**	-	2.13×10^{-11}	2.07×10^{-11}
$\boldsymbol{N_O^{617,TGO}}$ **(at. fr.)**	-	1.37×10^{-11}	1.08×10^{-11}

Table 5.2 Summary of the oxygen diffusion coefficients calculated from Equation (2.105) in comparison with that reported in pure nickel [107] at 850 °C.

$\boldsymbol{D_O^{617,IGO}}$ **(cm²/s)**	$\boldsymbol{D_O^{617,TGO}}$ **(cm²/s)**	$\boldsymbol{D_O^{Ni}}$ [107] **(cm²/s)**
9.79×10^{-4}	2.80×10^{-4}	1.15×10^{-9}

Table 5.3 Activation energies for surface Cr, intergranular Al and transgranular Al oxidation of IN617 in He-CO-CO_2 environments at 750 - 850 °C.

	Env. 9	**Env. 1320**
Surface Cr oxidation	169.0 ± 13.2	234.4 ± 8.9
Intergranular Al oxidation	233.1 ± 29.3	229.8 ± 41.7
Transgranular Al oxidation	358.1 ± 14.4	330.2 ± 23.7

Table 5.4 Comparison of the oxygen and carbon activities of the simulated IHX environment at 950 °C [5] with those of Env. 9 and Env. 1320.

T (°C)	IHX Helium - Cabet et al. [5]		Env. 9 - present work		Env. 1320 - present work	
	P_{O_2}	a_C	P_{O_2}	a_C	P_{O_2}	a_C
950	1.6×10^{-20}	1.6×10^{-4}	1.00×10^{-17}	2.00×10^{-6}	5.00×10^{-22}	4.00×10^{-2}
850	-		7.75×10^{-20}	8.11×10^{-6}	3.60×10^{-24}	0.17×10^{-1}
800	-		4.62×10^{-21}	1.90×10^{-5}	2.15×10^{-25}	4.10×10^{-1}
750	-		2.09×10^{-22}	4.85×10^{-5}	9.73×10^{-27}	1.00

Table 5.5 The values of the self diffusion coefficient of Cr in Cr_2O_3 at unit oxygen activity, $D_{Cr,i}^{o,Cr_2O_3}$, and at the equilibrium oxygen activity of Env.9, $D_{Cr}^{Cr_2O_3}$, calculated from the surface Cr oxidation rate constants determined in Env. 9 at 750 - 850 °C.

Temperature (°C)	$P_{O_2}^{ext}$ (atm)	$P_{O_2}^{int}$ (atm)	$D_{Cr,i}^{o,Cr_2O_3}$ Eqn (5.10)	$D_{Cr,i}^{Cr_2O_3}$ Eqn (5.11)
850	7.75×10^{-20}	2.02×10^{-25}	6.80×10^{-20}	2.90×10^{-15}
800	4.62×10^{-21}	1.28×10^{-26}	1.99×10^{-20}	1.42×10^{-15}
750	2.09×10^{-22}	6.21×10^{-28}	3.97×10^{-21}	5.01×10^{-16}

Table 5.6 The values of the self-diffusion coefficient of Cr at unit oxygen activity, $D_{Cr,i}^{o,Cr_2O_3}$, and at the equilibrium oxygen activity of Env.1320, $D_{Cr}^{Cr_2O_3}$, calculated from surface Cr oxidation rate constants determined in Env. 1320 at 750 - 850 °C.

Temperature (°C)	$P_{O_2}^{ext}$ (atm)	$P_{O_2}^{int}$ (atm)	$D_{Cr,i}^{o,Cr_2O_3}$ Eqn (5.10)	$D_{Cr,i}^{Cr_2O_3}$ Eqn (5.11)
850	3.60×10^{-24}	1.63×10^{-25}	1.97×10^{-19}	8.75×10^{-15}
800	2.15×10^{-25}	1.04×10^{-26}	3.40×10^{-20}	2.53×10^{-15}
750	9.73×10^{-27}	5.04×10^{-28}	5.90×10^{-21}	7.75×10^{-16}

Table 5.7 Comparison of the pre-exponential coefficients and the activation energy values of oxygen solubility in pure nickel with that in IN617.

	Activation energy (kJ/mol)	**Pre-exponential coefficient (at. fr.)**	**Temperature Range (°C)**	**Method**	**Reference**
$N_O^{Ni}(Ni/NiO)$	55	8.3×10^{-2}	800 - 1000	Potentiometric	Park and Altstetter [107]
$N_O^{Ni}(RP)$	94.4	2.2×10^{-6}	800 - 1000	Potentiometric	Park and Altstetter [107]
$N_O^{617}(RP)$	94.4	1.4×10^{-7}	800 - 1000	Thermodynamics [83]	This study
$N_O^{617}(Env.9)$	94.4	$5.1 - 5.2 \times 10^{-7}$	750 - 850	Thermodynamics [83]	This study
$N_O^{617}(Env.1320)$	94.4	$2.6 - 3.7 \times 10^{-7}$	750 - 850	Thermodynamics [83]	This study

Table 5.8 Pre-exponential coefficient and activation energy values of the oxygen diffusion coefficients in pure nickel, Ni-X (X = Al, Si, Cr, Be) binary alloys and in IN617.

	Activation energy (kJ/mol)	**Pre-exponential coefficient (cm^2/s)**	**Temperature Range (°C)**	**Method**	**Reference**
$D_O^{617,IGO}$	149.9 - 154.4	1.0×10^4 - 1.6×10^4	750 - 850	Internal oxidation	This study
$D_O^{617,TGO}$	244.8 - 284.0	6.3×10^7 - 4.2×10^9	750 - 850	Internal oxidation	This study
D_O^{Ni}	163.7 ± 0.5	4.9×10^{-2}	850 - 1400	Potentiometric	Park and Altstetter [107]
D_O^{Ni}	182.0	2.1	1000 - 1300	Electrochemical	Kerr [118]
D_O^{Ni}	239.8	12.1	350 - 1000	Desorption	Zholobov et al. [119]
D_O^{Ni}	413.2	8.9×10^7	1100 - 1200	Thermogravimetric	Alcock et al. [113]
D_O^{Ni}	338.7	1.9×10^4	900 - 1050	CO evolution	Smithells [134]
D_O^{Ni}	191.7	39.2	677 - 1327	Molecular dynamics simulation	Garruchet et al. [120]
D_O^{Ni}	158.7	5.5×10^{-3}	227 - 1453	First principals based modeling	Nam et al. [121]
$D_O^{Ni-Al}(eff)$ [9]	218.3 - 232	79.1 - 94.3	800 - 1100	Internal oxidation	Stott et al. [30,31]
$D_O^{Ni-Al}(int)$	183.4 - 197.2	2.2 - 2.6×10^4	800 - 1100	Internal oxidation	Stott et al. [30,31]
D_O^{Ni-Si}	309.2 - 311.1	7.9 - 9.5×10^4	800 - 1300	Internal oxidation	Barlow [114]
D_O^{Ni-Cr}	300.5	1.8×10^4	900 - 1300	Internal oxidation	Goto et al. [115]
D_O^{Ni-Be}	296.7	2.7×10^5	1000 - 1350	Internal oxidation	Lloyd [116,117]

[9] Effective oxygen diffusion coefficient calculated from $N_O \times D_O$ values reported by Stott et. al [30,31], using N_O^{Ni} value reported by Park and Altstetter [107]

Table 5.9 Chemical compositions of Udimet 500 and Udimet 710 [32] in comparison with that of IN617 [88].

	Element concentration (wt. % / at. %)								
	Ni	Cr	Co	Mo	Al	Ti	Fe	W	C
Udimet 500	47.9 / 45.2	19.0 / 20.2	19.0 / 17.8	4.0 / 2.3	3.0 / 6.2	3.0 / 3.5	4.0 / 4.0	-	0.08 / 0.4
Udimet 710	55.1 / 52.0	18.0 / 19.2	14.8 / 13.9	3.0 / 1.7	2.5 / 5.1	5.0 / 5.8	-	1.5 / 0.5	0.07 / 0.3
IN617	54.6 / 54.1	21.8 / 24.4	11.5 / 11.4	9.7 / 5.9	1.1 / 2.4	0.3 / 0.4	0.8 / 0.8	-	0.09 / 0.4

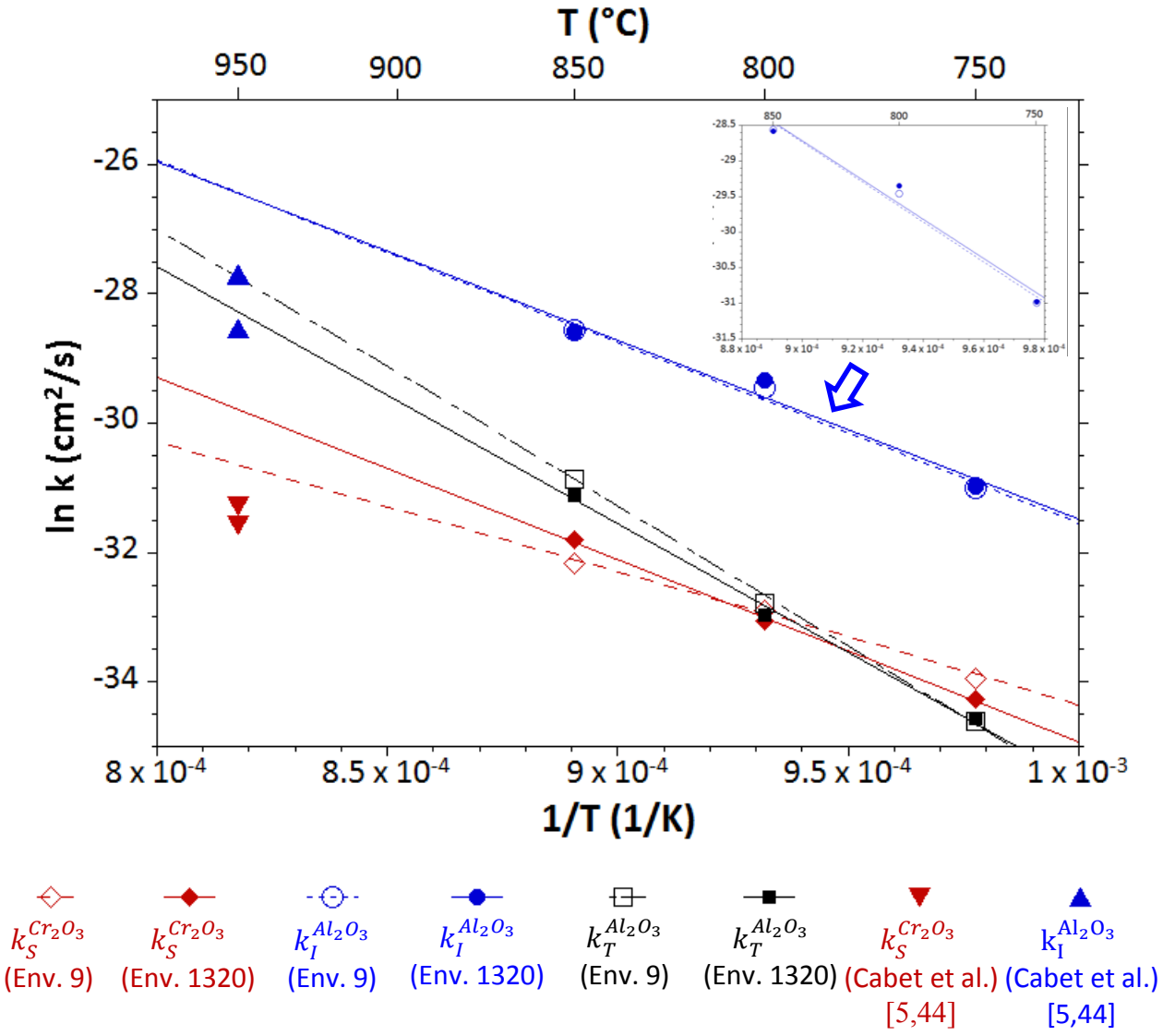

Figure 5.1. Arrhenius plot of the surface, intergranular and transgranular oxidation rate constants of IN617 exposed to Env.9 and Env.1320 at 750 - 850 °C. $k_S^{Cr_2O_3}$*(Cabet et al.)* and $k_I^{Al_2O_3}$*(Cabet et al.)* represents the surface Cr and intergranular Al oxidation rate constants measured by Cabet et al. [5,44].

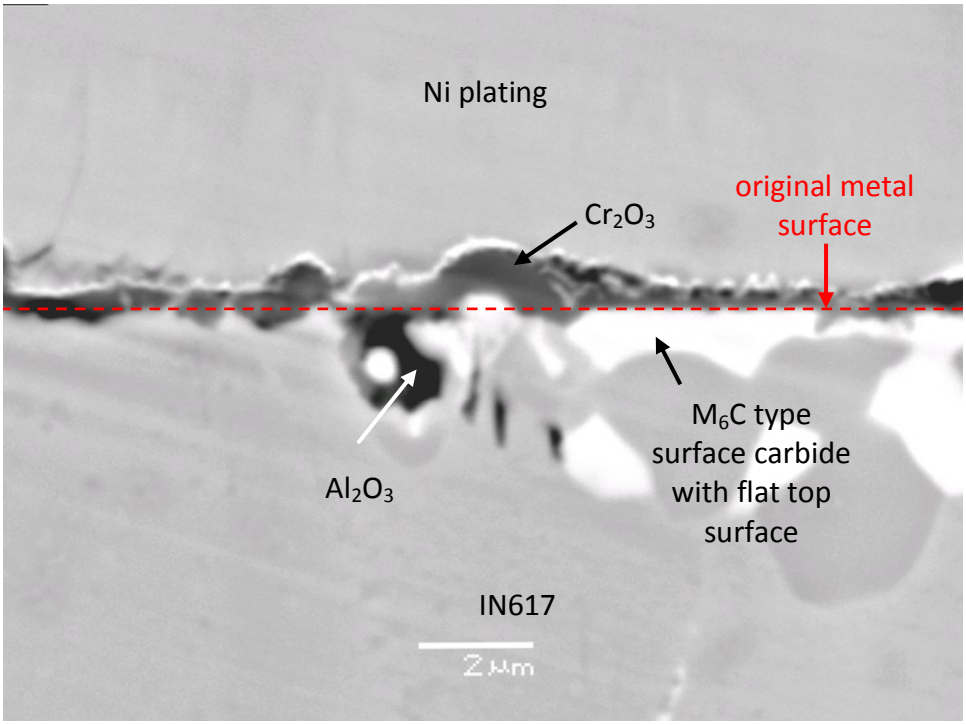

a)

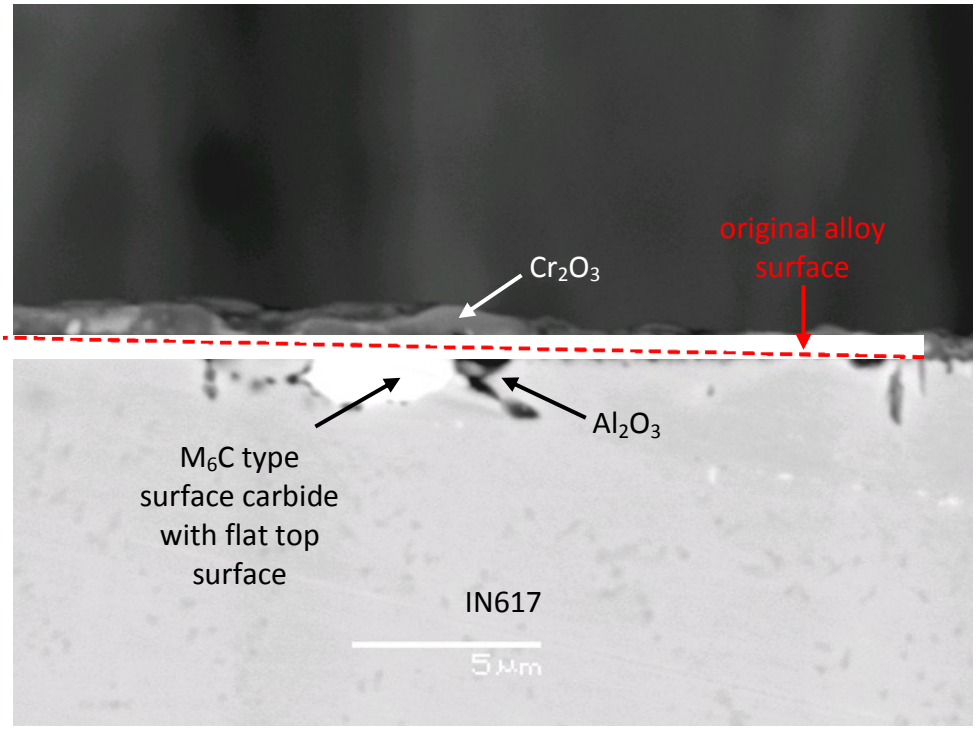

b)

Figure 5.2. Backscattered electron images of IN617 samples exposed to a) Env. 9 and b) Env.1320 at 800 °C for 225h. The flat top surfaces of the M_6C type carbides designate the original alloy surface marked with red dashed lines in each micrograph.

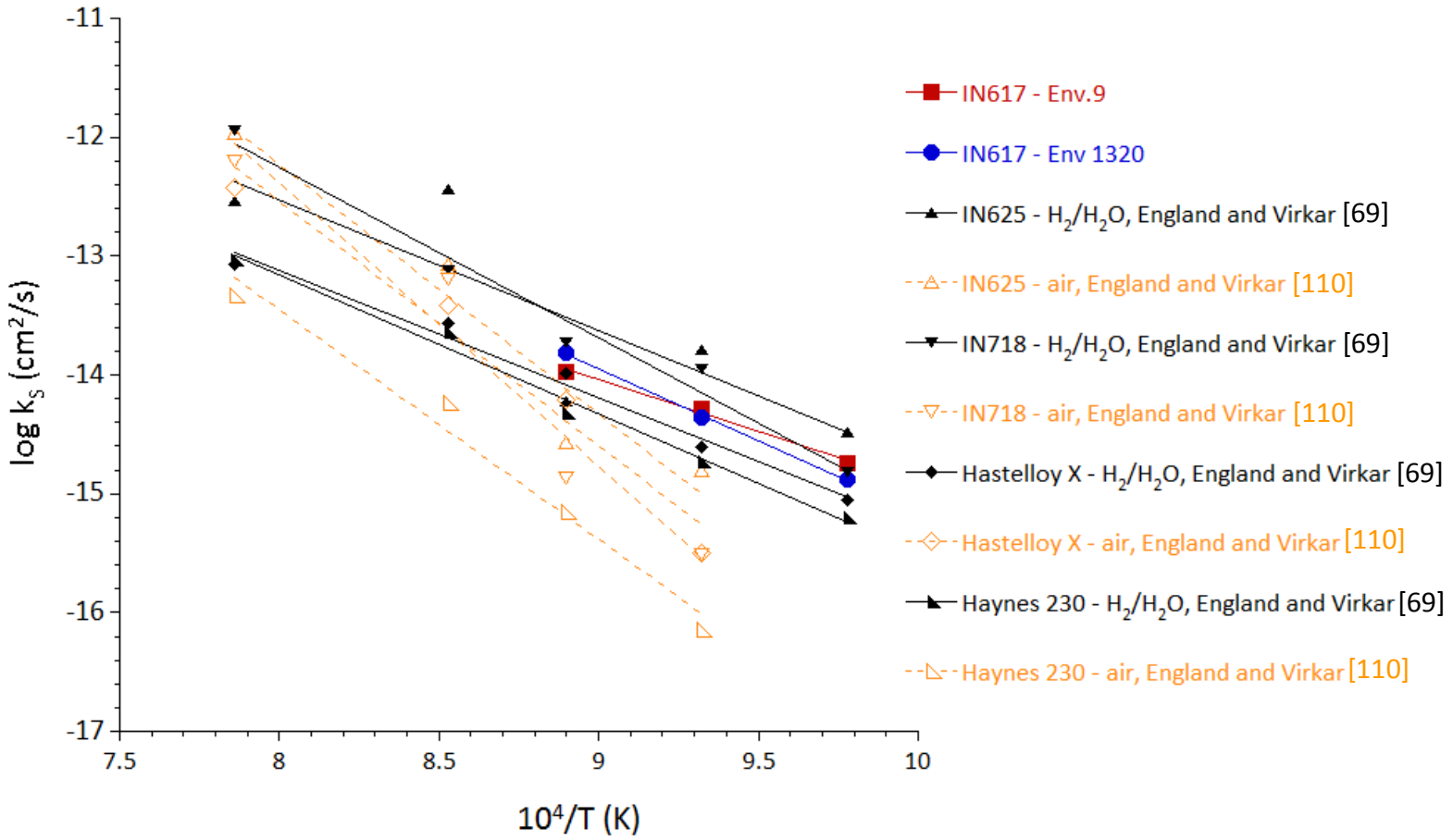

Figure 5.3. Comparison of the $k_S^{Cr_2O_3}$ values for surface Cr oxidation of IN617 in Env.9 and Env.1320 with those reported in the literature[10] for the oxidation of Ni-based superalloys in air (P_{O_2}= 0.21 atm) [110] and H_2 - H_2O ($P_{O_2} \cong 10^{-23}$ - 10^{-17} atm) [69] in the temperature range of 700 - 1100 °C.

[10] The oxidation rate constants reported by Virkar and England [69,110] were determined by analyzing the weight gain data according to the equation: $[\Delta W/A]^2 = k'_W \times t$, where $k'_W = 2 \times k_W$ given in Equation (2.28). For direct comparison with the surface oxidation rate constants determined in this study, k'_W values reported in the literature are divided by 2 and then converted into $k_S^{Cr_2O_3}$ values using Equation (2.24).

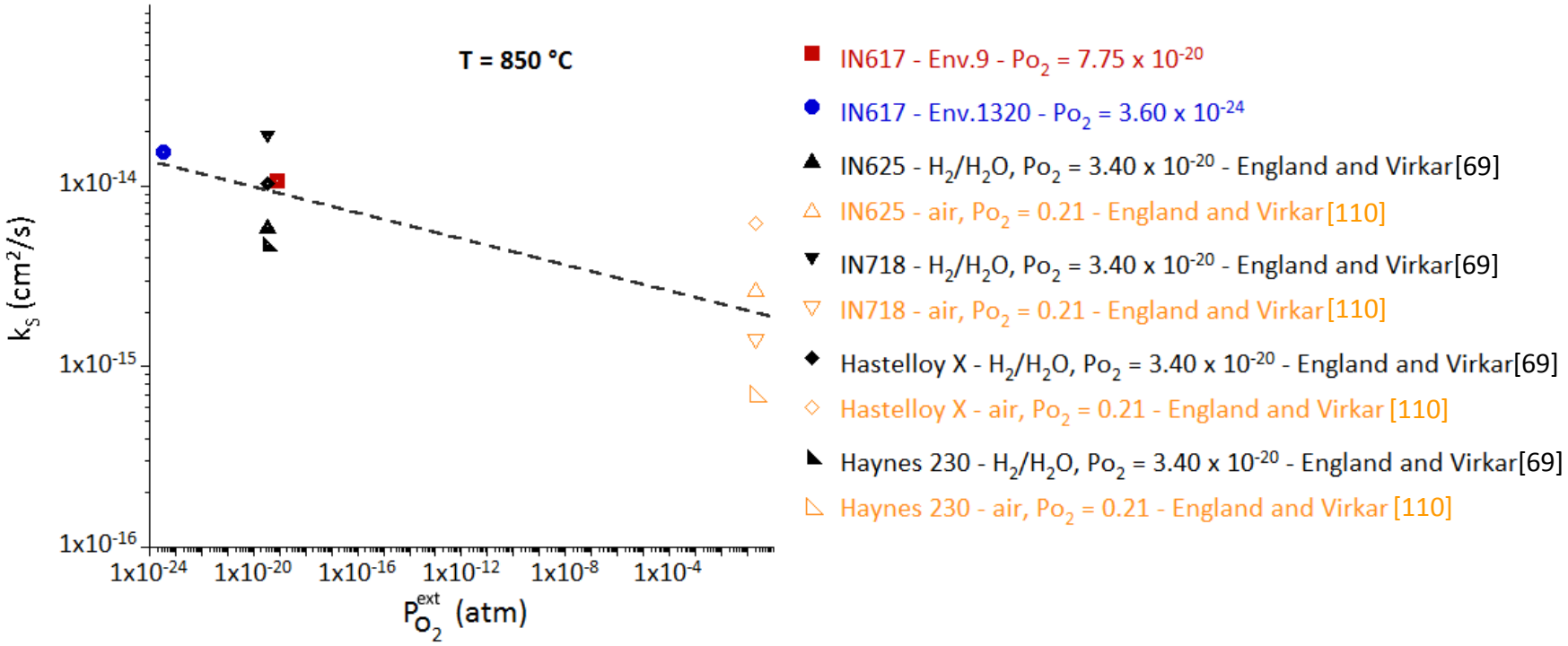

Figure 5.4. The ambient oxygen partial pressure dependence of the $k_S^{Cr_2O_3}$ values for the oxidation of IN617 in He - CO - CO_2, and those reported for the oxidation of IN625, IN718, Hastelloy X and Haynes 230 in H_2/H_2O and air at 850 °C [69,110] [11].

[11] The oxidation rate constants reported by Virkar and England [69,110] were determined by analyzing the weight gain data according to the equation: $[\Delta W/A]^2 = k'_W \times t$, where $k'_W = 2 \times k_W$ given in Equation (2.28). For direct comparison with the surface oxidation rate constants determined in this study, k'_W values reported in the literature are divided by 2 and then converted into $k_S^{Cr_2O_3}$ values using Equation (2.24).

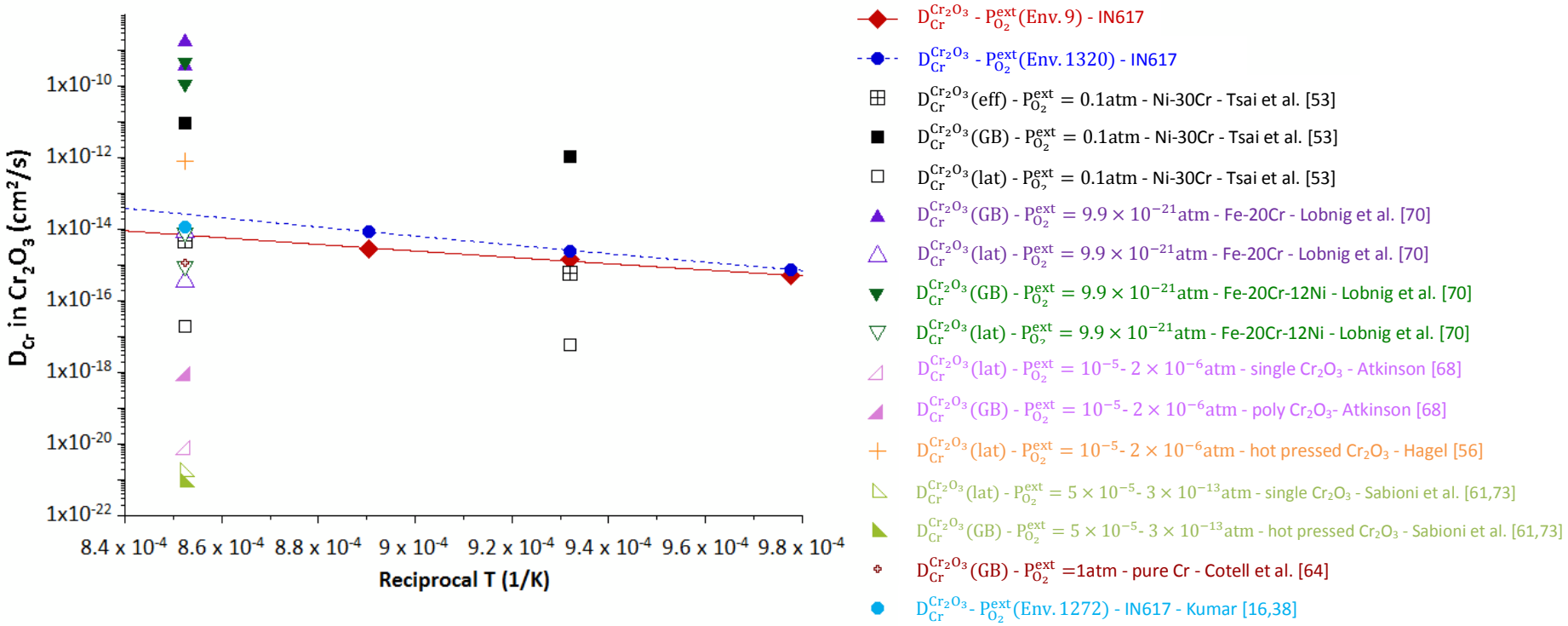

Figure 5.5. Comparison of the $D_{Cr,i}^{Cr_2O_3}$ values in Env. 9 and Env. 1320 calculated in this work using Equation (5.11) with the lattice, grain boundary and effective diffusion coefficients of Cr in Cr_2O_3 reported in the literature. The legend has the following format: [parameter] - [environment] - [Cr_2O_3 or the substrate material that the Cr_2O_3 is growing on] - [Citation]. Open and closed symbols designate the lattice and grain boundary diffusion coefficients of Cr in Cr_2O_3, respectively.

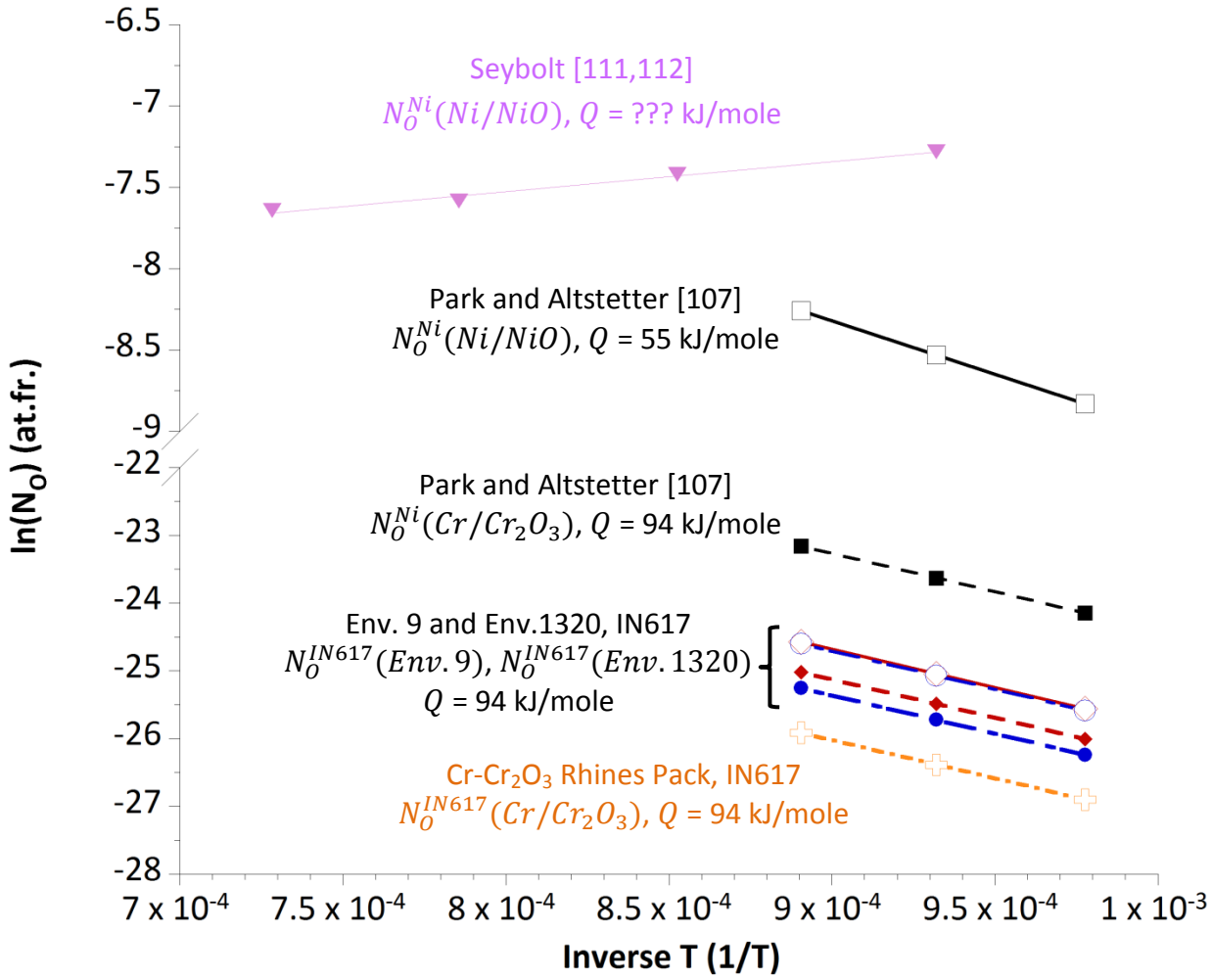

Figure 5.6. Comparison of the oxygen solubility values measured in IN617 in this work with the published values of oxygen solubility in nickel. $N_O^X(Y)$ indicates the oxygen solubility in X, at oxygen partial pressure of Y sustained at the metal/alloy surface. Q indicates the activation energy for oxygen solubility.

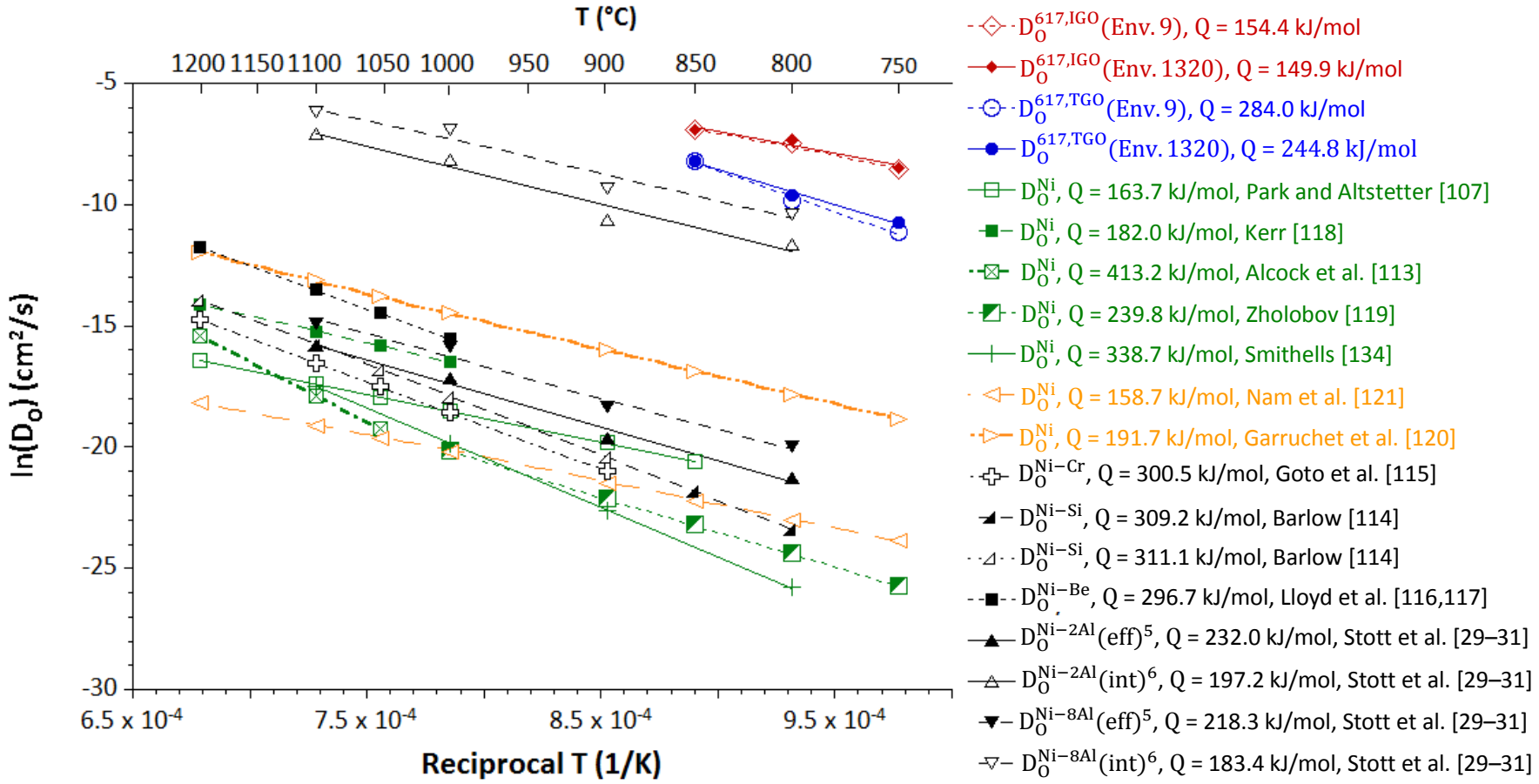

Figure 5.7. Comparison of the oxygen diffusion coefficients determined using Equation (2.114) based on the intergranular (red) and transgranular (blue) Al oxidation rate constants of IN617 in He-CO-CO_2 environments with those reported in pure nickel (green - experimental, orange - atomistic modeling) and in binary Ni based alloys (black). *Q* designates the activation energy of the diffusion coefficients.

[12] D_O^{Ni-xAl}(eff) represents the effective diffusion coefficient of oxygen in the internal oxidation zone of Ni-xAl, where x is the atomic fraction of Al [29–31].
[13] D_O^{Ni-xAl}(int) represents the interfacial diffusion coefficient of oxygen along the alloy-Al_2O_3 boundaries in the internal oxidation zone of Ni-xAl [29–31].

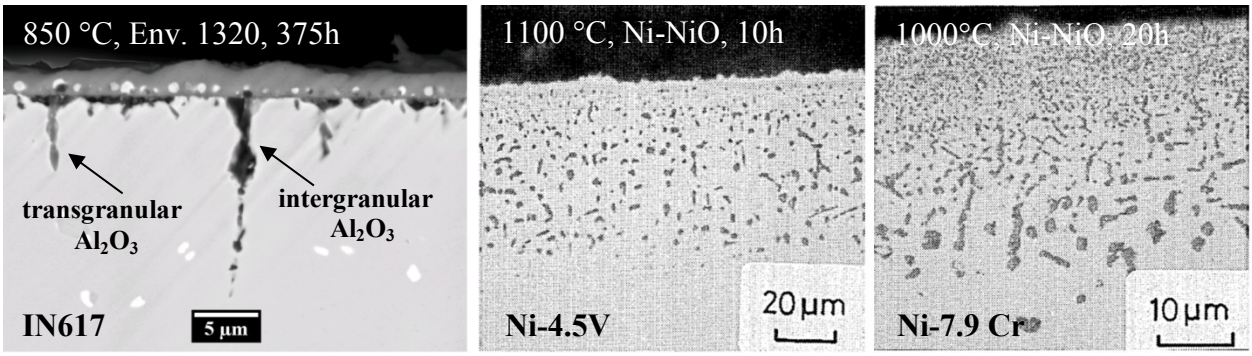

a) b) c)

Figure 5.8. Comparison of the a) plate-like morphologies of the intergranular and transgranular Al_2O_3 precipitates in IN617, which form continuous interfaces with the alloy matrix, with the discrete and globular internal b) V_2O_3 and c) Cr_2O_3 precipitates in the sub-surface regions of Ni-4.5V and Ni-7.9Cr alloys [31].

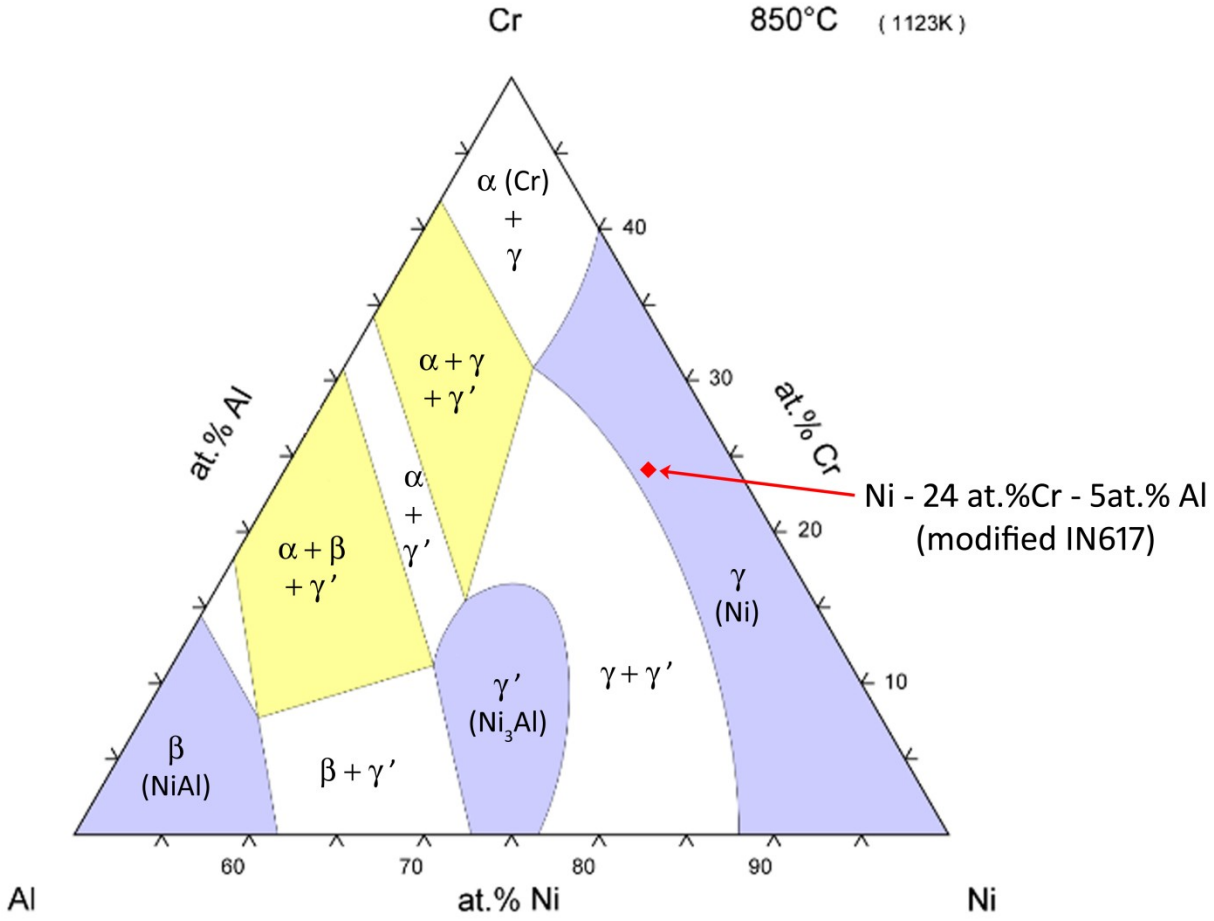

Figure 5.9. Isothermal section of the Ni-Cr-Al phase diagram at 850 °C [127] showing the composition of a Ni - 24 at.% Cr - 5at.% Al alloy.

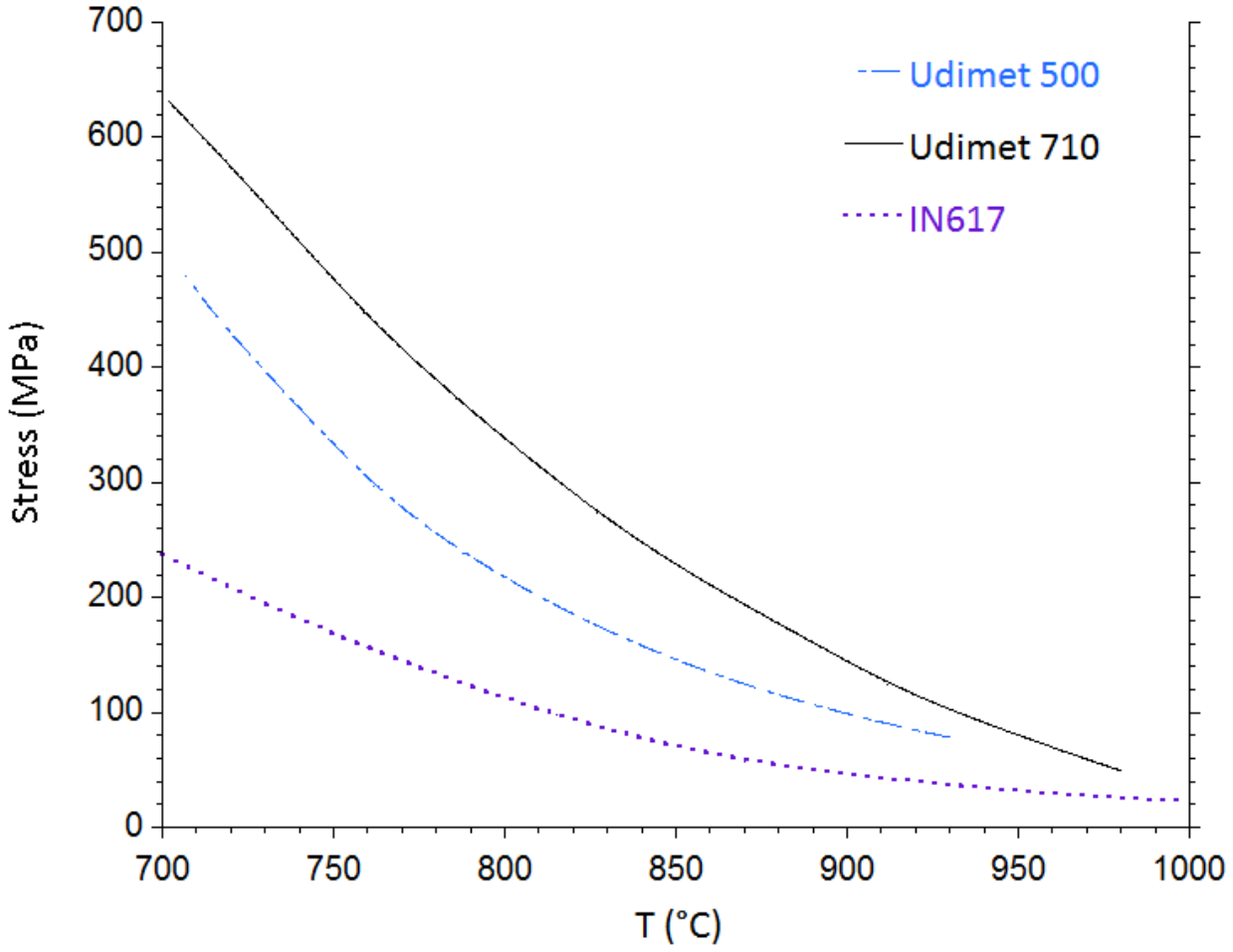

Figure 5.10. 1000h rupture strengths of 6.2 at.% Al containing Udimet 500 and 5.1 at.% Al containing Udimet 710 [32] in comparison with that of IN617 [88] as a function of temperature.

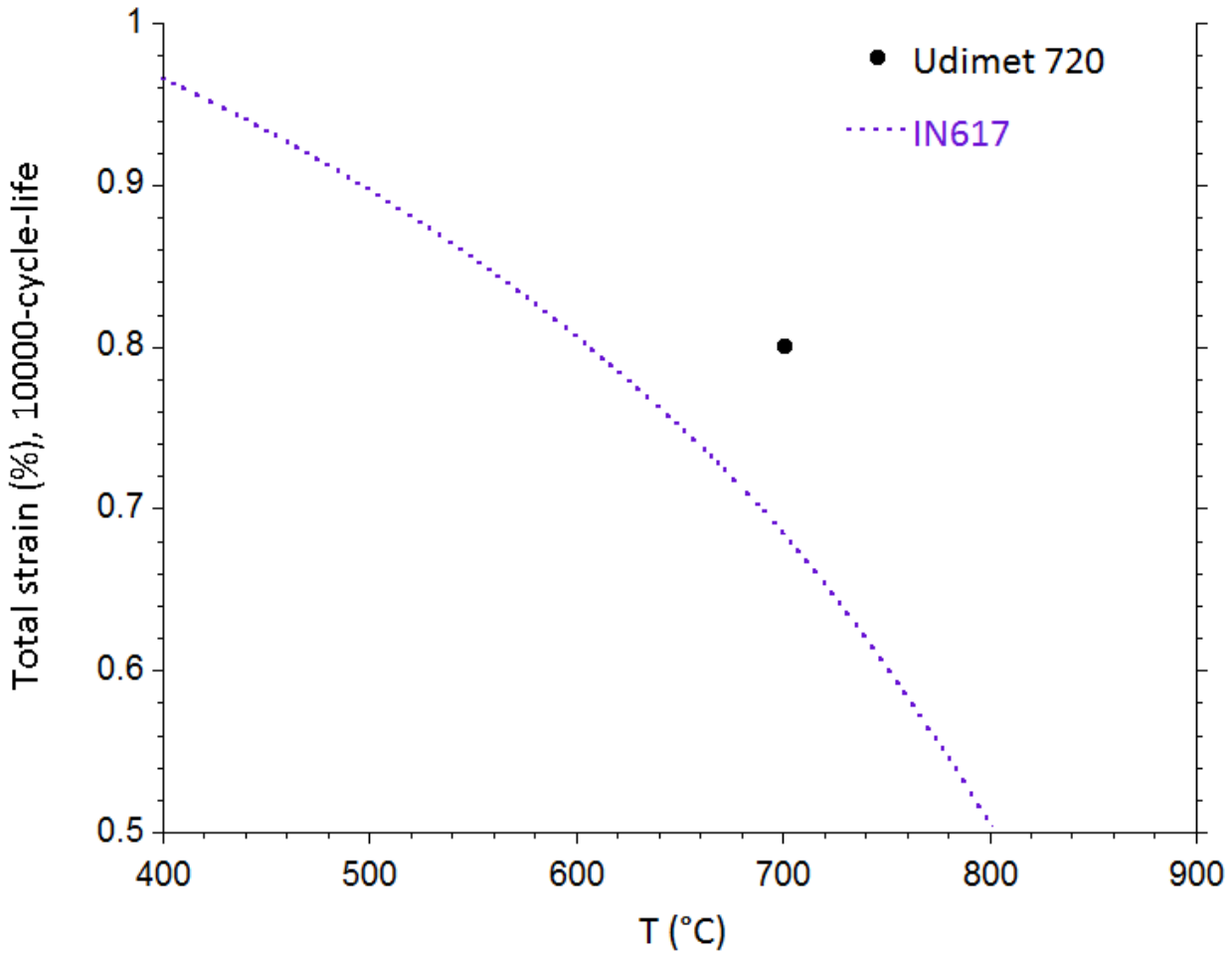

Figure 5.11. Comparison of the low cycle fatigue strength of IN617 [88] with that of Udimet 720 [130], which is very similar in composition to the alloys listed in Table 5.9.

CHAPTER 6

CONCLUSIONS

The conclusions of this dissertation work are as follows:

1. The life-limiting corrosion process for IN617 in He-CO-CO_2 environments is internal Al oxidation in the temperature range of 750 - 850 °C.
2. The governing mechanism for the rapid internal Al oxidation kinetics of IN617 in He-CO-CO_2 environments at 750 - 850 °C is enhanced oxygen diffusion along the incoherent Al_2O_3 - alloy interfaces. The oxygen diffusion coefficients along these interfaces are several orders of magnitude greater than that reported in pure nickel and binary nickel based alloys, indicating that oxygen diffusion through the alloy matrix surrounding the Al_2O_3 precipitates is too slow to sustain the observed internal Al oxidation kinetics of IN617.
3. Lower activation energy and greater magnitude of the oxygen diffusion coefficient along the intergranular Al_2O_3 - alloy interfaces than those along the transgranular Al_2O_3 - alloy interfaces indicates that the alloy grain boundaries facilitate intergranular Al_2O_3 precipitation.

4. A second mechanism that contributes to the rapid internal Al oxidation kinetics of IN617 is increased oxygen solubility at the alloy - Cr_2O_3 interfaces due to gas permeability of Cr_2O_3. The oxygen solubility at the alloy - Cr_2O_3 interface is a factor of 4 greater than that established at the alloy surface by the dissociation oxygen partial pressure of Cr_2O_3 in the Rhines pack exposure. This result is the first quantitative evidence confirming that surface Cr_2O_3 film is gas permeable.
5. Surface Cr oxidation of IN617 in He-CO-CO_2 environments is primarily controlled by the outward diffusion of Cr cations. Cr_2O_3 film appears to be an n-type oxide in which Cr interstitials are the predominantly mobile species. Cr_2O_3 grows on IN617 at a rate greater than that can be sustained by lattice diffusion of Cr cations in Cr_2O_3, indicating that grain boundary diffusion of Cr cations facilitates the Cr_2O_3 growth kinetics.
6. The critical concentration of aluminum required in IN617 to prevent severe internal penetration of Al_2O_3 in the He-CO-CO_2 environments at 850 °C is 5 at. %.

CHAPTER 7

FUTURE WORK

The key contribution of this dissertation to corrosion science is the identification of interface diffusion within the internal oxidation zone, and gas permeability of the passivation layers to be processes by which enhanced oxygen transport induces severe internal oxidation in aluminum containing nickel based alloys at high temperatures. Perhaps, one of the major limitations of the internal oxidation measurements presented in this work is that the values of the oxygen diffusion coefficients determined depend on the oxygen solubility values reported in the literature. The only independent and reliable oxygen solubility measurement was reported in pure nickel [107]. Even though the thermodynamic formalism provided by Guan and Smeltzer [83] predicts the oxygen solubility in a Ni-Cr-Al alloy from that reported in pure nickel (Section 5.1), the absolute value of oxygen solubility in IN617 could not be determined accurately because the interaction parameters of Co - O and Mo - O in a nickel based matrix are unknown. Therefore, it is necessary to determine the oxygen solubility in IN617 accurately to estimate more accurate oxygen diffusion coefficient values from the internal oxidation measurements. Here, it is proposed that the oxygen solubility in model Ni-Cr-Al alloys and IN617 can directly be measured using a coulometric titration technique in a similar experiment setup developed by

Park and Altstetter [107]. The basic idea is to sustain solid state diffusion of atomic oxygen by creating an electric potential gradient across a specimen and determine the oxygen solubility in the specimen from the change in the ionic current across the specimen as a function of time. This can be realized by building a double galvanic cell structure with one specimen electrode, two ZrO_2/Y_2O_3 electrolytes and two reference electrodes made of Al - Al_2O_3 heterostructure, one of which acts as oxygen source. Care must be taken to avoid ambient oxygen to react with the specimens; therefore it is recommended that the coulometric titration measurements to be done in an Al - Al_2O_3 Rhines pack at high temperatures.

Another important finding in this dissertation is the enhancement of oxygen diffusion coefficients along the incoherent Al_2O_3 - IN617 interfaces. However, the atomic arrangement and the chemistry of these boundaries have not been well characterized and the factors contributing to the increase in the oxygen diffusion coefficients have not been identified. A plausible approach to determine the Arrhenius parameters of the oxygen diffusion coefficient along the Al_2O_3-alloy interfaces could be exposing pre-oxidized IN617 samples to $C^{18}O$-$C^{18}O_2$ radiotracer containing environments in the temperature range of 750 - 850 °C and measuring the diffusion profile of ^{18}O along the Al_2O_3-alloy interfaces using SIMS technique featuring a spatial resolution of 50nm and sub-appm level detection limit for oxygen. For comparison, the diffusion profile of ^{18}O can be measured within the alloy matrix to determine the lattice oxygen diffusion coefficient in IN617. The comparison of the pre-exponential coefficients and the activation energies of both interfacial and lattice oxygen diffusion coefficients measured by the radiotracer technique can give an insight on the diffusion mechanisms that enhance oxygen transport along the Al_2O_3 - alloy interfaces.

Finally, from an alloy design point of view, internal oxidation must be avoided to achieve optimum oxidation resistance and mechanical properties. This dissertation work showed that increasing the concentration of aluminum in IN617 above 5 at.% can prevent severe internal penetration of Al_2O_3 in the He - CO - CO_2 environments at 850 °C. Formation of α-Al_2O_3 as a continuous sub-oxide beneath surface Cr_2O_3 or as a surface oxide can greatly improve the oxidation resistance of the alloy. Since the decarburization mechanism is limited by the reduction of surface Cr_2O_3 by carbon in the alloy matrix [16,38], formation of a surface α-Al_2O_3 can eliminate decarburization of IN617. As a result the service temperature of high Al containing IN617 (> 5 at.%) can be increased above 1000 °C for the IHX application. Therefore, it is imperative to test the internal oxidation behavior of Ni-Cr-Co-Mo-5Al and Ni-Cr-Co-Mo-10Al alloys in Cr - Cr_2O_3 Rhines packs and He-CO-CO_2 environments in the temperature range of 750 - 850 °C. Even though higher Al content in Ni-based alloys mainly contribute to precipitation of γ', the principal strengthening phase in the alloy [32], it has also been shown that high Al concentrations may result in formation of the brittle topologically closed pack (TCP) phases [135]. Therefore, special attention must also be given to assess the creep rupture properties of these model alloys at high temperatures.

BIBLIOGRAPHY

[1] J.K. Wright, Next Generation Nuclear Plant Steam Generator and Intermediate Heat Exchanger Materials Research and Development Plan; INL/EXT-08-14107, 2010.

[2] R.E. Mizia, Next Generation Nuclear Plant Intermediate Heat Exchanger Acquisition Strategy; INL/EXT-08-14054, 2008.

[3] R.N. Wright, Summary of Studies of Aging and Environmental Effects on Inconel 617 and Haynes 230; INL/EXT-06-11750, 2006.

[4] C. Cabet, J. Chapovaloff, F. Rouillard, G. Girardin, D. Kaczorowski, K. Wolski, M. Pijolat, J. Nucl. Mater. 375 (2008) 173.

[5] C. Cabet, A. Terlain, P. Lett, L. Guétaz, J.-M. Gentzbittel, Mater. Corros. 57 (2006) 147.

[6] 2010 ASME Boiler and Pressure Vessel Code, American Society of Mechanical Engineers, 2010.

[7] K. Natesan, A. Purohit, S.W. Tam, Materials Behavior in HTGR Environments; NUREG/CR-6824, ANL-02/37, Argonne, IL, 2003.

[8] J.K. Wright, L.J. Carroll, C. Cabet, T.M. Lillo, J.K. Benz, J. A. Simpson, W.R. Lloyd, J. A. Chapman, R.N. Wright, Nucl. Eng. Des. 251 (2012) 252.

[9] R. Wright, J. Wright, C. Cabet, in: Compr. Nucl. Mater., Elsevier Inc., (2012) 251.

[10] F. Rouillard, C. Cabet, K. Wolski, M. Pijolat, Oxid. Met. 68 (2007) 133.

[11] W.J. Quadakkers, H. Schuster, Mater. Corros. 36 (1985) 141.

[12] W.J. Quadakkers, Mater. Corros. 36 (1985) 335.

[13] W.J. Quadakkers, H. Schuster, Nucl. Technol. 66 (1984) 383.

[14] H. Christ, D. Schwanke, T. Uihlein, Oxid. Met. 30 (1988).

[15] H. Christ, U. Künecke, K. Meyer, H. Sockel, Oxid. Met. 30 (1988) 27.

[16] D. Kumar, R.R. Adharapurapu, T.M. Pollock, G.S. Was, Metall. Mater. Trans. A 42 (2011) 1245.

[17] Y. Hosoi, S. Abe, Metall. Trans. A 6 (1975) 1171.

[18] H. Yun, P. Ennis, H. Nickel, H. Schuster, J. Nucl. Mater. 125 (1984) 258.

[19] C. Wagner, Zeitschrift Fur Elektrochemie, Berichte Der Bunsengesellschaft Fur Phys. Chemie 63 (1959) 772.

[20] R. Rapp, Acta Metall. (1961) 730.

[21] D. Young, High Temperature Oxidation and Corrosion of Metals, 1st Ed., Elsevier, Oxford, UK, 2008.

[22] F. Gesmundo, Y. Niu, Oxid. Met. 60 (2003) 347.

[23] F. Gesmundo, Y. Niu, Oxid. Met. 62 (2004) 357.

[24] D.J. Young, Int. J. Hydrogen Energy 32 (2007) 3763.

[25] D.J. Young, S. Watson, Oxid. Met. 44 (1995) 239.

[26] X.G. Zheng, D.J. Young, Corros. Sci. 38 (1996) 1877.

[27] X.G. Zheng, D.J. Young, Oxid. Met. 42 (1994) 163.

[28] F. Rouillard, C. Cabet, K. Wolski, M. Pijolat, Corros. Sci. 51 (2009) 752.

[29] D. Whittle, Y. Shida, G. Wood, F. Stott, B. Bastow, Philos. Mag. A 46 (1982) 931.

[30] F. Stott, G. Wood, D. Whittle, B. Bastow, Y. Shida, A. Martinez-Villafane, Solid State Ionics 12 (1984) 365.

[31] F.H. Stott, G.C. Wood, Mater. Sci. Technol. 4 (1988) 1072.

[32] M.J. Donachie, S.J. Donachie, Superalloys - A Technical Guide, 2nd Ed., ASM International, 2002.

[33] S. Kihara, J.B. Newkirk, A. Ohtomo, Y. Saiga, Metall. Trans. 11 (1980) 1019.

[34] W. Mankins, J. Hosier, T. Bassford, Metall. Trans. 5 (1974) 2579.

[35] W. Ren, R. Swimdeman, J. Press. Vessel Technol. 131 (2009) 024002.

[36] Q. Wu, H. Song, R.W. Swindeman, J.P. Shingledecker, V.K. Vasudevan, Metall. Mater. Trans. A 39 (2008) 2569.

[37] P. Shankar, K. Natesan, J. Nucl. Mater. 366 (2007) 28.

[38] D. Kumar, Mechanisms of Oxidation of Alloy 617 in He-CO-CO_2 Environment with Varying Carbon and Oxygen Potentials, University of Michigan Ann Arbor, 2010.

[39] K.B.S. Rao, Mater. Sci. Eng. A 104 (1988) 37.

[40] K. Rao, H. Schiffers, H. Schuster, H. Nickel, Metall. Trans. A 19 (1988).

[41] C. Wagner, Zeitschrift Für Phys. Chemie 21 (1933) 25.

[42] H.J. Christ, L. Berchtold, H.G. Sockel, Oxid. Met. 26 (1986) 45.

[43] S. Guillou, C. Cabet, C. Desgranges, L. Marchetti, Y. Wouters, Oxid. Met. 76 (2011) 193.

[44] C. Cabet, B. Duprey, Nucl. Eng. Des. 251 (2012) 139.

[45] D. Kim, C. Jang, W.S. Ryu, Oxid. Met. 71 (2009) 271.

[46] N. Birks, G.H. Meier, F.S. Pettit, Introduction to the High-Temperature Oxidation of Metals, 2nd Ed., Cambridge University Press, Cambridge, 2006.

[47] E. Hart, Acta Metall. 5 (1957) 597.

[48] F. Pettit, R. Yinger, J. Wagner, Acta Metall. (1960).

[49] D.R. Gaskell, An Introduction to Transport Phenomena In Materials Engineering, 2nd Ed., Momentum Press, New York, NY, 2012.

[50] D. Caplan, G.I. Sproule, Oxid. Met. 9 (1975) 459.

[51] H. Hindam, D.P. Whittle, J. Electrochem. Soc. 130 (1983) 1519.

[52] H. Hindam, D.P. Whittle, Oxid. Met. 18 (1982).

[53] S. Tsai, A. Huntz, C. Dolin, Mater. Sci. Eng. A 212 (1996) 6.

[54] W. Smeltzer, D. Young, Prog. Solid State Chem. 10 (1975) 17.

[55] A. Atkinson, Corros. Sci. 22 (1982) 347.

[56] W.C. Hagel, A.U. Seybolt, J. Electrochem. Soc. 108 (1961) 1146.

[57] P. Kofstad, K.P. Lillerud, J. Electrochem. Soc. 127 (1980) 2410.

[58] K. Lillerud, P. Kofstad, J. Electrochem. Soc. 127 (1980) 2397.

[59] J. Park, K. Natesan, Oxid. Met. 33 (1990).

[60] B. Pujilaksono, T. Jonsson, M. Halvarsson, I. Panas, J.E. Svensson, L.G. Johansson, Oxid. Met. 70 (2008) 163.

[61] A. Sabioni, A. Huntz, J. Philibert, J. Mater. Sci. 27 (1992) 4782.

[62] A. Atkinson, Rev. Mod. Phys. 57 (1985) 437.

[63] P. Kofstad, K. Lillerud, Oxid. Met. 17 (1982) 177.

[64] C.M. Cotell, G.J. Yurek, R.J. Hussey, D.F. Mitchell, M.J. Graham, Oxid. Met. 34 (1990) 173.

[65] A. Huntz, J. Mater. Sci. Lett. 8 (1999) 1981.

[66] P. Kofstad, High Temperature Corrosion, Elsevier Applied Science, 1988.

[67] K. Lillerud, P. Kofstad, Oxid. Met. 17 (1982) 127.

[68] A. Atkinson, T. R., in: G. Simkovich, V.S. Stubican (Eds.), NATO ASI Ser. B (1984) 285.

[69] D.M. England, A. V. Virkar, J. Electrochem. Soc. 148 (2001) A330.

[70] R. Lobnig, H. Schmidt, K. Hennesen, H. Grabke, Oxid. Met. 37 (1992) 81.

[71] H. Sockel, B. Saal, M. Heilmaier, Surf. Interface Anal. 12 (1988) 531.

[72] A. Sabioni, A. Huntz, F. Millot, C. Monty, Philos. Mag. A 66 (1992) 351.

[73] A. Sabioni, B. Lesage, Philos. Mag. A 66 (1992) 333.

[74] A. Sabioni, A. Huntz, F. Millot, C. Monty, Philos. Mag. A 66 (1992) 361.

[75] C. Giggins, F. Pettit, Metall. Trans. 2 (1971) 1071.

[76] R. Rapp, Corrosion 21 (1965) 382.

[77] F. Maak, Zeitschrift Für Met. 52 (1961) 538.

[78] I. Wolf, H. Grabke, Solid State Commun. 54 (1985) 5.

[79] G. McAdam, D.J. Young, Oxid. Met. 37 (1992) 281.

[80] J. Unsworth, D. Young, Oxid. Met. 60 (2003) 447.

[81] F.H. Stott, G.C. Wood, J. Stringer, Oxid. Met. 44 (1995) 113.

[82] C. Wagner, Corros. Sci. 5 (1965) 751.

[83] S. Guan, W. Smeltzer, Oxid. Met. 42 (1994) 375.

[84] J. A. Nesbitt, R.W. Heckel, Metall. Trans. A 18 (1987) 2061.

[85] C.S. Giggins, F.S. Pettit, J. Electrochem. Soc. 118 (1971) 1782.

[86] F. Rhines, Trans. AIME 137 (1940) 246.

[87] ASTM Stand. E112 − 12, "Standard Test Methods Determ. Aver. Grain Size" (2013) 1.

[88] INCONEL® Alloy 617 Specifications, Special Metals

[89] G.S. Was, J.W. Jones, G. Gulsoy, A.O. Okello, NEUP 09-678 Quarterly Progress Report Y2Q4, 2011.

[90] D. Kumar, C.J. Torbet, G.S. Was, Meas. Sci. Technol. 20 (2009) 95708.

[91] J.R. Ferraro, K. Nakamoto, Introductory Raman Spectroscopy, 2nd Ed., Amsterdam: Academic Press, 2003.

[92] D. Briggs, M.P. Seah, Practical Surface Analysis, 2nd Ed., Chichester: Wiley, 1990.

[93] S. Hofmann, Auger- and X-Ray Photoelectron Spectroscopy in Materials Science, Springer Berlin Heidelberg, Berlin, Heidelberg, 2013.

[94] N. Fairley, Http//www.casaxps.com, ©Casa Softw. Ltd. (2005).

[95] M.C. Biesinger, B.P. Payne, A.P. Grosvenor, L.W.M. Lau, A.R. Gerson, R.S.C. Smart, Appl. Surf. Sci. 257 (2011) 2717.

[96] D.B. Williams, C.B. Carter, Transmission Electron Microscopy: A Textbook for Materials Science, New York: Plenum Press, 1996.

[97] B. Fultz, J. Howe, Transmission Electron Microscopy and Diffractometry of Materials, 3rd Ed., 2008.

[98] K.W. Andrews, D.J. Dyson, Interpretation of Electron Diffraction Patterns, 2nd Ed., New York: Plenum Press, 1971.

[99] J. Cowley, J. Electron Microsc. Tech. 3 (1986) 25.

[100] H. Yi, S. Guan, W. Smeltzer, A. Petric, Acta Metall. Mater. 42 (1994) 981.

[101] R. Farrow, P. Mattern, A. Nagelberg, Thin Solid Films 73 (1980) 353.

[102] Y. Mishima, S. Ochiai, T. Suzuki, Acta Metall. 33 (1985) 1161.

[103] W.E. Lee, K.P.D. Lagerlof, J. Electron Microsc. Tech. 2 (1985) 247.

[104] B. Strohmeier, Surf. Interface Anal. 15 (1990) 51.

[105] S. Tanuma, C. Powell, D. Penn, Surf. Interface Anal. 17 (1991) 911.

[106] C.H.P. Lupis, Chemical Thermodynamics of Materials, North-Holland, New York, 1983.

[107] J.W. Park, C.J. Altstetter, Metall. Trans. A 18 (1987) 43.

[108] O. Kubaschewski, C.B. Alcock, Materials Thermochemistry, 6th Ed., Oxford: Pergamon Press, 1993.

[109] J.A. Nesbitt, R.W. Heckel, Metall. Trans. A 18 (1987) 2075.

[110] D. England, A. Virkar, J. Electrochem. Soc. 146 (1999) 3196.

[111] A. Seybolt, R. Fullman, Trans. AIME J. Met 200 (1954) 548.

[112] A.U. Seybolt, Dissertation, Yale University, 1936.

[113] C. Alcock, P. Brown, Met. Sci. 3 (1969) 116.

[114] R. Barlow, P. Grundy, J. Mater. Sci. 4 (1969) 797.

[115] S. Goto, K. Nomaki, S. Koda, J. Japan Inst. Met. 31 (1967) 600.

[116] G.J. Lloyd, J.W. Martin, Met. Sci. 7 (1973) 75.

[117] J. Lloyd, J.W. Martin, 6 (1972) 7.

[118] R.A. Kerr, Ph.D. Thesis, Ohio State University Columbus, OH, 1972.

[119] S.P. Zholobov, M.D. Malev, Sov. Phys. Tech. Phys. 16 (1971) 488.

[120] S. Garruchet, O. Politano, P. Arnoux, V. Vignal, Solid State Commun. 150 (2010) 439.

[121] H.O. Nam, I.S. Hwang, K.H. Lee, J.H. Kim, Corros. Sci. 75 (2013) 248.

[122] I. Kaur, Y. Mishin, W. Gust, Fundamentals of Grain and Interphase Boundary Diffusion, 3rd rev., Chichester: John Wiley, 1995.

[123] S. Perusin, B. Viguier, D. Monceau, L. Ressier, E. Andrieu, Acta Mater. 52 (2004) 5375.

[124] S. Pérusin, High Temperature Oxidation of Metals : Vacancy Injection and Consequences on the Mechanical Properties, Centre Interuniversitaire de Recherche et d'Ingénierie des Matériaux - CIRIMAT Toulouse, France, 2004.

[125] S. Perusin, D. Monceau, E. Andrieu, J. Electrochem. Soc. 152 (2005) E390.

[126] Y. Shida, F. Stott, B. Bastow, D. Whittle, G. Wood, Oxid. Met. 18 (1982) 93.

[127] P. Rogl, in:, G. Petzow, G. Effenberg (Eds.), Ternary Alloy., VCH, 4 (1991) 400.

[128] M. Burke, J. Greggi Jr, G. Whitlow, Scr. Metall. 18 (1984) 91.

[129] N. Lambert, J. Drapier, J. Collin, D. Coutsouradisyc, in: Superalloys (1968) 312.

[130] M. Marchionni, G. Osinkolu, G. Onofrio, Int. J. Fatigue 24 (2002) 1261.

[131] A. Ardell, Metall. Mater. Trans. A 16 (1985) 2131.

[132] M.. Acharya, G. Fuchs, Mater. Sci. Eng. A 381 (2004) 143.

[133] H. Kim, S. Chun, X. Yao, Y. Fang, J. Choi, J. Mater. Sci. 32 (1997) 4917.

[134] E.A. Brandes, Smithells Metals Reference Book, 6th Ed., Butterworths, London, 1983.

[135] F. Ritzert, D. Arenas, D. Keller, V. Vasudevan, The Effect of Alloying on Topologically Close Packed Instability in Advanced Nickel-Base Superalloy Rene N6, 1998.